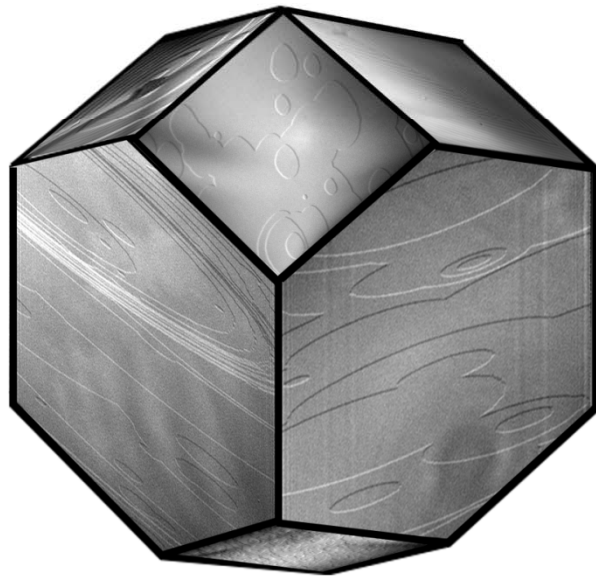


Laboratorio de Estudios Cristalográficos
Instituto Andaluz de Ciencias de la Tierra
CSIC - Universidad de Granada

In situ observation of protein crystal
growth by advanced optical techniques



TESIS DOCTORAL

Alexander E.S. Van Driessche



Laboratorio de Estudios Cristalográficos
Instituto Andaluz de Ciencias de la Tierra
CSIC – Universidad de Granada



In situ observation of protein crystal growth
by advanced optical techniques

Alexander Edgard Suzanne Van Driessche

TESIS DOCTORAL

GRANADA

2007

Laboratorio de Estudios Cristalográficos
Instituto Andaluz de Ciencias de la Tierra
CSIC – Universidad de Granada

Memoria presentada para optar al Grado de Doctor en Ciencias Geológicas

Fdo: Alexander E.S. Van Driessche
Licenciado en Ciencias Geológicas por la Universidad de Granada y Gante

Granada, 20 de Diciembre de 2007

Directores de la Tesis:

Fdo:
Fermín Otalora Muñoz
Científico titular
Instituto Andaluz de Ciencias de la
Tierra
Laboratorio de Estudios
Cristalográficos
CSIC – U. Granada

Fdo:
José Antonio Gavira Gallardo
Científico titular
Instituto Andaluz de Ciencias de la
Tierra
Laboratorio de Estudios
Cristalográficos
CSIC – U. Granada

Ensanguining the skies
How heavily it dies
Into the west away;
Past touch and sight and sound
Not further to be found,
How hopeless under ground
Falls the remorseful day.

TABLE OF CONTENTS

I. ABSTRACT	1
II. INTRODUCTION	3
1. Why study protein crystal growth?	3
2. Macromolecular crystallization from solution	6
2.1. Supersaturation.....	6
2.2. Nucleation.....	9
2.3. Crystal growth.....	12
2.3.1. Crystal growth mechanisms.....	14
2.3.2. Crystal growth kinetics.....	19
2.4. Cessation of growth	23
2.5. Impurities.....	24
2.5.1. Types of impurities.....	26
2.5.2. Impurity mechanisms.....	28
2.5.3. Trapping of impurities.....	31
3. Observation techniques.....	33
III. MATERIALS AND METHODS	
1. Model system.....	36
1.1. Lysozyme.....	36
1.2. Crystallization of lysozyme.....	38
1.3. Fluorescence labelled lysozyme.....	39
1.4. Contaminate HEWL – Impurities –	40
1.5. Solubility of tetragonal lysozyme.....	42
2. Observation techniques.....	44
2.1. Laser Confocal Interference Differential Contrast Microscopy (LCM-DIM).....	44
2.1.1. Setup.....	44
2.1.2. Single Molecule Visualisation (SMV).....	59
2.1.3. Observation cell preparation.....	63
2.2. Phase Shifting Michelson Interferometry (PSMI).....	67
2.2.1. Setup.....	69
2.2.2. Observation cell preparation.....	71
2.2.3. Processing of phase-shifting interferometry data.....	72
2.3. Atomic Force Microscopy (AFM).....	74
2.3.1. Setup.....	74

2.3.2. Sample preparation.....	77
3. Protocol of a typical crystal growth experiment.....	79
IV. RESULTS AND DISCUSSION	
1. Measuring growth kinetics using different observation techniques.....	85
1.1. Growth kinetics measured by atomic force microscopy, interferometry and LCM-DIM.....	86
1.1.1. Step velocities	86
1.1.2. 2D Nucleation rates	92
1.1.3. Normal growth rates.....	93
1.2. Discussion.....	96
1.3. Conclusions.....	104
2. Molecular level in situ observation of protein crystal growth by Phase –shifting Michelson Interferometry (PSMI).....	110
2.1. Observation of monolayer steps.....	110
2.2. Discussion and conclusions.....	113
3. Surface morphology and growth kinetics of tetragonal lysozyme in free solution.....	127
3.1. Introduction.....	127
3.2. Source of the growth steps – Growth mechanisms –	128
3.2.1. Spiral growth or two dimensional growth.....	129
3.2.2. Spiral dislocations as step source.....	131
3.3. Growth step kinetics.....	138
3.3.1. Step morphology.....	138
3.3.2. Step velocities and kinetic coefficient β	138
3.3.3. Surface kinetics versus volume diffusion.....	151
3.3.4. Step fluctuations.....	161
3.4. Impurity effect on growth step kinetics	167
3.4.1. Introduction.....	167
3.4.2. Step morphology.....	169
3.4.3. Impurity effect on step velocities.....	171
3.4.4. Adsorption sites of impure proteins.....	175
3.4.5. Adsorption sites and supersaturation dependencies of step velocities.....	179
3.4.6. Spiral growth versus 2D growth.....	181
3.4.7. Commercial lysozyme solution.....	183

3.4.8. Step bunching.....	187
3.5. Two dimensional nucleation kinetics.....	197
3.5.1. Introduction.....	197
3.5.2. Two dimensional nucleation behavior.....	199
3.5.3. Two dimensional nucleation rates	
– Surface free energy –	205
3.6. Normal growth rate.....	213
3.7. Summary and conclusions.....	219
4. Surface morphology and growth kinetics of tetragonal lysozyme	
in gelled solution.....	225
4.1. Introduction.....	225
4.2. Effect of agarose gel on growth kinetics.....	226
4.2.1. Step Morphology.....	227
4.2.2. 2D nucleation rates.....	228
4.2.3. Step velocities.....	230
4.3. Effect of impurities on growth kinetics in gelled solution.....	231
4.3.1. Step Morphology.....	232
4.3.2. 2D nucleation rates.....	233
4.3.3. Step velocities.....	234
4.4. Discussion.....	235
4.5. Conclusions.....	244
V. GENERAL CONCLUSIONS	247
VI. REFERENCES	253
VII. APPENDIX	271

I. ABSTRACT

In situ observation of protein crystal growth by advanced optical techniques

A.E.S Van Driessche, LEC-IACT, CSIC-U.Granada, 2007.

ABSTRACT

In the first part of this work the role of tapping mode Atomic Force Microscopy (TM AFM) and Phase Shifting Interferometry (PSI) as characterization techniques for crystal growth are compared with that of LCM-DIM. For doing so growth of model protein lysozyme was observed by these three techniques and several growth parameters such as step velocity, 2D nucleation rate and normal growth rate were determined. These parameters were measured in a broad supersaturation range for tetragonal crystals growing from a highly purified solution.

Without doubt AFM is the most powerful and useful technique for atomic level observations. This tool is capable of providing excellent spatial resolution on a molecular level which allows atomic level quantitative analyses of the morphological characteristics of protein crystal surfaces. Thus, provided a good model system, a skilled AFM operator is capable of determining thermodynamic and kinetic parameters of crystal growth at a molecular level. On the other hand it was shown that AFM is not the most appropriated choice for precise quantitative determination of mesoscopic and macroscopic growth parameters.

Laser confocal microscopy combined with differential interference contrast microscopy (LCM-DIM) is very effective to obtain non invasive high

Abstract

contrast images of surface micromorphologies of growing protein crystals visualizing an entire crystal surface. Step dynamics and the nucleation process can be observed undisturbed over long time periods. This technique also has a fast time resolution and good lateral and vertical resolution. Hence, this advanced optical microscopy technique is very suitable for mesoscopic growth kinetic measurements. This technique closes the gap between the atomic observations of AFM and macroscopic observations of interferometry.

Interferometry is the most appropriated technique for macroscopic level observations. The non-invasive character of PSI makes it possible to follow growth processes over long experimental times and the use of sealed growth cells ensures an undisturbed crystallization. The short exposure times needed for image acquisition (approx. 200 ms for each frame) enable the investigation of fast processes even under high supersaturation conditions. This technique is ideal to quantitatively characterize the morphology of the growth interface and its evolution over time providing detailed insight into the interface dynamics and associated step kinetics. The sources which generate growth steps can be determined as well as the relative importance of transport processes versus surface kinetics. Also the influence of impurity incorporation on macroscopic growth processes can be studied. It's ability to simultaneously gather morphological information with high resolution at several, widely-spaced positions on the crystal surface, allows studying the growth mechanisms by which a facet retains its morphological stability.

Abstract

In the second part of this work growth morphology and kinetics of tetragonal lysozyme crystals in unstirred solution with characterized protein composition have been studied using mainly LCM-DIM.

2D nucleation of the birth and spread type was found to be the dominant growth mechanism for both faces, {110} and {101}, of tetragonal lysozyme crystals under the conditions used in this study. Spiral growth was occasionally observed only when microcrystals were adsorbed on the crystal surface or the crystals suffered mechanical stress. For this reason most of the growth studies were done on faces showing 2D nucleation growth.

The intrinsic anisotropy of the step velocity is constant for the studied supersaturation range and kinetic coefficients for different crystallographic directions were determined for the {110} and {101} faces. Changing temperature has no effect on the kinetic coefficients which indicates that the activation energy for incorporation is relatively high. For lysozyme crystallization from unstirred solution the process of incorporation of molecules into the growing crystal contributes most to the value of β in the studied supersaturation range of $C-C_e < 0.45$ mg/ml. Thus growth is mainly kinetically controlled.

The effect of foreign proteins on the growth of elementary steps of 2D islands was also studied, using three kinds of proteins: fluorescence-labeled lysozyme (F-lysozyme), covalently-bonded dimers of lysozyme and 18 kDa polypeptide (18kDa). These three impurity proteins suppressed the advancement of the steps. However, they exhibited different supersaturation dependencies of the suppression of step velocities. As a measure of the

impurity effect the ratio R of step velocity in a purified lysozyme solution to that in a solution containing impure proteins at the same supersaturation was calculated. The R vs. supersaturation plot of F-lysozyme showed a convex shape, and R had the maximum in a middle supersaturation range. In contrast, the plots of dimer and 18kDa exhibited a concave shape, and R decreased monotonically with increasing supersaturation. To clarify the cause of this difference, we observed in situ adsorption processes of individual molecules of F-lysozyme and fluorescent-labeled dimer (F-dimer) on the crystal surfaces, using a single-molecule visualization technique. It was found that F-lysozyme adsorbed specifically on steps, whereas F-dimer adsorbed randomly on terraces. Using the different adsorption sites of F-lysozyme and F-dimer, the different effects of the impurities on the step velocities were successfully explained. These results strongly suggest that 18kDa also adsorbs randomly on terraces. This indicates that impure molecules whose intermolecular bonding is close to that of the solute molecule adsorbs preferentially on a step, and that impure molecules whose intermolecular bonding differs from that of the solute molecule adsorbs on a different sites on a crystal surface. The R vs. supersaturation plot of Seikagaku lysozyme exhibited a complex shape that could not alone be explained by taking into account the effects of two major impurities (dimer and 18kDa) present in Seikagaku lysozyme.

Two-dimensional (2D) nucleation behavior on $\{110\}$ and $\{101\}$ faces of tetragonal crystals of model protein lysozyme was also studied. 2D nucleation rates were measured using 99.99% pure lysozyme, 98.5% pure lysozyme (Seikagaku Co.), and 99.99% pure lysozyme with intentionally added impure proteins (fluorescent-labeled lysozyme, covalently-bonded dimer of lysozyme and 18 kDa polypeptide). It was found that 2D nucleation occurred randomly

Abstract

on the entire crystal surface irrespective of supersaturation within the range of $\sigma = \ln(C/C_e) = 0-1.4$ (crystal size: 0.2-0.3 mm). Repeated 2D nucleation, which continued for 3 to 4 layers, was also observed mainly when impure proteins were present. In addition, multilayered 2D islands were formed after adsorption of relatively large foreign particles on the crystal surface. From the comparison between 2D nucleation rates determined on the {110} faces with and without the impure proteins, it was concluded that homogeneous 2D nucleation occurred under a higher supersaturation range ($\sigma > 0.8$), irrespective of the presence of impurities. In contrast, under a lower supersaturation range ($\sigma < 0.8$), significant heterogeneous 2D nucleation dominated the growth mainly when impure proteins were present. The {101} faces, whose steps are smaller in height than those of the {110} faces, exhibited similar homogeneous and heterogeneous 2D nucleation, however more significant heterogeneous nucleation was induced by smaller amounts of impurities. Ledge free energies of homogeneous and heterogeneous nucleation were determined. Within the experimental conditions used in this study, no significant dependence of the ledge free energies of heterogeneous nucleation on the kinds of impure proteins was found.

In the second part of this work growth morphology and kinetics of {110} face of tetragonal lysozyme crystals in gelled solution with characterized protein composition were studied using LCM-DIM.

The joint effect of agarose gel and impurities on crystal growth kinetics was investigated *in situ* by comparing the two-dimensional (2D) nucleation rate and the step velocity of crystals growing from free and gelled (agarose) solutions including two different levels of purity. Highly purified (99.99%

Abstract

pure) and commercial grade (98.5% pure) Hen Egg White Lysozyme were used. 2D nucleation rate and step velocity were measured on {110} faces of tetragonal lysozyme crystals. 2D nucleation rates are enhanced by the presence of gel fibers that act as heterogeneous nucleation sites. From these results it was deduced that the specific surface energy are similar for the interface gel fiber / crystal and for the interface gel fiber / solution, which explains the incorporation of agarose fibers into the lysozyme crystal lattice and also confirms the small effect of gel fibers on step advancement. 2D nucleation in the presence of both gel and impurities is also enhanced but not as much as for gelled purified solutions. The presence of agarose has an almost negligible effect on the step kinetics in purified solutions but drastically modifies, by reducing step pinning, the step velocity in crystals growing from impure solutions, shifting these values closer to the velocities measured in purified solutions. This velocity increase corresponds to a 7 times smaller concentration of adsorbed impurities at the crystal surface than in the corresponding ungelled experiments. This indirect proof of the diffusive impurity filtering concept is also consistent with the qualitative observations on 2D island morphologies.

II. INTRODUCTION

1. Why study protein crystal growth?

The current status of protein crystal growth research is leading to a split of the discipline in two main directions: the technological development of, mostly high-throughput, crystallization equipment which is concerned with obtaining good diffracting crystals for structural analysis, and secondly the basic studies of the physics of crystal growth itself. The knowledge that has been accumulated during the last 20 years on the physics of biomolecular crystal growth has basically shown that there is no magic involved (unfortunately); protein crystals nucleate and grow by the same processes already known for small molecules. But more quantitative information is still needed on the physics of protein crystal nucleation and growth to stay advancing in the field by exploring the body of theories and hypothesis known from small molecule crystal growth. This knowledge is mainly required because of the particular properties of biomacromolecules, in particular the relatively low diffusion coefficients, low attachment energy, high concentration in solution, high nucleation barriers and high impurity content that control the behavior of protein crystal growth. Up to now only order of magnitude estimates and a few quantitative data are available for checking the effect of these parameters in the known crystal growth theories, which hinders the understanding of protein crystal growth in terms of: relative development and importance of different growth mechanisms, limits between growth regimes, influence of two-dimensional nucleation on the average growth rate, mechanisms of incorporation of impurities and effect of impurities on the growth process, etc. The study of intrinsic protein crystal growth kinetics ultimately tends to help to resolve to problem of obtaining good diffracting crystals. But, another, often unexploited application of protein crystallization is its use as a, particularly attractive, model for studies of fundamental crystal growth mechanisms. Given the resolution

Why study protein crystal growth?

limits of modern surface characterization techniques, the size of the protein molecules (a few nanometers) and the typical time scales for growth (a few seconds between sequential discrete growth events) are within reach of the current advanced experiment techniques. On the other hand, the molecular masses typical of most protein molecules still leave thermal equilibration times relatively short. Hence, protein crystallization is one of the most suitable model systems by which one can approach elementary processes, such as nucleation and growth on a molecular level. And thus, conclusions drawn from studies of protein model systems may still be meaningful for small molecule crystallization. In this regard, proteins could be a better model than, for instance, colloidal crystals.

2. Macromolecular crystallization from solution

The intention of this chapter is to provide a brief overview on the basics of crystal growth and to orientate the reader on relevant works of the field of crystal growth with emphasis on macromolecular crystal growth. Studies dealing with general crystal growth kinetics can be found in Markov (1973), Chernov (1984), Mullin (1993), Van der Eerden (1993). Specifically for macromolecular crystallization the reading of Chernov & Vekilov (2000) and DeYoreo & Vekilov (2005) are recommended.

The first question that should be answered is: *What is crystallization from solution?* Crystallization is one of several means (including nonspecific aggregation/precipitation) by which a metastable supersaturated solution can reach a stable lower energy state by reduction of solute concentration (Weber, 1991). The general processes by which substances crystallize is similar for small molecules (salts and small organics) and macromolecules (proteins, , viruses, DNA, RNA). In crystallization there are three stages common to all systems: nucleation, growth, and cessation of growth. But before any nucleation or crystal growth can take place we first need to create a supersaturated solution.

2.1. Supersaturation

To grow crystals from solution it is necessary to create a supersaturated state which provides the system with a thermodynamic force for crystallization (Delucas and Bugg *et al.*, 1987). To achieve this

thermodynamical unstable state (e.g. supersaturation) the solubility limit of the compound must be exceeded. This situation is best represented using a phase (or solubility) diagram. Figure 2.1 shows a typical solubility (phase) diagram used for crystallization plotting the solute concentration versus the precipitant concentration. Of course, the x-axis parameter could also be temperature, pH, or any other factor which influences solubility behaviour.

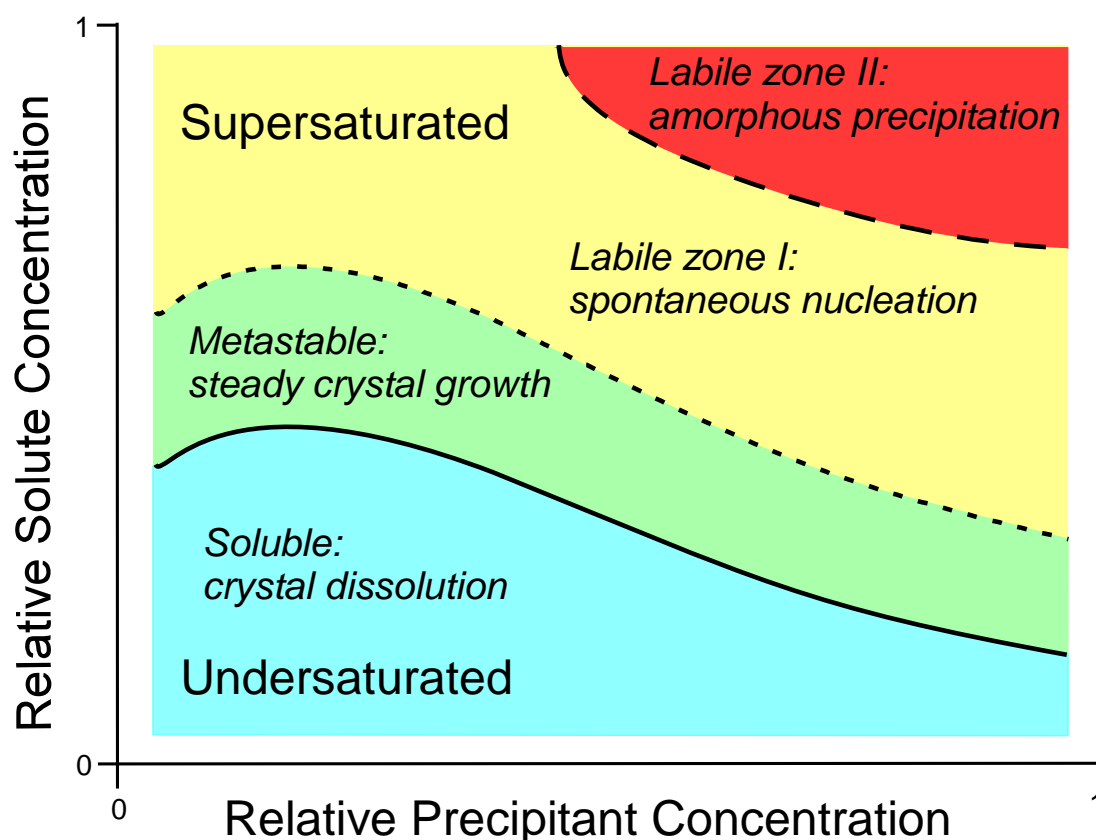


Figure 2.1 A typical solubility diagram for crystallization from solution, plotting the solute concentration versus precipitant concentration. The solid line represents the saturation limit of the solute in the solvent. Anywhere below this limit, the system is undersaturated and no crystal will form or grow from these conditions. Above the saturation limit, the system is supersaturated. In the metastable region, crystals and nuclei can grow but no nucleation occurs. However in the labile zone I high enough chemical potential is provided to form nuclei. Finally in labile zone II the driving force is too high for molecules to form ordered aggregates and amorphous precipitation will occur (Adapted from Jen and Meckle, 2000).

Supersaturation can be defined in thermodynamic terms as the dimensionless difference in chemical potential between a molecule in an equilibrium state and a molecule in its supersaturated state and is the driving force for crystallization. Mathematically, it is expressed as

$$\Delta\mu = k_B T \ln \frac{C}{C_e} \quad (2.1)$$

where k_B is the Boltzmann constant, T the absolute temperature, C the actual concentration before crystallization, and C_e the concentration of the solute at equilibrium. We assume an ideal solution (e.g. infinite dilution), so that the activity coefficient becomes unity and thus solute activity and concentrations are equal.

The supersaturation of a system may be expressed in a number of different ways, and considerable confusion can be caused if the basic units of concentration are not clearly defined. The temperature must also be specified. Among the most common expressions of supersaturation is the concentration driving force Δc , the supersaturation ratio S , and a quantity sometimes referred to as the absolute or relative supersaturation σ . These quantities are defined by:

$$\Delta c = c - c_e \quad (2.2)$$

$$S = \frac{c}{c_e} \quad (2.3)$$

$$\sigma = \frac{\Delta c}{c_e} = S - 1 \quad (2.4)$$

Conventionally, supersaturation is created by methods such as solvent evaporation, temperature variations, or addition of organic solvents. These strategies are, however, unsuitable and destructive for biological macromolecules as they drive protein denaturation and preclude any hope of

crystal formation (McPherson, 1999). The strategy applied in biomacromolecular crystallization is to guide the system slowly towards a state of decreased solubility modifying the properties of the solution. This is accomplished by increasing the concentration of precipitating agents or altering physical properties, e.g. pH, ionic strength, etc. (McPherson, 1982; 1985a; 1985b; Wieneck, 1999; Riès-Kautt and Ducruix, 1997). However, crystals do not grow spontaneously once the supersaturation limit is exceeded because the thermodynamic force of the system is not sufficient to surpass the energetic barrier associated with the creation of a new phase (solid phase). This is the reason why the supersaturated state can physically exist. Without this barrier molecules would immediately precipitate out of solution the instant the solubility limit was exceeded. Indeed, at low levels of supersaturation, the amplitude of the energy fluctuations in solution may not be large enough to exceed this energy barrier and thus, such solutions are often unable to promote the initial formation of nuclei, but can support crystal growth. This region is known as the metastable zone (see figure 2.1). However, when the system is sufficiently supersaturated the energy barrier will be surmounted and solute molecules will begin to coalesce into aggregates, which if of sufficient dimensions, create nuclei. This represents the first step of crystal growth and is known as nucleation. On the other hand, if the saturated state is too high random precipitation of the solute will occur (Figure 2.1).

2.2. Nucleation

Nucleation is a vital step in the crystallization process, and is of immense practical importance in biological systems. It can be defined as the process by which molecules or noncrystalline aggregates (dimers, trimers, etc.) which are free in solution come together in such a way as to produce a

thermodynamically stable aggregated new phase with a repeating lattice. The formation of crystalline aggregates from supersaturated solutions does not however imply the formation of macroscopic crystals. Instead, the aggregate must first exceed a specific size (the critical size) defined by the competition of the ratio of the aggregate surface area to its volume. Once the critical size is exceeded, the aggregate becomes a supercritical nucleus capable of further growth. If the nucleus decreases in size such that it is smaller than the critical size, spontaneous dissolution will occur. The formation process of nonspecific aggregates and noncrystalline precipitation from a supersaturated solution does not involve the competition between surface area and volume (n -mers add to the aggregate chain in a head to tail fashion forming a linear arrangement), and thus generally occurs on a much faster time scale than crystallization (Feher and Kam, 1985; Boistelle and Astier, 1988).

The process of nucleation is discussed at length for crystals of biological importance by McPherson (1999) and Garcia-Ruiz (2003). Without doubt, the most complete work on nucleation physics is presented by Kashchiev (2000).

It is important when studying macromolecular nucleation to understand protein interactions in solutions for under - and supersaturated protein solutions. A wide variety of techniques such as light scattering (static, dynamic, quasi-elastic, small-angle, multi-angle, time-resolved), neutron and X-ray scattering (Rosenberger and Meehan, 1988; George and Wilson, 1994; Eberstein *et al.*, 1994; Muschol and Rosenberger, 1995; Niimura *et al.*, 1995; Georgalis *et al.*, 1997; Lafont *et al.*, 1997; Schaper *et al.*, 1997; Guo *et al.*, 1999; Tardieu *et al.*, 2001, 2002; Finet and Tardieu, 2001; Bonnete and Vivares, 2002) have been used for studying macromolecular interactions in solution. From these experiments information on sample homogeneity,

molecular interactions and aggregate sizes have been obtained. An important advancement in the study of protein interactions was to correlate the success of crystallization to a narrow range of intermolecular potentials with the second virial coefficient (B_2) of the osmotic virial expansion equation (Rosenberger and Meehan, 1988; Wilson, 1990; George and Wilson, 1994; Ducruix *et al.*, 1996; Malfois *et al.*, 1996; Rosenbaum *et al.*, 1996; George *et al.*, 1997; Neal *et al.*, 1998, 1999; Bonnete *et al.*, 1999; Budayova *et al.*, 1999; Guo *et al.*, 1999; Bonnete and Vivares, 2002). This slot of B_2 values can be used as a crystallization predictor since it is neither protein nor precipitant dependent. Haas *et al.* (1999) and Ruppert *et al.* (2001) provided a theoretical basis for the direct link between virial coefficient and solubility.

Some areas of nucleation are still under heavy discussion. Such as; interpretations of the nucleus structure, interfacial free energy, and nucleation rates. While some authors claim the absence of sub-critical aggregates in crystallizing solutions (Miyashita *et al.*, 1994; Muschol and Rosenberger, 1994; 1995; Kuehner *et al.*, 1997; Finet *et al.* 1998; Yoshizaki *et al.*, 2005), others presume the existence of aggregates (Mikol *et al.*, 1989; Azuma *et al.*, 1989; Wilson and Pusey, 1992; Boué *et al.*, 1993; Niimura *et al.*, 1995, 1999; Wang *et al.*, 1996; Tanaka *et al.*, 1999), compact crystalline structures (Kam *et al.*, 1978; Malkin and McPherson., 1993b, 1994), fractals (Georgalis *et al.*, 1993, 1995, 1999; Eberstein *et al.*, 1994; Schaper *et al.*, 1997; Guo *et al.*, 1999) or even quasi planar structures (Yau and Vekilov, 2000a, 2001). This controversial situation might be due to the few studies that have attempted to measure the critical nucleus size in real space, partly due to the transient nature of the process. There are some microscopic studies attempting to characterize these structures at molecular resolution (Yonath *et al.*, 1982; Durbin and Feher, 1990; Michinomae *et al.*, 1999; Braun *et al.*, 2000; Yau and Vekilov, 2000a, 2001; Gasser *et al.*, 2001; Mühlig *et al.*, 2001; Hirsch *et al.*, 2001). The disagreement in nucleus structures has led to a

discordant interpretation of the nucleation mechanisms and kinetics. Classical theories predict the formation of large spherical aggregates (7-80 molecules) with continuous changes in size (Feher and Kam, 1985; Malkin and McPherson, 1993b, 1994). While modern theories suggest the formation of small aggregates (2-10 molecules) whose sizes remain invariant within wide ranges of supersaturation (Galkin and Vekilov, 2000). On the topic of nucleation rate determination, interesting discussions can be found in the works of Galkin and Vekilov (2000), Dixit *et al.* (2001), Vekilov and Galkin (2003) and Zukoski *et al.* (2003).

2.3. Crystal growth

Once the nucleation step has been overcome, nuclei grow and eventually develop into macroscopic crystals. This stage of the crystallization process is known as crystal growth. The mechanisms of protein crystal growth are similar to those for small molecule crystals grown from solution and the process can be separated into two stages: 1) mass transfer of building blocks to the surface, and 2) incorporation of building blocks into the crystal lattice after sticking to the growth surface. The slowest process determines the crystal growth rate, and thus the growth is either transport or kinetic controlled.

For crystal growth to proceed, the surface of the crystal must first be able to capture growth units arriving from solution and subsequently integrate them into the crystal lattice. While this process is dependent on a number of factors, the most important is the availability of so-called kinked sites on the developing crystal surface. In the case of protein crystals growth, proceeds from solution by the layer spreading mechanism because the surfaces are far below their roughening temperature*. The surface consists of

**The mechanism of crystal growth is unambiguously determined by the structure of the crystal surface. Crystal faces are classified as F, S or K. S and K faces are atomically rough. F faces are generally atomically flat but above a thermodynamic roughening temperature entropic factors become more favourable and so an initially flat F face will become atomically rough.*

flat regions called terraces and raised partial layers called steps (Chernov, 1984). The steps themselves are incomplete, containing kinks. Growth only takes place at the steps (i.e. kink sites at the steps). Moreover, terraces between steps will be rather smooth, even on atomic scales. For such surface structures, resistance to growth will be relatively large, and the rate-determining step of the crystal growth process is formed by surface kinetics. Figure 2.2 schematically illustrates atomic processes occurring at a crystal surface.

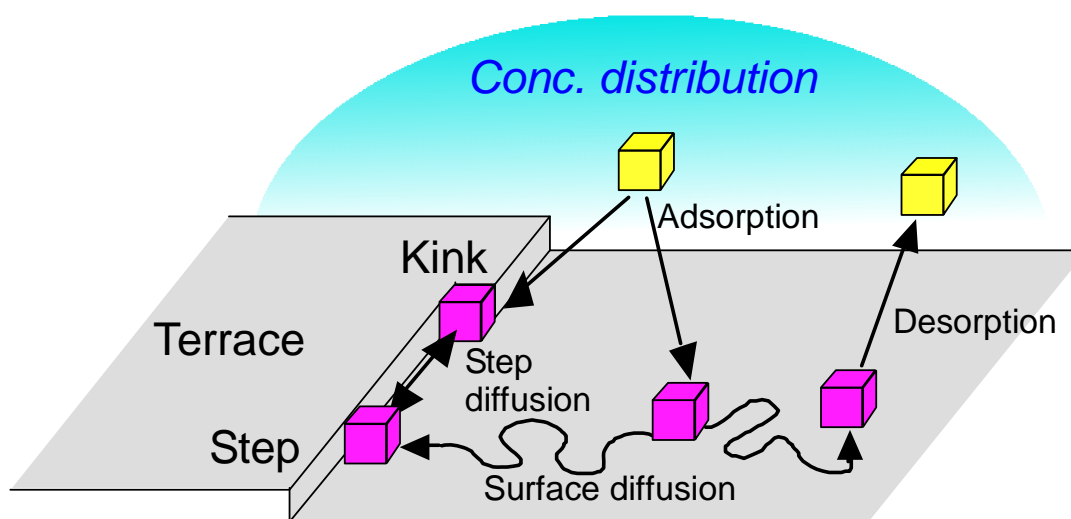


Figure 2.2 A schematic illustration of the Terrace-Ledge-Kink (TLK) model. In this model, growth units adsorb to the crystal terrace and either attach to a kink position directly after adsorption to the crystal surface, adsorb onto a terrace and migrate across to a step, where it locates a kink site (step diffusion) and subsequently becomes incorporated into the crystal lattice or desorbs from the surface. The repeated addition of such growth units to kink sites results in the progression of the step across the terrace.

This situation is described as a Terrace-Ledge-Kink model of crystal growth (Stranski, 1928). The growth unit is first transported from the bulk solution to the developing crystal surface. At this point, the solute molecule will be in one of three situations (i) it is able to integrate into the crystal lattice directly because it has landed at a site with an available kink position, (ii) it will first adsorb to the crystal surface terrace, and migrate to a step and finally adhere at a kink position, or (iii) it desorbs from the surface and

returns to the fluid phase. Kink positions are crucial to the crystal growth process because they offer energetically preferred binding conditions to a growth unit. Indeed, lattice integration from a kink site offers interactions in three dimensions to the arriving growth unit from the ledge beneath it, the step behind it, and its neighbouring solute molecule that had previously been integrated into the lattice. Energetically, this is preferred to the two interactions offered by the step position, and one by the terrace position.

Growth from a supersaturated solution occurs when the flux of molecules attaching to the crystal surface exceeds the flux of molecules detaching from the surface. The probability that a molecule will detach from the crystal is solely determined by the strength of its bonds to neighbors. Since the strength of bonding is a function of temperature rather than flux to the surface, total flux from the surface is nearly independent of concentration. In contrast, the flux to the surface is proportional to solution concentration. The solubility is then the concentration at which two fluxes are equal (Equation 2.1).

2.3.1. Crystal growth mechanisms

As previously discussed, presence of steps and kink sites on crystal surfaces (F faces) is the key to crystal growth. However, it is equally important from a crystal growth point of view to understand how these steps come into existence. The possible pathways by which a molecule passes from solution to integration into the crystal lattice are known as *growth mechanisms*. Three growth mechanisms are known to dominant almost all forms of crystal growth; continuous growth, surface nucleation, and spiral growth.

Microscopic studies have revealed that growth steps of protein crystals are mainly formed by dislocations and two-dimensional nucleation. An additional, and presumably unique, mechanism for protein crystals has been observed and consists in the tangential development of *three dimensional nuclei* which deposit on the crystal surface (Chernov and Vekilov, 2002).

Continuous growth

Continuous growth or, normal growth as it is sometimes termed, occurs when the energy required to form a step on the crystal surface is low resulting in the surface containing many kink and step sites. On a molecular level such surfaces will be extremely rough, thus providing all arriving growth units with a lattice integration point (Davey and Garside, 2000). This process is rare for conventional systems and is restricted primarily to crystals grown from a melt or from the vapour phase (Chernov, 1984). There has been only one report (Malkin *et al.*, 1996) of normal growth of a protein: apoferritin, the hollow shell of iron-transport protein ferritin.

Surface nucleation

Generally the way in which a “perfect” solution grown crystal develops is via a method of surface nucleation called two-dimensional nucleation (Burton *et al.*, 1951). The process is often termed the Birth and Spread (B+S) model, and is illustrated schematically in figure 2.3. This mechanism occurs when some of the growth units arriving at the surface do not immediately find a growth site. Such units either return to the fluid phase or join other adsorbed molecules on the crystal surface to form the characteristic two-dimensional (2D) islands seen in Figure 2.3. Newly adsorbed growth units may continue to add to kinks formed at this growth step, until a complete monomolecular layer has expanded laterally across and covered the entire crystal surface. Importantly, the system must be provided with high enough

energy in order to surpass the energetic barrier associated with the creation of new 2D nuclei (e.g. similar to 3D nucleation). As growth proceeds, the supersaturation of the solution slowly diminishes due to loss of solute molecules to the expanding crystalline surface.

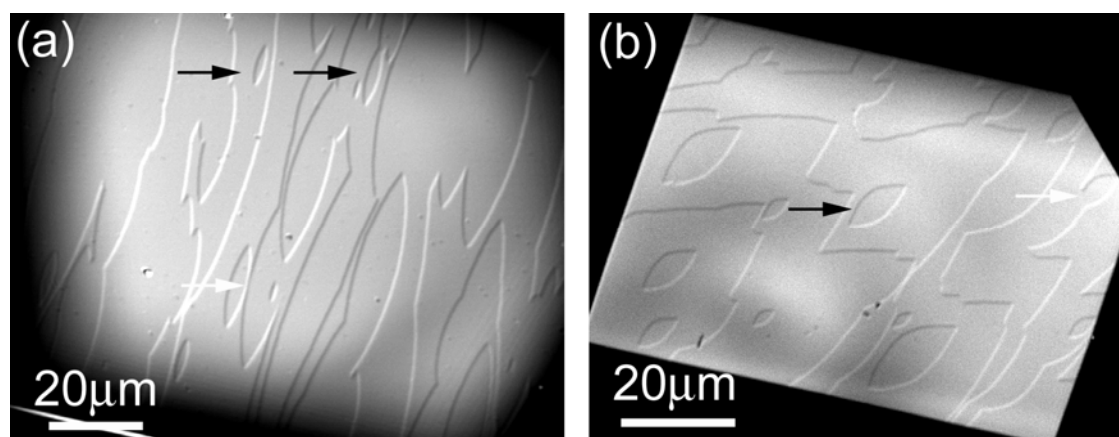


Figure 2.3 The formation and expansion of two-dimensional nucleation islands on a crystal surface. (a) {110}-face of tetragonal lysozyme covered with 2D islands (black arrows).. (b) {101}-face of tetragonal lysozyme covered with 2d islands (black arrow). The white arrows show the coalescence of two growing 2D islands

Two-dimensional (2D) nucleation has been observed numerous times for a variety of protein crystals such as: lysozyme (Durbin and Carlson, 1992), thaumatin (Malkin *et al.*, 1996), catalase (Malkin *et al.*, 1999), canavalin (Land *et al.*, 2000), trypsin (Plomp *et al.*, 2001) and apoferritin (Lin *et al.*, 2003) to name just a few. 2D nucleation growth is an important crystal growth mechanism under middle and high supersaturation ranges, particularly for protein crystallization due to the relatively high supersaturation necessary for initial three-dimensional (3D) nucleation and consequent growth (McPherson, 1999; Van Driessche *et al.*, 2007). This will be discussed in section IV.3. Theoretically, growth on a perfect crystal surface will come to a halt when the level of supersaturation becomes too low to support the formation of new 2D nuclei. However, because the vast majority of crystals

are not perfect, another growth mechanism, named spiral growth, can become prominent.

Spiral growth

Due to the presence of screw dislocations, a defect that is commonly found in growing crystals, spiral growth can originate on a crystal surface. A screw dislocation is formed when one region of the crystal is pushed up through one (or more) unit cells relative to another region (Figure 2.4). This discontinuity acts as a step source to which solute molecules can attach. Once a screw dislocation has been formed, the crystal face can grow perpetually 'such as a spiral staircase', even at very low levels of supersaturation. It is generally considered that spiral growth is the most important growth mechanism at low supersaturation. Figure 2.4 indicates the successive stages in the development of a growth spiral starting from a screw dislocation. The most important feature of such dislocations is that they are not annihilated as the dislocation propagates, thus imposing a permanent step at the crystal surface (Frank, 1949).

Spiral growth has been observed and studied extensively for protein crystals, mainly by AFM and interferometry. Recently, Sasaki and coworkers (2005), using LCM-DIM, birefringence and phase-contrast microscopy, were able to observe *in-situ* that inclusions were the source of dislocations which give birth to spiral growth on {110} faces of tetragonal lysozyme crystals.

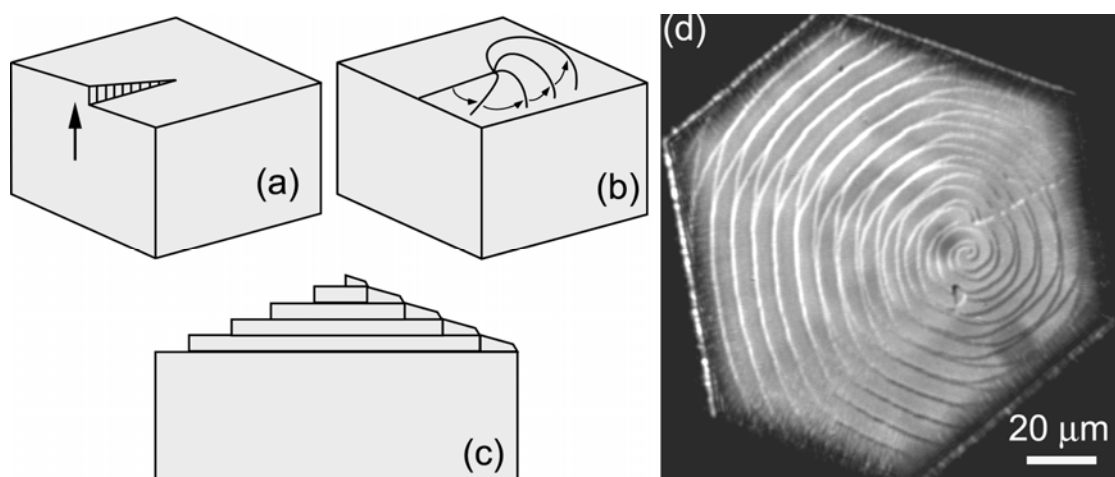


Figure 2.4 A schematic representation of the development of a grow spiral starting from a screw dislocation. (a) The creation of a screw dislocation by one region of the crystal being pushed up through one (or more) unit cells relative to another region, (b) spiral growth at the dislocation outcrop, (c) transversal view of a grow spiral and (d) photomicrograph of a double spiral step source at a dislocation outcrop on the $\{001\}$ face of a hexagonal lumazine synthase crystal.

Three-dimensional (3D) nucleation

At higher levels of supersaturation in macromolecular solution sometimes large quantities of solute molecules are able to aggregate in solution and subsequently adsorb on a crystal surface, at which point they form misaligned microcrystals or multilayered stacks (Figure 2.5) which will tangential develop across the surface (Malkin *et al.*, 1995a; 1995b; McPherson *et al.*, 1995; Durbin and Feher, 1996; Yip *et al.*, 1998; 2000). This type of surface nucleation is believed to be unique to macromolecular crystal growth.

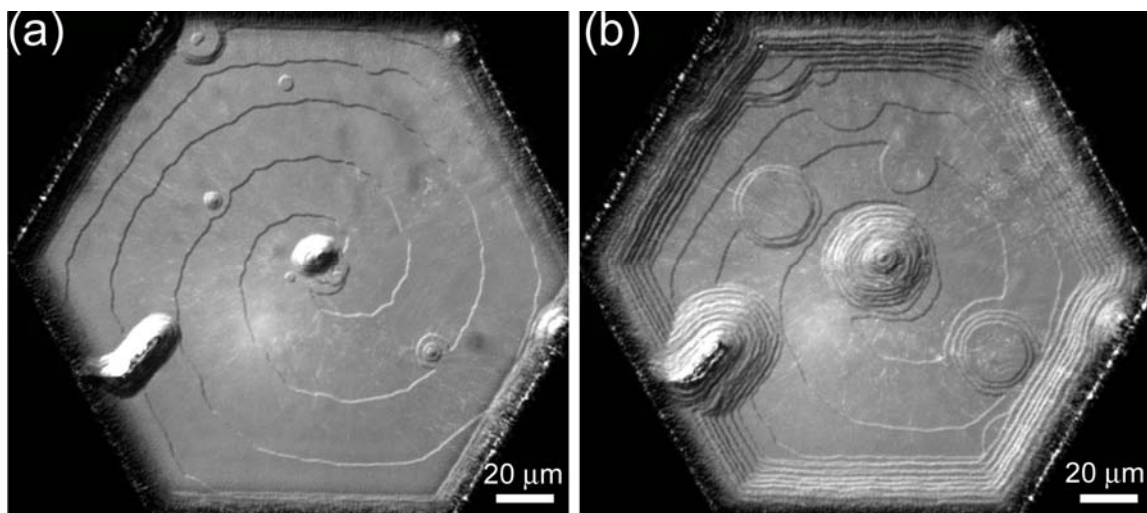


Figure 2.5 Multilayered stacks and 2D islands appear on the {001} face of a hexagonal lumazine synthase crystal (a) and layer growth starts form these multilayer stacks (b).

2.3.2. Crystal growth kinetics

When characterizing crystal growth two different growth models are usually considered: normal growth and tangential growth (step advancement). In the former growth proceeds by the addition of nascent layers on top of those already present. In the latter addition of molecules to step edges causes their lateral extension. Normal growth rate R and step velocity v are experimentally measured and used to derive the step kinetic coefficient β_{st} which is one of the fundamental parameters of layerwise growth kinetics (Chernov, 1998).

Step velocity is often expressed as a function of the protein concentration and is related to β_{st} by following relationship

$$v = \Omega \beta_{st} (C - C_e) \quad (2.5)$$

This expression can be derived from basic kinetic principles (see Markov, 1973; Chernov, 1984). However, this derivation requires strong assumptions about the mechanism of incorporation of molecules into the steps. Molecules

are assumed to enter the steps directly from the solution without undergoing adsorption or surface diffusion. In equation 2.5, Ω is the crystal volume per protein molecule, C is the protein concentration of the solution and C_e is the equilibrium concentration. The kinetic coefficient represents the rate at which molecules are incorporated into the lattice at steps (via kinks). The step speed scales with the absolute supersaturation not the actual supersaturation. This means that if two types of crystals are placed in solutions of the same supersaturation, the crystal that is more soluble will grow faster simply because there is a larger flux of molecules to the surface. In other words **step speed scales with solubility**, and one cannot assume that faster growth rates imply faster kinetics at kink sites. In the case of protein crystals only few studies have directly measured step velocities over broad range of supersaturations (Land and DeYoreo, 1997; Long *et al.*, 2000; Yau *et al.*, 2000; Dold *et al.*, 2006). From these observations no general conclusions can be drawn regarding the relationship of step velocities *versus* supersaturation.

The normal growth rate R is related to step velocity by following relation (Chernov, 1984):

$$R = pv = p\Omega\beta_{st}(C - C_e) \quad (2.6)$$

where p is the local vicinal slope (step density times step height) of the surface. The relation between normal growth rate and supersaturation is depended on the growth mechanism. Thus, different relations are found for spiral growth and surface nucleation. In the case of surface nucleation different models can be considered: mononuclear two-dimensional model, polynuclear two-dimensional model and birth and spread model (Ohara, 1973). These models will be discussed later on in section IV.3.

AFM and MI have been used to study crystal growth kinetics of biological macromolecules by measuring step velocities, normal growth rates

and surface morphologies. Growth rates were found to be three to four orders of magnitude lower than those found for small molecules (see e.g. Chernov, 2003) despite the much higher supersaturations applied in macromolecular crystallization. Consequently the values of the kinetic step coefficients were estimated in the range of 10^{-4} to 10^{-5} cm/s for biological crystals versus 10^{-1} cm/s for inorganic crystals. This difference was postulated to be associated to the lower probability of incoming biomacromolecules to present the proper orientation for getting incorporated into the lattice (Chernov and Komatsu, 1995; Rosenberger *et al.*, 1996; Vekilov and Chernov, 2002). These steric restrictions – higher entropic barrier – for association of protein molecules would be the result of the highly inhomogeneous surface of protein molecules (Nanev, 2007).

Until now the first step of crystal growth, mass transfer of building blocks to the surface, has been ignored. But transport can play an important role for macromolecular crystallization because the size of the building blocks impose them to have extremely low diffusion coefficients, two to three orders of magnitude lower than for inorganic molecules (McPherson *et al.*, 1999b). There are observations to support that the growth of crystals can be influenced by the mass transport regimen (diffusion or convection). (Wilcox, 1983, Baird *et al.*, 1986; Pusey *et al.*, 1988), although Grant and Saville (1991) argue that crystal prepared in growth rates studies are usually too small to be affected by either diffusion or convective mass transport. Nonetheless, it is not at all clear how transport processes directly affect crystal quality, resolution of their diffraction patterns, or their final size (McPherson *et al.*, 1999b). It must also be pointed out that the slow growth rate of most macromolecular crystals, compared to conventional crystals, would tend to dampen the effects of possible convective instabilities.

On the other hand, it has been experimentally demonstrated that around growing protein crystals a zone depleted in protein concentration relative to the bulk solution surrounding them is formed, called depletion zone (Kam *et al.*, 1978; Feher and Kam, 1985; Baird *et al.*, 1986; Miyashita *et al.*, 1994; Kurihari *et al.*, 1996; McPherson *et al.*, 1999; Gorti *et al.*, 2001; Otálora *et al.*, 2002; Duan *et al.*, 2002). If depletion is significant, a crystal may grow at a local supersaturation noticeably lower than that of the bulk solution. Hence, the rate of diffusion of proteins (and impurities) in and out of these halos provides a growth limiting factor. Equation 2.6 for the face growth rate R allows rough estimate of the contribution to the growth rate of the transport of protein species from the bulk solution to the crystal surface if we assume p to be known. C designates protein concentration in solution immediately at the crystal surface and in the bulk solution concentration, away from the boundary diffusion layer – the protein depletion zone of thickness δ – is defined as C_∞ . Protein diffusivity in solution is denoted by D and the crystal size L . Thus diffusion flux to the surface is $\approx (D/\delta)(C_\infty - C)$. This flux must be equal to the flux R/Ω of molecules incorporated to the crystal:

$$(D/\delta)(C_\infty - C) = p\beta_{st}(C - C_e) \quad (2.7)$$

Solving this equation with respect to C , we find the growth rate (Chernov, 1984),

$$R = p\beta_{st}\Omega(C - C_e)/(1 + p\beta_{st}\delta/D) \quad (2.8)$$

Here $p\beta_{st}$ is the average incorporation rate of protein molecules to the crystal at its surface while D/δ is the typical diffusion rate in solution. Two limiting growth regimes and a smooth transitions between them can be defined as a function of the ratio of surface incorporation to the bulk transport rate ($p\beta_{st}/(D/L)$), the slower one being the rate controlling process. Three regimes are differentiated, surface kinetic, mixed and bulk diffusion. In the mixed regime the concentration and growth rate have intermediate values controlled by both mass transport and surface kinetics, neither of them being

negligible. Thus, the sensitivity of the limiting stage to growth parameters requires careful surface and bulk kinetic measurements for each specific protein, taking into account growth conditions and crystal size before drawing the conclusion that the protein depletion zone is significant (Chernov, 2003). But one has also to consider that the relative importance of each of the two processes – diffusion and incorporation of growth units – and even the growth regime can change during the growth history of a single crystal (Otálora *et al.*, 2002).

The formation of halos due to lowered solute concentration around growing crystals also has the effect of producing density gradients in these areas. These in turn, under the effects of gravity, result in the formation of convection currents which may dominate the rate of simple diffusion and adversely effect crystal growth (Rosenberger, 1986). As the formation of concentration gradients around growing crystals is directly proportional to the rate at which molecules add to the surface (crystal growth rate), slower growth results in decreased convection currents due to density fluctuations. Pure diffusive growth can be accomplished by growing crystals in porous gel media (Robert and Lefauchaux, 1988) or crystal growth in zero (effective) gravity to remove convective and sedimentary effects (Littke and John, 1986; DeLucas *et al.*, 1986). On the other hand it has been shown that pure kinetic growth can be obtained in stirred solution or forced flow experiments (see for example Vekilov and Rosenberber, 1998).

2.4 Cessation of growth

Cessation of growth of crystals can occur for several reasons. The most obvious is the decrease in concentration of crystallizing solute to the point where the solid and solution phases reach equilibrium. In this case, addition

of more solute can result in continued crystal growth. However, some crystals reach a certain size beyond which growth does not precede irrespective of solute concentration. This may be a result either of cumulative lattice strain effects or poisoning of the growth surface. Despite the variety of surface studies with different proteins, it still remains unclear if impurity and/or defect accumulation in the lattice (Feher and Kam, 1985) or surface contamination due to adsorption of impurities (Malkin *et al.*, 1999) is responsible for cessation of growth.

2.5 Impurities

Macromolecular impurities have been demonstrated to cause profound effects on biomacromolecular crystallization. These effects include reduced or increased solubility (Lorber *et al.*, 1993; Skouri *et al.*, 1995), suppressed or enhanced nucleation (Abergel *et al.*, 1991; Thomas *et al.*, 1998; Burke *et al.*, 2001), changes in growth kinetics (Vekilov *et al.*, 1995; 1996b; 1996c), and rate (Thomas and Chernov, 2001), as well as in growth habit and morphology (Provost and Robert, 1995; Hirschler and Fontecilla-Camps, 1996; Bhamidi *et al.*, 1999). This is understandable given extensive evidence for conventional molecule and ionic crystals that impurities dramatically effect these properties (for discussions, see Burton *et al.*, 1951; Chernov, 1984; Hull and Bacon, 1984; Tiller, 1991; the series by Hurle 1993, 1994a,b). Impurity incorporation into crystals of all types, including macromolecular crystals, as shown in Figure 2.6, introduces stresses into the lattice. The important point to bear in mind when considering these defects, is that their extent and their influence on the surrounding lattice is not confined to their immediate neighborhood, but is propagated through the crystal for long distances. Thus many unit cells are affected by only one such defect (McPherson *et al.*, 1999b) As sites of impurity incorporation accumulate in crystals, the attendant

strains mechanically interact, generally in unfavorable ways; this further weakens the physical properties and ultimately the diffraction properties of the crystals (McPherson, 1999; Yoshizaki *et al.*, 2004; Yoshizaki *et al.*, 2006).

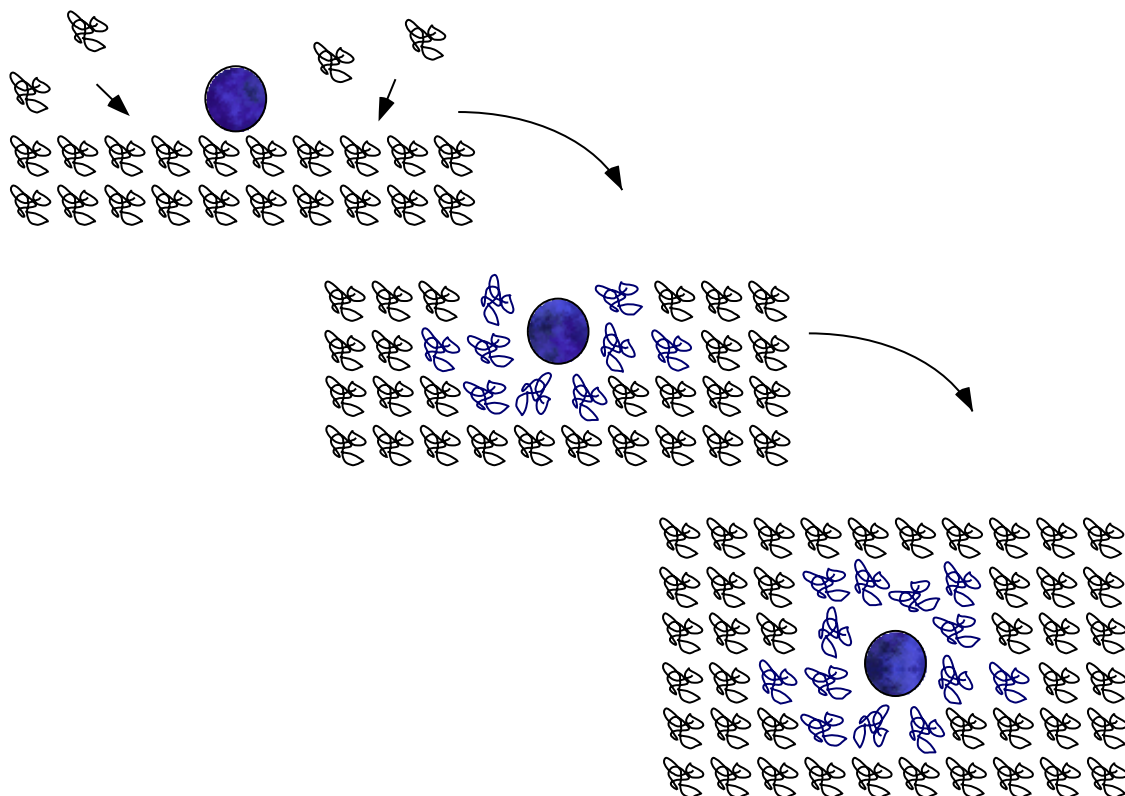


Figure 2.6 The incorporation of an impurity or a foreign particle that improperly fits a lattice site impacts the disposition of neighboring molecules. This in turn produces strain, which is subsequently propagated through the lattice, although differentially according to direction (adapted from McPherson, 1999).

Proteins are by their very nature, difficult to purify to homogeneity and to free from contaminant macromolecules compared to inorganic materials. In biochemical studies, a protein that is 99% pure is considered exemplary (in the case of silicon 99.9999% purity is reached). Even highly purified macromolecules may, for a variety of reasons, be chronically heterogeneous due to modifications, denaturation, the binding of ligands, or a host of other effects. In addition, macromolecules are crystallized from

generally complex solutions that include not only the target macromolecule, but also buffers, salts, precipitating agents, water, and any number of small effector molecules (McPherson, 1999).

2.5.1. Types of impurities

Crystallizing solutions can contain a variety of impurities which strongly adsorb on growing crystal surfaces and alter the growth process. The impurities in protein solution may be tentatively classified as follows:

(1) **Macroheterogeneous**: These are molecules of foreign proteins and are the most obvious source of impurity. A classical example is the case of commercially available lysozyme where several foreign proteins are found (Thomas *et al.*, 1996).

(2) **Microheterogeneous (homologous)**: The term microheterogeneity is used to describe the heterogeneity in the protein of interest. Sequence variation and incomplete or uneven proteolysis are sources of microheterogeneity in the polypeptide chain itself. In addition, post-translational modification of the protein (Seifter and England, 1990; Wold and Moldave, 1984), e.g. covalent attachment of saccharides, phosphorylation, and methylation, may not be complete and moieties attached may be heterogeneous as well. Other microheterogeneities are dimers, trimers and rarer higher oligomers of the protein, and fragments of the protein, especially if the protein consists of several units. The nature of binding in oligomers varies from protein to protein. It might be associated with oxidation, modified, or even regular sites on the molecule surfaces. Variation of charge on molecule globulae and conformational changes within molecules are other types of microheterogeneity. The conformations are variations in mutual arrangements of subunits within the molecule. Protein crystallization depends upon specific weak attractive interactions between protein molecules

which are repeated over many thousands of molecules to form an ordered three-dimensional lattice. While most of the surface of a crystalline protein is in contact with only solvent, the interacting surfaces are quite specific. Microheterogeneity, if it occurs at or near the interaction surfaces, could easily terminate crystal growth at that point or cause serious lattice perturbations (Bott *et al.*, 1982). Hence the incorporation into a crystal lattice may have the same effect as the incorporation of entirely foreign proteins (McPherson, 1999). Examples of the effect of microheterogeneities on protein crystal growth have been demonstrated by several groups (Thomas *et al.*, 1998a,b; Thomas and Chernov, 2001; Matsui *et al.*, 2006).

(3) Conventional molecules: Small molecules such as metabolites, salts, etc. can also be an important source of impurities in crystal growth. Vekilov and co-workers (1996) studied the partitioning of NaCl and protein impurities in lysozyme crystallization and found that the crystal nucleus incorporates higher levels of salts than the rest of the crystal.

(4) Foreign materials: Foreign particles, microbes, fibers, bubbles, and any other large polymers or surfaces might get incorporated into the crystal lattice and induce defects in the crystal structure. Especially protein crystals are prone to incorporate foreign particles (McPherson *et al.*, 2003 and references therein).

(5) Aggregates and clusters of the target protein: These can also be a source of impurities, especially because macromolecular crystals are generally grown from concentrated solutions at very high levels of supersaturation. It has been shown that these aggregates, be they ordered or not, may be incorporated into crystals (Land *et al.*, 1995, 1996; Malkin *et al.*, 1995b, 1996a,b,c).

(6) Temperature variation, vibrations, and shock are not contaminants *per se*, but they, like material impurities, induce discontinuities in growth. In a sense, they are physical impurities and they act to produce similar kinds of growth anomalies and disruptions.

An alternative and more extensive classification of impurities present in protein solutions is given by McPherson and co-workers (1996). For further reading on impurities see also Giege and Ducriux (1999) and McPherson (1999).

2.5.2. Impurity mechanisms

There are four mechanisms by which ions or molecules can modify growth kinetics, either by changing the step speed or by altering the step edge energy. The main mechanisms through which impurities can affect step motion typically discussed in literature are: step pinning and kink blocking. The incorporation and step edge adsorption are also considered as impurity mechanisms. Each of these mechanisms for growth inhibition exhibits a characteristic dependence of step speed on supersaturation and impurity concentration as illustrated in Figure. 2.7 (Dove *et al.* 2004).

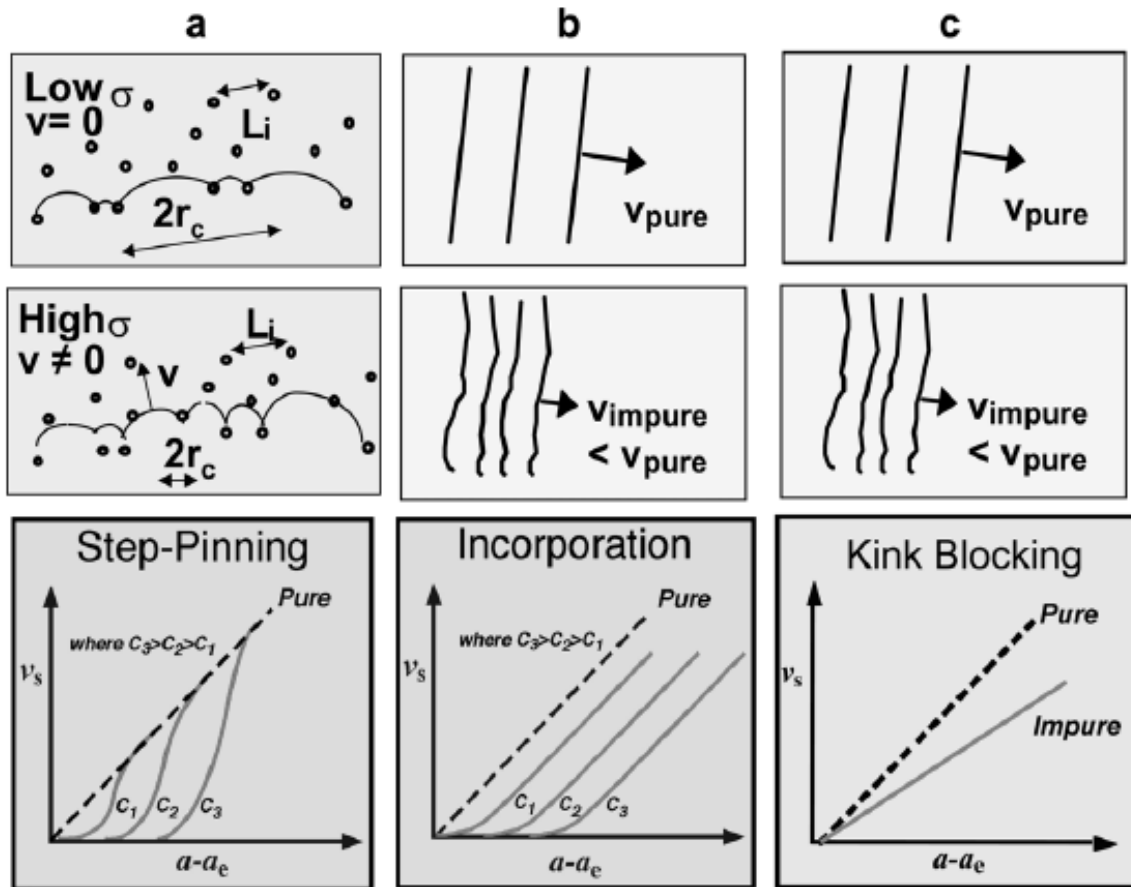


Figure 2.7 Three models for impurity interactions and their effect on step kinetics: (a) step pinning, (b) incorporation and (c) kink blocking (adapted from Dove *et al.*, 2004).

Step pinning

The step pinning mechanism assumes that impurity molecules are adsorbed on the interface and the only way the step can continue to advance is by growing around those blocking sites (Cabrera and Vermileya, 1958). The resulting curvature in the step line increases the chemical potential of the steps (Gibbs –Thomson effect), lowering the potential difference that drives step motion and as a consequence slows down the steps. In terms of supersaturation, for a given impurity content, there is a critical supersaturation below which the crystal surface enters a so called “dead zone” where no growth occurs (Cabrera and Vermileya, 1958; Chernov, 1984;

Raskovich, 1991; Voronkov and Rashkovich, 1992; Voronkov and Rashkovich, 1994). At supersaturations exceeding a critical range of supersaturations, step velocity is unaffected by the impurities (Fig. 2.7). Step pinning is highly dependent upon the details of the impurity-step interactions. Consequently, the same impurities that may block one type of step can leave steps on adjacent faces unimpeded. A beautiful example of this impurity mechanism can be found in Nakada *et al.* (1999), which showed how strong step pinning is produced by lysozyme dimers adsorbed on the {101} face and almost none is observed for the {110} face of a tetragonal lysozyme crystal. Vekilov and coworkers (1995, 1996) also found evidence for this type of impurity action for lysozyme crystallization. Theoretical approaches to this problem can be found in (Potapenko *et al.*, 1993; van der Eerden, 1993; van Enkevort and van den Berg, 1998).

Kink blocking

This impurity action mechanism assumes that impurities adsorb on kink sites for very short residence times, leading to an effective reduction in kink site density (Bliznakov, 1958; Chernov, 1961), with or without incorporation. And thus, decrease the step kinetic coefficient, while the linear relation between step velocity and driving force is preserved over the entire range of supersaturations (Figure 2.7). This effect is also highly dependent on specific impurity-step interactions. Evidence for this type of impurity action has been found during lysozyme growth in the presence of other proteins (Vekilov *et al.*, 1995).

Incorporation

Impurity incorporation occurs when foreign ions or molecules are captured by advancing steps or otherwise incorporate at kink sites along a step edge to become part of the growing crystal. Typically the impurity

molecules distort the crystal structure, thereby increasing internal energy of the solid through an enthalpic contribution (van Enkevort and van der Berg, 1998, Davis *et al.*, 2000). The resulting increase in free energy is manifested as an increase in solubility of the crystal, leading to a lower effective supersaturation. Hence, the slope of v versus C remains unchanged but the absolute magnitude of the step always remains below that of a pure system at the same supersaturation. This type of impurity incorporation has not yet been reported for protein crystal growth since precise measurements of step velocities are needed. But Skouri *et al.* (1995) showed indirect evidence by measuring higher solubility for lysozyme crystals grown in solutions containing a higher amount of impurities compared to crystals grown in more pure solutions.

Surfactants

Impurities that lower the interfacial energy by adsorbing to surfaces modify many aspects of the surface dynamics and are known as surfactants. Impurities that adsorb to step edges can have similar effects, modifying growth by lowering the step edge energy. Evidence for this type of impurity effect comes from changes in microscopic (step edge direction) and macroscopic (expression of crystal facets) morphology in the absence of a kinetic effect. Impurity interactions by step edge adsorption are unique because step rates can exhibit little deviation from the pure system.

2.5.3. Trapping of impurities

Of course not all impurities incorporate equally, and some not at all, into the crystal lattice. For this reason it is important to quantify the trapping of impurities. Trapping of impurities is determined by two interrelated distribution coefficients k and K . In the latter case the impurity

(i) distribution between the bulk solution (l) and the growing crystal (s) is characterized by the distribution coefficient with respect to the crystallizing protein (p):

$$K = (C_{is}/C_{ps})/(C_{il}/C_{pl}) \quad (2.9)$$

Here C denotes the concentrations of the corresponding species. If $K > 1$, growing crystals sequester the impurity from solution and thus, re-crystallization cannot be used to purify the protein from this impurity and vice versa in the case of $K < 1$. Measurements have shown that for at least some homologous impurities $K > 1$, while for foreign proteins, $K < 1$.

Trapping of impurities can also be determined by distribution the coefficient k , which characterizes the concentration of an impurity in a crystal lattice relative to that of whole solution, while K is a measure of the impurity trapped related to the major crystallizing protein ignoring the solvent. k is expressed as:

$$k = C_{is}/C_{il} = K(C_{pl}/C_{ps}) \quad (2.10)$$

Since protein solubility is usually low, $C_{ps} \gg C_{pl}$ and $k \gg K$. Preferential trapping of homologous impurities suggests a possible explanation for why crystals grown in microgravity are sometimes of higher quality than those grown in the presence of convection. In stagnant solution, the just nucleated crystal engulfs homologous impurity. Since $k \gg 1$, the solution around the crystal becomes depleted with respect to this impurity, while the crystal is essentially enriched by the impurity because $K > 1$. As the crystal grows, it preferentially extracts impurity from the solution, making the latter cleaner. Thus, a crystal growing from a stagnant solution (or gel) purifies the solution around itself from homologous impurities and may grow more perfect-provided that mosaicity was not introduced upon crystal nucleation (Carter *et al.*, 1999; Thomas *et al.*, 2000; Chernov, 2003).

3. Observation techniques

In the field of crystal growth several experimental setups have been applied to observe surface morphologies of growing crystals. These observations can be divided into two fields: *ex situ* and *in situ* observations. In the former case Transmission Electron Microscope (TEM) and Scanning Electron Microscope (SEM) are most commonly used. These techniques have been very useful for the identification of nucleation and growth mechanisms (McPherson, 1985; Durbin and Feher, 1986; Durbin and Feher, 1990; Michinomae *et al.*, 1999; Braun *et al.*, 2000) and defect characterization (Braun *et al.*, 2000; Rodriquez, 2003) in protein crystals because of their high resolution. But both SEM and TEM exhibit similar limitations for performing crystal growth studies. The acquisition of *in situ* data is not possible as the sample is typically studied under vacuum, and non-conducting samples may need to be gold-coated prior to analysis to reduce surface charging effects. For *in situ* observations, Atomic Force Microscopy and Interferometry are the most widely used techniques, but also optical microscopy has been frequently applied. Recently, several advanced optical techniques were implemented to study crystal growth, such as; Phase transmission microscopy (Tsukamoto, 1983; Tsukamoto *et al.*, 2003; Yai, 2003; Dold *et al.*, 2006), Laser confocal microscopy (Muhlig *et al.*, 2003) and Laser confocal differential interference contrast microscopy (Sazaki *et al.*, 2004; 2005; Van Driessche *et al.*, 2007a, 2007b; 2007c). In Table 2.1 a summary of the most relevant *in situ* observation techniques is given.

This work is focused on measuring directly growth kinetics of protein crystals, thus, *in situ* observations are the appropriated choice for this type of research. Mainly Laser confocal differential interference microscopy (LCM-DIM) was used, but also atomic force microscopy and Michelson interferometry were applied. These different techniques are discussed in detail in section III.

III. MATERIALS AND METHODS

1. Model system

1.1. Lysozyme

What is it?

Lysozyme is a globular protein made of a single polypeptide chain of 129 amino acids cross-linked with four disulfide bridges. This protein was discovered in 1922 by Alexander Fleming.

What does it do?

It is an antibacterial enzyme that acts by hydrolyzing the polysaccharide portion of the cell wall of certain bacteria.

Where does it come from?

Lysozyme is found in almost all animal and plant life, with one particularly rich source being found in hen egg white (known as HEW lysozyme, or HEWL, hereafter lysozyme and HEWL will be used indifferently). HEWL is commercially available and can be obtained from different companies. In Table 1.1 an overview is given of the different “brands” of lysozyme used in this work.

Table 1.1 Overview of commercially available hen egg white lysozyme.

Name	Purity	Purification	Lot	availability
Seikagaku	98.5%*	6xcrystallization	E02Z03	Seikagaku, Co.
Purified	99.99%**	HPLC	-----	Not available***
Sigma	94.3%*	3xcrystallization	114K0626	Sigma-Aldrich
Fluka	-	crystallization	62970	Sigma-Aldrich

* Thomas *et al.*, 1996.

**Purified from Seikagaku HEW lysozyme.

*** Commercial production of highly purified lysozyme by Maruwa food inc. was stopped in 2007.

When did it all start?

For the last 60 years lysozyme has been synonymous for protein crystallization. Tetragonal HEWL crystals were first reported in 1946 by Alderton and Fevold (1946). Pioneering X-ray crystallographic investigations carried out in the 1960s led to the elucidation of both the atomic structure of lysozyme at 2 Å, and its mechanism of action (Blake *et al.*, 1965; Johnson and Phillips, 1965; Blake *et al.*, 1967). Since this time many more unique crystallographic structures of lysozyme (and closely related molecules) have been produced, including an ultrahigh resolution structure at 0.94 Å (Sauter *et al.*, 2001). All structures are available in the PDB (Berman *et al.*, 2000) and also in a database dedicated exclusively to lysozyme structures (Mohan *et al.*, 2004). Besides the resolution of many structures also a great number of physical chemical characteristics have been determined. In Table 1.2 the most relevant physical chemical characteristics of HEWL are summarized. Needless to say that lysozyme has been, and still is, the leading protein for studying growth kinetics of protein crystals. Lysozyme makes a very good model system just because so much is already known about this protein. It should be mentioned that there is discussion about the fact if lysozyme is really a good model system for protein crystallization or not.

Table 1.2 Some physical chemical characteristics of hen egg white lysozyme.

Physical chemical characteristics					
N° Amino acides	pI	MW	Adsorbance ϵ_{280}	D_0 , diffusion coefficient	Ω , molecular volume
129	11.3 pH	14.296 Da	2.64 mg/ml*	10.6×10^{-7} $\text{cm}^2/\text{s}^{**}$	2.7×10^{-30} cm^3 ***

* Sophianopoulos *et al.*, *J. Biol. Chem.* 237, 1107, 1962.

** Dubin *et al.*, *J. Chem Phys.* 54, 5158, 1971.

*** Steinrauf, L.K. *Acta Cryst.* 12, 77-79, 1949.

1.2. Crystallization of lysozyme

There have been found a wide variety of crystallization conditions for lysozyme (Ries-Kautt and Ducrieux, 1989; Guilloteau *et al.*, 1992), in this work all crystallization was carried out using lysozyme solutions prepared in a 50mM Na-acetate buffer (pH 4.5) and 25 mg/ml NaCl as precipitant, also prepared in a 50mM Na-acetate buffer (pH 4.5). Batch crystallization* was employed, and under these conditions only tetragonal lysozyme crystals with space group $P4_32_12$ were obtained.

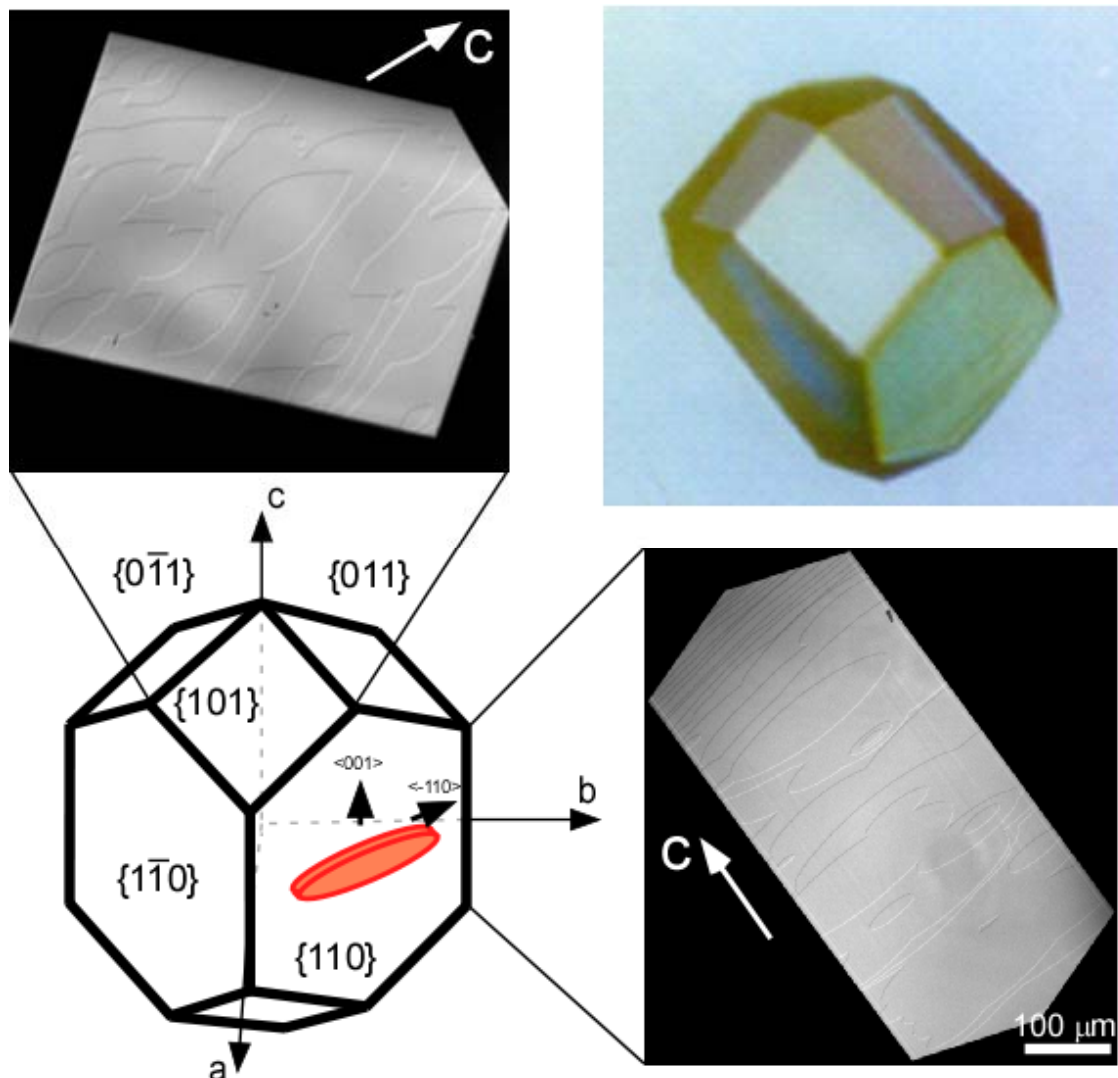


Figure 1.1 The habit of lysozyme crystallized in the tetragonal form. The two major faces of the crystal are the $\{110\}$ and $\{101\}$. Additionally, the shape and orientation of two dimensional islands that form on $\{110\}$ and $\{101\}$ faces are illustrated by LCM-DIM micrographs.

* Batch crystallization is the simplest form of macromolecular crystallization and consists in mixing concentrated protein with concentrated precipitant to produce a final concentration which is supersaturated in terms of the solute macromolecule and therefore leads to crystallization. 47

A schematic view of the crystal habit adopted by the tetragonal form of lysozyme and the crystallographic coordinates are shown in Figure 3.1. The habit is formed by a combination of prismatic $\{110\}$ and pyramidal $\{101\}$ faces. Eight molecules of lysozyme make up the unit cell in this form, the dimensions of which are $a = 79.1$, $b = 79.1$, $c = 37.9$ Å (Nadarajah and Pusey, 1996). For a detailed description of the relation between surface morphology and internal structure of tetragonal lysozyme crystals the works by the group of Pusey are recommend (Nadarajah and Pusey, 1996; Nadarajah *et al.*, 1997; Li *et al.*, 1999a; Li *et al.*, 1999b).

1.3. Fluorescence labeled lysozyme

For single molecule observations (see chapter III section 2.1.2) the ϵ -amino group of the N-terminal of HEWL was specifically labeled with a fluorescent reagent, tetramethylrhodamin-5-isotiocyanate (5-TRITC, MW = 443 g/mol, Molecular Probes T-1480), according to the recipe of Matsui *et al.* (2006). Since the molecular weight of a fluorescent label after the reaction (tetramethylrhodamin) is less than 3% of that of fluorescent-labeled HEWL (F-lysozyme), the fluorescent label does not affect the translational and rotational diffusion of the protein molecule (Figure 1.2). F-lysozyme molecules are incorporated into tetragonal lysozyme crystals as native lysozyme molecules (Matsui *et al.*, 2006) but will affect the step advancement because the intermolecular contacts are disturbed (Figure 1.2).

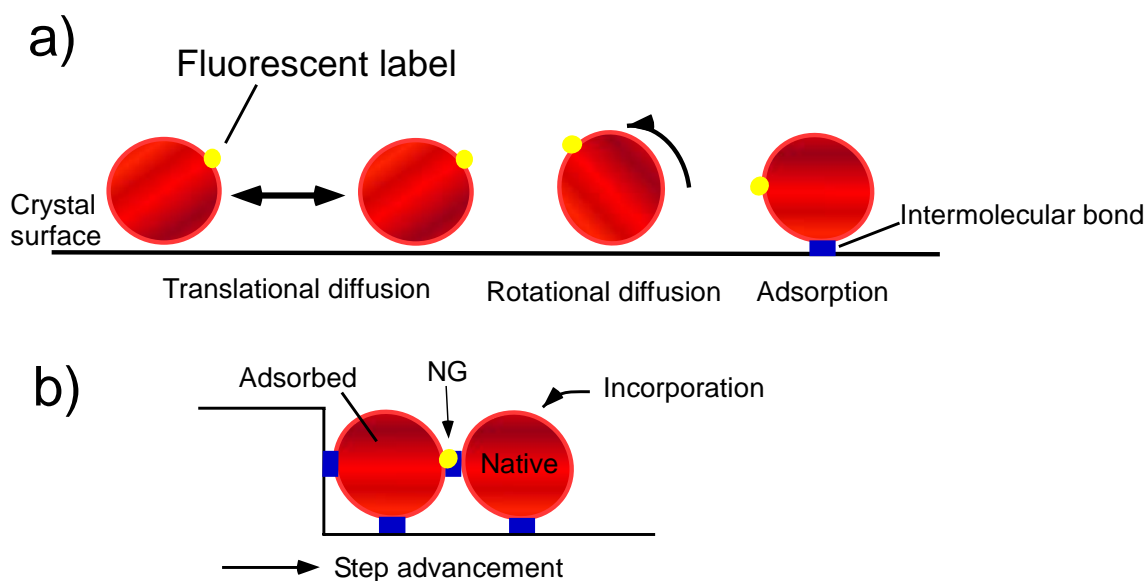


Figure 1.2 Schematic representations of diffusion and incorporation processes of a fluorescent labeled lysozyme monomer. a) F-lysozyme behaves as solute molecule for diffusive processes but b) behaves like a impurity molecule for step advancement.

Lysozyme dimer was also chemically labeled with 5-TRITC according to the same recipe (hereafter fluorescent-labeled dimer is called F-dimer). In the case of F-dimer, precise identification of the molecular surface at which 5-TRITC was chemically attached was difficult to achieve because of very limited amount of dimer available for the experiments. However, since the mole ratio of 5-TRITC to amino groups, which are expected to appear on a molecular surface of dimer, was the same as that of the preparation of F-lysozyme, it is reasonable to assume that only one amino group on a molecular surface of dimer is modified with 5-TRITC.

1.4. Contaminate HEWL – Impurities –

Seikagaku, Sigma and Fluka lysozyme were used as samples that include impurities. In the case of Seikagaku and Sigma, the impurities were identified and quantified by Thomas *et al.* (1996), using sodium dodecyl sulfate polyacrylamide gel electrophoresis with enhanced silver staining,

reversed-phase fast protein liquid chromatography (FPLC) and immunoblotting with comparison to authentic protein standards. In Table 1.3 an overview is given of the foreign proteins found in commercially available lysozyme samples.

Table 1.3 Summary of contaminating proteins present in commercially available lysozyme.

Name	Purity	Impurities	MW (kDa)	Concentration
Seikagaku lysozyme*	98.5%	Lysozyme dimer,	28	0.5%
		polypeptide	39	Trace (<0.1%)
		polypeptide	18	1.0%
Sigma lysozyme*	94.3%	Ovotransferrin,	73	0.2%
		Ovalbumin	43	3.8%
		Lysozyme dimer,	28	0.7%
		polypeptide	18	1.0%
Fluka lysozyme	—	—	—	—

* Thomas *et al.* (1996)

Three kinds of “purified” impure proteins (Table 1.4) were used to study their possible effects on the growth kinetics of tetragonal lysozyme crystals. One is Fluorescence-labeled lysozyme (F-lysozyme, see section 1.3). The two other impurities are covalently-bonded dimer of lysozyme (dimer) and an 18 kDa polypeptide (18 kDa), which were purchased from Maruwa food industries, Inc. Both, dimer and 18 kDa, are known as major impurities present in commercially available lysozyme (Thomas *et al.*, 1996). These impurities were separated by High Performance Liquid Chromatography (HPLC) from commercially available Seikagaku lysozyme and concentrated afterwards; in Figure 1.3 a typical SDS-page gel of these samples is shown.

Table 1.4: Overview of impure proteins used in this work

Name	Description	Origin	Preparation
F-lysozyme	Fluorescence labeled lysozyme monomer	Prepared in the lab	Fluorescence labeling of Purified lysozyme (see section 1.3)

Dimer	Lysozyme covalently bounded dimer	Seikagaku lysozyme	HPLC lysozyme	from	Seikagaku
18kDa	18kDa polypeptide	Seikagaku lysozyme	HPLC lysozyme	from	Seikagaku

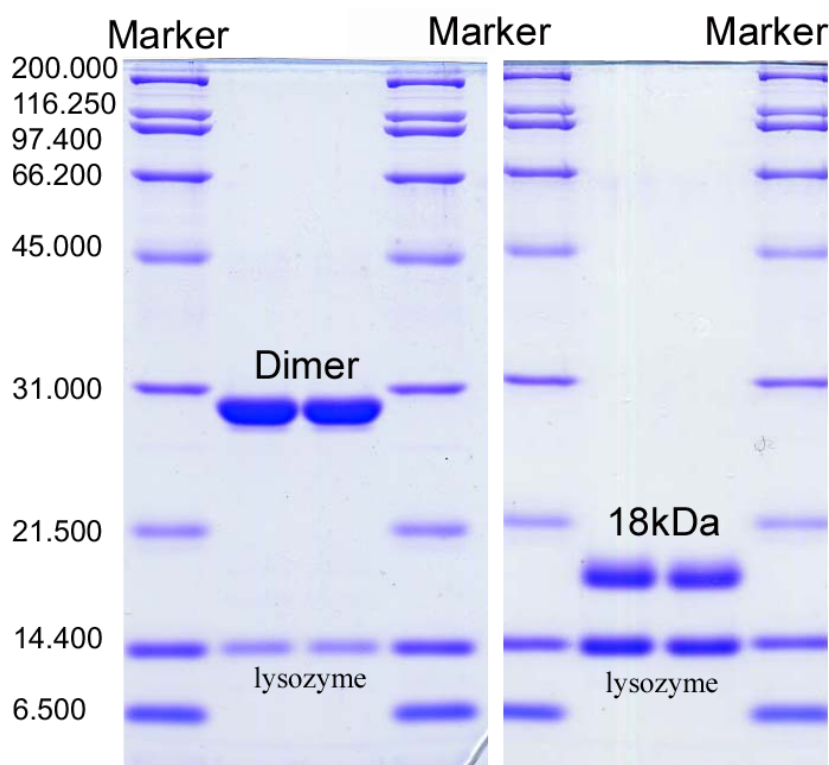


Figure 1.3 SDS-Page of purified and concentrated lysozyme dimer and 18kDa polypeptide samples obtained from Seikagaku lysozyme by high-performance liquid chromatography using a cation-exchange column.

1.5. Solubility of tetragonal lysozyme

Determination of protein solubility in solution is a necessity when studying growth kinetics since solubility determines the supersaturation which is the main driving force for crystallization. Lysozyme solubility's in the presence of the tetragonal crystal form in sodium chloride solutions have been determined by many researchers already: Meehan *et al.*, 1988; Cacioppo *et al.*, 1991; Pusey *et al.*, 1991; Rosenberger *et al.*, 1993; Sazaki *et al.*, 1996; Forsythe *et al.*, 1999; Gray *et al.*, 2001). Different Na-acetate buffer solutions (pH, concentrations) were used. Lysozyme solubility was

found to increase with increasing temperature and decreasing salt concentration (Cacioppo *et al.*, 1991; Forsythe *et al.*, 1999). It was also found that pH has a varied and unpredictable effect on solubility (Cacioppo *et al.*, 1991; Forsythe *et al.*, 1999).

In Figure 1.4 lysozyme solubility in 50mM Na-acetate (pH 4.5) buffers, determined by different methods, are shown. In the case of Rosenberger *et al.* (1993) solubility was determined by a scintillation method, Sazaki *et al.* determined solubility using two-beam interferometry (solution Michelson interferometry), Pusey and coworkers (1999) used a miniature column solubility apparatus to measure lysozyme solubility and Gray and collaborators (2001) applied surface Michelson Interferometry to correlate surface fringes of crystals with solubility. During this work we used the solubility curve determined in 50mM Na-acetate (pH 4.5) buffer contain 25 mg/ml NaCl by Sazaki *et al.* (1996). In Figure 1.5 the curve fitting for data points at low (<18°C), and high (>18°C) temperature are represented. The obtained equations from the fitting were used in this work to calculate the solubility at different temperatures.

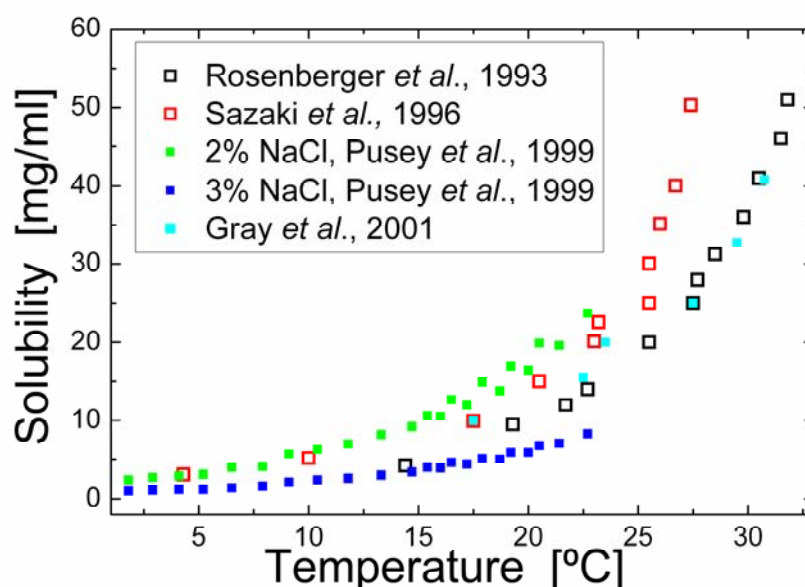


Figure 1.4 Comparison of the solubility curves of tetragonal crystal of lysozyme measured by different groups and methods. Lysozyme solubility was determined at different temperatures in a 50mM Na-acetate (pH 4.5)

buffer containing 2.5% NaCl (in the case of Pusey *et al.* 2% and 3% NaCl were used).

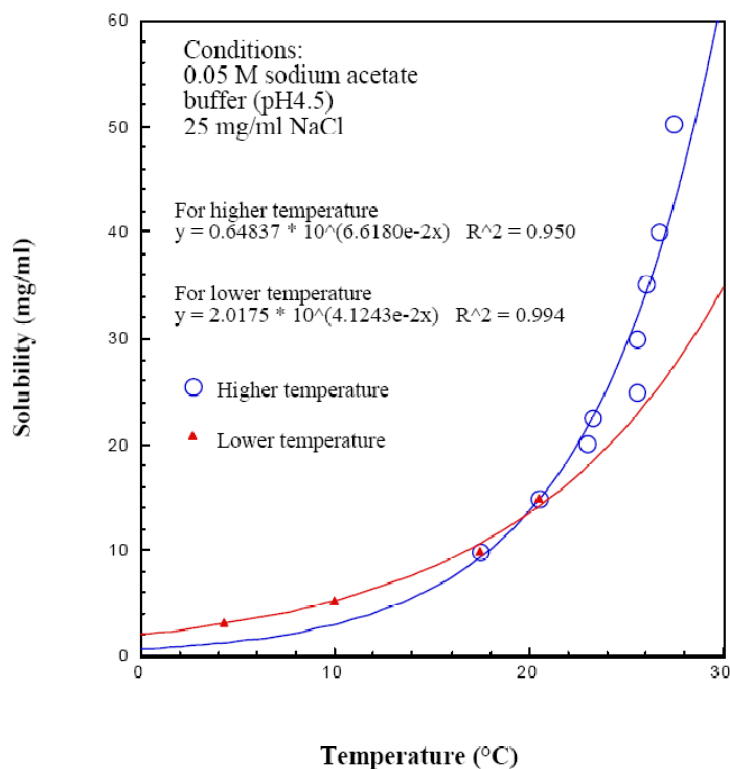


Figure 1.5 Solubility curve of tetragonal lysozyme crystals determined at different temperatures by two-beam interferometry. Conditions: 2.5% NaCl, in 50mM Na-acetate buffer (pH 4.5). (Adapted from Sasaki *et al.*, 1996)

2. Observation Techniques

2.1. Laser Confocal Differential Interference Contrast Microscopy

2.1.1. Setup

Laser confocal differential interference contrast microscopy (hereafter referred to as LCM-DIM) is a new technique for non-invasive in situ observation of crystal growth developed by Sasaki and coworkers (2004). LCM-DIM is the main tool used in this work and therefore is described in detail. Figure 2.1 shows a schematic drawing of a typical LCM-DIM setup which consists in a confocal system (FV300, Olympus Optical Co. Ltd.) attached to an inverted optical microscope (IX71, Olympus Optical Co. Ltd.), and a Nomarski prism (UDICTHC: large shear length type) inserted into the optical path to utilize differential interference contrast (DIC). In order to obtain a sufficient DIC effect, an analyzer is inserted in front of the photomultiplier such that the orientations of the analyzer and polarizer are perpendicular. Hence, the strength of this experimental configuration resides in the combination of the main advantages of two, already well known, microscopy techniques; laser confocal microscopy (LCM) and differential interference contrast microscopy (DICM). In this optical microscope illumination is provided by a SLD light source with a wave length of 680 nm and images of growing crystal surfaces are obtained with different high resolution objective lenses. Next, the main parts of this experimental setup will be explained in detail.

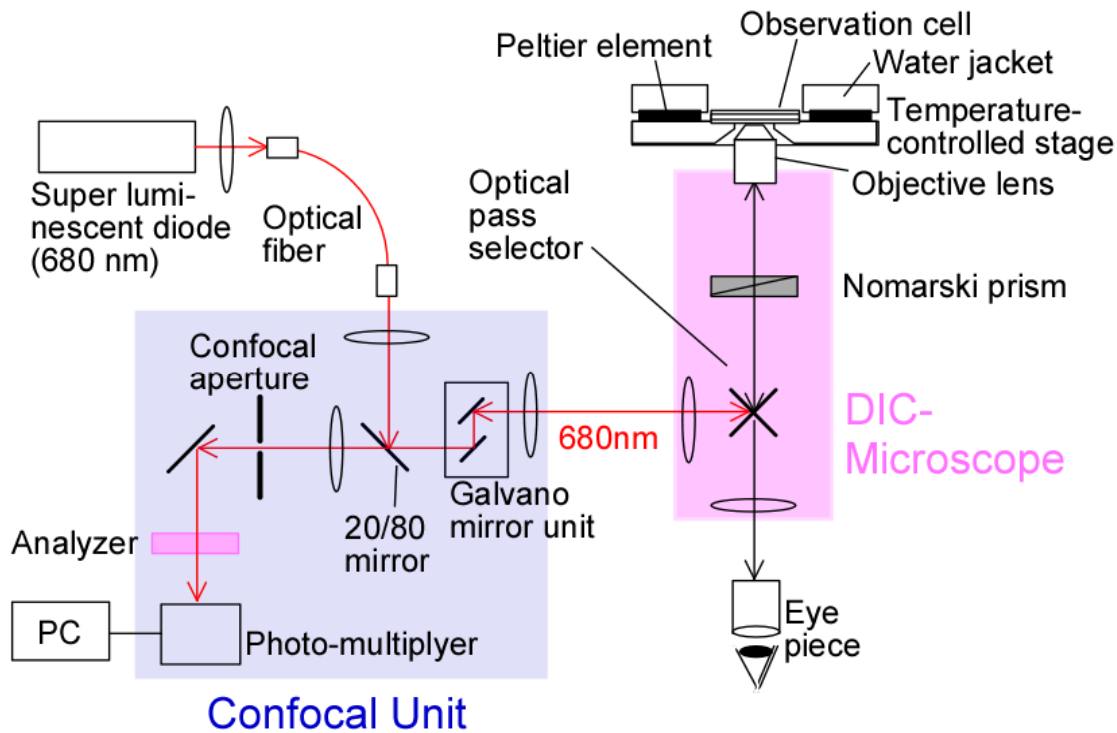


Figure 2.1. Schematic drawing of optical components integrated in the experimental setup of a LCM-DIM system.

A. Laser confocal microscopy

The principle for this microscopy type was developed in 1953 by Marvin Minsky (1957, 1988). The basic modern laser confocal scanning microscope is an integrated electronic system commonly based on a widefield epi-fluorescence instrument. However, it has the additions of multiple laser illumination sources, a scan head containing electronic and optical components, a computer and monitor for image display, and associated software for control of signal acquisition, processing, and image analysis. This technique is mainly used for imaging live cells. A reflection laser confocal microscope (confocal unit) is integrated in the LCM-DIM setup (Figure 2.1) using only one laser source and collecting only reflected light from the specimen surface. No epi-fluorescence is applied in this setup.

A laser scanning confocal microscope incorporates two basic principles: point by point illumination of the sample and rejection of out of focus light. Confocal imaging relies upon the sequential collection of light

from spatially filtered individual specimen points, followed by electronic signal processing, and the visual display as corresponding image points. In this way images are taken point by point and then reconstructed via computer to the 2D image plane one pixel at a time rather than projecting it through an eyepiece. The key feature of confocal microscopy is its ability to produce blur-free images and provide a significant improvement in lateral resolution. Additionally a 3D reconstruction of the sample can be performed by combining a series of 2D image planes taken at different depths. In the case of biological cells this is one of the main advantages of confocal microscopy. However, when observing protein crystals this feature has little application.

Image generation

The generation of a 2D image from the focal plane (i.e. object plane) of a confocal microscope is essentially comprised of three process steps:

- Line by line scanning of the specimen with a focused laser beam deflected in the X and Y directions by means of two galvanometric mirrors.
- Pixel by pixel detection of the reflected light by the scanned specimen details, by means of a photomultiplier tube (PMT).
- Digitization of the object information contained in the electrical signal provided by the PMT (for presentation, the image data are displayed, pixel by pixel, from a digital matrix memory to a monitor screen).

Confocal beam path

The term confocal refers to the condition where two lenses are arranged to focus on the same point. The major optical difference between a conventional microscope and a confocal microscope is the presence of the confocal pinholes. The pinholes serve to allow only light from the plane of focus to reach the detector (Figure 2.2). In practice the confocal principle is combined with a scanning system (not shown in Figure 2.2) utilizing a laser

source to scan a point of laser light across the sample in both X and Y directions.

The light path of a typical confocal microscope is straight forward as seen in Figure 2.2. Coherent light emitted by the laser system is first expanded and reflected by a dichromatic mirror to completely fill the objective rear aperture (a critical requirement in confocal microscopy). The laser light is then focused by the lens system to a very small spot and scanned across the specimen (X-Y plane) in a defined focal plane. Reflected light coming from points on the specimen, in the same focal plane, pass back through the dichromatic mirror and are focused as a confocal point at the detector (photomultiplier tube) pinhole aperture. A significant amount of reflected light that comes from points above and below the objective focal plane is not confocal with the pinhole (aka out of focus light rays). Because only a small fraction of the out of focus reflected light is delivered through the pinhole aperture, most of this extraneous light is not detected by the photomultiplier and does not contribute to the resulting image. In this method the out of focus points are suppressed. The result is a sharper image compared to conventional microscopy techniques. Refocusing the objective in a confocal microscope shifts the reflecting points on a specimen to a new plane that becomes confocal with the pinhole apertures of the light source and detector. One of the most important components of the scanning unit is the pinhole aperture, which acts as a spatial filter at the conjugate image plane positioned directly in front of the photomultiplier.

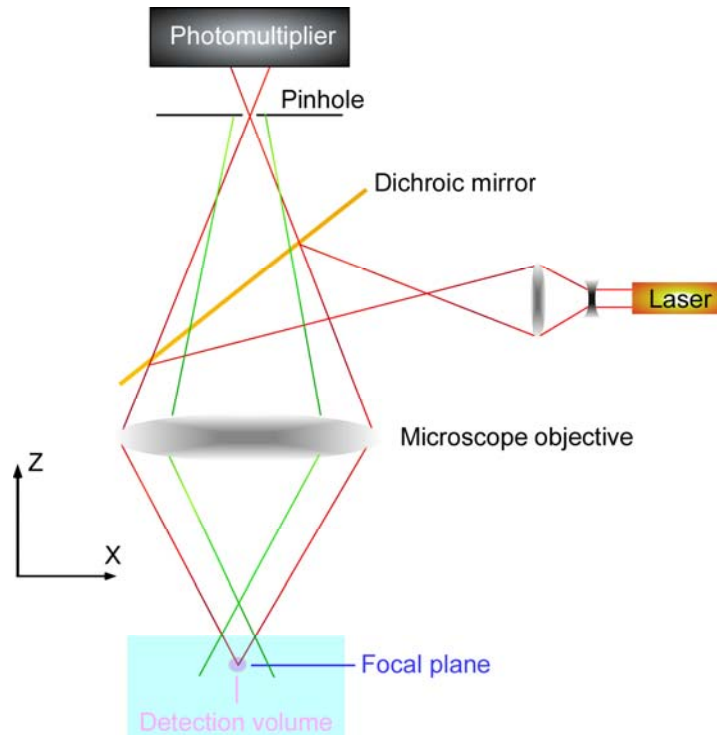


Figure 2.2 Beam paths in a confocal microscope. A microscope objective is used to focus a laser beam onto the specimen. The reflected light is collected by the objective and efficiently directed onto the detector via a dichroic beam splitter. The pinhole is arranged in front of the detector, on a plane conjugate to the focal plane of the objective. Light coming from planes above or below the focal plane is out of focus when it hits the pinhole (green lines), so most of it cannot pass the pinhole and therefore does not contribute to forming the image.

Pinhole Feature

The pinhole is the decisive design feature of a confocal microscope because it determines the sharpness of the image. The pinhole diameter is variable (ideally infinitely small) and depending on the diameter of the pinhole, light coming from object points outside the focal plane are slightly or completely obstructed and thus excluded from detection by the PMT. As the corresponding object areas are invisible in the image, the confocal microscope can be understood as an inherently depth discriminating optical system. By varying the pinhole diameter the degree of confocality can be adapted to practical requirements. With the aperture fully open, the image is nonconfocal (or completely visible) and will act as a conventional widefield microscope. In addition the pinhole suppresses stray light, which helps to improve image contrast.

Scanning unit

The scan unit is at the heart of the confocal system and is responsible for rasterizing the emitted laser light, as well as collecting the reflected light from the sample surface that is required to assemble the final image. The classification of confocal microscope designs is usually done on the basis of the method by which the specimens are scanned. In the case of LSCM a single-beam scanning method is used. The scanning of the beam is achieved by use of computer controlled mirrors driven by galvanometers (Figure 2.1). One of the mirrors moves the beam from left to right along the lateral X axis, while the other translates the beam in the Y direction. After each single scan along the X axis, the beam is rapidly transported back to the starting point and shifted along the y axis to begin a new scan in a process termed flyback. During the flyback operation image information is not collected. The speed of the confocal microscope is limited by the rate at which the mirrors can scan the entire sample plane. In our setup a scan rate of 9.6 sec/image is achieved for 1024x1024 pixels images.

B. Differential interference contrast microscopy

Differential interference contrast microscopy (DICM) is an excellent mechanism for rendering contrast of transparent specimens. Reflected DICM is one of the most common techniques used to enhance the contrast of opaque specimens. Slopes, valleys, and other discontinuities on the surface of the specimen create optical path differences, which are transformed by reflected light DIC microscopy into amplitude or intensity variations that reveal a topographical profile. The image created in reflected light DIC can often be interpreted as a true three dimensional representation of the surface geometry, provided a clear distinction can be realized between raised and lowered regions in the specimen. But this technique is not suitable for accurate measurements of physical heights and depths.

The microscope is a beam shearing interference system in which the reference beam is sheared by a minuscule amount. This technique produces

a monochromatic shadow cast image which effectively displays the gradient of optical paths for both high and low spatial frequencies present in the specimen. The regions of the specimen where the optical paths increase along a reference direction appear brighter (or darker), while regions where path differences decrease appears in reverse contrast. Pixel intensity is proportional to the local optical path gradient and thus, when the gradient grows steeper image contrast will be dramatically increased. In reflected light DIC microscopy, the optical path difference produced by a reflecting specimen is dependent upon the topographical geometrical profile of the specimen and the phase retardation that results from reflection of sheared and deformed orthogonal wave fronts by the surface.

The light path and optical components of a DIC microscope

In Figure 2.1 schematic diagram of the key optical train components forming part of the reflected light differential interference contrast microscope integrated in our LCM-DIM is presented. Linearly polarized light (East-West direction) exiting the laser is reflected from the surface of a 20/80 mirror placed at a 45 degree angle to the incident beam. The reflected light waves are deflected by an optical pass selector and are now travelling along the optical axis of the inverted microscope. The light waves are now entering a Nomarski prism (Figure 2.3a) housed below the objective, where they are separated into two polarized orthogonal components and sheared according to the geometry of the birefringent prism (Figure 2.4). The two beams are travelling in slightly different directions. Acting in the capacity of a high numerical aperture, perfectly aligned, and optically corrected illumination condenser, the microscope objective focuses the sheared orthogonal wave fronts produced by the Nomarski prism onto the surface of a reflecting specimen. The two beams travel parallel and extremely close to each other with a slight path difference. However, they are vibrating perpendicular to each other and therefore are unable to cause interference. The distance between the rays, called the shear, is so minute that it is less than the resolving ability of the objective.

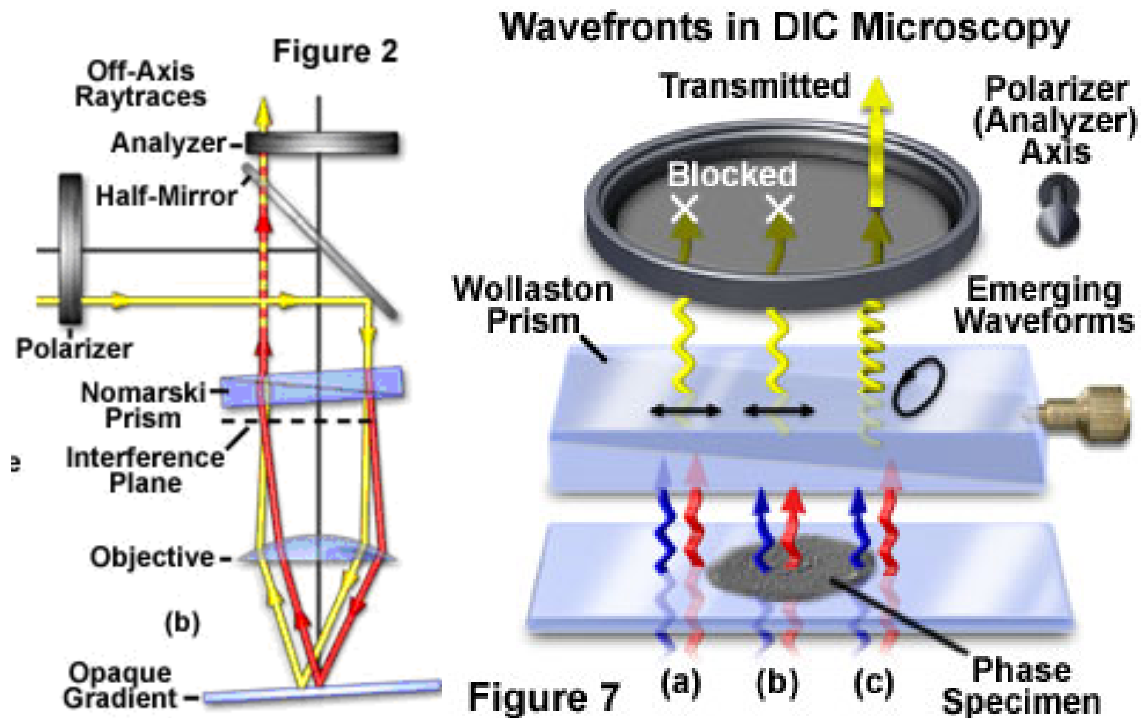


Figure 2.3. (a) Typical light path in a reflection DIC microscope. (b) Orthogonal wavefronts reflected from the specimen are being joined by the Normaski prism and made to interfere by the polarizer.

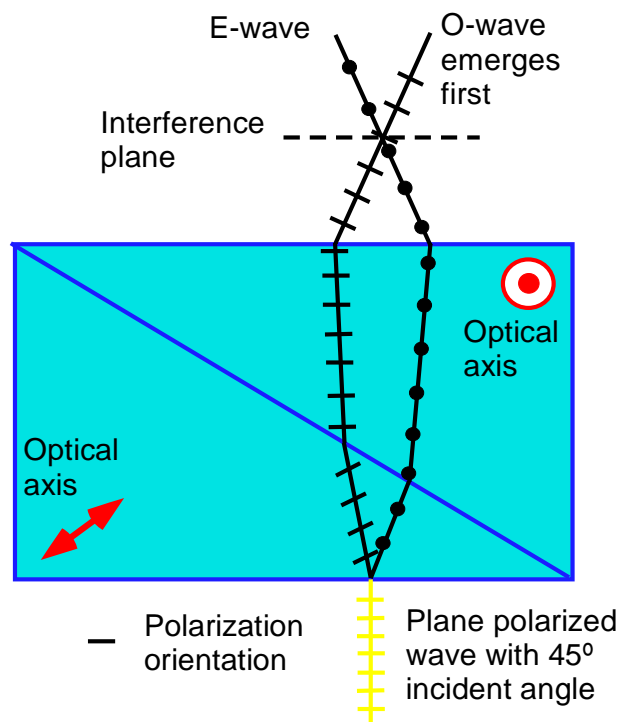


Figure 2.4. Schematic drawing of a Nomarski prism used in DIC microscopy.

In the case represented in this manuscript the reflecting specimen is a protein crystal surface in solution. The reflection is produced at the crystal-solution interface because of the difference in refractive index

(solution $\approx 1.33n$, protein crystal $\approx 1.44n$). Reflected wave fronts, which experience varying optical path differences as a function of specimen surface topography, are gathered by the objective and focused on the interference plane of the Nomarski prism. When entering the prism they are recombined to eliminate shear and the original path difference between the beam pairs and generate elliptically polarized light. Upon exiting the Nomarski prism, the elliptical wavefronts are deflected by the OPS and enter the confocal unit where they pass through a 20/80 mirror on a straight trajectory and finally encounter, in front of the photomultiplier, an analyzer positioned with the transmission axis oriented in a North-South direction. Components of the elliptical wavefronts that are parallel to the analyzer transmission vector are able to pass through in a common azimuth, in contrast to linearly polarized light (see Figure 2.3b), and subsequently undergo interference in the plane of the photomultiplier to generate amplitude fluctuations and form the DIC image.

Nomarski prism

The Nomarski prism employed in reflected light DIC microscopy is composed of two precisely ground and polished wedge-shaped slabs of optical quartz that are identical in shape, but have differing orientations of the optical axes (Figure 2.4). The axis of one wedge is parallel to the flat surface, while the axis of the other wedge is oriented obliquely. The Nomarski prism interference plane is positioned at a remote location in space, outside the prism itself. Incident linearly-polarized light waves (parallel to the optical axis of the microscope) that enter a Nomarski prism are divided into two mutually perpendicular (**orthogonal**) components, termed the **ordinary** and **extraordinary** wave, which have identical amplitudes (70.7 percent of the original polarized wave) and are coherent (provided, of course, that the illumination source is also coherent). In order to produce orthogonal components having equal amplitudes, the linearly polarized light entering a Nomarski prism is oriented with the direction of the electric vector at a 45-degree angle with respect to the principal optical

axis in the upper wedge of the prism. The wedge having an oblique optical axis produces wavefront shear at the quartz air interface, and is responsible for defining the shear axis.

The Nomarski prism (Figure 2.4) not only separates linearly polarized light into two orthogonal components, it also produces a relative phase shift (often termed an optical path difference) in each wavefront relative to the other. The degree of phase shift between the wavefronts varies linearly with the location of the input light beam in relation to the shear direction. In the LCM-DIM setup, the prism can be laterally translated along the optical axis of the microscope in the shear direction (a process known as introduction of bias retardation) to enable adjustment of the optical path difference introduced between the orthogonal wave components. In this manner, fine-tuning of the relative intensity in the image can be manipulated to produce the distinctive shadow cast appearance typically produced by DIC microscopy. Images appear as if they were illuminated from a highly oblique light source originated from a single azimuth as shown in Figure 2.5.

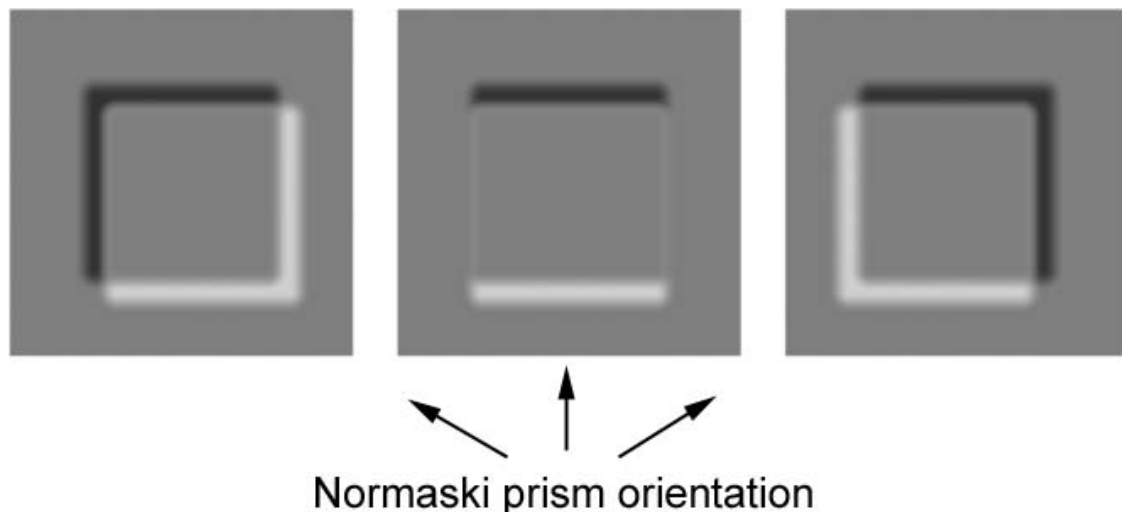


Figure 2.5. Orientation specific imaging of a transparent cuboid in DIC.

The ordinary and extraordinary wavefronts propagating toward the specimen through a Nomarski prism experience optical path differences that

have a magnitude dependent upon the location of the wave as it enters the prism. Once the wavefronts exit the prism, they enter the objective lens system (acting as a condenser) from the rear, and are focused into a parallel trajectory before being projected onto the specimen. Reflection of the orthogonal wavefronts from a horizontal, opaque specimen returns them to the objective, but on the opposite side of the front lens and at an equal distance from the optical axis. The waves gathered by the objective are focused on the Nomarski prism interference plane (again on the opposite side from their journey down, see Figure 2.3a), which results in a phase shift that exactly offsets the original difference produced before the waves entered the objective. As a result, the positional exchange of incident and reflected waves results in cancellation of relative phase shifts across the entire microscope aperture. A system of this type is referred to as being self compensating, and the image produced has uniform intensity.

In reflection DIC microscopy only a single birefringent Nomarski prism is required and the objective serves as both the condenser and image forming optical system. As shown in Figure 2.1, in the LCM-DIM setup there is also only one analyzer, and no polarizer, because laser light is used which is already linearly polarized in a certain direction. Thus in the setup of a LCM-DIM the correct aligned of the laser polarization direction and direction of the analyzer (90°) is crucial. Input waves also have to be parallel (or nearly so) to the optical axis. A poorly collimated input beam will result in nonuniform compensation across the prism (and the resulting image), destroying the unique phase relationship between orthogonal components at each image point. In a reflected light DIC microscope, the Nomarski prism is oriented so that the interference plane is perpendicular to the optical axis of the microscope (as is the objective rear focal plane).

The image

The image is generated from two identical bright field images being overlaid slightly offset from each other. The subsequent interference, due to

phase difference converting changes in phase (and so optical path length) to a visible change in darkness. This interference may be either constructive or destructive giving rise to the characteristic appearance of three dimensions. Because of this characteristic the image has the appearance of a three dimensional object under very oblique illumination, causing strong light and dark shadows on the corresponding faces (Figure 2.5). The direction of apparent illumination is defined by the orientation of the Nomarski prism. The sheared orthogonal wavefront components are separated by only fractions of a micrometer (usually between 0.15 and 0.6 μm), which is much less than the resolution of the objective. To the observer, it is not apparent that the resulting image visualized in the eyepieces is composed of these two superimposed components because their separation is too minute to be resolved by the microscope. Surface features become distinguishable because shadow directions are reversed for specimen details that possess either a higher or lower topographical profile than the surrounding surface.

Orientation Effects on Reflected Light DIC Images

Since reflected light DIC images are inherently bestowed with a pronounced azimuthal effect, many reflecting specimens imaged in differential interference contrast have a prerequisite orientation limitation in order to achieve maximum contrast (either parallel or perpendicular to the shear axis) that restricts freedom of specimen rotation. By rotating the specimen with respect to the shear axis, the contrast effects for selected specimen features can be maximized or minimized.

C. SLD light source

A super luminescent diode (Amonics 680nm SLD) is used as light source to illuminate the crystal surface. A super luminescent diode (SLD) is an edge-emitting semiconductor light source that combines high power and brightness of laser diodes with low coherence of Edge Emitting Light Emitting Diode (ELED). It can emit a single spatial mode light of the same

power as a single mode diode laser with ELED graded spectrum width. The main advantage of this illumination system is the short coherence length, typically less than 10 μ m. This short coherence length ensures that all unnecessary interference will be eliminated from the light path and only relevant information from the crystal surface will reach the photomultiplier (PMT). The SLD source is connected to the confocal unit of the experimental setup with a fiber optic coupler followed by a beam expander that enables the thin laser beam waist to completely fill the objective rear aperture. Expanded laser light that passes through the microscope objective forms an intense diffraction limited spot which is scanned by the coupled galvanometer mirrors in a raster specimen plane (point scanning) as explained above.

D. Objective lenses

An overview of the lenses used in the experimental setup is listed in table 1. Low magnification lenses (4x and 10x) were used for locating the crystals inside the observation cell. High magnification lenses (20x and 60x) were used for observing *in situ* crystal growth processes on a crystal surface. In the case of single molecule observation (see section 2.1.4) a 60x oil-immersion objective lens (60x TIRFM3) was used.

Table 2.1 Summary of the most relevant characteristic of the objective lenses used for LCM-DIM observations.

Type	Magnification	Numerical Aperture	Working distance (mm)	Lateral resolution (μ m)	Company
UPlanFL	4x	0.13 P	13.0	3.2	Olympus
UPlanFL	10x	0.30 P	3.1	1.4	Olympus
LUCPlan FL	20x	0.45 P	6.9	0.92	Olympus
LUCPlan FL	40x	0.60	3.4	0.68	Olympus
PlanApo	60x	1.45	0.15	0.28	Olympus

U: Universal lens type; Plan: “plain” lens, aberration for different wavelengths, color aberration, is corrected; Fl: lens for Fluorescent light; P: lens for Polarized light.

Shown in Figure 2.6 is a typical high magnification objective lens. High magnification objectives are prone to aberration artefacts due to variations in cover glass thickness and dispersion. Most objectives are designed to be used with a cover glass that has a standard thickness of 0.17 millimeters and a refractive index of 1.515, which is satisfactory when the objective numerical aperture is 0.4 or less. However, when using high numerical aperture dry objectives (numerical aperture of 0.8 or greater), variations of only a few micrometers of the cover glass thickness result in dramatic image degradation due to aberration, which gets worse with increasing cover glass thickness. In order to compensate for this error, the highly corrected objectives are equipped with a correction collar that allows adjustment of the central lens group position to coincide with fluctuations of the cover glass thickness. The **correction collar** is the key feature of these lenses and is very important for obtaining sharp images with a good contrast. The correct use of a correction collar requires a considerable amount of practice and careful attention.

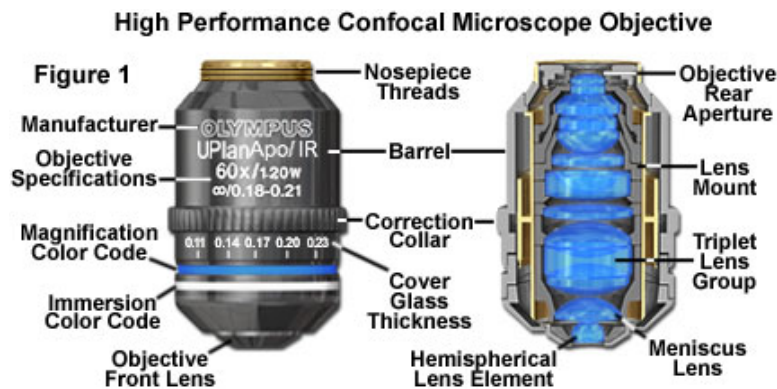


Figure 2.6. (a) View of a typical high magnification lens. (b) Transversal section of a high magnification lens.

The maximum obtainable resolution with these lenses (see table 2.1) can be calculated from Abbe's formula,

$$d \geq 0.61 \frac{\lambda}{NA} = 0.61 \frac{\lambda}{n(\sin \mu)} \quad (2.1)$$

where d is the minimum distance separating two objects, λ is the wavelength of the light source, NA the numerical aperture, n the index of

refraction and μ one half of the angular aperture of the lens. Conventional Abbe's theory describes the interaction of the parameters that can be modified to improve lateral resolution, including decreasing the wavelength of the incident light, increasing the refractive index of the specimen medium, and increasing the numerical aperture of the optical system.

Image acquisition

The fluoview program, developed by Olympus is the standard tool for the confocal microscopes of Olympus for image acquisition. Photomicrographs of 1024x1024 pixels were acquired over a 9.6 sec scan time, and the images are recorded at 10 to 300 sec intervals depending on the growth kinetics.

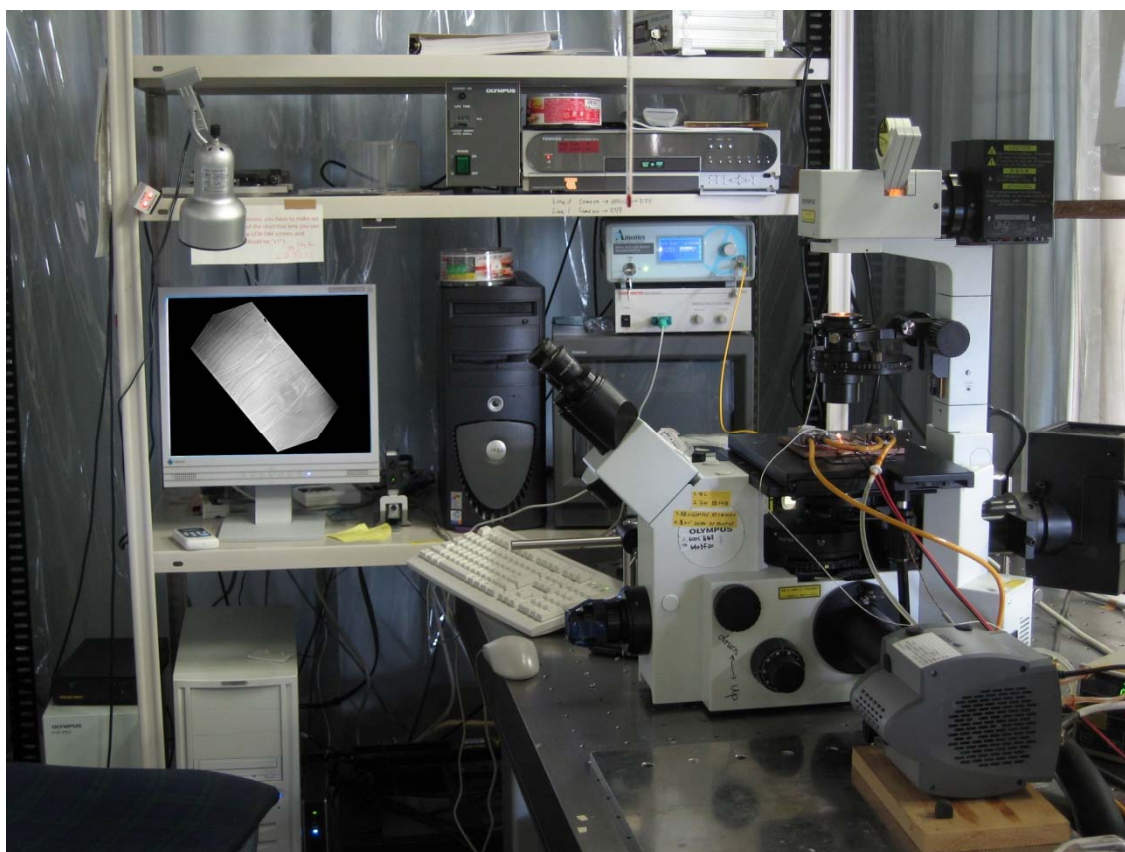


Figure 2.7 Photograph of a the Laser Confocal Differential interference contrast microscope with attached Single Molecule Visualization system and temperature controlled stage

2.1.2. Single Molecule Visualisation (SMV)

For *in situ* observation of individual fluorescent molecules at the solution-crystal interface of protein crystals a novel observation technique was used, Single Molecule Visualisation (SMV) (Funatsu, 1995; Wazawa, 2005). Single Molecule Visualization is obtained by employing total internal reflection fluorescent microscopy (Figure 2.9a). This technique has already been used in a variety of studies, making use of a near field developed on a transparent substrate (glass, fused silica, etc.), to visualize individual fluorescent molecules on a transparent substrate or in specimens (like cells or membranes) fixed on a transparent substrate. With this technique individual fluorescent molecules can be observed in the vicinity of the transparent substrate, but cannot be observed on an arbitrary crystal surface. If a near field is developed on the surface of a crystal fixed on a transparent substrate (Figure 2.9b), single molecules can only be visualized on the crystal surface when the thickness of the crystal is larger than several tenths of a micron because large aberrations caused by light transmitted through the crystal deteriorate the image seriously. The preparation of crystals that are thinner than several tenths of a micron is very difficult, and almost impossible in the case of protein crystals.

To overcome this difficulty, the newly devised optical arrangement shown in Figure 2.10 was used. In this optical arrangement, a solution layer of 1 μ m thickness is placed between a crystal surface and a bottom glass plate. Individual molecules at this solution-crystal interface can be visualized without any limitation on the thickness of the crystal as aberration is reduced to a minimum (Figure 2.9c).

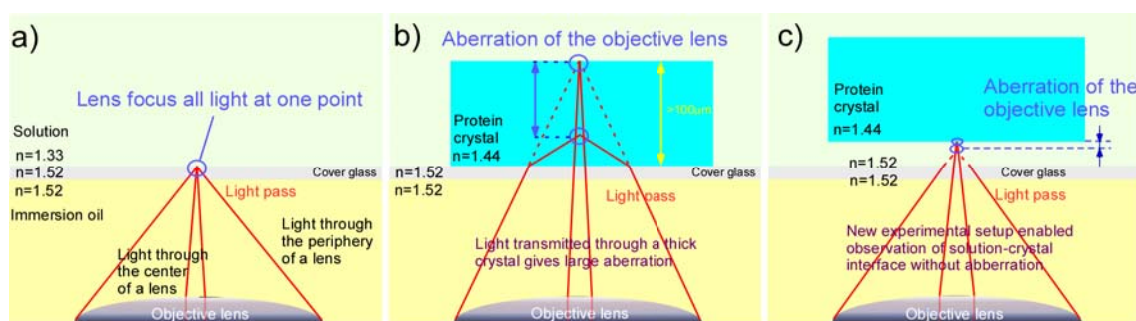


Figure 2.8. Schematic illustrations of optical arrangements of conventional total internal reflection microscopy (a) and (b), and the newly devised experimental setup used in this study (c).

Figure 2.9 shows a schematic illustration of the experimental setup used for single molecule observation. A diagonal illumination system using several mirrors (this way the angle and movement of the laser beam can be adjusted easily) was coupled to an inverted fluorescence microscope (IX70, Olympus, forming part of the LCM-DIM setup) equipped with a 60x oil-immersion objective lens (see table 1). Fluorescence labeled molecules are illuminated with a 532 nm laser, and emission at ≥ 580 nm, from the fluorescence-labeled molecules is recorded with an electron multiplying charge coupled device camera (EM-CCD, DV887, Andor Technology). The CCD camera is connected to a timer, digital video recorder, and a CRT-screen. To avoid rapid photo bleaching of the fluorescence labeled molecules, an electromagnetic shutter (timer) of the laser was sequentially opened and closed to prolong the lifetime of the fluorescence labels.

In Figure 2.10 a schematic illustration of the optical arrangement of the *in situ* observation of fluorescence labeled molecules at the interface between the solution and a crystal surface face is shown. A crystal is placed on $1\mu\text{m}$ spacer beads adsorbed on the bottom glass plate. The solution-crystal interface is illuminated by a laser beam tilted almost parallel to the crystal surface (several degrees from a horizontal direction) to avoid the increase in background intensity of fluorescent light. In this optical arrangement, an area of about $25\mu\text{m}$ in diameter is illuminated by the laser beam, and fluorescence labeled molecules inside this area are observed *in situ*. This experimental setup allows the observation of both, single

molecules and the crystal surface at the same time. This can be done by switching from SMV to LCM-DIM observation simply by turning the optical pass selector (Blue arrow in Figure 2.9). During SMV observation the SLD has to be turned off to reduce noise in the images and the room has to be dark.

When using fluorescent labeled protein molecules and the Brownian motion of the target molecules should not be affected by the presents of the fluorescence molecules because of the much larger size of the protein molecules (Sazaki, 2007).

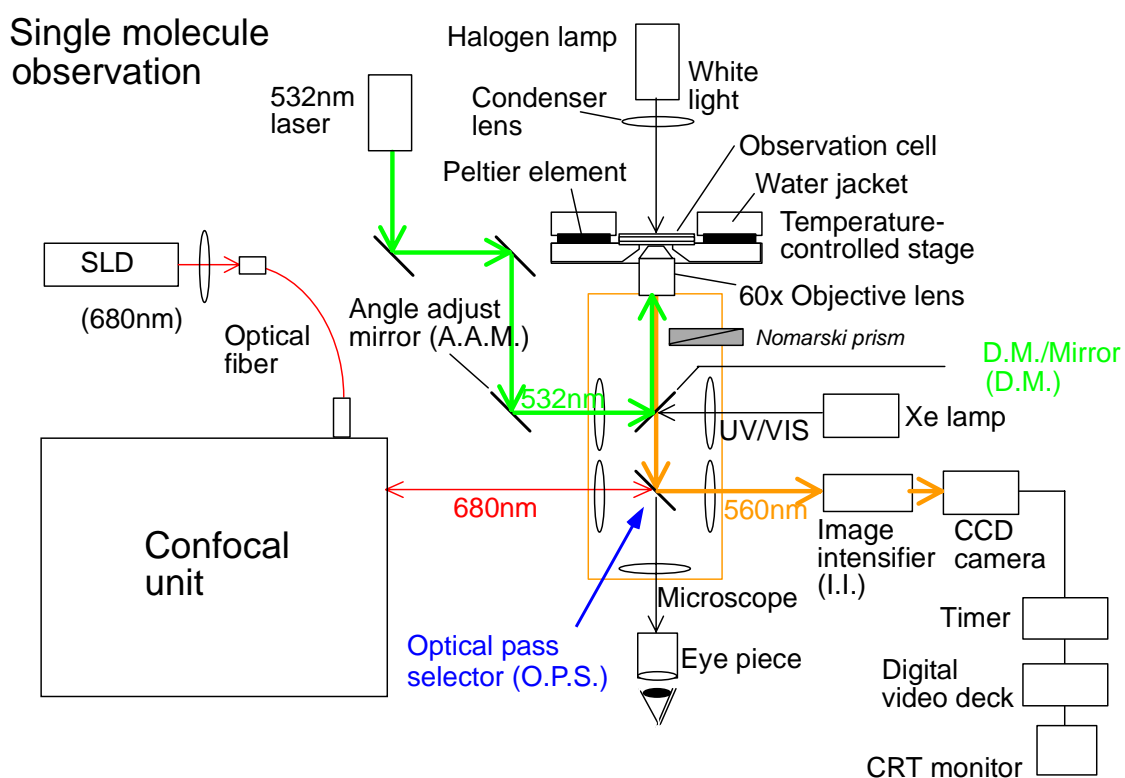


Figure 2.9. Schematic view of the experimental setup used for single molecules visualization (SMV) incorporated into the LCM-DIM setup.

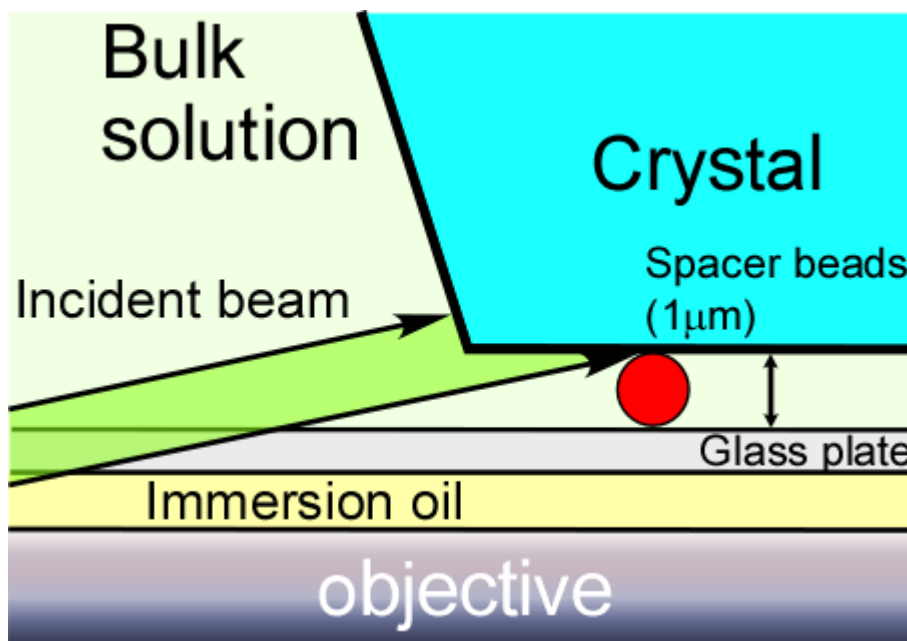


Figure 2.10. Schematic view of the optical arrangement of single-molecule visualization used in this study.

2.1.5. Observation cell preparation

LCM-DIM observation cell

The observation cell is made out of two glass plates (0.17 mm thickness) and polystyrene spacers of 1.0 mm thickness: all of these parts are glued together by silicone adhesive (see Figure 2.11). Before introducing the seed crystal and after solidification of the adhesive, the cell was carefully washed by ultrasonic cleaning with pure (Milli-Q) water. Once the seed crystals are introduced into the cell the top cover glass is fixed and the cell is sealed with silicone adhesive to avoid evaporation. Growth cells sealed in such a way provide stable conditions for several weeks, and possibly even months. Figure 2.12 shows a cross section view of a typical observation cell used for LCM-DIM observations.

The thickness of the bulk (protein) solution between the two glass plates is 1.0 mm and the final volume is approximately 250 μl . The arrow in Figure 2.12a indicates the crystal–solution interface on which surface microtopography was observed by the LCM–DIM system. The observed

crystals surfaces have to be almost completely parallel to the bottom glass plate.

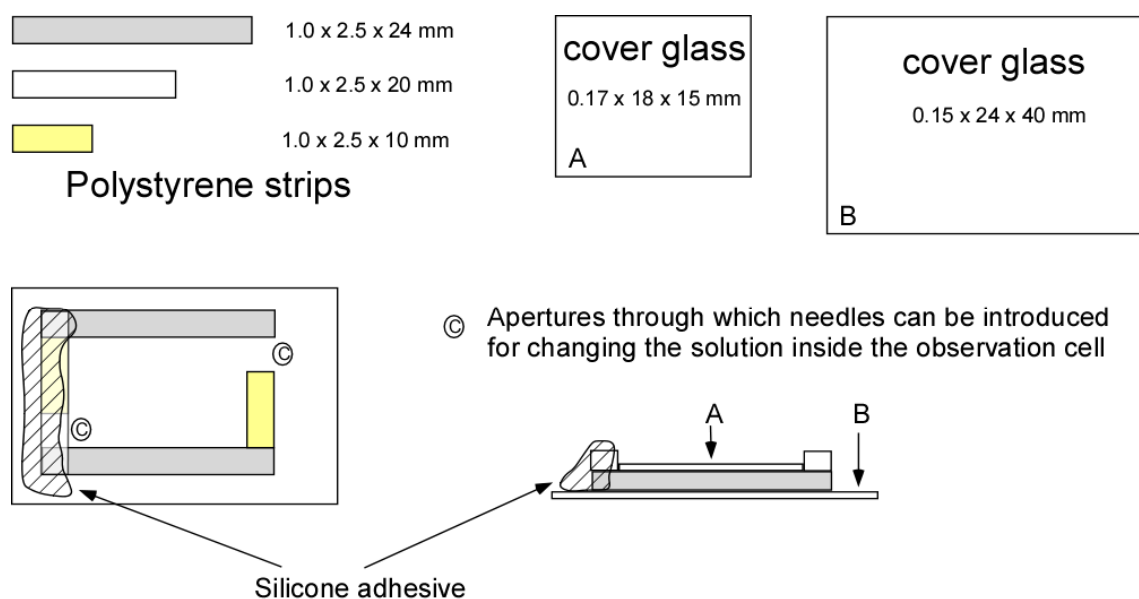


Figure 2.11. Materials used in the preparation of a typical observation cell.

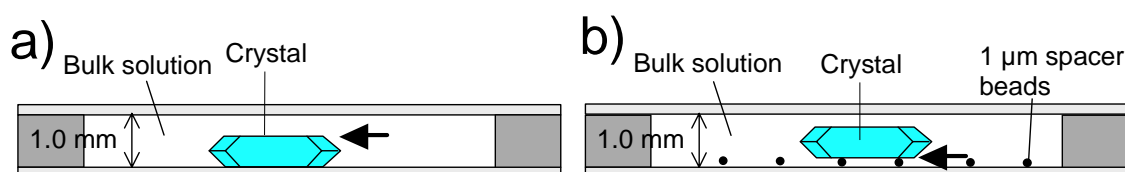


Figure 2.12. (a) Schematic cross section view of an observation cell used for LCM-DIM. (b) Configuration for single molecule visualization experiments.

All observation cells were handmade and allow great flexibility in the design as a function of the each experiment requirement. For example in the case of few available samples, the volume of the cell can be drastically reduced by reducing the dimensions of the cell. This design also allows the use of needles (see Figure 2.11) coupled to a peristaltic pump so that the solution inside the observation cell can be easily changed.

SMV observation cell

The observation cell used for SMV observation is very similar to one used for LCM-DIM observation. But before starting single molecule visualization experiments, the observation cell (Figure 2.12b) should be carefully washed to remove the dust particles inside it which strongly

disturb the study of individual fluorescent labelled molecules. Hence, the inside of the observation chamber was sequentially washed by ultrasonic cleaning with solutions of 2% NaClO, 0.01 M KOH, and ultra pure water. Then, to adsorb beads of 1 μ m diameter on the bottom glass plate, a suspension containing 0.2 mg/ml polystyrene beads of 1 μ m diameter (FluoSpheres F8814, Molecular Probes, Inc.), 0.01 mg/ml HEWL, 25 mg/ml NaCl and 50 mM sodium acetate (pH 4.5) was placed in the chamber for 15 min. The polystyrene beads are necessary to make a suitable distance, 1-5 μ m, between the bottom glass plate and the observed crystal surface, so that the fluorescence of single fluorescent labeled molecules can be detected properly. The inside of the chamber was rinsed with ultra-pure water and left to dry. The bold arrow in Figure 2.12b indicates the crystal–solution interface on which surface microtopography was observed by the SMV system.

Temperature control

The observation cell is placed on a temperature controlled stage as shown schematically in Figure 2.13. In this way the temperature of the solution inside the growth cell can be adjusted in the range of 12.0–35.0°C. Peltier elements are used for heating and cooling. For temperature control a NETSU–DENSHI (thermomodule controller model MT802-07P12) temperature controller is used, which automatically switches from heating to cooling mode, if the set point rises above the reference temperature. Thermic silicon (SUNHAYATO Model SCH-20) is serves to improve the thermal contact between the copper socket and the observation cell. For the calibration of the system, we have implemented a test cell with a thermocouple inside, which measured the temperature at the position of the seed crystals. The obtained calibration curve (Figure 2.14) is used to calculate the temperature inside the cell for each experimental condition. The room temperature was kept constant during the experiment to improve the accuracy of the temperature controlled stage.

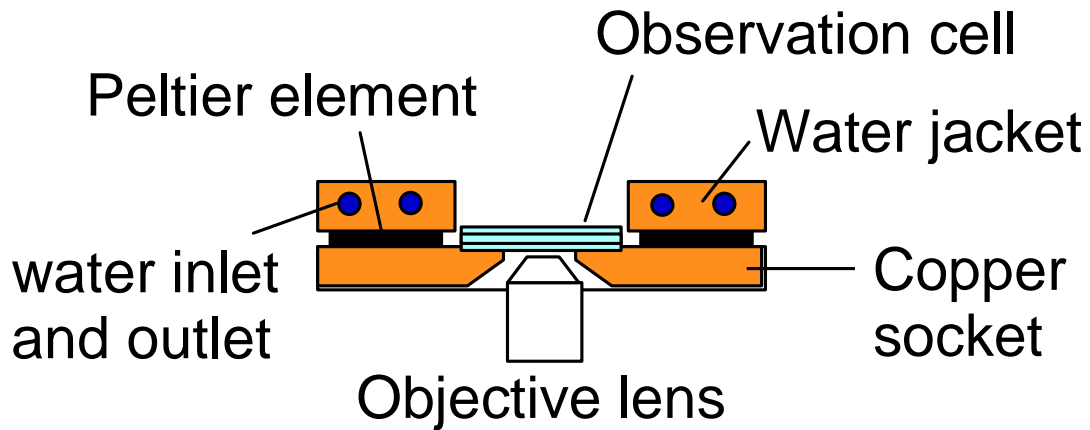


Figure 2.13 Schematic representation of temperature controlled stage used for LCM-DIM and SMV observations.

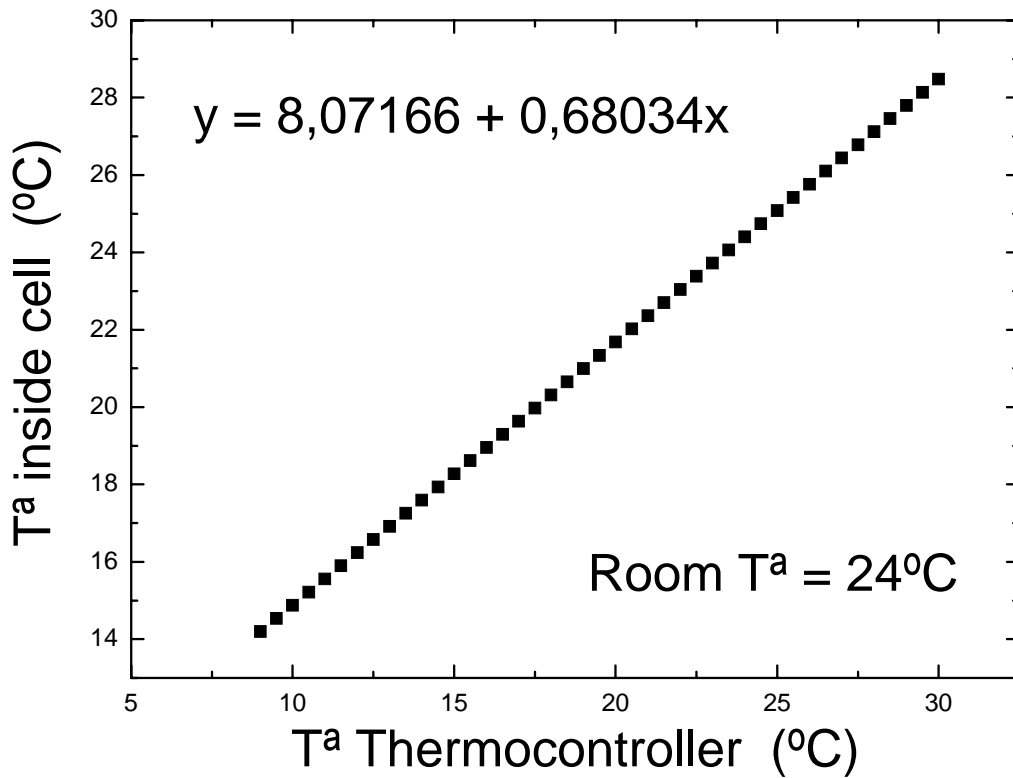


Figure 2.14 Calibration curve between the applied temperature of the thermocontroller to the observation cell and the measured temperature inside a typical observation cell at constant room temperature (24°C).

2.2. Phase-shifting Michelson Interferometry

The Michelson interferometer is the most common configuration for optical interferometry. An interference pattern is produced by splitting a beam of light into two paths, bouncing the beams back and recombining them. The basic principle of the Michelson interferometer is illustrated in Figure 2.15. A beam emitted by a light source is split in two beams of equal intensity by a 50/50 mirror. One of these beams is directed onto a flat reference mirror and the other onto the specimen surface. The reflected light of these two beams is then made to interfere. Since light waves reflected by the sample and the reference mirror originate from the same light source, these waves are mutually coherent, and as consequence a two-beam interference pattern is obtained. The compensating plate inserted between the 50/50 mirror and reference mirror is a glass plate of the same composition and thickness as the 50/50 mirror. Owing to the presence of this plate, the two divided light beams arrive at the CCD after propagating through the same optical path (i.e., refractive index and thickness). The recording of a optical interference pattern by an detector (e.g. CCD camera) is called interferogram. An example of an interferogram from a protein crystal surface is shown in Figure 2.15b.

Michelson interferometry has been successfully applied to the study of growth kinetics and surface morphology of inorganic (Malkin *et al.*, 1989; Onuma *et al.*, 1994) and protein crystals (Gliko *et al.*, 2002 and reference therein) grown from solution. While inferior in spatial resolution to AFM, this technique is nonintrusive and allows imaging and monitoring of entire crystal faces. In addition, time resolution is greater, only limited by the CCD maximal frame rate. Thus interferometry is certainly not new, but combining old interferometry techniques with modern electronics,

computers and software has produced extremely powerful measurement tools.

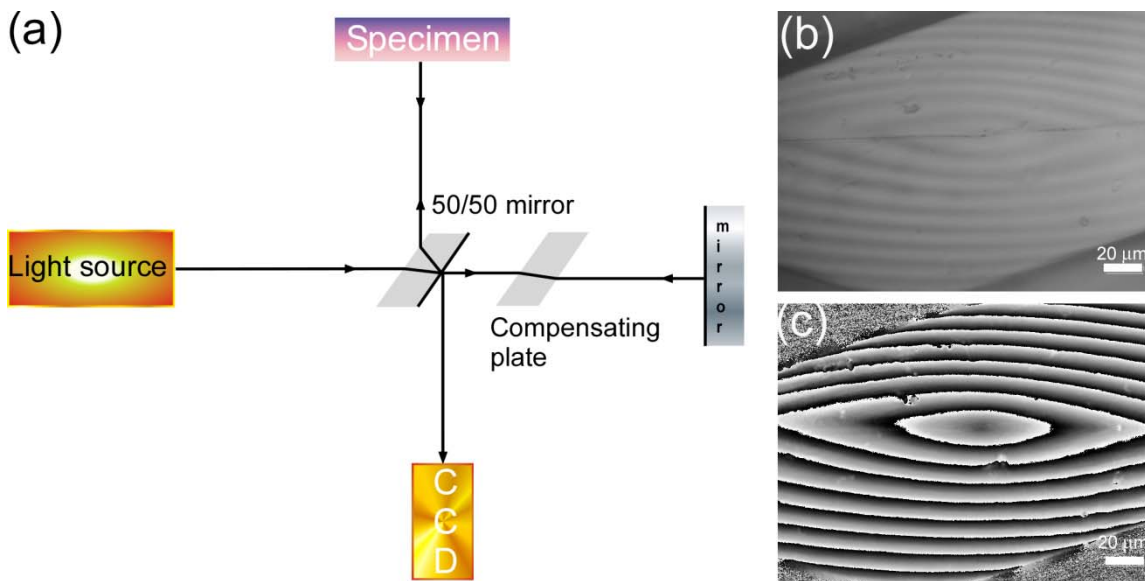


Figure 2.15 (a) Schematic drawing of a Michelson type interferometer. (b) Typical interferogram obtained from a protein crystal surface. (c) Phase shift image obtained from three successive interferograms.

Phase Shifting has been widely adopted in optical interferometry for retrieving phase information encoded in the interference fringes. The technique functions primarily by acquiring a number of intensity images (interferograms) with induced phase increments between successive frames. These controlled phase increments are generally induced using a piezoelectric device (PZT). From these successive interferograms, by applying an algorithm, the required information can be retrieved immediately and a reference image is no longer needed as is the case in normal interferometry. A typical example of a phase shift image is shown in Figure 2.15c. The development of phase-shifting interferometry (Burning *et al.*, 1974) and its application to the field of crystal growth (van Eckenwort, 1992) has significantly increased the depth and time of resolution of the obtained crystal growth data (Gliko *et al.*, 2002).

2.2.1 Setup

A schematic diagram of the phase-shifting Michelson interferometer (PSMI) is presented in Figure 2.16. The modified MI used for this work is based on a Fabulous interferometer (Olympus Optical Co. Ltd) which adopts modified Michelson-type interference optics. A Xe-lamp is used as a non-coherent white light source. The white light from the Xe-lamp passes through a monochromatic filter selecting in this way a single wavelength, 523 nm. The beam is then divided in two by a beam splitter. The surface of a growing crystal reflects one of the arms, while a high flatness mirror is used in the reference arm. The sample and reference arm are mounted on two independent focusing stages. The beams are focused on the sample and mirror by high magnification objective lenses (Linnik configuration*) which have super long working distances. Uniform intensity along the cross section of the two beams is a crucial requirement for quantitative surface characterization. This is achieved by using high quality optical components, and by careful alignment of all optical components using mechanical mounts with micrometerscale adjustments. Glass plates of appropriate thickness acting as compensators have to be inserted into the reference beam to adjust precisely the optical path of both beams, which is important for obtaining interference fringes with good contrast. The depth resolution of the method is determined by the flatness of the reference mirror (the best serially produced mirrors have a guaranteed flatness of “1/20 of the wavelength”). The reflectivity of the mirror is adjusted to the reflectivity of the crystal surface by inserting an appropriate grey filter because practical resolution limits depends strongly on the reflectivity of the crystal face. Also important is the disturbance originated by the solution or cover glass and overall quality of the optical parts as discussed above. The use of white light instead of a laser shortens the coherent wavelength, which makes it more difficult to achieve interference between sample and mirror, but strongly reduces the noise and thus improving the quality of the

**This instrument uses a high magnification objective lenses in order to apply the interference technique to the observation of minute details. The principle employed is the same of the Michelson interferometer. Since uniform objective lenses are difficult to manufacture, only a small number of such instruments have been marketed.*

interference fringes. To minimize any kind of shift during the measurements, ambient air temperature has to be stabilized and the system protected from air drag. Also an adequate anti-vibration system is essential and for this reason the microscope and all optical components are mounted on a floating optical table. The working distance of approximately 30 mm enables the use of sealed and well insulated growth cells to ensure stable growth conditions.

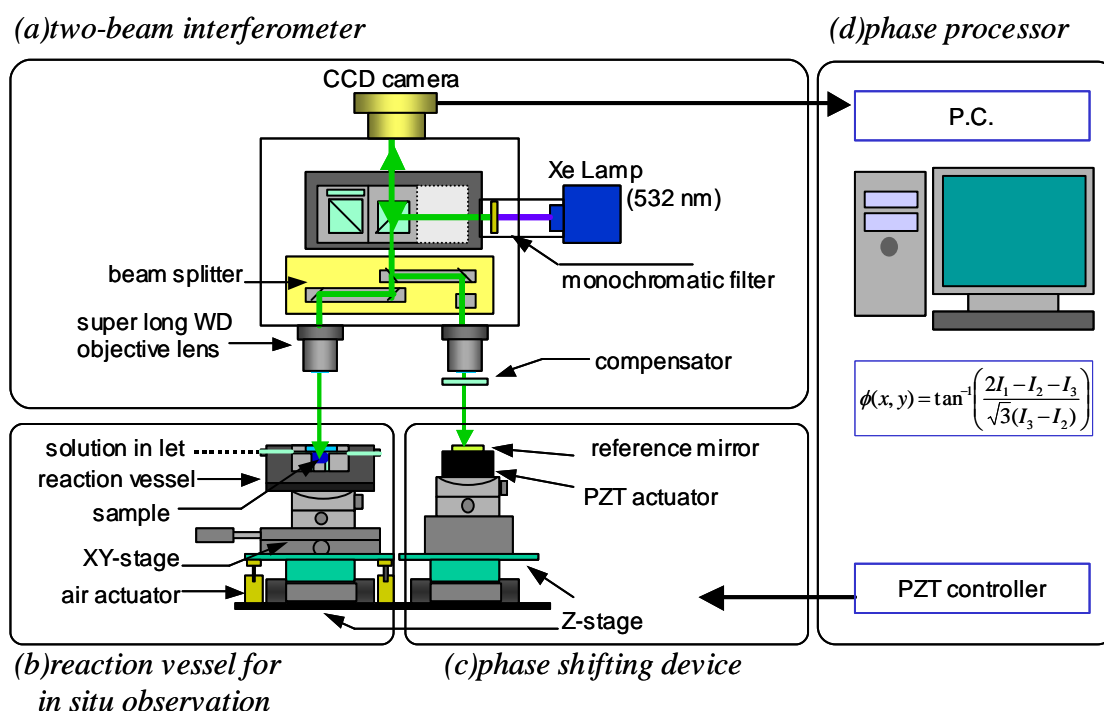


Figure 2.16 Schematic drawing of a modified Michelson type phase-shifting interference microscope: a) two-beam interferometer, b) observation stage, c) phase-shifting and reference mirror stage, d) Piezo electro controller and phase processor.

The *phase-shifting process* is achieved by slightly moving the vertical position of the reference mirror. The Z-stage of the reference mirror is driven by a piezo actuator and a three-step phase-shift method of equal step displacement is applied. As a result, the optical pathway of the reference beam is varied, shifting the phase position of the interferograms by 0 , $2/3\pi$ and $4/3\pi$. It takes about 2.6 seconds to capture a series of 3 interferograms (I_1 , I_2 and I_3), from which a phase shifting interferogram is constructed.

For image acquisition, a 1360x1024 pixel CCD camera with 8 bit grayscale resolution is used. Images are taken automatically; the image acquisition is typically time-lapsed on the order of 10 to 300 seconds, depending on supersaturation and growth velocity. For acquisition of single PSI images, exposure time of the CCD is short enough (in the range of 200 ms) to prevent any disturbance due to external shifts or due to the progressing step front. But for dynamic processes extending over several minutes or hours a fixed reference point is necessary to correct external drift (n.b. the range of normal growth rates, which are possible to measure with this system goes down to 10^{-3} to 10^{-4} nm/s). In interferometry, due to the separation into two independent beams, thermal or mechanical shifts cannot be avoided completely. Coating part of the surface with e.g. gold, as it is often used for the measurement of dissolution processes of inorganic materials, is not feasible for organic macromolecular crystals. The use of a reference mirror outside the growth cell (Gliko *et al.*, 2002a; 2002b) has the drawback that it requires change of the focus position disturbing the measurement. The fact that with this set-up individual terraces and growth steps can be distinguished (see chapter IV section 3) is of great advantage. Specific terraces can be used as internal reference points: If a molecularly flat crystal area is moving into the Z-direction (without a new layer spreading over the surface), it has to be attributed to an artificial shift and can be corrected after measurement. Practically, the gray value of a specific terrace or growth step is fixed and the following images are corrected with respect to this gray value.

2.2.2. Growth cell

The growth cell used for interferometry experiments is identical to that used in LCM-DIM experiments and is explained in detail in chapter III section 2.1.3.

2.2.3. Processing of phase-shifting interferometry data

A three-step phase-shifting algorithm is employed. The phase shift interferograms obtained with this system are composed of three conventional interferograms taken at different phase positions 0 , $2/3\pi$ and $4/3\pi$. The intensity distribution at a point (x,y) within each of the three interference fringe is described by:

$$I(i)_{x,y} = a_{x,y} + b_{x,y} \cos(\phi_{x,y} + \delta(i)) \quad (2.1)$$

where $I(i)$ is the intensity of the conventional interferogram at each phase shifting position i , a is the background and b is the amplitude of the fringe wavelet, ϕ is the phase and $\delta(i)$ is the phase shift, which is exactly known for each position i . When we measure $I(i)$ at positions $\delta(i) = 0, 2/3\pi$ and $4/3\pi$ (i.e. $i=3$), ϕ as a linearized interferogram can be obtained from each $I(i)$ by canceling the other independent variables :

$$\phi_{x,y} = \arctan\left(\frac{\sqrt{3}(I(3)_{x,y} - I(2)_{x,y})}{2I(1)_{x,y} - I(2)_{x,y} - I(3)_{x,y}}\right) \quad (2.2)$$

The conversion from the contrast of the phase shift interferogram $\phi_{x,y}$ to a height profile can be performed according to:

$$h_{x,y} = \frac{\lambda_{532}}{2 \cdot n} \cdot \frac{I_{x,y}}{256} \quad (2.3)$$

where $h_{x,y}$ is height in nanometer at position (x,y) , λ is wavelength in nm, n is refractive index, $I_{x,y}$ is the image intensity at position (x,y) . With a refractive index $n=1.4$ (lysozyme crystal), a grayscale information of 8 bit corresponds to 190 nm and the resolution limits in vertical direction calculates to $190/256 = 0.74$ nm.

The advantages of phase-shifting interferometry to conventional two-beam interferometry are two-fold. The first benefit is linked to the inversion of the signal to obtain the phase and hence the surface height. Conventional interferometry relies on the arccosine function, which has an area of very

low sensitivity (small changes in the function in response to large variations in the argument) around the center and boundaries of each domain limited by discontinuities. In contrast, the arctangent function, employed by the phase-shifting algorithm, has linear sensitivity at the center, and near-exponential sensitivity near the boundaries of each domain. One could say that to avoid areas of low sensitivity of a conventional one-image interferometry, we shift the phase and collect other images in which these areas are viewed at high sensitivity.

The second advantage is the subtraction of the intensities in Eq. 2. It eliminates all noise, which is not due to interference with the reference mirror, the level of this latter type of noise varies as the phase of the reference beam is shifted, and it will not be eliminated by subtraction. The disadvantages of the phase-shifting interferometry are longer time required to collect one characteristic image from a surface, and a significantly higher level of complexity (e.g. adjustment of the interferometer is very delicate).

The phase data along one line selected on the monitor is calculated in real-time and lined up on the monitor (x-t) diagram. This x-t diagram is useful to measure and visualize the change of height at all positions along the line in-situ. Data processing is carried out after all data has been collected. From these data normal growth rate and surface topography were obtained.

2.3. Atomic force microscopy

This is already a very well known *in-situ* observation technique in the field of protein crystal growth. For this reason it will only be shortly reviewed pointing out the essential features since extensive and detailed descriptions already exist in the literature (e.g. McPherson *et al.*, 2003; and references therein).

3.3.1. Setup

Atomic force microscopy (hereafter AFM) is one of a number of microscopical techniques broadly referred to as Scanning Probe Microscopy (SPM). In the early 1980's Binnig and co-workers invented the Scanning Tunneling Microscope (STM, Binnig and Rohrer, 1982; Binnig *et al.*, 1982). In 1986 they reported a new SPM-based technique, called atomic force microscopy (AFM, Binnig *et al.*, 1986). Like any SPM techniques, in AFM (Figure 3.1), the sample surface is scanned with a probe, an ultrasharp microfabricated tip, mounted on the end of a flexible cantilever. Lateral and vertical movements of either the tip or the sample are controlled by piezoelectric positioners with sub-Ångstrom precision (Binnig *et al.*, 1986). AFM was applied, for the first time, to observe a growing macromolecular crystal surface by Durbin and Carlson in 1992. Both possible operations modes, tapping and contact have been used to study biological macromolecules crystal growth (Hansma *et al.*, 1994). In contact mode, the AFM tip remains in contact with the sample during scanning, while in the tapping mode the tip oscillates a few Ångstroms above the sample surface, approaching the surface only during a short interval in its oscillation cycle. In both tapping and contact modes, a feedback mechanism adjusts the vertical height of the sample (or AFM tip) using the piezoelectric positioner to

maintain a constant tip oscillation amplitude (tapping mode) or a constant cantilever deflection (contact mode).

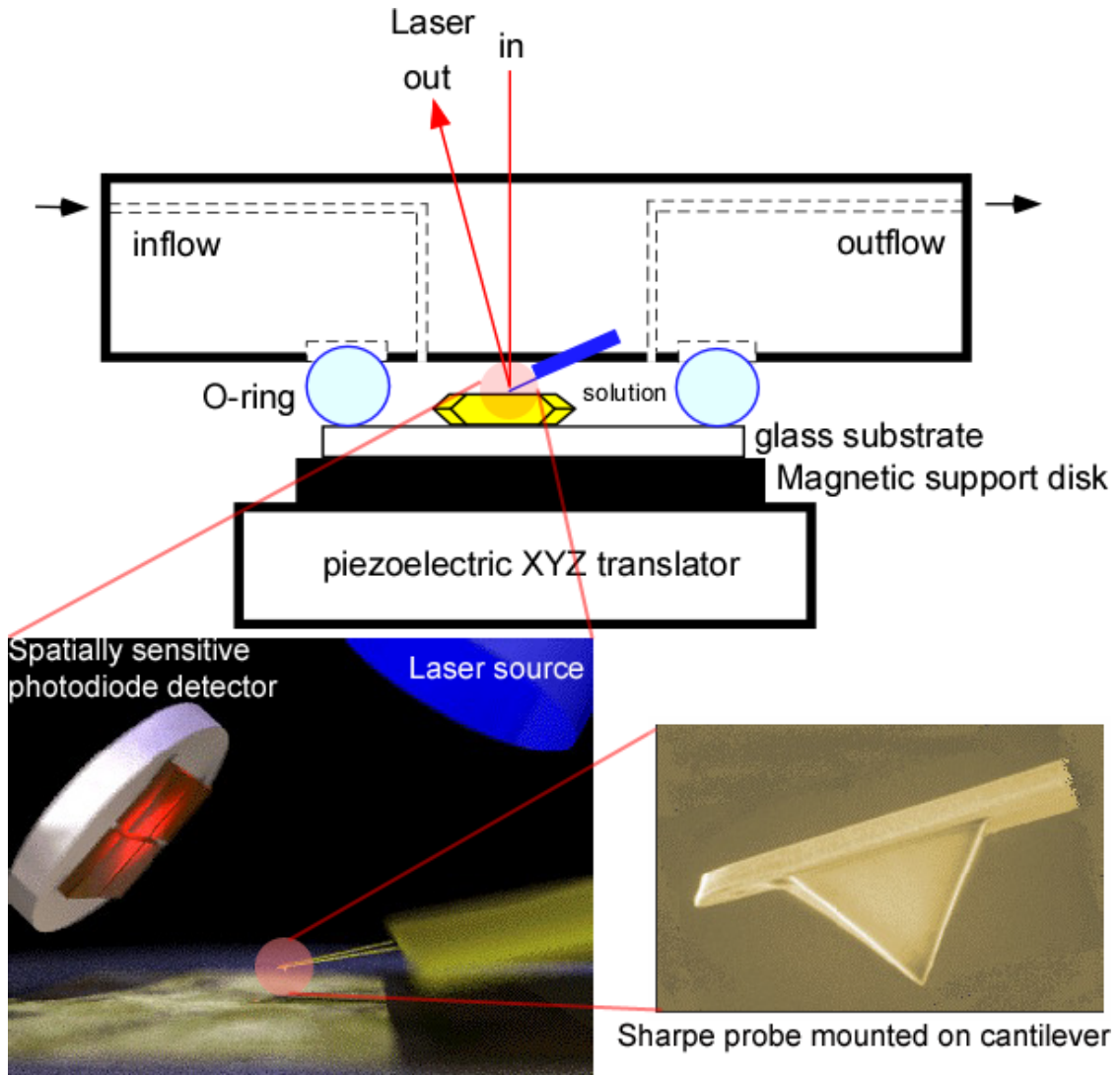


Figure 2.17 Schematic diagram of an atomic force microscope: a) a laser beam is reflected from the upper surface of the cantilever and detected with a fourquadrant photodetector. Scanning takes place in a fluid filled cell of about 50–75 μl volume. The sample is rastered relative to the tip by a piezoelectric positioner upon which the fluid cell is mounted, b) Schematic representation of a typical AFM scanning head set up, c) The inset shows an STEM image of a cantilever tip.

Tapping mode minimizes tip–sample interactions and greatly reduces lateral forces. Both contact and tapping modes have successfully been utilized

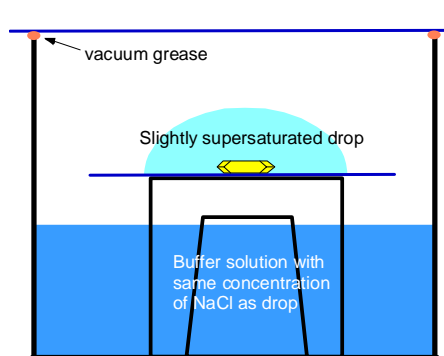
to image macromolecular crystals. Some very soft or fragile crystals which could be mechanically damaged in contact mode will only be successfully imaged using tapping mode. For more robust crystals, the stronger tip-sample interactions in contact mode can cause detachment of macromolecules from the crystalline surfaces, so that tapping mode is better suited for high-resolution imaging of macromolecular crystal growth processes. In section 1 of Chapter IV the advantages and disadvantages of the use of AFM for biological macromolecule crystal growth kinetics studies will be discussed.

A key parameter in tapping mode is the amplitude set point, which defines the tip oscillation amplitude to be maintained by the feedback loop. The oscillating tip and cantilever can produce fluctuations of the local concentration when imaging in supersaturated solutions, so the set point should be constantly adjusted to minimize perturbation of the surface structure and processes being imaged. For tapping-mode imaging in liquid, the amplitude set point is usually gradually decreased under manual control from an out-of-contact value that yields no image until a good tracing of the sample is reached. Another important parameter in tapping mode imaging is the oscillating cantilever's drive amplitude, which should be kept in the range of 0.3–0.5 V to avoid damaging the sample. Tapping mode AFM images are typically collected from height data. Height data shows the change in the piezo height needed to keep the cantilever's oscillation amplitude constant. Simultaneous images can be collected from amplitude data, which shows changes in the cantilever's oscillation amplitude and often displays the greatest contrast.

3.3.2. Sample preparation

For *in-situ* AFM experiments, a seed crystal must be immobilized on a substrate which is then attached to the AFM sample base. One commonly used method is to grow seed crystals on a rough surface (e.g., frosted glass). If many crystals nucleate and grow on the substrate accurate estimation of supersaturation during AFM observations of crystal growth will be difficult. Another method is to grow seed crystals using either the vapor diffusion or batch techniques in a crystallization box. The seed crystal in a droplet of mother liquor is then transferred to a substrate and can be clamped in place beneath flexible carbon fibers attached to the substrate. The substrate with the seed crystal should then immediately be mounted on the AFM base and the AFM fluid cell sealed to prevent crystal dehydration.

In this work an improved methodology was designed to obtain a single crystal with proper orientations and without the need of external materials



such as carbon fibers. Seed crystals were first grown using the batch technique in 200 μ l eppendorf tubes (70 mg/ml Seikagaku lysozyme, 25 mg/ml NaCl, 50 mM sodium acetate buffer, pH 4.5). Once the seed crystals reached a desirable size (0.1-0.3 mm in height), one seed crystal was transferred to

a glass substrate in a slightly supersaturated solution and incubated in a limbro plate with buffer solution and sealed to prevent evaporation. After 24 hours of incubation the seed crystal was sufficiently attached to the glass substrate and was immediately mounted on the AFM base and the AFM fluid cell sealed to prevent evaporation.

Crystallization processes of a single crystal under different supersaturation conditions can be examined by changing the solution in the fluid cell. Typically, the supersaturation is controlled by the macromolecule or precipitant concentration. But in the case of lysozyme the high dependency of solubility on temperature allows to control the supersaturation by varying the temperature. An “environmental hood” from Digital Instruments was used for a suitable temperature control of the fluid cell. Temperature inside the fluid cell was monitored with PT element.

3. Protocol of a typical crystal growth experiment

3.1. Solution preparation

Seikagaku lysozyme is dissolved in a 50mM Na-acetate buffer (pH 4.5) and dialyzed against the same buffer at 4°C. The solution is filtered (0.2µm) and the lysozyme concentration is determined by measuring the absorbance at 280 nm. Stock solutions of approximately 180mg/ml are stored at 4°C for further usage, also stock solution of 200 mg/ml NaCl are prepared in a 50mM Na-acetate buffer (pH 4.5) and filtered (0.2µm).

Highly purified solution was used as received. The concentration was approximately 200 mg/ml, no further dialysis is necessary since during the process of purification the samples are already dialysed.

3.2. Seed crystals

Batch crystallization is used to grown tetragonal crystals of model protein hen egg-white lysozyme at $20.0 \pm 0.1^\circ\text{C}$ from a solution containing 70 mg/ml Seikagaku lysozyme, 25 mg/ml NaCl and 50 mM sodium acetate (pH 4.5) buffer. Volumes of 150 µl crystallization solution are guarded in 200 µl Eppendorf containers. At these conditions approximately 50-100 seed crystals of 100 µm height are obtained after 2 -3 days.

3.3. Seed crystal transfer to observation cell

Once seed crystals of a desirable size are obtained and an observation cell is prepared tetragonal lysozyme crystals can be transferred from the eppendorf containers to the observation cell. Fig. 3 gives a schematic overview of how seed crystals are transferred. An eppendorf containing seed crystals is filled until the rim with a “washing solution”, this is a slightly supersaturated solution (20 mg/ml lysozyme, 25 mg/ml NaCl and 50 mM sodium acetate (pH 4.5)). Seed crystals are detached by locally increasing the temperature, and hence the solubility, by using the fingertips. After a desirable amount of crystals are detached from the eppendorf walls this should be turned around and detached crystals will sediment to the air-solution interface. This interface is brought in contact with a drop of washing solution placed on a siliconized cover slip, this way seed crystals will pass from the eppendorf to the drop. Once enough crystals are present in the washing solution a pipet can be used to transfer a selection of optical perfect crystal to a series of drops of washing solution. Final a couple of seed crystals are selected and transferred with a pipet to the bottom glass plate of the observation cell where a drop of washing solution is present. If necessary, crystals can be orientated properly by using a pipet before the observation cell is sealed off with a top cover slip and made air tight using silicon adhesive as explained in section III.2.2.3.

For AFM experiments the bottom glass cover slip, with seed crystals, is placed in a sitting drop configuration in a 24 well plate containing buffer solution to prevent evaporation of the solution drop with seed crystals. The reservoirs are sealed off with cover slips and vacuum grease and kept at 20°C

Protocol of a typical crystal growth experiment

for 24h. After this time period lysozyme crystals are fixed strong enough to the bottom cover slip preventing the cantilever tip from moving the crystals during scanning of the crystal surface. This method provides single crystals of lysozyme with proper orientations for the AFM experiment without having to use external materials to keep the crystals in place during scanning of the cantilever.

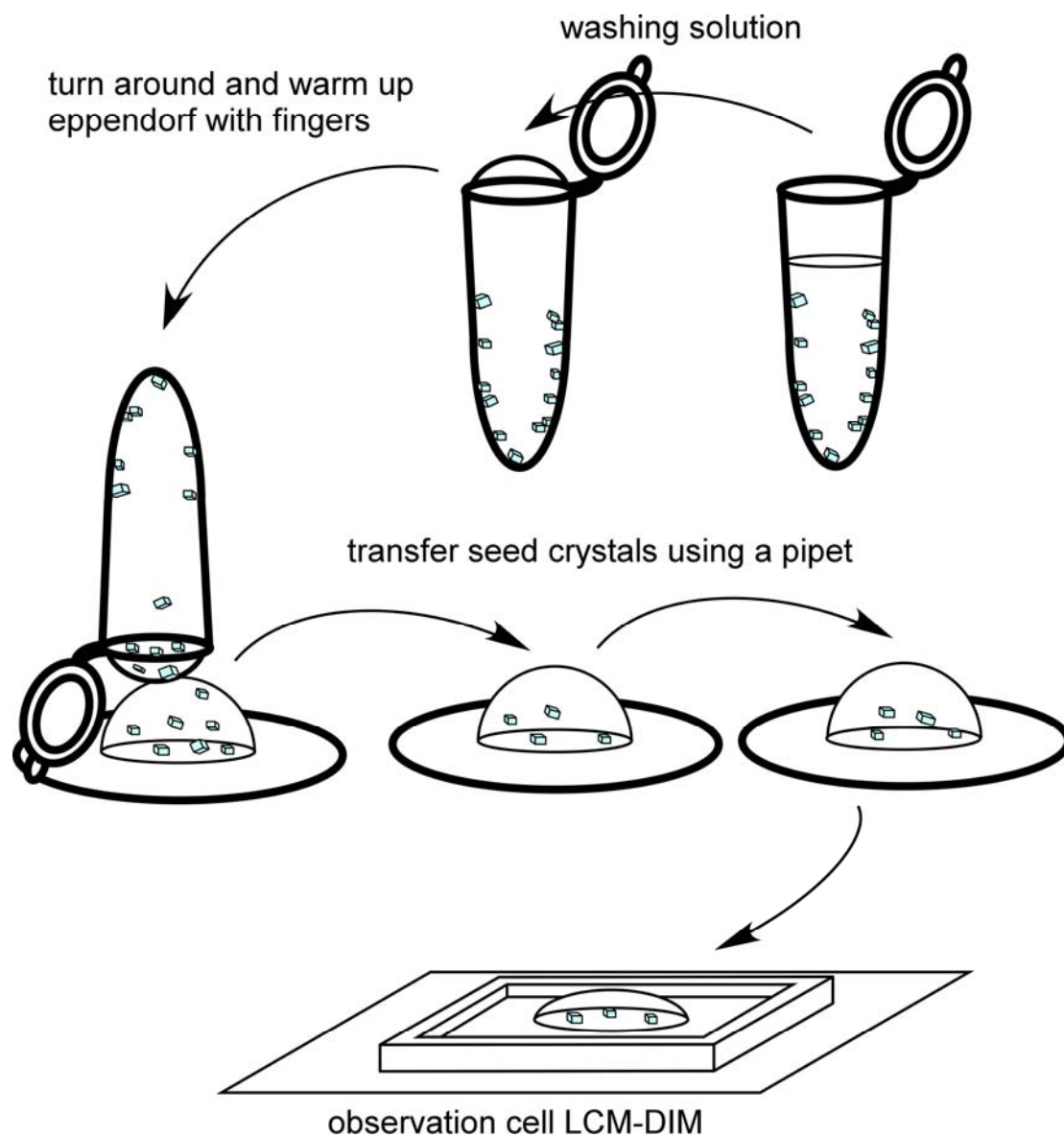


Fig. 1 Schematic representation of the transfer process of seed crystals from an eppendorf to an observation cell.

Protocol of a typical crystal growth experiment

In the case of LCM-DIM and interferometry experiments the observation cell with seed crystals was sealed and stored at 20°C. Once the seed crystals were firmly fixed to bottom glass plate the solution inside the observation cell was changed with a solution of desired characteristic and experiments could start. In case of experiments using purified lysozyme, after seed crystals are prepared in an observation cell using Seikagaku lysozyme, the solution inside was replaced with a supersaturated solution of purified lysozyme (99.99%: Maruwa food industries, Inc) and is incubated for 5-6 hours until the surface is covered with purified lysozyme. Just before the observation, the solution is replaced again with purified lysozyme solutions of given concentrations. More specific details of experimental procedures are mentioned when necessary in further sections of this work.

3.4. Temperature control

The solubility of lysozyme is temperature depended (see section III.1) and a temperature controlled stage is used to maintain and/or change temperature during/between experiments. Temperature is normally changed in jumps of 0.5°C – 2.0°C. After changing the temperature a certain time is waited before starting any new measurements to ensure that the solution inside the observation cell has reached stable conditions.

3.5. Image acquisition and analyses

Images are taken automatically by the Fluoview program of the Olympus confocal microscope. The image acquisition is typically time-lapsed in the order of 10–300 s, depending on the supersaturation and the growth velocity. Image J, a freeware program, is used for data analysis of the 1024x1024 pixel images.

IV. RESULTS AND DISCUSSION

1. Measuring growth kinetics using different observation techniques

Surface morphologies and growth kinetics of crystals growing from aqueous solution have been studied *in situ* applying different techniques such as AFM, interferometry or optical microscopy. In the case of surface profile measurements extensive comparative studies exist in the literature discussing strengths and weaknesses of each technique (Komatsu and Miyashita, 1984; Li *et al.*, 1998; Lindseth and Bardal, 1999; Conroy and Armstrong, 2005; Koyunca *et al.*, 2006). On the other hand experimental data of growth kinetics obtained from different observation techniques for a same model system have never been directly compared.

Until now many crystal growth studies have broadened the level of comprehension of the growth process of macromolecular crystals (e.g. Vekilov and Chernov, 2002), but for a more profound understanding of protein crystal growth kinetics, detailed quantitative data are necessary to stay advancing in the field. As will be shown in this manuscript an appropriated choice of observation method is vital. Therefore a comparative study is definitely useful, since no bad or good techniques exist per se, but each technique has its own limitations and inappropriate usage can lead to biased experimental data. For example in the case of AFM the effect of the scan of a cantilever, can potentially disturb solute concentration distributions in the vicinity of a crystal surface affecting the growth kinetics (Land *et al.*, 1996; Gliko *et al.*, 2005). But the effects, if any, of the cantilever movement on growth kinetics have not yet been studied in detail. Thus before starting an in depth study of crystal growth kinetics a comparative study of the available observations techniques using a model system was done.

The role of tapping mode Atomic Force Microscopy (TM AFM) and Phase Shifting Interferometry (PSI) as characterization techniques for crystal growth are compared with that of LCM-DIM. For doing so growth of model protein lysozyme was observed by these three techniques and several growth parameters such as step velocity, 2D nucleation rate and normal growth rate were determined. These parameters were measured in a broad supersaturation range for tetragonal crystals growing from a highly purified solution. A detailed description of the applied observation techniques is given in Chapter III.

1.1. Growth kinetics measured by atomic force microscopy, phase shifting interferometry and LCM-DIM

1.1.1. Step velocities

LCM-DIM (Sazaki *et al.*, 2004; 2005; Van Driessche *et al.*, 2007) and AFM (McPherson *et al.*, 2003 and references therein) can visualize 2D islands and spiral hillocks and step advancement over time can be directly measured. With interferometry, it was impossible, until recently (see section IV.2) to achieve a resolution, which enables the observation of individual 2D islands or monolayer steps on spiral hillocks. So far, most measurements of step velocities using interferometry have been performed on spiral hillocks (e.g. Kuznetsov *et al.*, 1995; Vekilov *et al.*, 1993; 1995; 1996). Step velocities were obtained indirectly by analyzing the slope of a hillock and the normal growth rate (Chernov, 1984):

$$R = pv, \tag{1.1}$$

where p is the slope of a hillock, R the normal growth rate and v the step velocity.

Highly purified lysozyme solution was used for measuring step velocities directly by TM AFM and LCM-DIM and indirectly by PSI on $\{110\}$ faces of tetragonal lysozyme crystals. The tangential rates of step advancement for different crystallographic directions were measured in the supersaturation range of $C-C_e = 0 - 45$ mg/ml. With AFM step advancement was measured in the $\langle 001 \rangle$ direction only, while with LCM-DIM and interferometry step advancement was also determined in the $\langle \bar{1}10 \rangle$ direction. For each supersaturation condition, at least two experiments with different seed crystals were carried out. At a same supersaturation, tangential rates were typically measured for a large number of two-dimensional islands. For a detailed discussion on step velocities of $\{110\}$ and $\{101\}$ faces of tetragonal lysozyme crystals see section IV.3.4.

Direct observation of step velocities by AFM and LCM-DIM

In figure 1.1 some typical AFM images of growing $\{110\}$ faces of lysozyme crystals are shown. In the lower part of Figure 1.1a a pseudo image, recorded with the Y scan axis disabled (e.g. Kitamura *et al.*, 1993), is showing 2D nucleation growth on a $\{110\}$ face at relatively high supersaturation ($C-C_e = 54.6$ mg/ml). When the scan in the Y-direction is disabled the growth along one line is followed over time, i.e. Y-axis represents time. Above the black arrow in image (a) the scan in the Y direction was enabled again and a 2D scan shows a high density of 2D islands, indicating the relatively high supersaturation at which the crystal is growing. Figure 1.1b shows a 1D scan of steps on a $\{110\}$ face growing at low supersaturation ($C-C_e = 6.9$ mg/ml). Step trains are moving at constant velocity and the interstep distance stays constant over time. Since the scan speed of each frame is known step velocity can be directly determined from these 1D pseudo images. If step advancements are measured this way one has to ensure that the scanning direction is perpendicular to the step movement. If this is not the case step velocities will be overestimated. Even so, real velocities can still be obtained if the angle between the scanning

direction and the direction of the step advancement is known (Astier *et al.*, 2001).

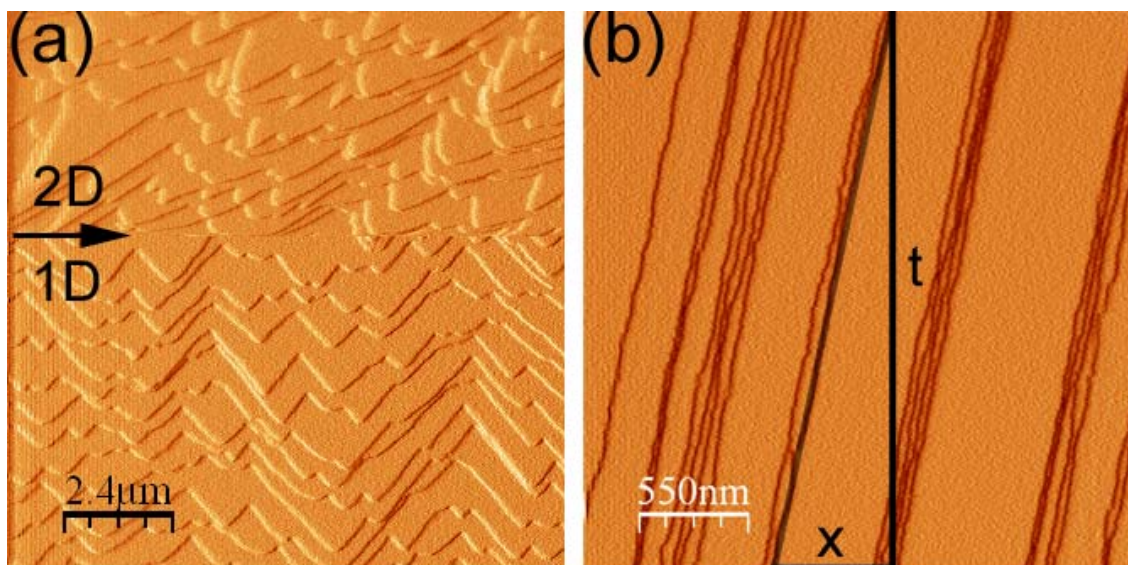


Figure 1.1 AFM images of monolayer steps on $\{110\}$ faces of tetragonal lysozyme crystals. (a) Nucleation and growth of 2D islands, the black arrow indicates transition from 1D scan to 2D scan (b) 1D scan of step trains advancing at constant velocity. In a 1D scan Y-axis represents time.

Using tapping mode AFM, step velocities were measured in the $\langle 001 \rangle$ direction on $\{110\}$ faces of tetragonal lysozyme crystals at different supersaturations. Step velocities were first determined during long time runs ($>1\text{h}$), without changing the solution during the experiment. Results of these measurements are shown in Figure 1.2a. The colored lines with arrows indicate the increment of experiment duration. During these observations step velocities increased none linearly over time in function of supersaturation (blue and red dots Figure 1.2a). Also step advancement was faster over time even when supersaturation was kept constant (green dots Figure 1.2a). From these results it becomes clear that step velocities increase considerably over time. To qualitatively understand these observations an additional experiment was designed. Step advancement was measured at constant temperature for over 3 hours without changing the solution inside of the AFM fluid cell (Fig. 1.2b). This graphic shows clearly that steps move at a constant velocity (within experimental error) for approximately half an hour, after which a linear increase in time of the step

velocity is found. This is most likely due to evaporation from the liquid cell, even though it was properly sealed. Once evaporation starts, supersaturation will increase rapidly. Based on these observations the graphic shown in Figure 1.2a is replotted eliminating all data points which were obtained after more than half hour of continued measurement (Figure 1.2c). In this graphic step velocities obtained by Nakada (2005) for the $\langle 001 \rangle$ direction using AFM under identical experimental conditions are also shown (measurements were performed with a NanoScope II (“contact” type, Digital Instruments Inc.) equipped with a glass fluid cell). In these measurements supersaturation was varied by change the lysozyme concentration C . During AFM measurements temperature was maintained constant at $24 \pm 1^\circ\text{C}$ inside of the fluid cell. The large error bars shown for these data are the consequence of poor temperature control during the experiments (1.0°C). Even so, both data are in good agreement. Nakada (2005) used contact mode AFM, while for this work tapping mode AFM was applied. Data obtained by tapping mode appear more scattered then in the case of contact mode measurements. Also shown in Figure 1.2c are step velocities measured by LCM-DIM for identical experimental conditions. Step velocities measured by AFM were significantly faster than those measured by LCM-DIM.

Step height on the $\{110\}$ face was measured with AFM, and a typical averaged value of 6.0 nm was found (Figure 1.2d) which is relatively close to the lattice plane distance $d_{(110)}$, which amounts to 5.55 nm ($a=78.54 \text{ \AA}$, $c=37.77 \text{ \AA}$). These measurements confirm previously obtained data by several groups using also AFM (Durbin and Carlson, 1992; Konnert *et al.*, 1994; Li *et al.*, 1999).

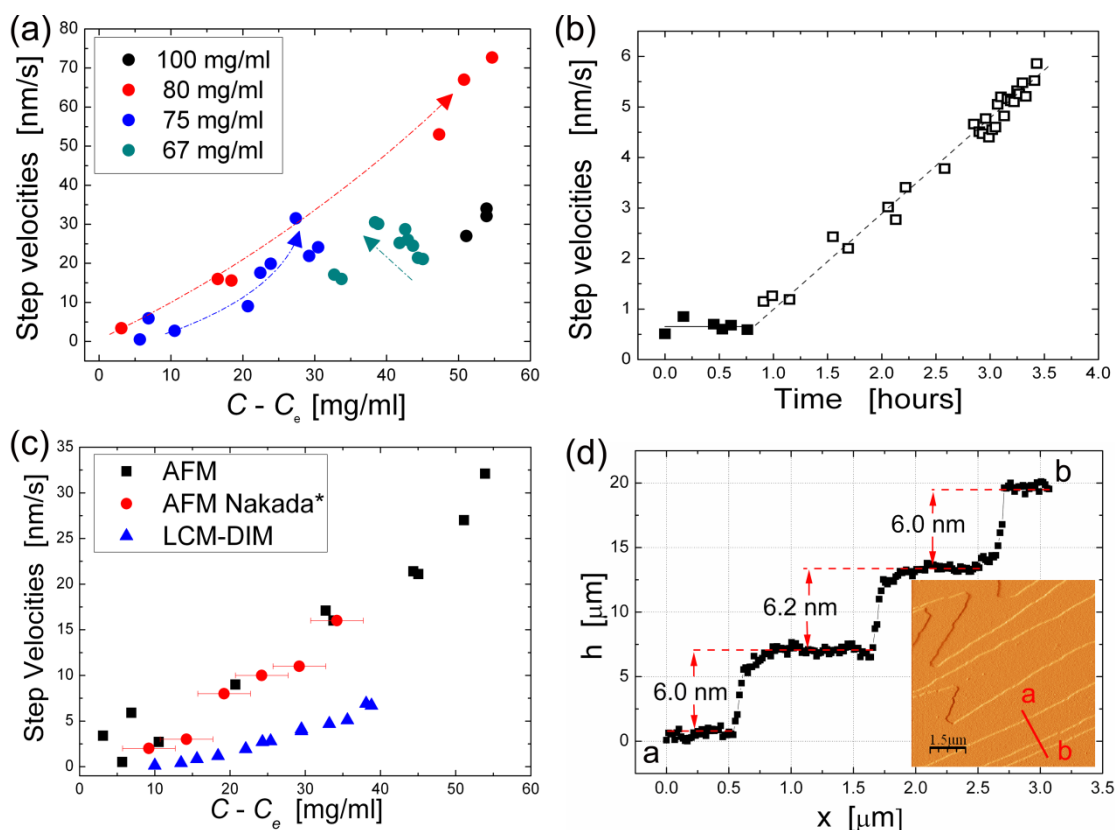


Figure 1.2 Step velocities measured in the $\langle 001 \rangle$ direction on $\{110\}$ faces of tetragonal lysozyme crystals growing from purified lysozyme solution. (a) Step velocities measured by AFM in long time runs ($>1\text{h}$). (b) Evolution of step advancement in function of experiment duration. (c) Comparison of step velocities measured by AFM and LCM-DIM for identical experimental conditions. (d) Step height of monolayers measured by AFM. *Data obtained by Nakada (2005). All data are represented using solubility data obtained by Rosenberger and coworkers (1993).

Indirect observation by MI

In case of interferometry observations, normal growth rates and slopes need to be determined first, from which step velocities can be calculated using Equation 1.1. Normal growth rate measurements are described later on in this section. In Figure 1.3 step velocities in the $\langle 001 \rangle$ directions obtained by AFM, PSI and LCM-DIM under identical experimental conditions are shown. If PSI values are compared with those from LCM-DIM experiments, a reasonable correspondence is found. Except for data points obtained above supersaturation levels of $C - C_e = 30$ mg/ml (open blue triangles), or more precisely, $\ln(C/C_e) > 1.2$, because when dealing with nucleation thermodynamic supersaturation should be used (Vekilov

and Chernov, 2002). One data point is found at $C - C_e = 42$ mg/ml (half filled blue triangle) which corresponds well with the curve obtained by LCM-DIM. For the PSI measurements a larger dispersions between data points is found then in the case of AFM and LCM-DIM.

In ideal circumstances step height of individual steps can be measured with advanced interferometry techniques (for detailed discussion see section IV.2). In case of monolayer 2D islands steps on the $\{110\}$ face a value of 5.6 nm was obtained, this is slightly lower than the value obtained by AFM.

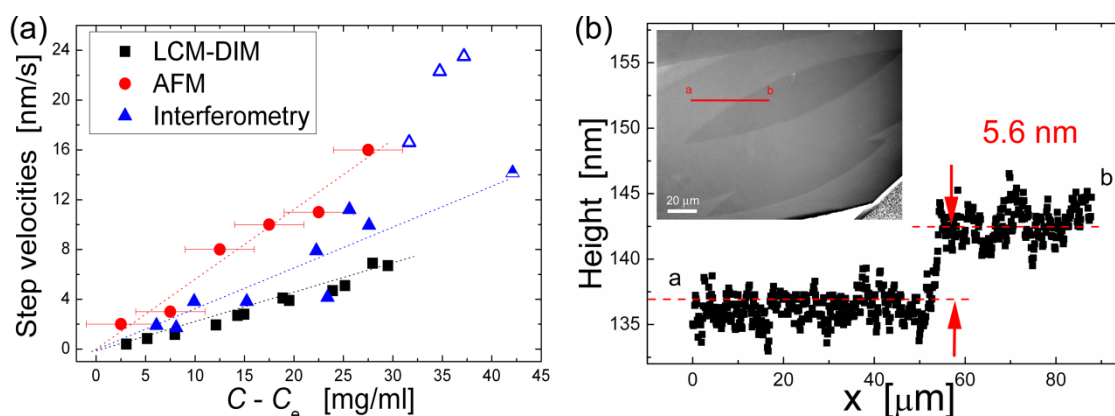


Figure 1.3 (a) Step velocities measured by PSI, AFM and LCM-DIM in the $\langle 001 \rangle$ direction on $\{110\}$ faces of tetragonal lysozyme crystals. (b) Step height of a 2D island on a $\{110\}$ face measured by phase shifting interferometry. All data are represented using solubility data of Sazaki and coworkers (1996).

1.1.2. 2D Nucleation rates

Two dimensional nucleation rates were directly determined using AFM and LCM-DIM by counting the number of newly appeared 2D islands between consecutive images, results are shown in Figure 1.4. 2D nucleation rates measured by AFM are considerably higher than those measured with LCM-DIM. Figure 1.4b,c shows typical AFM and LCM-DIM images of $\{110\}$ faces growing by the 2D nucleation mechanisms. The AFM image was

scanned in 256 sec and covers an area of $10 \times 10 \mu\text{m}$. With LCM-DIM 9.6 sec were necessary to scan an area of $800 \times 800 \mu\text{m}$. The phenomenon of 2D nucleation observed on $\{110\}$ and $\{101\}$ faces of tetragonal lysozyme with LCM-DIM is discussed at length in section IV.3.5.

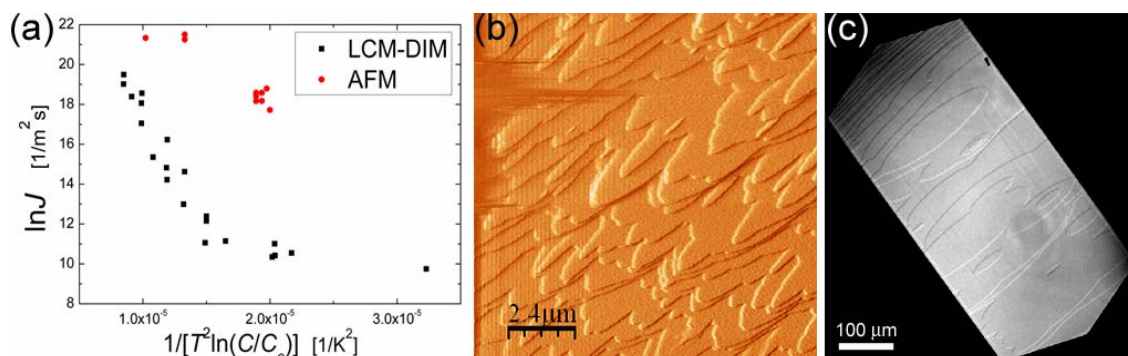


Figure 1.4 (a) Two-dimensional nucleation rates measured with AFM and LCM-DIM. Typical images of AFM (b) and LCM-DIM (c) showing 2D islands on a $\{110\}$ face of tetragonal lysozyme.

2D nucleation rate by Interferometry

By analyzing the supersaturation dependency of normal growth rates using a 2D nucleation growth model of the birth-and-spread type, one can indirectly determine 2D nucleation rates and ledge free energies of crystals (e.g. Malkin *et al.*, 1989, Kurihara *et al.*, 1996). Unfortunately most of the normal growth data obtained with PSI were from spiral growth and thus no 2D nucleation data could be derived.

1.1.3. Normal growth rates

Measurements by MI

Michelson interferometry is a widely used method for measuring surface morphologies and normal growth rates of crystals. With this method long continuous growth rate measurements of entire faces are possible. Two interferometry techniques, PSMI and confocal phase shifting interferometry (CPSI)*, were used to measure growth rates of $\{110\}$ faces of tetragonal lysozyme for identical experimental conditions as those used for AFM and

*See appendix for a brief description of this observation

LCM-DIM observations. Almost all measurements were done on spiral hillocks. Normal growth rate data obtained at different supersaturation are shown in Figure 1.5.

A typical phase shift interferogram of a spiral hillock is shown in Figure 1.4b, from such a interferogram slopes in the $\langle\bar{1}10\rangle$ and $\langle 001\rangle$ directions can be directly obtained using

$$h_{x,y} = \frac{\lambda_{532}}{2 \cdot n} \cdot \frac{I_{x,y}}{256} \quad (1.2)$$

where $\lambda = 532$ nm is the wavelength, I the intensity of one pixel and $n = 1.4$ the refractive index of a tetragonal lysozyme crystal $n=1.4$ (section III.2). From a series of interferograms taken over time (one every 60 s) a time-space plot along a certain line can be constructed. These time-space plots are obtained by extracting the pixels of a specific line (red line in Figure 1.5a) along which the normal growth rate will be observed. Intensity values of pixels from this line in the first image are transferred into the first row of a new image; the pixels from the same line in the second image are put into the second row and so on, until a complete time-space plot is created (Figure 1.5b). From this type of image normal growth rate can be directly determined. Figure 1.5b shows clearly that under constant conditions growth rate remains constant during the length of an experiment (24h). Results of normal growth rate measurements are shown in Figure 1.5c. From the obtained normal growth rates, step velocities were calculated in the $\langle\bar{1}10\rangle$ and $\langle 001\rangle$ directions using Equation 1.1 (Figure 1.5d). If these values are compared with those from LCM-DIM experiments, a reasonable correspondence is found. Except for data points obtained above supersaturation levels of $C-C_e = 30$ mg/ml ($\ln(C/C_e) > 1.2$, open blue diamonds in Figure 1.5d). A more detailed discussion on normal growth rates of tetragonal lysozyme crystal is given in section IV.3.6.

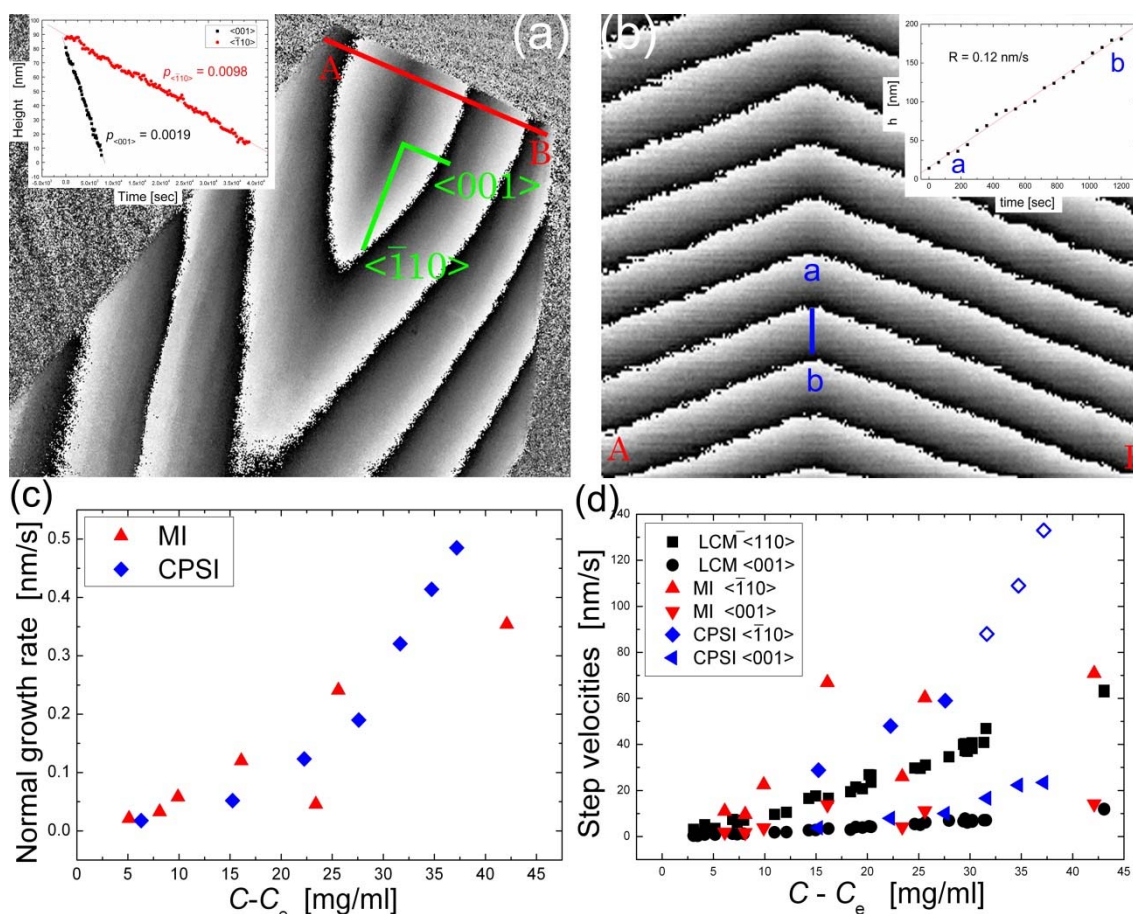


Figure 1.5 PSI Measurements of normal growth rates and slopes of $\{110\}$ faces of tetragonal lysozyme crystals. (a) Typical phase shift interferogram of a spiral hillock on a $\{110\}$ face. In the inset the slopes of this hillock in the $\langle\bar{1}10\rangle$ and $\langle 001\rangle$ directions are shown. Along the line a-b a space-time plot is constructed for the length of the experiment (24h) (b). From this space-time plot the normal growth rate is directly measured as shown in inset graphic. (c) Normal growth rates versus supersaturation. (d) Step velocities in the $\langle\bar{1}10\rangle$ and $\langle 001\rangle$ direction calculated from normal growth rates and slopes compared to step velocities measured directly by LCM-DIM.

Measuring normal growth rates with AFM and LCM-DIM

With AFM and LCM-DIM normal growth rates can be directly measured for low supersaturations by simply counting the newly formed layers over time. Of course for AFM the observation area is small and only a very local value will be obtained. On the other hand AFM has the advantage of precise measurement of the surface topography. With LCM-DIM the whole crystal surface can be observed, but previous data about the step

height are necessary for direct growth rate determination. Unfortunately these measurements are little relevant because the supersaturation range for which the normal growth rate can be directly determined the face advancement is so slow that growth rates are not representative for a typical crystallization experiment (i.e. at such low growth rates a crystal would take several months, or more, to grow to a reasonable size). LCM-DIM can be used to measure growth rates by recording the advancement of a certain face in time (see arrows in Figure 1.3b). This is similar to growth rates measurements done by optical microscopy. But this method is slow, allowing few measurements to be carried out, and symmetric faces may contribute differently to the enlargement, which leads to inaccuracy. Additionally surface morphologies cannot be observed and thus the growth mechanisms cannot be directly observed.

For middle to higher supersaturation levels, and thus dominant 2D nucleation growth, normal growth rates can be estimated by applying equations based on 2D nucleation models. This will be discussed in section 3.6 of this chapter.

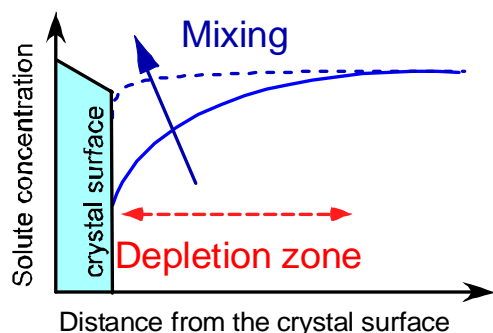
1.2. Discussion

Atomic force microscopy

Of the three techniques presented here, only AFM is invasive and therefore this feature will be discussed in a detailed way. In the literature a lot has been written about the fact that the invasiveness of AFM has no major effect on the observed growth processes (McPherson *et al.*, 2000; 2001; 2003; and reference therein), which in many cases is probably true, but nevertheless it should not be accepted as a general rule. A brief overview of artefacts produced by AFM are given and supported with experimental data.

1. Cantilever movement

Step velocities measured by AFM were significantly faster than those measured by LCM-DIM. In case of tapping mode AFM, the cantilever is oscillating at a high frequency inside of the solution, close to the crystal



surface. Hence, the most probable cause of the difference in measured step velocities is due to the cantilever movement. The scan of a cantilever significantly stirs the diffusion boundary layer or the concentration-depleted zone at high supersaturation, developed in

the vicinity of a growing crystal. Solute concentration at the surface will increase, resulting in faster step velocities measured by AFM. In case of contact mode, the cantilever stirs the solution because the tip is scanned across the growing crystal surface at relatively high velocity. Since data obtained from TM AFM and CM AFM correspond well, it seems both have a comparable effect on mixing of the boundary layer. In case of TM AFM measurements some dispersion of the data is found, this could be the result of the rapidly oscillating cantilever producing significant fluctuations of solute concentration at the step front.

Effects of cantilever movement were also observed by Land and coworkers (Land *et al.*, 1996) who reported that the growth rates of canavalin crystals were enhanced by the scan of a cantilever, and Gliko and coworkers (2005) argued that the variations in step velocities of lumazine synthase crystals would be the result of the cantilever movement.

Of course the measured growth rates with AFM are not incorrect but one has to be aware that these measurements are taken under specific transport conditions (similar to forced flow experiments). For this peculiar

type of solute transport no models are available. Thus kinetic data obtained by AFM cannot be considered as equal to data obtained in stagnant solution, where only natural convection is present. Some researchers argue that data obtained by AFM lead to a more correct estimation of the kinetic coefficient β because the diffusion factor is almost completely eliminated.

2. Temperature control

The first temperature controlled AFM observation of protein crystal growth was done by Astier and co-workers in 2001. They showed that without temperature control the temperature between tip and crystal surface raised from 17.72°C to 27.5°C in a time period of 3h, this was also observed by Gavira (2000). The increase of temperature is caused by the piezoelectric translator. If the liquid cell is directly on top of the piezoelectric translator temperature increase will be more drastic. Hence, depending on the design of the AFM equipment more or less temperature fluctuations inside the observation cell can be expected. Hence, all AFM observations before 2001 were conducted without precise temperature control. In most cases protein solubility is temperature depended. If this is the case quantitative data obtained of the growth processes without precise temperature control are unreliable, at least for precise growth kinetics studies.

In the observations done for this work evaporation was a serious problem, even though the fluid cell was properly sealed (i.e. when solution was introduced through the inlet in the liquid cell a similar volume of solution left the liquid cell through the outlet). Observations were done at relatively high temperature ($>27^{\circ}\text{C}$) because the temperature control had a bound dynamic range allowing only set point temperatures above the equilibrium temperature of the operating AFM. Such “high” temperatures considerably increase the evaporation rate. Also the reduced volume of the liquid cell makes the experimental setup extra sensitive to evaporation. Even so, in most cases evaporation from an AFM fluid cell is not a problem.

Nevertheless special attention has to be paid to make sure that evaporation does not bias the obtained experimental data. Some researchers use AFM in an enclosed environment with controlled humidity (close to 100%) to prevent evaporation. This is a very effective method but has the drawback that it complicates considerably the experimental setup.

3. Non-zero acquisition time

With AFM, image acquisition is in a serial way, in contrast to optical microscopy, where all parts of the image are acquired parallel in a fraction of a second. Typical AFM acquisition times are several minutes for large scan areas ($> 10 \mu\text{m}$) and about one minute for smaller regions. In case of *in situ* crystal growth observation this puts serious limitations in recording fast propagating steps. Hence, AFM remains limited to low step speeds and low supersaturation. For this reason step velocities on $\{110\}$ faces of tetragonal lysozyme could only be measured in the slow $\langle 001 \rangle$ direction, because growth in the fast $\langle \bar{1}10 \rangle$ direction was already too fast to be followed, even at relatively low supersaturation levels.

4. Tip-sample interaction

In contact mode AFM the interaction between cantilever and crystal takes place in the small tip-sample contact area only. Despite the low applied forces in AFM (typically nN), pressures at the tip can become so high that soft samples can be damaged. For tapping mode the physical contact with the sample is reduced to a minimum, but even so interactions are still present.

In Figure 1.6 the effect of driving the cantilever tip into the growing surface are shown. It is quite clear that interactions of the tip with the crystal surface produces enhanced 2D nucleation. Mainly multilayered 2D islands are formed. Probably lysozyme macroclusters are created after sharp contact of the tip with the crystal surface causing material to be ejected from the surface. It seems that these lysozyme clusters instantaneously fall

down on the surface serving as nucleation sites for 2D multilayer islands. Large plateau on top of these multilayer islands as growth continues outward. Figure 1.6 also shows that these nuclei grow epitaxially on the crystal without, apparently, introducing defects because step trains of the multilayer islands merge flawlessly with those of the growing crystal. Tip-induced 3D macroclusters landing and consequent formation of multilayer islands was also observed for growing canavalin crystals (Land and DeYoreo, 2000) and thaumatin crystals (Kuznetsov et al., 1999b).

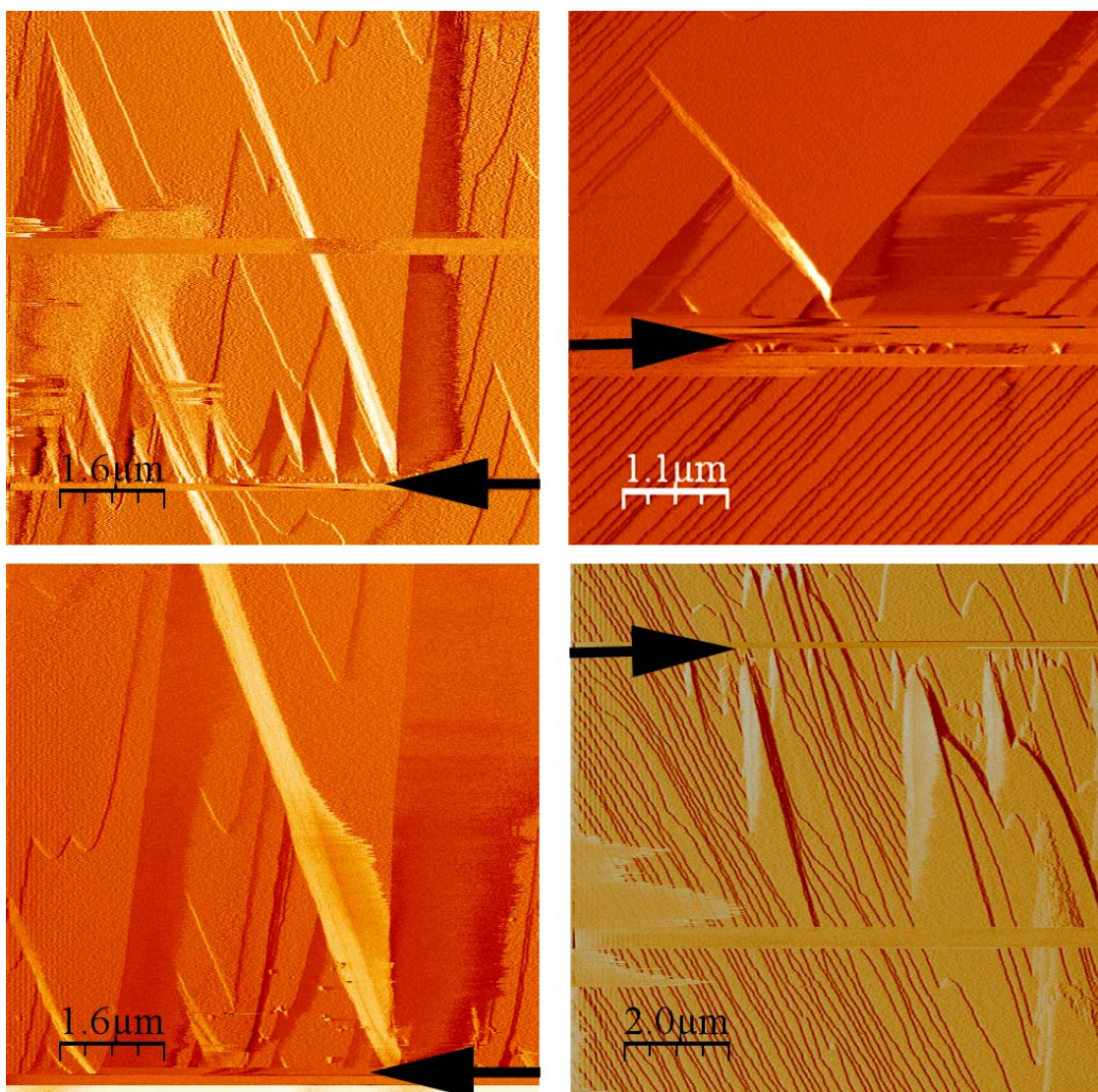


Figure 1.6 Effect of AFM tip interactions with the crystal surface. The black arrows indicate in each AFM images where the cantilever tip was brought into contact with the crystal surface, as a consequence severe 2D multilayer nucleation was provoked. The multilayer islands spread laterally across the surface.

5. Scan size

One of the principle drawbacks of AFM is the relatively small area that can be scanned at any given time. The maximum scan area for most AFMs is approximately $120 \mu\text{m}^2$. This limitation is principally due to the operational set up of the AFM and the size of the single cantilever used to produce an AFM image. Such a limited scan size makes it difficult to determine how representative the measured image may be of the surface at large. Most likely the small observation area is the main reason of the large discrepancy between the obtained 2D nucleation rates by AFM and LCM-DIM, besides possible influence of solution stirring and evaporation. Also the stirring of solution can increase the amount of foreign particles arriving at the surface. The presence of particles on the surface can alter the 2D nucleation rate (Liu *et al.*, 1997)

Another example of the limitation of the scan size of AFM is shown in Figure 1.7. The growth of $\{001\}$ faces of hexagonal lumazine synthase crystals was observed using AFM by Vekilov and coworkers (2005a, 2005b). They did not find any spiral dislocations in the entire supersaturation range. Growing $\{001\}$ faces of hexagonal lumazine crystals were also observed by LCM-DIM under identical experimental conditions. Mainly spiral growth was found, as is demonstrated very nicely in Figure 1.7a. At higher supersaturation levels 2D nucleation was observed (Figure 1.7b,c).

Additionally, it is difficult to characterize surfaces where the changes in height are dramatic ($\Delta h > 5 \mu\text{m}$) in which contact may be lost between the tips and sample, or the tip may become damaged.

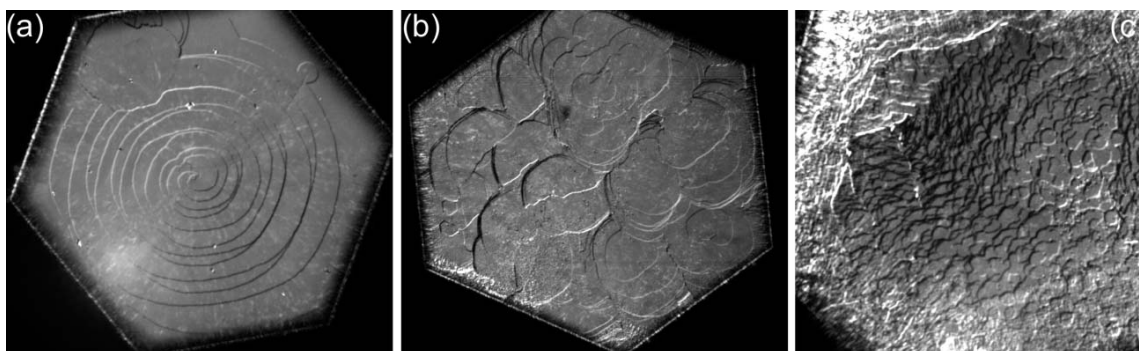


Figure 1.7 Growth mechanism of $\{001\}$ faces of hexagonal lumazine synthase crystals. (a) Double spiral dislocation dominating the entire crystal surface. (b) At moderated supersaturation 2D islands are covering the surface. (c) At high supersaturation abundant 2D nucleation island are formed.

6. Crystal drift

Drift of crystals during AFM measurements can be a serious inconvenience. For this work a method was designed to prevent drift without having to fix large crystals with foreign materials (e.g. carbon fibers) or nucleating a lot of crystals directly on the substrate of the AFM observation cell (McPherson *et al.*, 2003). With the approach used for this work only one crystal is fixed to the bottom side of the fluid cell by letting it grow overnight in a slightly supersaturation solution (for details see section III.2.3.2). This method proved very reliable and during AFM observations no movement of crystals was observed. An added advantage of this method is that crystals can be orientated so that the desired face can be observed.

In short, AFM has strong limitations for precisely measuring certain growth parameters of growing protein crystals, such as step velocities, 2D nucleation rates and normal growth rates, especially at middle to high supersaturation levels. The importance of these limitations increases with supersaturation.

Interferometry

Interferometry is the most appropriated technique for measuring normal growth rates when compared with AFM or LCM-DIM. A strong

point of advanced PSI is the possibility to observe time-dependent growth processes with a high time resolution (typically 0.1 - 0.05 Hz) over long experiment times (hours or even days) under constant, undisturbed conditions (sealed growth cells). The wide dynamic range in vertical direction (within one image, a height difference of $\approx 1.5 \mu\text{m}$ can be measured) with nanometer scale resolution allows for a comprehensive analysis of surface morphology.

Thus with this method long continuous measurement of growth rates of entire faces are possible, but only averaged data are derived. From the measured normal growth rates and surface morphologies other parameters can be calculated such as 2D nucleation rates or step velocities. The indirectly measured step velocities with PSI were comparable to those directly obtained by LCM-DIM. But from a certain supersaturation, $\ln(C/C_e) > 1.2$, a large discrepancy is found. This is the result of significant 2D nucleation on the terraces of spiral hillocks. Because of this additional 2D nucleation the slope of the hillock is reduced and the calculated step velocities are anomalously high. One data point is found at $C - C_e = 42 \text{ mg/ml}$ which shows a good correspondence with the curve obtained by LCM-DIM. This is easily explained when supersaturation is expressed in the form of $\ln(C/C_e) = 1.25$. Thus, in this experiment supersaturation was still not high enough to produce significant 2D nucleation on the growth hillock to change the slope. As a consequence the obtained value for tangential step advancement is reasonable. These biased data are the result of the limited resolving power of interferometry for direct observations of detailed surface processes even though the theoretical vertical resolution is around 2 nm the badly reflecting protein surface lowers considerably this resolution. It has to be mentioned that the recently developed advanced phase shifting interferometers used in this work are able to observe single steps at low supersaturation (see section IV.2). For the PSI measurements a larger dispersion between data points is found than in the case of AFM and LCM-DIM. This is most likely the result of slope variations. Slope variations can

also produce additional problems such as artificial step fluctuations; this is discussed in section IV.3.4. Slope variations are a major problem when analyzing step velocities from normal growth data obtained from interferometry.

Not enough interferometry data were obtained from 2D nucleation mediated growth to do a meaningful analysis of nucleation rates but Kurihara and coworkers (1999) measured normal growth rates of tetragonal lysozyme crystals and obtained ledge free energies which are comparable to values obtained from direct 2D nucleation rate measurements by LCM-DIM under similar experimental conditions, this is discussed in detail in section IV.3.5. However, since 2D nucleation rates are determined indirectly from averaged normal growth rates, only averaged information is obtained. Also with interferometry obtaining data at low supersaturation is difficult because the normal growth rates are almost zero in the case of 2D nucleation mediated growth. For example 2D heterogeneous nucleation at low supersaturation has never been observed with interferometry for protein crystal growth, while AFM studies were able to detect heterogeneous nucleation for thaumatin (Malkin *et al.*, 1996; 1999) and catalase (Malkin *et al.*, 1999) crystal growth. With LCM-DIM heterogeneous nucleation has been studied in detail for tetragonal lysozyme crystals (Van Driessche *et al.*, 2007).

A serious disadvantage of Interferometry is the high level of skill needed for correct adjustment of the equipment to obtain interference fringes which makes this technique very labour intensive for performing routine experiments. In case of CPSI adjustment of the equipment is straight forward and interference fringes are more readily obtained. Also the high sensitivity of the Michelson setup for vibrations (simply air drag can be noticed in the images) and temperature fluctuations is a setback. This high sensitivity is the result of the two beam paths which increase the susceptibility of the interferometry for noise because each beam path will

respond differently to external influences. The difference in optical quality of the components of both beams paths can also introduce noise in the interferometry image. Part of these problems is solved by using white light because of the shorter coherence length compared to laser. This short coherence length will filter out part of the unwanted interferences.

It can be concluded that advanced PSI closes the gap between invasive AFM measurements (slow, but providing molecular resolution in quantitative manner) and optical microscopy (fast, but only of qualitative nature) for measuring surface morphology evolution over time.

Laser confocal differential interference contrast microscopy

LCM-DIM is a non-invasive technique with fast time resolution, large observation field, excellent vertical resolution and good lateral resolution (the lateral resolution is limited by the laws of optics and cannot surpass approximately 250 nm). With LCM-DIM surface morphology can be visualized with very high contrast and time-dependent processes of stepped faces can be observed over long time periods under constant conditions (temperature controlled sealed observation cell).

As was shown above, step velocities and 2D nucleation rates can be accurately measured on entire {110} faces. Clear disadvantage of LCM-DIM is that the surface morphology cannot be determined quantitatively, i.e. no height information is available. On the other hand LCM-DIM is a very stable technique, e.g., thermal fluctuations and mechanical vibrations have less impact on the optical setup, mainly because the incoming light beam and the reflected beam travel through the same optical path. Hence, both beams experience the same distortion produced by for example vibrations or imperfection in the optical materials. As a result this type of artifacts will have little effect on the image quality. Also the confocal pinhole will block out of focus light reducing considerably unwanted interferences.

Additionally the use of a superluminescent diode as light source improves image quality because of the short coherence length ($<10\ \mu\text{m}$).

1.3. Conclusions

All three techniques have their pro's and contra's and before starting a crystal growth study one has to carefully determine which growth parameters want to be studied and choose the most appropriate technique, or combination of techniques, for doing so. On the other hand the description of a stepped surface can be given on different levels, each with its own typical length scale (van der Eerden, 1993). Which description is most relevant depends on the application that one has in mind. The descriptions can be made on three levels: at an (1) atomic level, where individual atoms play their role, at (2) mesoscopic level, where steps are seen as smoothly curved lines, but each step is treated individually, and at (3) macroscopic level where steps are not discernible any more, and their density becomes a smooth function of surface position. Ideally, a complete description of the growth process will involve a combination of all three levels. For a much more detailed discussion on this subject the work of van der Eerden (1993) is strongly recommended.

Here a tentative classification is given, linking each technique with a specific level of observation. The parameters determined most accurately by each method are also pointed out. During this work it was also observed that each technique has its own ideal supersaturation range for operation, this is discussed.

Atomic level: without doubt AFM is the most powerful and useful technique in this area. This tool is capable of providing excellent spatial resolution on a molecular level which allows atomic level quantitative analyses of the morphological characteristics of protein crystal surfaces. Thus, provided a good model system, a skilled AFM operator is capable of

determining thermodynamic and kinetic parameters of crystal growth at a molecular level. Some examples are:

- Kink densities and dynamics of kink sites (e.g. Chernov *et al.*, 1999; Yau *et al.*, 2000a; 2000b; Chen and Vekilov, 2002, Georgiou and Vekilov, 2006).
- Impurity incorporation and step pinning (e.g. McPherson *et al.*, 1996; Nakada *et al.*, 1999; Matsuzuki *et al.*, 2002,)
- Molecular packing determination (e.g. Li *et al.*, 1999b; Kuznetsov *et al.*, 1999a)
- Generation of defects (e.g. Malkin *et al.*, 1996b; Malkin and McPherson, 2002; McPherson *et al.*, 2001; Yau *et al.*, 2000a; Yau *et al.*, 2001; Hondoh and Nakada, 2005)
- Observation of aggregates on crystal surfaces (e.g. Kuznetsov *et al.*, 1999a; Land *et al.*, 1997; Malkin *et al.*, 1999a; Yau *et al.*, 2000a; 2000b; Yip *et al.*, 2000)
- Molecule attachment to growth steps (e.g. Kuznetsov *et al.*, 1999a; Li *et al.*, 1999a; Yau *et al.*, 2000, Chen and Vekilov, 2002)
- Vacancies, empty unit cells and partially filled unit cells (e.g. Malkin *et al.*, 1996a; Yau *et al.*, 2000b, Waizumi *et al.*, 2003)
- Visualize and measure critical 2D nuclei (e.g. Malkin *et al.*, 1993, 1995a,b)
- Nucleus structure and nucleation pathways (Yau and Vekilov, 2000)
- Incorporation of denatured macromolecules, aggregates, microcrystals, helical fibers, etc... (e.g. McPherson *et al.*, 1995; Malkin *et al.*, 1996a,b,c; McPherson *et al.*, 1996; Kuznetsov *et al.*, 1998, 2001b; Hondoh and Nakada, 2005)
- Burgers vector of a spiral dislocation (e.g. Land *et al.*, 1997)

On the other hand it was shown before that AFM is not the most appropriated choice for precise quantitative determination of mesoscopic and macroscopic growth parameters.

Neither LCM-DIM nor interferometry has any useful application on this level of observation, except for the single molecule visualization technique that can be attached to the LCM-DIM.

Mesoscopic level: In principle, all three techniques can be applied in this area, but it was shown before that both AFM and Interferometry present a series of difficulties. Laser confocal microscopy combined with differential interference contrast microscopy (LCM-DIM) is very effective to obtain non invasive high contrast images of surface micromorphologies of growing protein crystals visualizing an entire crystal surface. Step dynamics and the nucleation process can be observed undisturbed over long time periods. This technique also has a fast time resolution and good lateral and vertical resolution. Hence, this advanced optical microscopy technique is very suitable for mesoscopic growth kinetic measurements. This technique is also very suitable to observe *in situ* the effect of impurities on step dynamics (see section IV.3.4) and 2D nucleation (section IV.3.5). Other examples are observation of growth kinetics in gelled solution (section V) or under high pressure (Suzuki et al., 2005). Also advanced optical techniques such as single molecule visualization and interferometry can be easily attached to the experimental setup. This technique closes the gap between the atomic observations of AFM and macroscopic observations of interferometry.

A more economic alternative for non-invasive and direct observation of step dynamics is available in the form of transmission type phase-contrast microscopy. *In-situ* observations of monomolecular steps were made on inorganic crystals (Tsukamoto, 1993) and protein crystals (Tsukamoto *et al.*, 2003; Yau, 2003; Dold *et al.*, 2006) with this technique. Contrast is not as high as in the case of LCM-DIM, but good image quality is certainly obtainable. The major disadvantage of this method is the relatively large size needed for crystals (>300 μm), because internal reflection of the

sidewalls of too small crystals deteriorates the image quality considerably (Dold, 2005).

Macroscopic level: Interferometry is the most appropriated technique for this type of studies. Neither AFM nor LCM-DIM is a good choice for measuring macroscopic growth kinetics. Even so, from the obtained data some macroscopic parameters can still be determined by applying growth models, but these techniques have severe limitations for this type of observations as was discussed before. The non-invasive character of PSI makes it possible to follow growth processes over long experimental times and the use of sealed growth cells ensures an undisturbed crystallization. The short exposure times needed for image acquisition (approx. 200 ms for each frame) enable the investigation of fast processes even under high supersaturation conditions. Together with the probe-less character of PSI, this is a clear advantage of MI, compared to AFM. Thus this technique is ideal to quantitatively characterize the morphology of the growth interface and its evolution over time providing detailed insight into the interface dynamics and associated step kinetics. The sources which generate growth steps can be determined as well as the relative importance of transport processes versus surface kinetics. Also the influence of impurity incorporation on macroscopic growth processes can be studied (Kuznetsov *et al.*, 1995). It's ability to simultaneously gather morphological information with high resolution at several, widely-spaced positions on the crystal surface, allows studying the growth mechanisms by which a facet retains its morphological stability (Vekilov *et al.*, 1995).

The most recent development of phase shift interferometry allows for the measurement of heights of elementary growth steps on protein crystals (see section IV.2). This nanometer scale resolution allows, for example, the simultaneous observation over time of the movement of large macrosteps together with un-bunched growth steps (Dold *et al.*, 2007).

Supersaturation range: Each of these three techniques has an optimum supersaturation range of operation. In the case of AFM observation are most reliable and meaningful at low supersaturation levels where, for example, kinetics at step edges can be observed *in situ*. For LCM-DIM excellent observations can be carried out in the low to middle supersaturation range. While at very high supersaturation levels the lateral resolution is not high enough to distinguish individual steps of 2D islands. The use of interferometry is most appropriated in the middle to high supersaturation range. In the case of low supersaturation growth processes are very slow and measurements become sensible to large errors.

2. Molecular level *in situ* observation of protein crystal growth by Phase-Shifting Michelson Interferometry

Previously published works about interferometry and PSI studies of protein crystal growth (Vekilov *et al.*, 1995a; 1995b; Kuznetsov *et al.*, 1995; 1996b; Vekilov and Rosenberger, 1998a; Vekilov *et al.*, 1999; Gliko *et al.*, 2002a; 2002b) were beyond the resolution of molecular steps, in which case, step velocities could not be measured directly. The use of external fixed references points was also required, which is always a source of errors because the focus position has to be changed during the experiments. The capability of this recently developed advanced high resolution Phase Shift Michelson Interferometer PSMI (see chapter III section 2.2) will be demonstrated for the observation of 2D-island growth and the measurement of monolayer step height of 2D islands and steps of spiral hillocks.

2.1. Observation of monolayer steps

For the first time, direct observation of 2D islands steps of molecular height during protein crystal growth was achieved by PSMI (Figure 2.1). The crystal was grown from high purity solution at a supersaturation of $C - C_e = 5.3$ mg/ml. Step height can be derived from the obtained phase shift interferograms by applying following equation (see section III.2.2 for more details):

$$h_{x,y} = \frac{\lambda_{532}}{2 \cdot n} \cdot \frac{I_{x,y}}{256} \quad (2.1)$$

where $\lambda = 532$ nm is the wavelength, I intensity of one pixel and $n = 1.4$ is the refractive index of a tetragonal lysozyme crystal. Using these values the height of a 2D island is calculated to be approximately 5.6 nm. This value

agrees well with previously obtained data from AFM measurements (Durbin and Carlson, 1992; Konnert *et al.*, 1994; Li *et al.*, 1999) and is also consistent with the $d_{(110)}$ lattice plane distance, 5.55 nm ($a=78.54 \text{ \AA}$, $c=37.77 \text{ \AA}$). Further, it proves the double-layer structure of the growth layers on the $\{110\}$ face. Layers with a height of 2.8 nm, as would be expected from the size of lysozyme molecules, were not observed on this face.

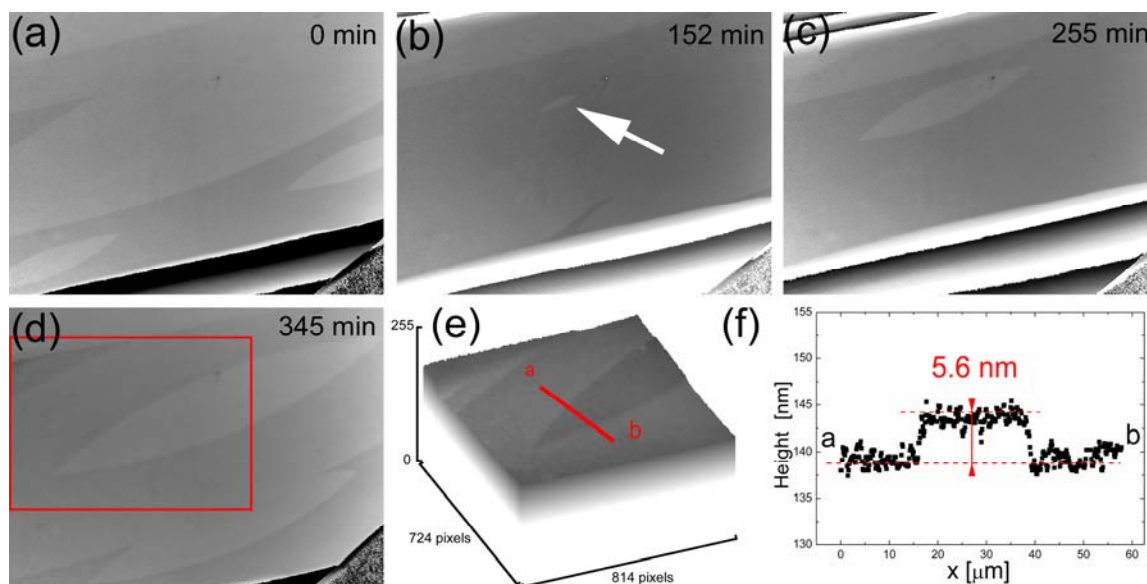


Figure 2.1 Birth and spread of 2D-islands on a $\{110\}$ face of a tetragonal lysozyme crystal growing from a highly purified solution (a,b,c,d). (e) A 3D surface plot of the crystal surface is shown along the line a-b (f). The measured step height of a 2D island was approximately 5.6 nm.

The birth of a new 2D island at $t=152$ min is seen in image (b) of Figure 2.1. Between consecutive phase shift interferograms steps advancement can be measured directly. The step velocity into the fast growing $\langle 110 \rangle$ direction reaches 6.6 nm/s, the one into the slow growing $\langle 001 \rangle$ direction amounts to 1.1 nm/s. Steps moved at constant velocity for the complete experiment duration (9h). The fluctuation of step velocities cause by intrinsic kinetic processes postulated by Vekilov and coworkers were not observed (Vekilov *et al.*, 1996; Vekilov and Rosenberger, 1998; Vekilov *et al.*, 1999). A more exhaustive analysis of step velocities fluctuations is giving in section 3.3.4 of this chapter. Nucleation sites of new

2D-islands are found to be random. This is in good agreement with LCM-DIM observations (Van Driessche *et al.*, 2007) and AFM observations (Durbin *et al.*, 1993).

The observation of steps of molecular height on a spiral hillock was also achieved by PSMI. The crystal shown in Figure 2.2 is growing from highly purified lysozyme solution at a supersaturation of $C-C_e = 4.4$ mg/ml. The step velocity reaches 5.7 nm/s along the fast growing $\langle 110 \rangle$ direction and 0.98 nm/s along the slow growing $\langle 001 \rangle$ direction. Applying equation 2.1 and a refractive index of 1.4, a step height of approximately 11.5 nm is obtained (Figure 2.2c), which corresponds with two times the lattice plane distance $d_{(110)}$ (5.55 nm). This indicates that the spiral dislocation has a burgers vector of $b=2$. In Figure 2.2b a LCM-DIM image of this same spiral hillock is shown. In this image growth steps are visualized with much better contrast than in the case of the PSMI image but from LCM-DIM images it is impossible to derive that the spiral dislocation has a double burgers vector.

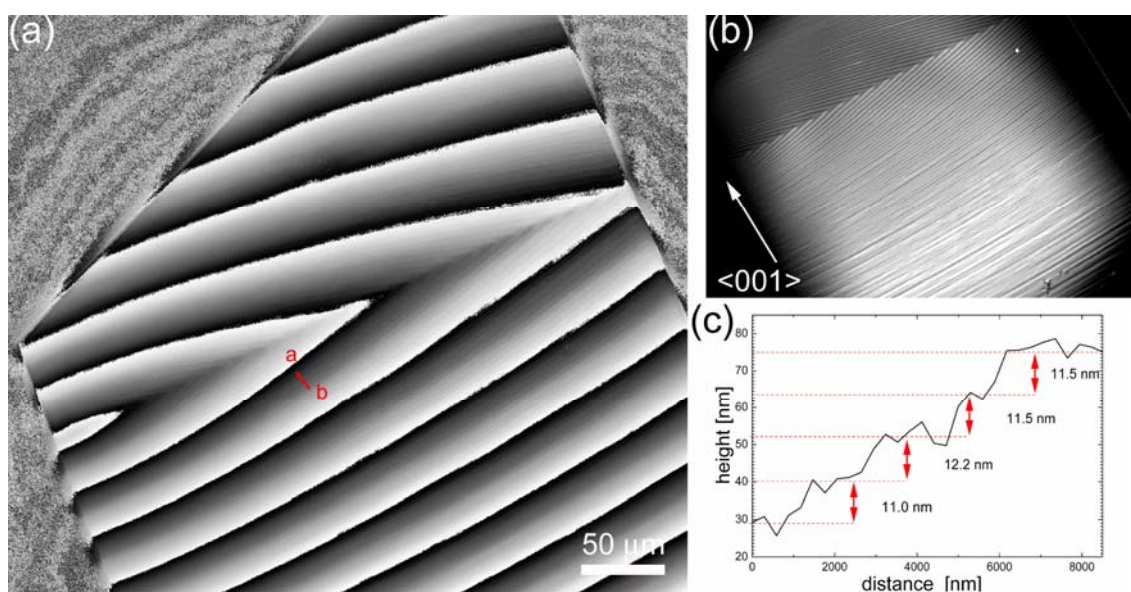


Figure 2.2 Spiral growth hillock on a $\{110\}$ face of tetragonal lysozyme (high purity solution). The island height was determined to be 11.5 nm. (a) Michelson phase shift interogram of a growth hillock. (b) LCM-DIM image of the same spiral growth hillock. (c) Height profile of line a-b, showing the step height.

2.2. Discussion

Besides the highly improved depth resolution of this new PSMI, this system has an added advantage. In most MI setups a reference mirror outside the growth cell is used (Gliko *et al.*, 2002a; 2002b), but the use of an external reference mirror has the drawback that it requires the change of focus position and this can considerably disturb the measurement. The fact that individual terraces and growth steps can be distinguish with this setup is of great advantage, because specific 2D island terraces can be used as a reference surface to eliminate artificial shift of the interference fringes due to drift of the observation cell. A specific 2D island terrace or step can be used as an internal reference point because the gray value is fixed and following images can be corrected with respect to this gray value. Of course this method is only valid at low and medium supersaturation levels, when 2D nucleation rates are relatively low.

Thus with advanced phase-shifting interferometry direct and simultaneous measurement of step velocity and normal growth rate on a molecular level during growth of macromolecular crystal can be obtained. Also the non-invasive character of PSMI makes it possible to follow growth processes over long experimental times and the use of sealed growth cells ensures an undisturbed crystallization environment. The short exposure times needed for image acquisition (approx. 200 ms for each frame) enable the investigation of fast processes even under high supersaturation conditions. Together with the probe-less character of PSMI, this is a clear advantage compared to AFM. But this technique has the inconvenient of requiring very expensive optical equipment and a very high level of expertise to correctly operate and adjust the interferometer to obtain molecular level resolution. This makes routine experiments very laborious. Since the same type of observation cell is used for PSMI and LCM-DIM

experiments, the combination of both advanced optical techniques makes a very powerful non-invasive observation system for studying crystal growth kinetics.

3. Surface morphology and growth kinetics of tetragonal lysozyme crystals in free solution

3.1. Introduction

The physics of macromolecular crystallization is still rather poorly understood therefore precise quantitatively data about growth mechanisms, kinetics of growth and development of surface morphology, transport processes, and defect structure in macromolecular crystals are necessary. The fundamental thermodynamic and kinetic parameters which govern the crystallization process have to be estimated precisely. For layerwise growth the two fundamental parameters are the effective step energy α and the step kinetic coefficient β (Chernov, 1997).

It is well known that impurities can considerable affect the kinetic parameters of crystal growth. In case of inorganic salts the purity level of solution reaches 10^{-5} while a 99% pure protein solution, i.e. 10^{-2} , is considered as ultrapure in the case of macromolecules. Until now most studies on protein crystal growth were preformed with 99% pure, or lower in most cases, samples, mainly without knowledge of the principal characteristics of the present impurities. For lysozyme crystal growth, Vekilov and coworkers (1996) found that the purity of lysozyme solution had a drastic influence on the step kinetic coefficient of $\{110\}$ faces of tetragonal crystals. Thus, the use of highly purified protein solution is necessary for studying intrinsic growth kinetics of protein crystals and solutions. On the other hand identification and characterization of impurities is necessary for a better understanding of incorporation mechanisms and effect on growth kinetics. Additionally the influence of impurities on growth kinetics should be quantified.

In this chapter growth of tetragonal lysozyme crystals is observed *in situ* with LCM-DIM. Observed surface morphologies and growth mechanisms are discussed. To study intrinsic growth kinetics a highly purified lysozyme solution (99.99% pure) was used. Both, effective step energy α and step kinetic coefficient β were estimated. Commercial lysozyme solutions and purified solution with intentionally added impurities were applied to quantify the effect of impurities on the intrinsic growth kinetics and Single Molecule Visualizations of fluorescence labeled molecules was used to obtain a better understanding of the incorporation mechanisms of impurities.

3.2. Sources of growth steps

Most protein crystals display well-defined crystal faces and it has been confirmed by *in situ* observations that growth occurs via the spreading of layers from growth step sources such as dislocations and 2D nuclei (Vekilov and Chernov, 2002). For tetragonal lysozyme crystals *ex situ* electron microscopy (Durbin and Feher, 1990) and *in situ* atomic force microscopy (Durbin and Carlson, 1992; Durbin *et al.*, 1993; Konnert *et al.*, 1994) produced instructive images of growth step generations at screw dislocations out crops and of 2D nucleation induced islands.

Using LCM-DIM, in accordance with previous studies, mainly 2D islands (Figure 4.1a,b) and spiral dislocations (Figure 4.1c,d) were observed on growing $\{110\}$ and $\{101\}$ faces of tetragonal lysozyme crystals. Besides growth hillocks and 2D islands also some less common features were distinguished on growing surfaces, such as: multilayer islands, repeated nucleation, sudden “death” of a spiral dislocation etc. All these observations will be discussed in this chapter. The 2D nucleation growth process is described in detail in section IV.3.5 and spiral growth will be revised in this

section, but first the relative importance of the two main growth mechanisms of tetragonal lysozyme crystals is discussed.

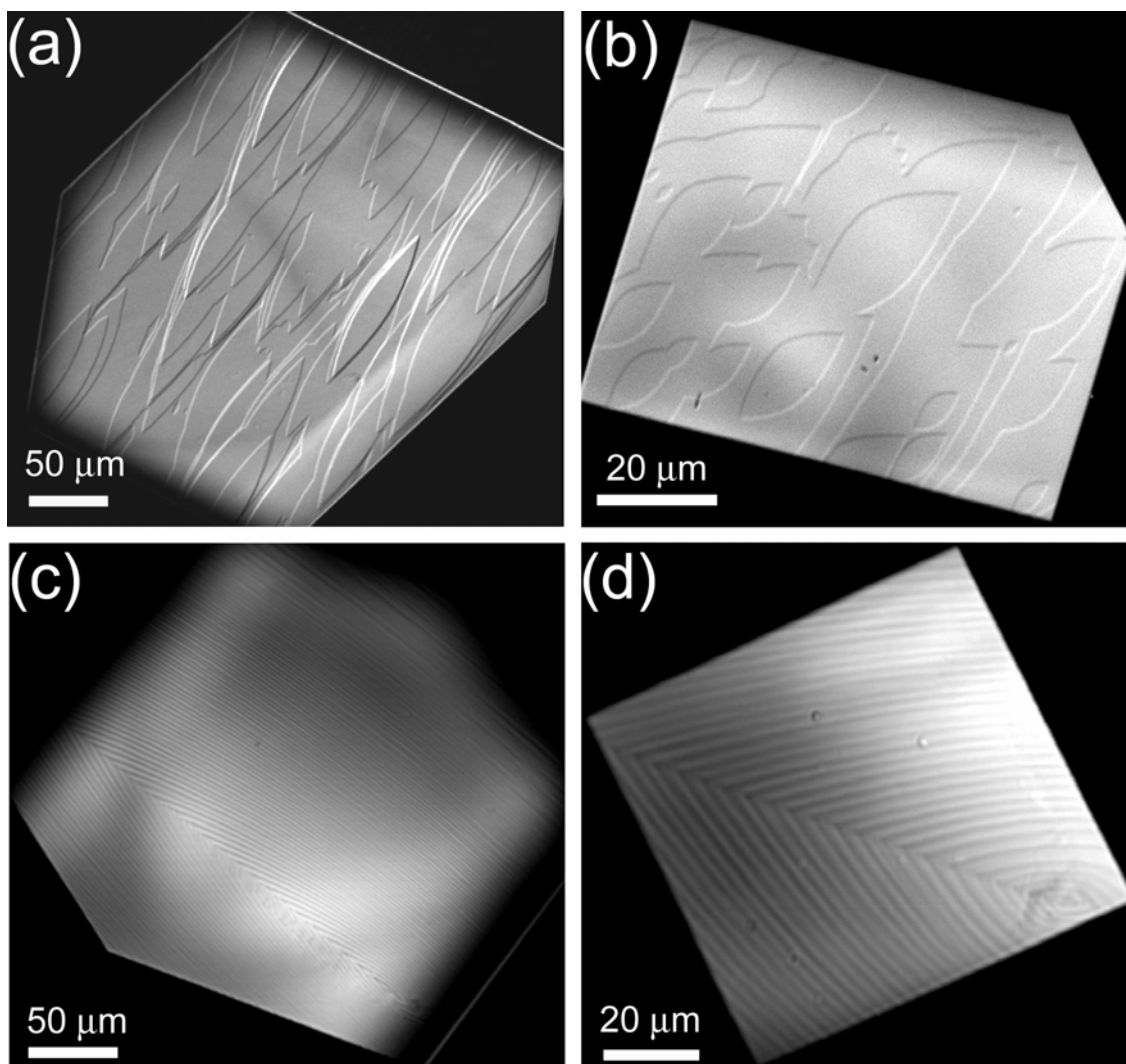


Figure 3.1 LCM-DIM images of step sources on tetragonal lysozyme crystals showing 2D islands on a $\{110\}$ face (a) and a $\{101\}$ face (b), and spiral growth hillocks on a $\{110\}$ face (c) and a $\{101\}$ face (d).

3.2.1. Spiral growth or two-dimensional growth

To estimate the ratio of tetragonal lysozyme crystals grown by 2D nucleation and spiral growth, a series of experiments was carried out crystallizing tetragonal lysozyme crystals under widely adopted conditions (98.5% pure lysozyme from Seikagaku Co., batch crystallization in containers with 1mm height) and monitoring the growth mechanisms of crystals for 22 days. Lysozyme solutions with an initial concentration of 70

mg/ml and 25 mg/ml NaCl were transferred into 10 observation cells, and crystals nucleated directly in the cells. The growth of the {110} and {101} faces was observed from the moment the crystals reached the minimum size needed for observation (>30 - 50 μm) until step advancement became almost zero (i.e. close to equilibrium conditions).

The results of the observations on {110} and {101} faces are summarized in Figure 3.2. At the beginning of the observations, all crystals were growing by 2D nucleation on both faces, and after 22 days still 80% of the crystals were growing by 2D nucleation. Figure 3.2b shows the breakdown of the crystals after 22 days. Spiral growth hillocks appeared occasionally; mainly when microcrystals were adsorbed on a crystal surface or when crystals suffered mechanical stress, i.e. two or more crystals bumped into each other during their growth (Disturbed crystals in Figure 3.2b). From these results, we can conclude that 2D nucleation is the dominant growth mechanisms of tetragonal lysozyme crystals under the crystallization conditions used in this experiment. Since these conditions fall in the range of widely adopted ones, Figure 3.2 shows typical results, although growth mechanisms strongly depend on growth conditions (e.g. initial supersaturation). In addition, as reported in a previous study (Sazaki *et al.*, 2005), Figure 3.2b clearly indicates that solid inclusions play an important role in the generation of dislocations and hence appearance of spiral growth hillocks. These experiments were also repeated with highly purified lysozyme solution but no significant difference could be found.

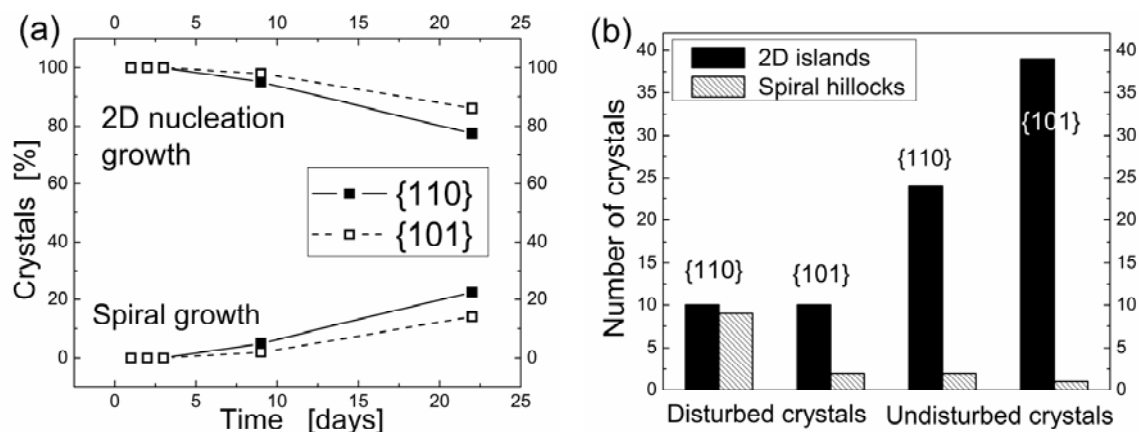


Figure 3.2 Importance of 2D nucleation growth on {110} and {101} faces of tetragonal lysozyme crystals. (a) Changes in the ratio of the crystals on which the growth of {110} or {101} face was dominated by 2D nucleation growth or spiral growth, as a function of time. (b) Number of the crystals whose {110} or {101} face was grown by 2D nucleation growth or spiral growth, after 22 days. The notation “Disturbed crystals” refer to the cases in which microcrystals were adsorbed on the crystal surfaces or the crystals suffered mechanical stress, and the notation “Undisturbed crystals” refers to the crystals that were free from such incidents.

3.2.2. Spiral dislocations as step source

Even though spiral dislocations don't seem to be the most important growth mechanism, i.e. source of steps, under middle and high supersaturation for tetragonal lysozyme crystals, it still plays an important role at low supersaturations $C-C_e \leq 30$ mg/ml, because once a spiral growth hillock is generated, it will dominate the whole crystal surface because of the higher step generation rate compared to 2D growth by the birth-and-spread mechanism. Also some peculiar observations were made during this work concerning spiral growth which are believed to be relevant for crystal growth and consequent quality of crystals.

In Figure 3.1c,d typical spiral growth hillocks on {110} and {101} faces are shown. Growth steps and interstep distances on a spiral growth hillock could be observed with sufficient contrast at low supersaturation, but at medium supersaturation levels this becomes more difficult since the

interstep distance is dramatically reduced, even so, steps can still be distinguished. Once high supersaturation levels are reached the spiral hillocks are completely covered with 2D islands. Because of the higher step generation rate of the birth and spread mechanism (Figure 3.3) the morphology of the growth hillock will eventually disappear. When the supersaturation is lowered again the spiral hillock will reappear, e.g. the typical shape of a spiral hillock will become visible again, which proves that spiral dislocations do not disappear when supersaturation is increased.

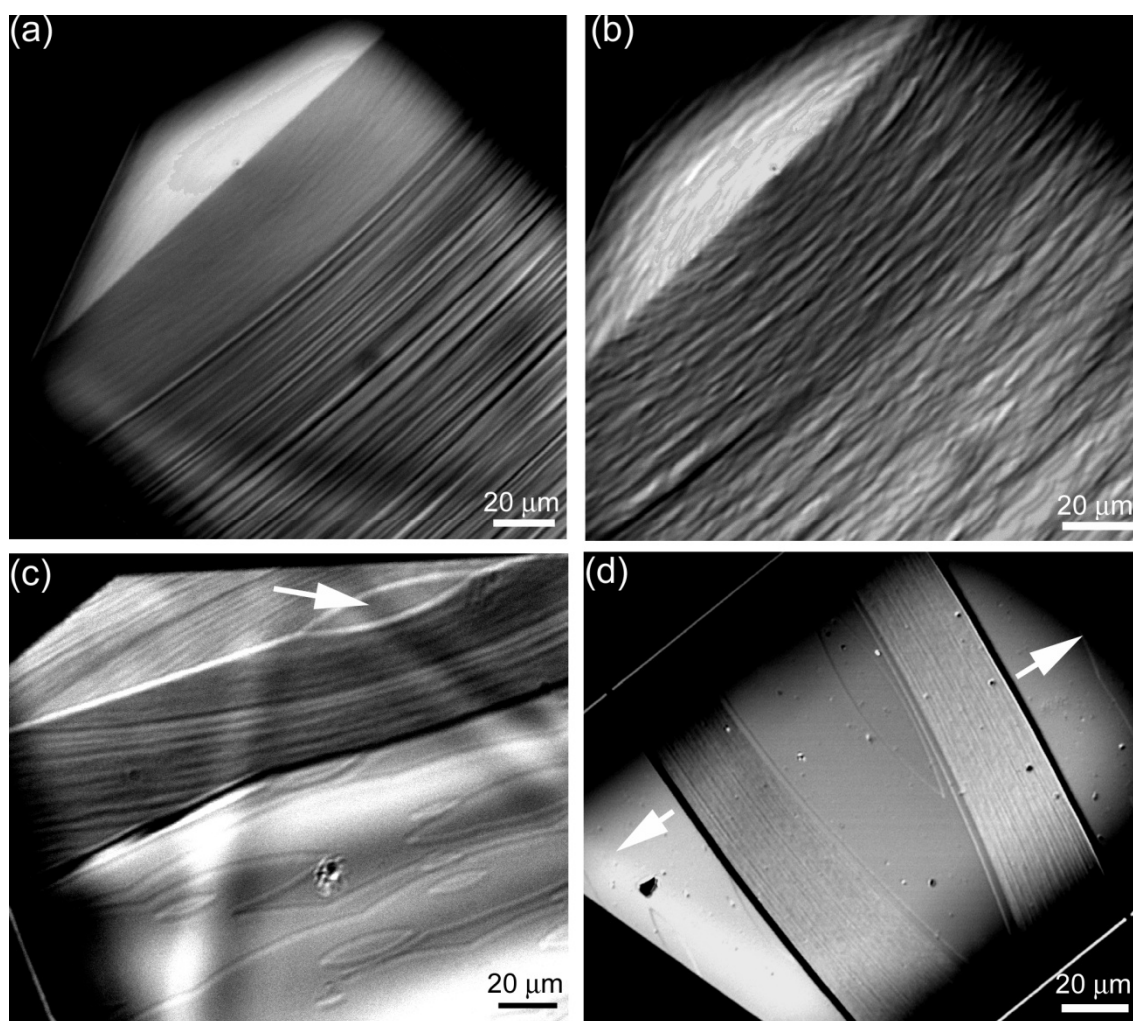


Figure 3.3 LCM-DIM images of spiral growth. (a) Spiral growth at middle supersaturation, only straight steps are observed. (b) Spiral growth at high supersaturation; the growth hillock is being covered with 2D islands and steps become irregular. (c) Sudden “dead” of a spiral dislocation, the white arrow indicates where moments before a spiral dislocation was still generating steps. (d) After a spiral dislocation suddenly disappeared a multilayered islands is advancing laterally across the crystal surface.

On the other hand, it was observed that a spiral dislocation sometimes suddenly “died” leaving behind a large macro-island (multilayer stack) that expands laterally across the surface (Figure 3.3). No references of this type of events was found in the literature, only Durbin and coworkers (1993) observed similar multilayer islands on tetragonal lysozyme crystals but they were not able to see the origin of these steps probably because when using AFM only a small part of the crystal surface could be visualized. Unfortunately the mechanism(s) behind the sudden “death” of a spiral dislocation is/are unclear. This process was relatively frequent observed and thus should be studied more in detail to understand it’s mechanism(s) and assess it’s possible effects on crystal quality.

Origin and density of spiral dislocations

Spiral growth in lysozyme crystals is most likely related to crystal defects caused by engulfed foreign particles or microcrystals (e.g. Land and DeYoreo, 2000, Sazaki *et al.*, 2004). It is well know that protein and virus crystals easily incorporate microcristales (e.g. McPherson *et al.*, 1995, Malkin *et al.*, 1996c; Land and DeYoreo, 2000). With LCM-DIM it is also possible to make observations inside of growing crystals by shifting slightly the focal plane inside of the crystal volume. This is demonstrated nicely by Figure 3.4 where microcrystals incorporated into a crystal are clearly visualized. These particles are single crystals that land randomly on the surface and do not have necessarily the same orientation as the substrate. As they become incorporated into the crystal they most likely generate defects such as complex dislocation sources, areas with misaligned lattices and planar defects such as stacking faults (Land and DeYoreo, 2000). But it was also observed, for catalase crystals, that large amounts of microcrystals can be incorporated into the crystal volume without producing any spiral dislocation or stacking faults (Malkin *et al.*, 1997). Most likely the elastic mechanical property of a crystal lattice determines the amount of defects generated by incorporated microcristales.

Excellent *in situ* observation of dislocations in protein crystals during growth was done by Sazaki and coworkers (2005) using LCM-DIM, phase contrast microscopy and birefringence microscopy. They were able to observe strain fields around dislocations with much higher resolution than possible with X-ray topography. They found that the dislocations appeared in bundles and were probably generated at the periphery of relatively large inclusions inside the crystal. Taking into account these observations and the once made for this work, those large inclusions are most likely incorporated microcrystals as was also suggested by Sazaki and coworkers (2005). Also, Land and DeYoreo (2000) found that complex dislocation hillocks were formed by microcrystals imbedded into growing crystals of canavalin.

It must be mentioned that single spiral hillocks observed by LCM-DIM are actually, in most cases, an agglomeration of several screw dislocations, a situation commonly found during protein crystal growth, as demonstrated by direct AFM observations (Land and DeYoreo, 2000). This corresponds very well with the bundles of dislocation observed below spiral dislocation outcrops by Sazaki and coworkers (2005).

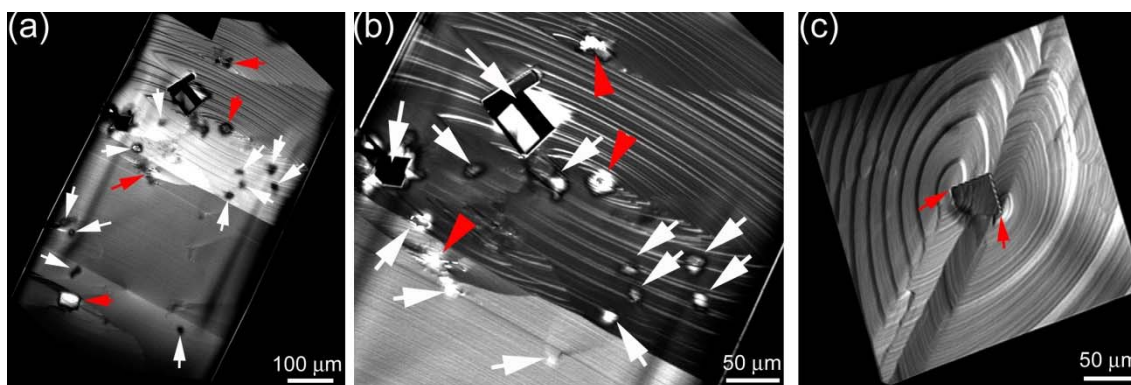


Figure 3.4 Microcrystals as source of spiral dislocations. a) Microphotograph of $\{110\}$ face with incorporated microcrystals (white arrows) and spiral dislocation outcrops generated by microcrystals (red arrows), a detail is shown in (b). (c) Microphotograph of $\{101\}$ face with a partially incorporated microcrystal which gives birth to two spiral dislocations (red arrows).

As shown in Figure 3.4 only a reduced number of incorporated microcrystals give rise to the formation of actual spiral growth hillocks. Why some microcrystals give birth to a spiral hillock and others no, still remains an open question. But it is clear that protein crystals have a great capacity for incorporating large particles into their lattice, this is confirmed by previous AFM observations (e.g. McPherson *et al.*, 1995, Malkin *et al.*, 1996c; Land and DeYoreo, 2000).

In Figure 3.5 the number of growth hillocks found on growing crystal surfaces is represented. Mostly 1 or 2 spiral hillocks are present on a crystal surface. There is no apparent difference between the $\{110\}$ or $\{101\}$ face. Also no direct relation could be found between purity of the lysozyme solution and number of spiral hillocks found on a growing surface.

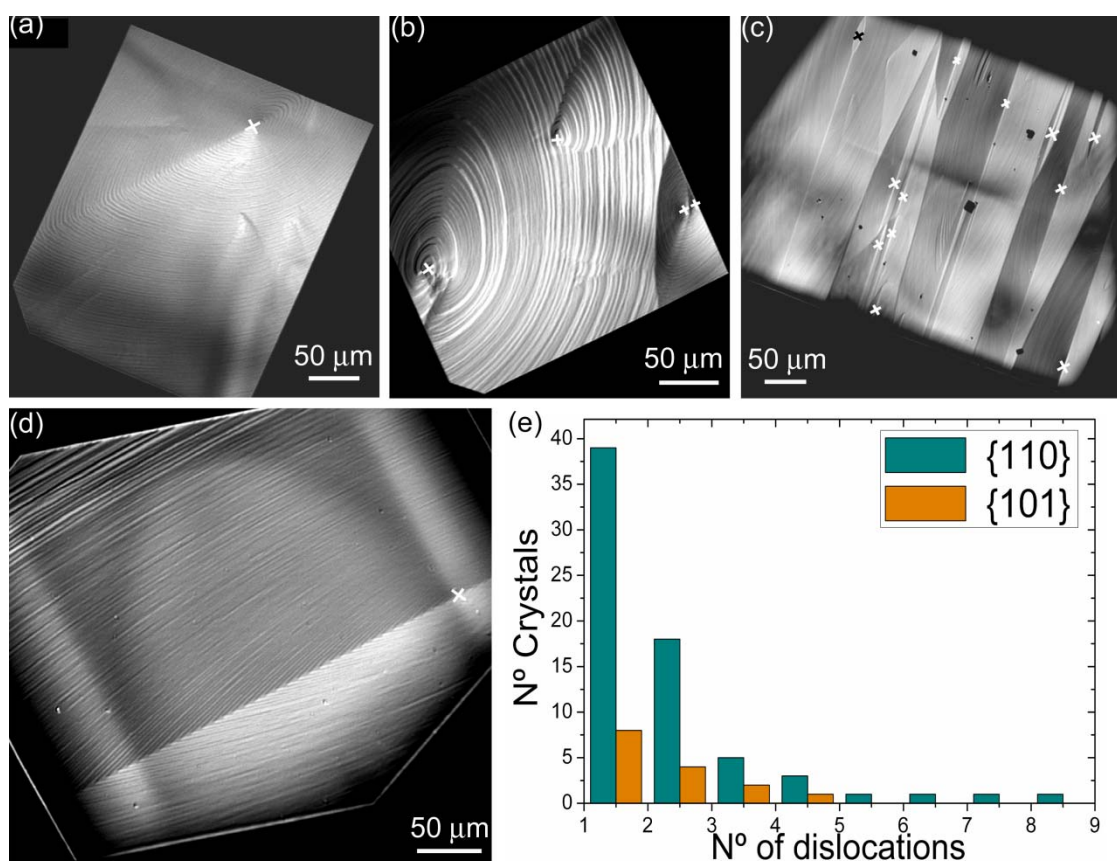


Figure 3.5 Density of spiral hillocks on $\{110\}$ and $\{101\}$ faces of tetragonal lysozyme. Microphotographs of $\{101\}$ faces with one spiral hillock dominating the faces (a) or with several spiral hillocks (b). Microphotograph of $\{110\}$ face covered with several growth hillocks (c) or by a single spiral hillock (d). (e) Amount of spiral growth hillocks observed

on {110} (orange) and {101} (green) faces, white arrows indicates the spiral dislocation outcrop. White cross marks indicate the center of spiral hillocks. Black cross mark in image (c) indicates a spiral dislocation that suddenly died.

Evolution of spiral hillocks at constant supersaturation

Several growth hillocks can develop simultaneously on a crystal surface and contribute to the growth rate of the crystal, but typically only one dislocation, with the bigger burgers vector, will be dominant, i.e. the source putting out steps at the highest rate. This will eventually lead to one spiral hillock covering the entire surface and determining the face growth rate, even so, small secondary spiral dislocations can exist on the surface without significantly contributing to the growth rate. In Figure 3.6 the birth and evolution of several spiral hillocks is shown at constant supersaturation. At the beginning a large number of spiral hillocks are formed on the surface (centers are indicated with white cross marks in Figure 3.6a). After 24 hours the number of growth hillocks is already strongly reduced and the source putting out new steps at the highest rate will eventually dominate the crystal surface, but it will still take several days before this hillock will cover the entire surface. Possibly some of the other sources will exist as dislocations on the terraces but these could not be resolved by LCM-DIM. Similar observations were made by AFM for canavalin crystallization (Land and DeYoreo, 2000). These observations also fit well with the dislocation bundles observed below spiral hillocks by Sasaki and coworkers (2005). Below dislocation(s) having the bigger burgers vector many smaller ones exist. Thus for lysozyme, the majority of crystals have only one or two growth hillocks dominating the growth rate of the crystal face but many more dislocations are present in the crystal volume. In Figure 3.6 step bunching is also observed (white arrows), a typical feature of spiral growth, this is discussed in more detail in section IV.3.4.7.

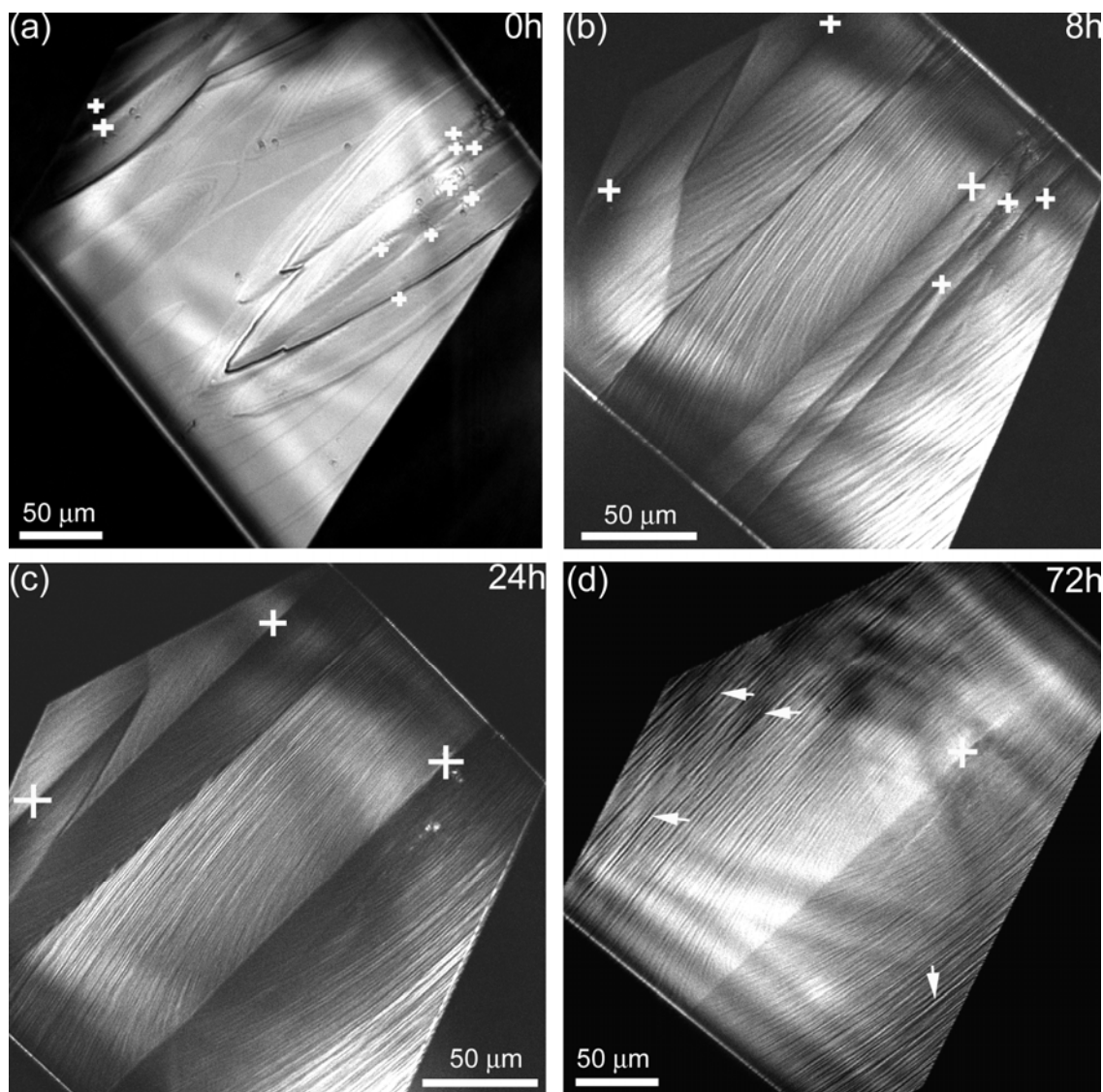


Figure 3.6 Series of LCM-DIM images showing evolution of spiral hillocks on a {110} face of a tetragonal lysozyme crystal growing at constant supersaturation. (a) Appearance of several hillocks on a surface growing by 2D nucleation. (b) After 8 hours the surface is completely covered with several hillocks. (c) 24 hours later the surface is showing three hillocks. (d) After three days only one spiral hillock dominates the surface. In (a-d) cross marks correspond to the centers of spiral hillocks and white arrows indicate step bunching.

3.3. Growth step kinetics

In this section step velocities of spiral hillocks and 2D islands measured on tetragonal lysozyme crystals by LCM-DIM are discussed. From the obtained experimental data the kinetic coefficient is estimated and the importance of bulk diffusion and surface kinetics is discussed. Intrinsic growth kinetics are studied thus all experiments were performed using highly purified lysozyme (99.99%) solution.

3.3.1. Morphology of steps

Spiral hillocks and two dimensional islands formed in a 99.99% purity solution on {110} faces are lens-shaped with sharp tips (Figure 4.1a,b) and leaf-shaped (lozengeshape) with sharp tips on the {101} face (Figure 4.1c,d). These steps shape are the result of different packing of molecules in different crystallographic directions and the consequent kinetic anisotropy in the step advancement on both faces. This will be discussed in the next section. The ratio of the short and long axis of 2D islands and spiral hillocks on the {110}-face is approximately 6 and does not change with supersaturation. On the {101}-face the 2D islands and spiral hillocks are not symmetric and the step edges are apparently parallel to the crystal side faces (Figure 4.1c,d). The island morphology is maintained over the entire supersaturation range.

3.3.2. Step velocities and kinetic coefficient β

– Kinetic Anisotropy of growth steps –

Step speeds are typically analyzed in accordance with

$$v = \Omega\beta(C - C_e) \tag{3.1}$$

where Ω is the volume of one lysozyme molecule inside a tetragonal crystals, β is the kinetic coefficient, C is the bulk concentration of lysozyme and C_e the solubility at a given temperature. This expression has both a theoretical basis (Chernov, 1961; Gilmer *et al.*, 1971; Chernov, 1984; Chernov and Komatsu, 1995) and experimental verification for a number of inorganic systems (Malkin *et al.*, 1989; Vekilov *et al.*, 1992; Maiwa *et al.*, 1990) and macromolecules (Kuznetsov *et al.*, 1995; Malkin *et al.*, 1996; Land *et al.*, 1997). Often this expression is also written as

$$v = \Omega\beta C_e \sigma \quad (3.2)$$

where σ represents the relative supersaturation

$$\sigma = \frac{C - C_e}{C_e} \quad (3.3)$$

Unfortunately, σ is also often expressed as

$$\sigma = \ln \frac{C}{C_e} \quad (3.4)$$

and is appropriated to use in case of nucleation kinetic studies (Chernov and Vekilov, 2003). In certain occasions the expressions of σ have been mixed up and in a number of publications following expression for step velocity was used (Vekilov *et al.*, 1993, 1995; Vekilov and Rosenberger, 1996; Rong *et al.*, 2000; Dold *et al.*, 2006)

$$v = \Omega\beta C_e \ln\left(\frac{C}{C_e}\right) \quad (3.5)$$

which is of course incorrect (see derivations in Chernov, 1984). The only two meaningful way's of representing step velocities versus supersaturation are: $v - C - C_e$ or $v - (C - C_e)/C_e$, since $v - \ln(C/C_e)$ has no physical meaning.

The tangential rates of step advancement for different crystallographic directions were measured over a wide supersaturation range $C - C_e = 0 - 45$ mg/ml on {110} and {101} faces of tetragonal lysozyme crystals using highly purified lysozyme solution. For each supersaturation condition, at least two to three experiments with different seed crystals were carried out. At a same supersaturation, tangential rates were typically

measured for a large number of two-dimensional islands and steps on spiral hillocks. Variations in step velocities for different 2D islands or spiral hillocks on a same crystal surface at constant supersaturation were typically within 1-2%.

Step velocities measured by other researchers

There exist several reports on step velocity measurements of tetragonal lysozyme crystals using interferometry (Vekilov and Rosenberger, 1996), atomic force microscopy (AFM) (Nakada et al., 1999; Yoshizaki et al., 2002) or Phase contrast microscopy (Dold *et al.*, 2006). Under comparable conditions with respect to the supersaturation and protein solution purity (99.99%), the reported values of the step velocities differ by more than one order of magnitude. Vekilov and Rosenberger (1996) published step velocities of several hundred nm/s up to more than 1 $\mu\text{m/s}$ ($\{110\}$ face, $\ln(C/C_e) = 1 - 1.5$, Interferometry measurements). Values reported by other groups are considerably lower: Yoshizaki and coworkers (2002) have measured a step velocity of $\approx 10 - 700$ nm/s in the supersaturation range $C-C_e = 15 - 200$ mg/ml ($\{110\}$ face; *ex situ* AFM). Dold and coworkers measured step velocities on $\{110\}$ faces of tetragonal lysozyme crystals growing from purified lysozyme solution using phase contrast microscopy and obtained values in the $\langle 110 \rangle$ direction of 0-80nm/s in the supersaturation range $C-C_e = 0 - 58$ mg/ml.

Nakada and coworkers (1999) were the first and, only ones, to measure step velocities on $\{101\}$ faces growing from purified lysozyme solution. Using AFM they found step velocities around 10nm/s for a supersaturation of $C-C_e = 22$ mg/ml.

Step velocities $\{110\}$ -face

A series of *in situ* LCM-DIM images of a $\{110\}$ face growing by 2D nucleation is shown in [Figure 3.7](#). A new 2D nucleus is born in image (b) and spreads continuously in subsequent images. The tangential velocity of

the step fronts* advancing in the $\langle\bar{1}10\rangle$ direction was about 10.3 nm/s, which is approximately 6 times higher than the tangential velocity of the steps moving in the $\langle 001\rangle$ direction, $v = 1.6\text{nm/s}$.

Step anisotropy arises because of a difference in molecular structure of growth steps advancing in different crystallographic directions and has been observed in several occasions for protein crystal growth (Malkin *et al.*, 1996; Ko *et al.*, 1999; Plomp *et al.*, 2001; Waizumi *et al.*, 2003). In the case of tetragonal lysozyme the step anisotropy was first observed and explained in detail by Durbin and Feher (1990, 1991). The elongated shape of 2D islands and growth hillocks on $\{110\}$ faces does not depend strongly on the relative binding energies. Rather, it results from the different nature of the bond chains running in $\langle 001\rangle$ and $\langle\bar{1}10\rangle$ directions. Chains along $\langle\bar{1}10\rangle$ can be extended by forming two new bonds as each molecule is added, one to the end of the chain and one to the layer below. By contrast, when molecules are added to helices along $\langle 001\rangle$, two new bonds are formed when the molecules are added in the lower layer, but only one is formed when they are added in the upper layer. The latter molecules are very likely to detach before the chain can be further extended. This kinetic effect slows down the growth of islands in the $\langle 001\rangle$ direction, resulting in the observed elongation (Durbin and Feher, 1991). Thus, on the $\{110\}$ face the island morphology results from an intrinsic anisotropy in the step velocity in two directions, being $\langle 001\rangle$ the slow direction and $\langle\bar{1}10\rangle$ the fast direction.

Grimbergen and coworkers (1999) did a connected net analysis of tetragonal lysozyme crystals, and from this analysis it was found that steps along the $\langle 001\rangle$ direction (corresponding step velocity is $v_{\langle 001\rangle}$) have a small step energy compared to steps along $\langle\bar{1}10\rangle$ ($v_{\langle\bar{1}10\rangle}$). Therefore the growth rate of a step in the $\langle 001\rangle$ direction will be relatively high as compared with the growth rate of steps in the $\langle\bar{1}10\rangle$ direction resulting in the elongated shape of the 2D islands or spiral hillocks.

*In the $\langle\bar{1}10\rangle$ direction no real step front is present but solute molecules do attach in this directions. So, for convenience, this will be called step front throughout the manuscript. 41

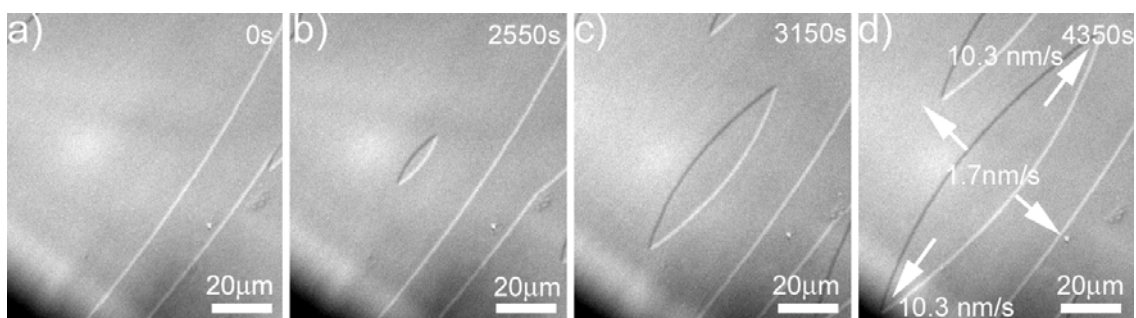


Figure 3.7 Time series of *in situ* LCM-DIM images of birth and spread of a 2d island on a $\{110\}$ surface of a tetragonal lysozyme. A new 2D nucleus is born in (b) and spreads continuously across the crystal surface (c-d).

In a first series of experiments temperature was maintained constant and protein concentration was changed to control supersaturation for each experiment. The tangential rates of step advancement for different crystallographic directions were measured over a wide supersaturation range at four different temperatures (16.5°C, 20°C, 24°C and 27°C), for clarity only data of three temperatures are shown in Figure 3.8. Over the entire supersaturation range step rates in both crystallographic directions, $\langle\bar{1}10\rangle$ and $\langle 001\rangle$, varied approximately 6-fold. Thus the intrinsic anisotropy of the step velocity is constant for the studied supersaturation range.

When representing step velocities versus relative supersaturation $C/C_e - 1$, different dependencies are found for different temperatures (Figure 3.8a). But if step velocities are plotted versus absolute supersaturation one master curve can be found for each crystallographic direction and hence, no temperature effect is observed on the step advancement (Figure 3.8b). This will be discussed later on in this section.

For the further part of this work temperature variations are used as the controlling parameter of supersaturation inside of the observation cell. The advantage of this approach, once the experiment has been set up, lies in its simplicity and the possibility to perform long experiments without necessity to change the solution inside the airtight observation cell. Only few crystals are present in a relatively large volume ($\approx 500 \mu\text{l}$), thus bulk

concentration is supposed to remain constant during a long experiment. Before and after each experiment the concentration of the solution was measured and no significant difference could be found when the observation cell was properly sealed, i.e. made airtight.

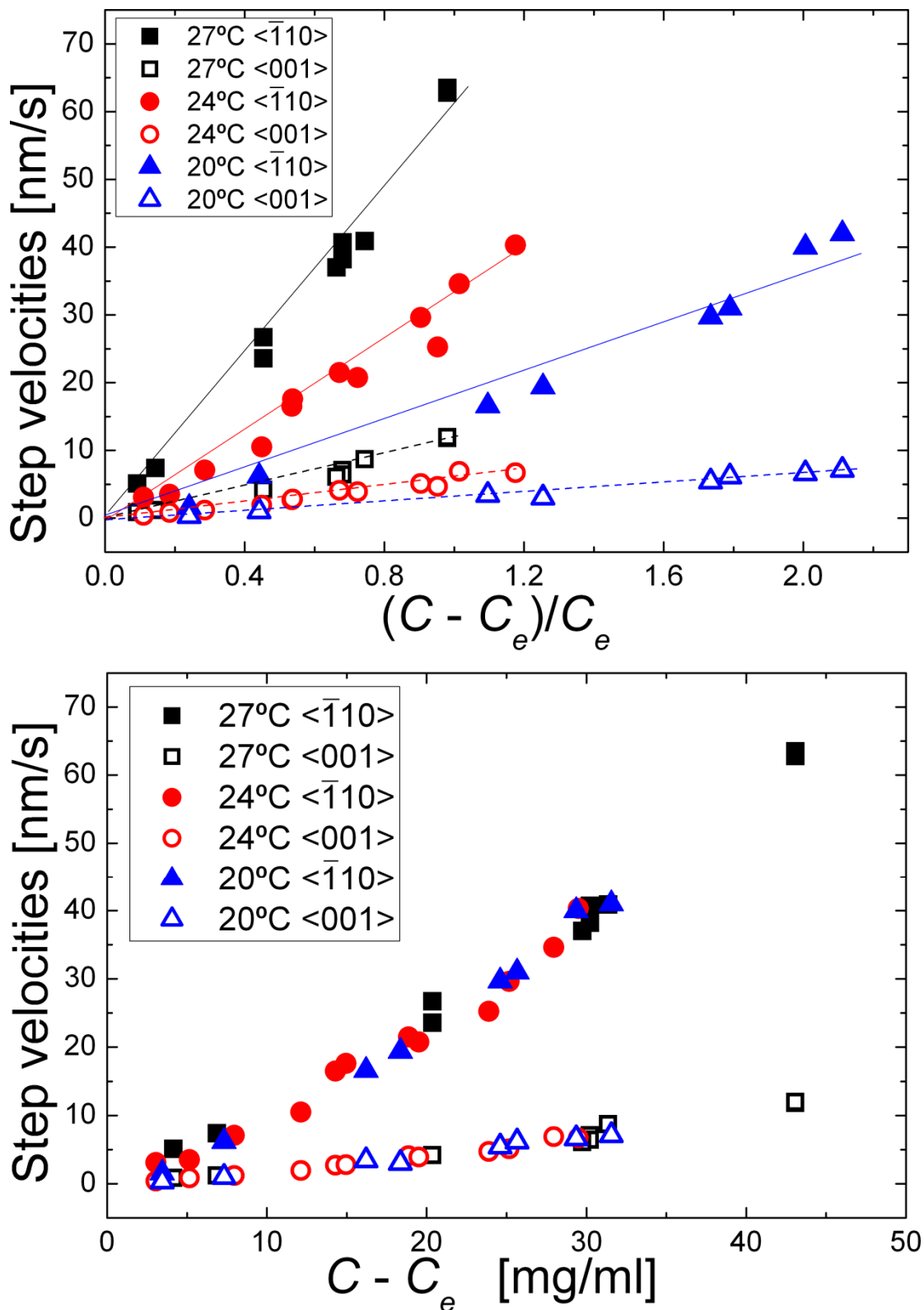


Figure 3.8 Supersaturation dependencies of tangential step growth rates in

different crystallographic directions. (a) Step velocities versus relative supersaturation, and (b) step velocities versus absolute supersaturation. The lines shown in (a) are guides for the eye.

Step velocities {101}-face

A series of *in situ* LCM-DIM images of a {101} face growing by 2D nucleation is shown in Figure 3.9. A new 2D nucleus is born in Figure 3.9b and spreads continuously in subsequent images. The observed step anisotropy is in accordance with the difference in molecular orientation of growth steps advancing in different crystallographic directions. The {101} surface has no such strong asymmetry bonding as is the case for the {110} faces and therefore the islands are more isometric. A detailed PBC analysis should be able to explain these small differences.

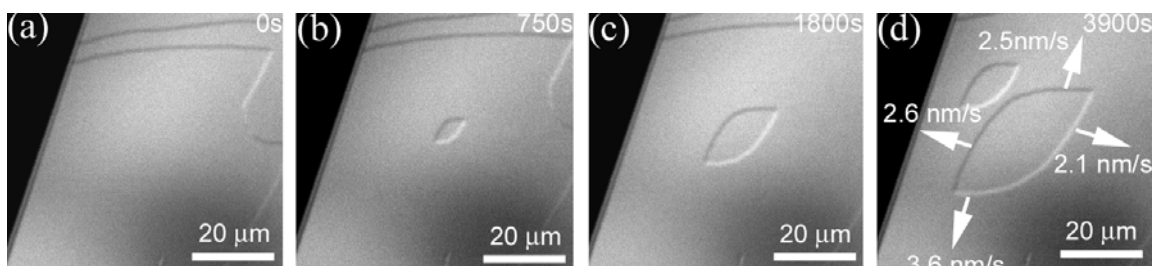


Figure 3.9 A series of *in situ* LCM-DIM images of birth and spread of a 2D island on a {101} face of tetragonal lysozyme. A new 2D nucleus is born in (b) and spreads continuously in subsequent images (c,d). The tangential velocity of the step advancing downwards within the images was about 2.6 nm/s, which is about 30% higher than the rate of 2.5 -2.6 nm/s of the other two steps as indicated in (d). The step advancing to the right moves at a rate of about 15% lower than the rate of 2.5-2.6 nm/s.

The tangential rates of step advancement for different crystallographic directions were measured over a wide supersaturation range (Figure 3.10a). No important differences in step velocities are found for the four crystallographic directions. The largest difference is found for step rates in the crystallographic directions $\langle 110 \rangle$ and $\langle \bar{1}10 \rangle$ which varied approximately 1.5-fold. The intrinsic anisotropy of the step velocity is constant for the studied supersaturation range.

In Figure 3.10b step velocities in the fast and slow directions of the {110} face and {101} face are compared. The fast step velocity on the {110} face is considerably higher than that found on the {101} faces. This would partially explain why {101} faces grow slower at low supersaturation. Step rates in the slow direction are very similar. Step velocities could not be measured above supersaturation of $C-C_e = 20$ mg/ml because 2D nucleation is very high and single steps cannot be visualized with sufficient contrast.

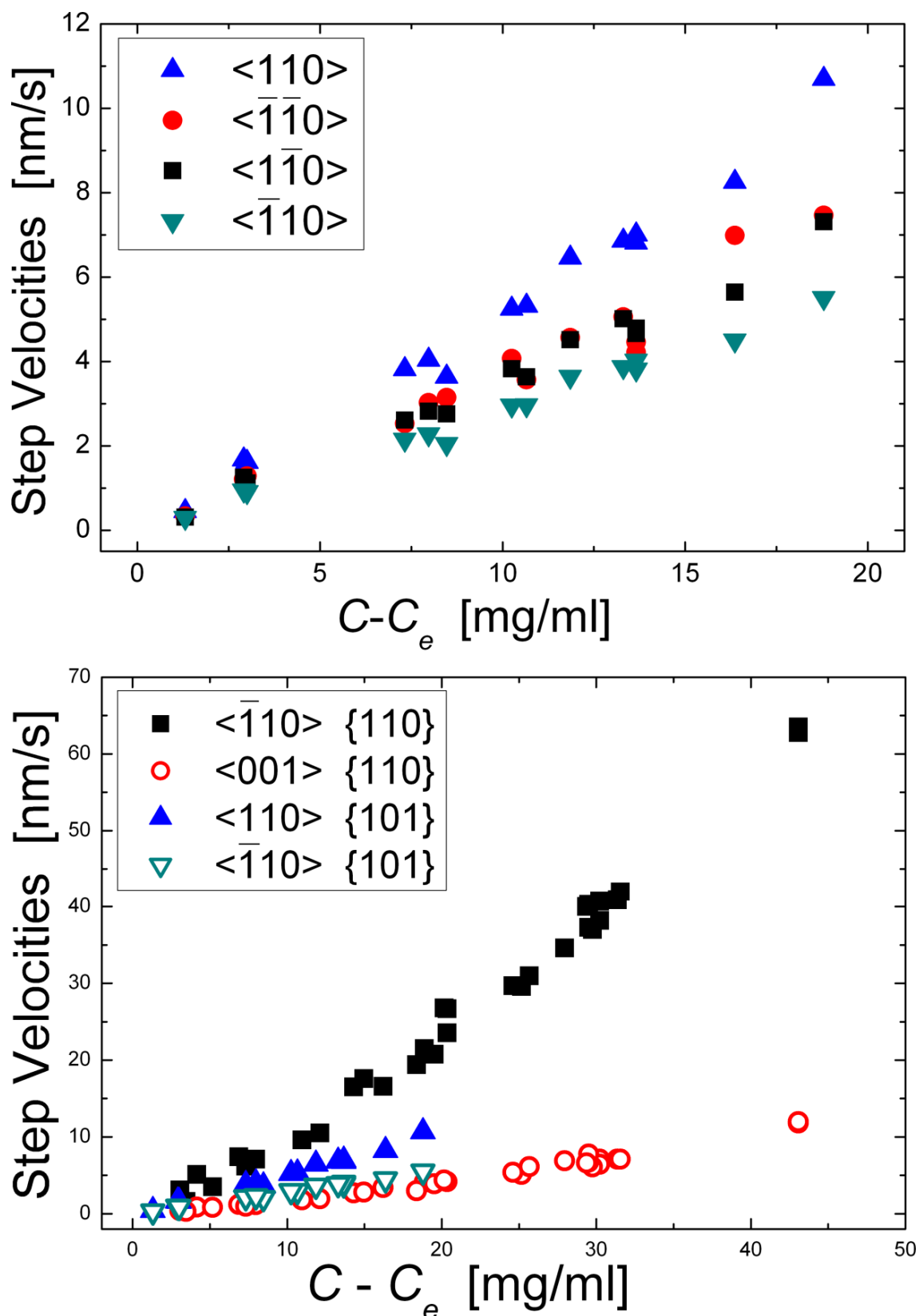


Figure 3.10 Supersaturation dependencies of tangential step growth rates in different crystallographic directions on {101} faces of tetragonal lysozyme. (a) Step velocities versus absolute supersaturation. (b) Comparison of supersaturation dependency of step velocities in the fast and slow directions on {110} and {101} faces.

It is very difficult (sheer luck) to obtain crystals in the observation cell with a $\{101\}$ face parallel to the bottom glass plate. This is the main reason why most experimental observations in this work were carried out on $\{110\}$ faces of tetragonal lysozyme, because the observation cell preparation is straight forward and a great number of experiments could be performed in a relatively short time period.

Spiral growth versus 2D growth

Step advancements measured for spiral hillocks were compared to those obtained for 2D islands (Figure 3.11). The same step anisotropy was found as in the case of 2D islands and no different supersaturation dependencies between step velocities of spiral hillocks and 2D islands could be found for the $\{110\}$ and $\{101\}$ face (Figure 3.11). Thus attachment kinetics of molecules to the surface are independent on the step source.

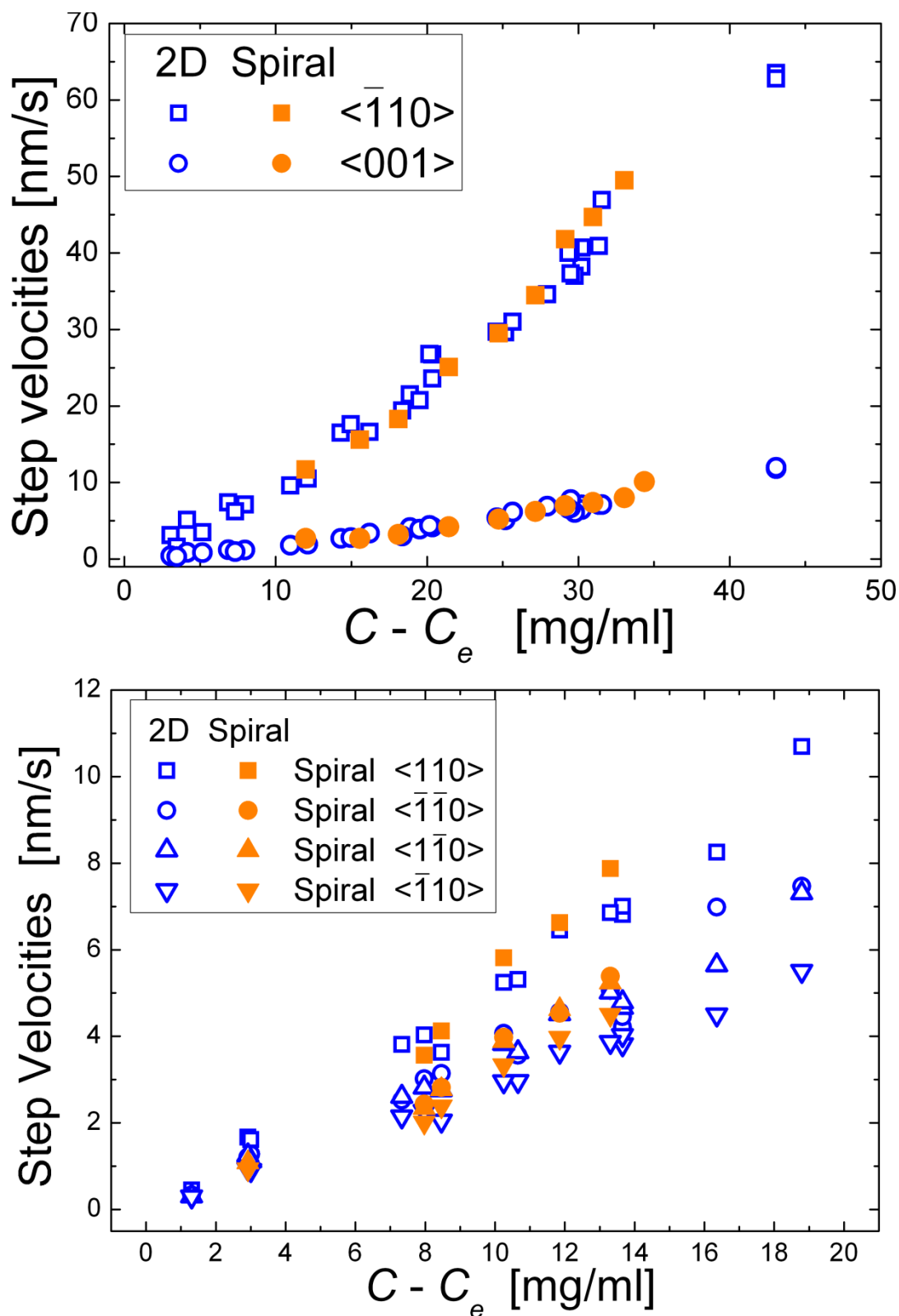


Figure 3.11. Supersaturation dependencies of tangential step growth rates in different crystallographic directions spiral hillocks and 2D islands on $\{110\}$ (a) and $\{101\}$ faces (b) of tetragonal lysozyme crystals.

Kinetic coefficient β

Now that one master curve has been obtained for the dependency of step velocity on supersaturation for both faces the kinetic coefficients in different crystallographic directions can be estimated. From tangential step rates on $\{110\}$ faces in the directions $\langle\bar{1}10\rangle$ and $\langle 001\rangle$ kinetic coefficients were estimated according to Eq. 3.1 based on a linear fit of experimental data in the supersaturation range $C-C_e = 0 - 45$ mg/ml (Figure 3.12). If $\Omega = 2.7 \times 10^{-20}$ cm³ is the specific volume of one lysozyme molecule (Steinrauf, 1954) than $\beta_{\langle\bar{1}10\rangle}$ is 1.03×10^{-4} cm/s and $\beta_{\langle 001\rangle}$ is 1.85×10^{-5} cm/s. For $\{101\}$ faces following values were obtained: $\beta_{\langle\bar{1}10\rangle} = 4.8 \times 10^{-5}$ cm/s, $\beta_{\langle\bar{1}10\rangle} = 3.4 \times 10^{-5}$ cm/s, $\beta_{\langle 110\rangle} = 3.3 \times 10^{-5}$ cm/s and $\beta_{\langle\bar{1}10\rangle} = 2.6 \times 10^{-5}$ cm/s. This is the first time that the kinetic factor is determined for different crystallographic directions. Vekilov and coworkers (1995, 1996) determined averaged kinetic coefficient for the $\{110\}$ and $\{101\}$ faces of tetragonal lysozyme under similar experimental conditions using Michelson interferometry. The obtained values for β_{st} differ approximately one order of magnitude from our results.

Similar values for the kinetic coefficient were found for example for the crystallization of canavalin (Land *et al.*, 1995; Kuznetsov *et al.*, 1995), STMV (Malkin *et al.*, 1995) and thaumatin (Malkin *et al.*, 1996). A typical value of β_{st} for inorganic crystals grown from solution is in the order of 10^{-2} to 10^{-1} cm/s, i.e, 2-3 orders of magnitude higher. The low value of β_{st} for macromolecular crystals is probably due to a lower probability of the proper molecular orientation of incoming molecules for incorporation into the crystal. Indeed it was estimated (Chernov and Komatsu, 1995) that the steric probability factor (probability of the correct spatial orientation of the incoming molecule for incorporation in the lattice, relative to all other orientations) for macromolecules is in the order of $10^{-2} - 10^{-3}$ compared with values close to unity for small inorganic molecules. Nanev (2007) argues that this steric restriction for the association of the protein molecules is due to their highly inhomogeneous surfaces. Land and DeYoreo (2000) argue

that in general β_{st} scales with molecular size, i.e. the larger the molecule the slower the kinetics.

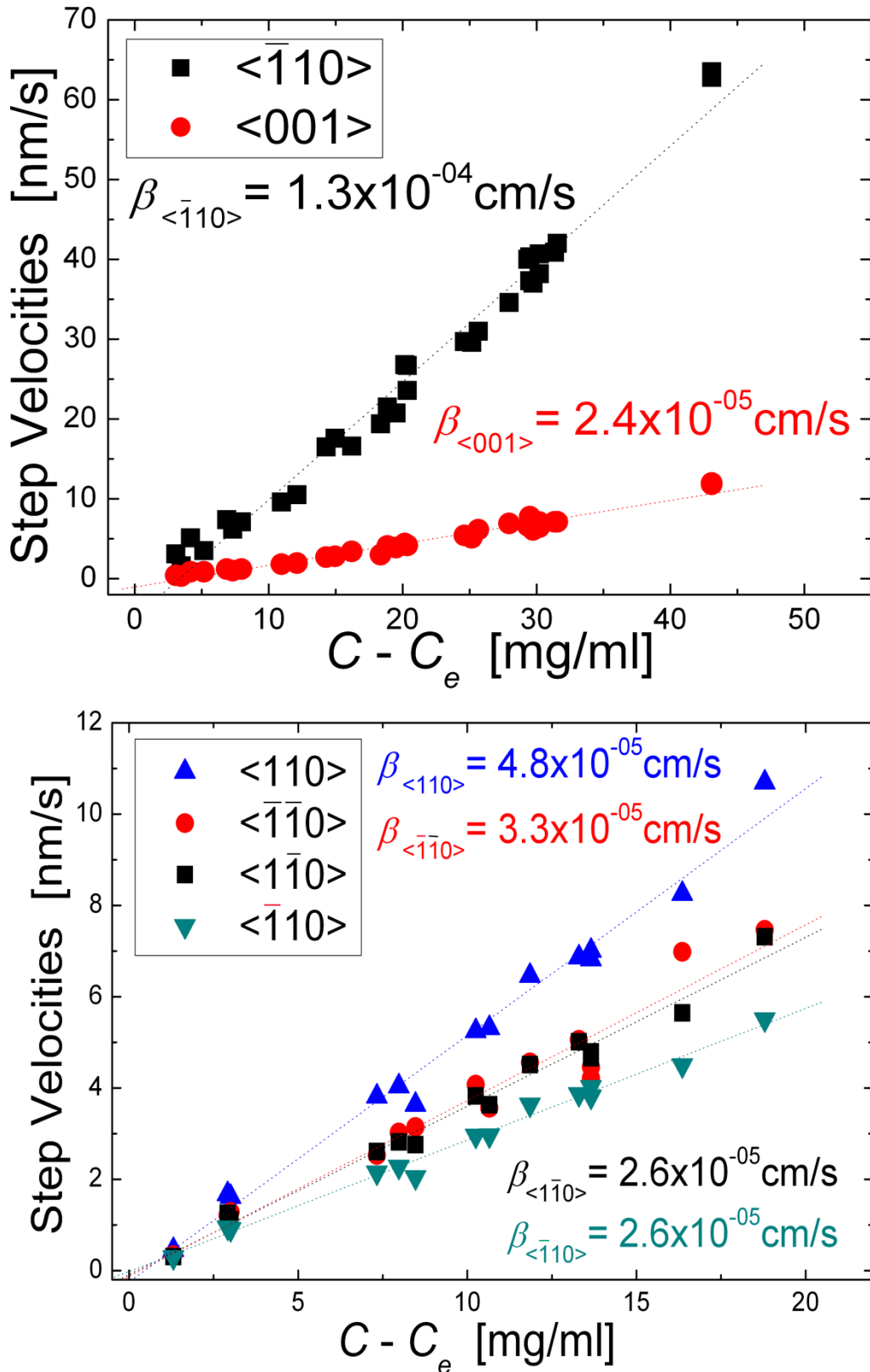


Figure 3.12. Determination of the kinetic coefficient for different crystallographic directions on the $\{110\}$ faces (a) and $\{101\}$ face (b).

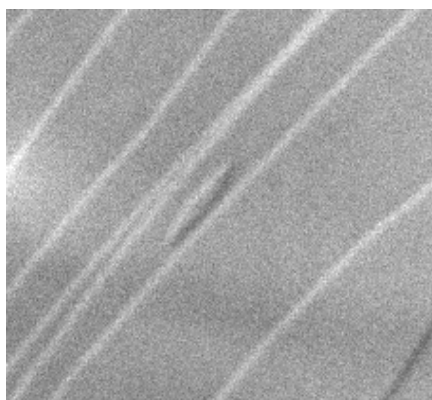
Before it was shown (Figure 3.8) that step velocities do not depend on temperature in the range of 20°C – 27°C and all data form one master curve. From these data the kinetic coefficient was determined. This parameter includes the term $\exp(-E/kT)$, where E is the activation energy barrier for the incorporation of molecules at a kink, k the Boltzman constant and T the absolute temperature (Chernov, 1984). At different temperatures, in principle, the probability by which molecules overcome the activation energy barrier should be different. Thus, the measurements under different temperatures includes step velocities measured with different $\exp(-E/kT)$. In our case, the results of the series of step velocities measured changing lysozyme concentration at four fixed temperatures are different when data are represented against the relative supersaturation. However, when data are plotted versus absolute supersaturation all data form one master curve. This indicates two fundamental aspects: (1) growth kinetics depend on absolute supersaturation and (2) under the studied temperature range the probability term $\exp(-E/kT)$ does not change significantly. Biomacromolecules are typically stable in a narrow range of temperature (~0-40°C) and until now there are no direct reliable measurements of the activation energy (Chernov, 2003). But from the obtained experimental data it can be estimated that the activation energy is relatively high.

3.3.3. Surface kinetics versus volume diffusion

The relative rates of mass transport and attachment kinetics determine how a crystal grows. Crystal growth can be divided into two consecutive steps: (1) first a molecule reaches the surface from the bulk solution and (2) than the molecule is incorporated into the crystal. Two distinct growth regimes can be observed depending on which step is rate-limiting. Between the two limiting growth regimes a smooth transition exist, called the mixed regime. When mass transport is rate-determining, molecules attach to the surface as fast as they arrive and the region adjacent to the surface is depleted in protein relative to the bulk. At the

other extreme, when attachment controls growth, mass transport maintains the protein concentration at the surface equal to the average protein concentration in the bulk. In case of growth from solution usually direct incorporation is considered, but in some cases surface diffusion can be significant.

From the analysis of step velocity dependency on supersaturation some indications can be found about the rate limiting step for tetragonal lysozyme growth. Tangential growth rates of macrosteps (multilayers) and growth spiral consisting of a number of layers were measured and compared with rates of single steps at different supersaturation conditions (Figure 4.11 and 4.13a). For steep macrosteps and spiral hillocks (see above), no



significant differences in their growth rates, compared with single steps, were found. The interstep distance of steps originating from spiral hillocks is in the range of 1 μm to tens of nanometers, depending on the supersaturation and the crystallographic orientation. In case of macrosteps interstep

distance is even smaller, typically lower than 100 nm. On the other hand the interstep distance of 2D islands can easily reach several micrometers. Even so, all steps velocities show the same dependency on supersaturation. These observations indicate that there is no significant overlap of diffusion fields surrounding steps of multilayer islands or spiral hillocks and that surface diffusions has no significant contribution to the step advancement. This suggests, indirectly, that lysozyme crystal growth, in the studied supersaturation range, is limited by the kinetics of incorporation rather than by surface or volume diffusion. This is also the case for thaumatin crystallization, a molecule of similar size as lysozyme (Malkin *et al.*, 1996). The fact that two-dimensional islands often form close to step edges provides further evidence that the supersaturation at a step edge is virtually the same as for a terrace.

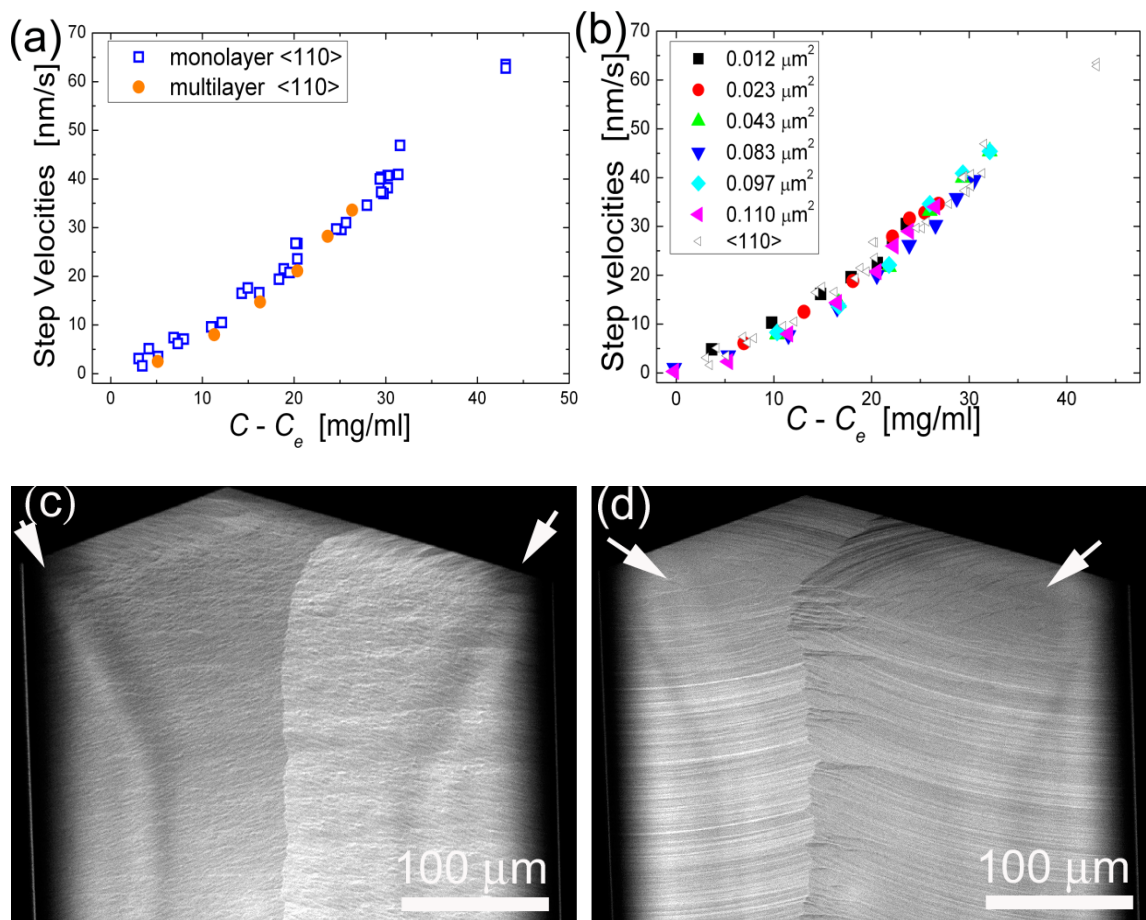


Figure 3.13. Step velocities as a function of layer height (a) and crystal size (b). (c) Growth at high supersaturation showing preferential nucleation at crystal corners (white arrows). (d) After lowering supersaturation the surface morphologies becomes more evident and large terraces appear on top of hillocks at the crystal corners (white arrows).

Additionally the influence of crystal size on step dynamics was studied. In Figure 3.13 step rates measured on 6 crystals of increasing size are shown. No significant differences in step velocity could be found, i.e. all data fit well with the master curve obtained earlier (gray open triangles). Berg effect (Berg, 1938), e.g. preferentially nucleation at crystal edges, was observed at high supersaturation levels, $C - C_e > 45 \text{ mg/ml}$. This indicates the existence of a depletion zone (\approx boundary layer) with a spherical symmetry which leads to higher nutrient concentrations at edges and corners of growing crystals than at facet centers. Berg effect was observed before by Vekilov and coworkers (1995) for tetragonal lysozyme crystals and explained quantitatively by numerical simulations (Lin *et al.*, 1996).

Pusey and coworkers (1986a, 1986b), argued, based on experimental results, that the growth of lysozyme crystals will always be limited by surface kinetics in normal gravity because convective transport is sufficient to supply solute to the growth interface as fast as it can be incorporated into the lattice. Also Grant and Saville (1991) showed by numerical simulation that natural convection is sufficient to maintain the surface concentration at the bulk level so that crystal growth is entirely kinetically controlled.

Kurihara (1998) measured depletion zones around growing tetragonal lysozyme crystals in observation cells with different heights, $h = 1.8\text{mm}$ and 0.15 mm . Results are reproduced in Figure 3.14. From these observations it becomes clear that width and depth of a depletion zone is reduced in case of natural convection inside the observation cell. Even so a boundary layer* still exist around the growing crystals where solute transfer is achieved by diffusion (Chernov, 1984). For the experiments performed for this work a free space ($600\text{-}850\text{ }\mu\text{m}$) was present between the top surface of the crystal and the cover glass, filled with solution. This was not the case for the experiments of Kurihara because crystal had approximately the same height as the observation cell. Surely the presence of this extra “free space” increased the convective flow, reducing the width and depth of the depletion zone even more. This idea is supported by the observation of Komatsu and coworkers (1993, 1994) who determined the concentration distribution around growing tetragonal lysozyme crystals (similar size as the ones used in this work) with an observation cell of 0.9mm height, and found that the depletion zone had a width of $170\text{ }\mu\text{m}$ and solute concentration at the surface only decreased 2%.

** The solute concentration also shows a gradient in this boundary layer and thus concentration at the solid/liquid interface will be smaller than the bulk concentration. In case of AFM experiments this boundary layer is homogenized by cantilever movement and therefore interface concentrations will be closer to bulk concentrations.*

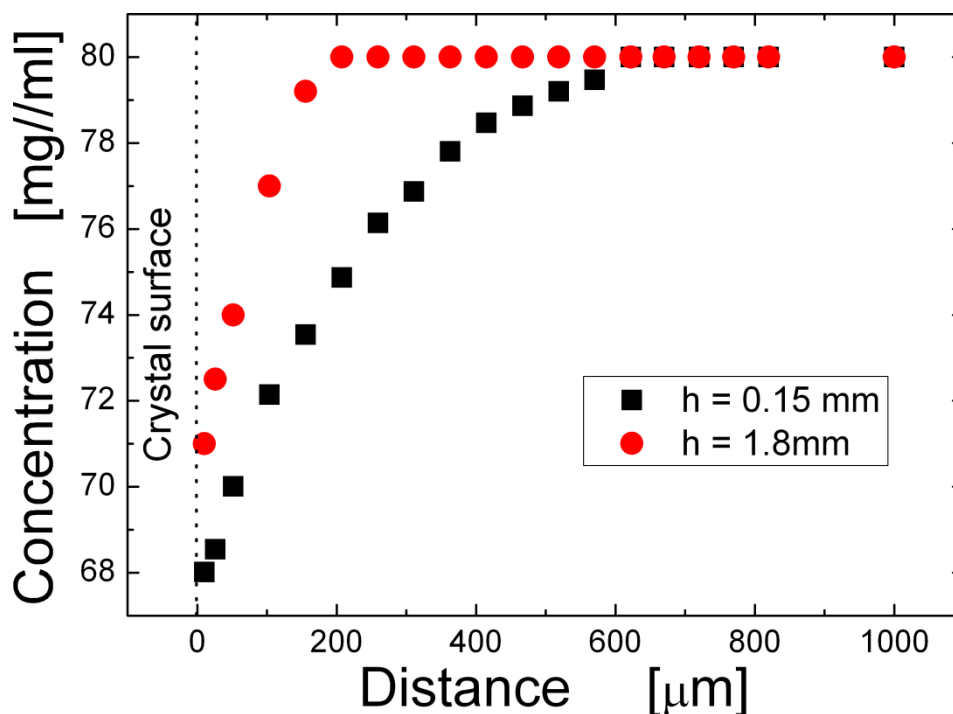


Figure 3.14 Concentration profiles around a growing tetragonal lysozyme crystal using different height cells. (Kurihara, 1998; Miyashita et al., 1998)

Thus by reducing the height of the observation cell convective flow is damped and the depth and width of the depletion zone is increased or vice versa. Therefore a new type of experiment was designed to study the possible influence of the observation cell geometry on the growth kinetics. The height of the observation cell (h) was changed from 2 mm to 0.25 mm. Step velocities were measured on crystals of similar size growing in cells with height of 2 mm, 1 mm, 0.5 mm and 0.25 mm (Figure 3.15). No significant difference was found between steps growing in convective conditions ($h = 2 \text{ mm}$) and those growing in reduced convection ($h = 0.25 \text{ mm}$). All data points coincide with the earlier shown mastercurve (measured in cell's with $h = 1 \text{ mm}$). Thus even if the depletion zone is larger around a growing crystal in conditions of reduced convection, the decrease in surface concentration is not enough to significantly lower the interface supersaturation and consequently step velocities on the growing crystals.

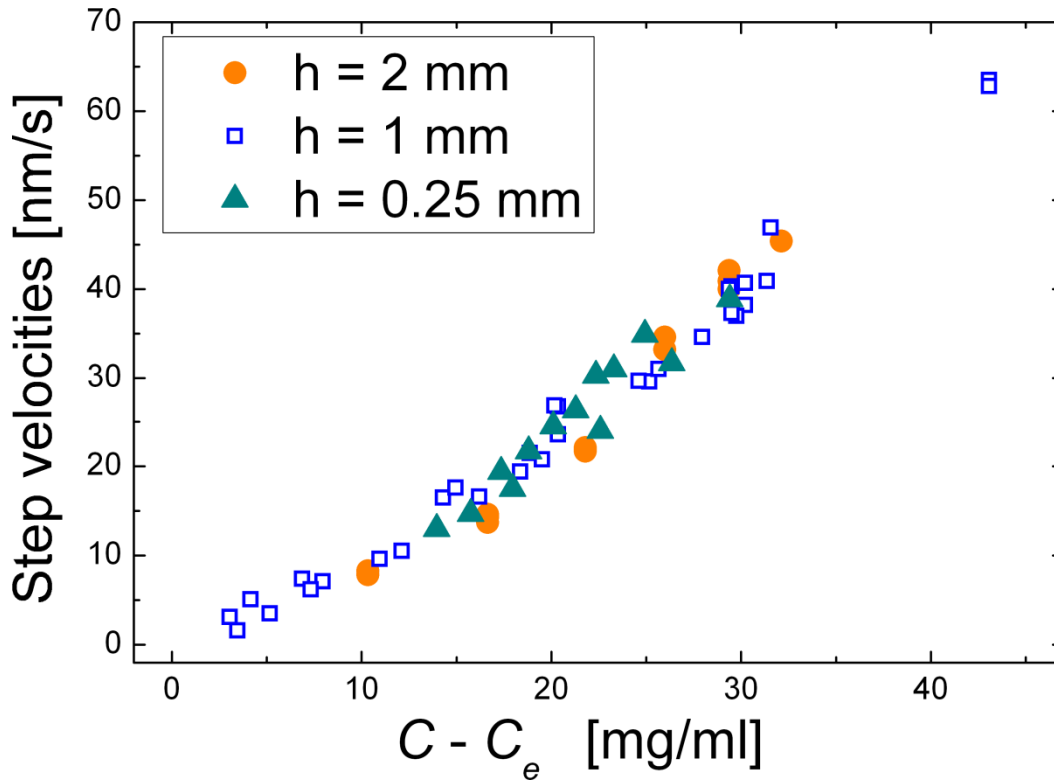


Figure 3.15 Step velocities as a function of supersaturation and as a function of the observation cell height.

Kurihara (1998) also measured depletion zones for tetragonal lysozyme crystals growing at different supersaturations. (Figure 3.16a). The cell height was 0.15 mm and crystals had the same height as the observation cell. In Figure 3.16b it is shown that the depletion width is increased with supersaturation but the depth is little affected. Thus besides the presence of natural convection also supersaturation has an influence on the dimensions of the depletion zone. When taking into account that observation where done for reduced convection (cell height was 0.15 mm) it can be deduced that depletion zones for larger cell's are even smaller, especially at low supersaturation.

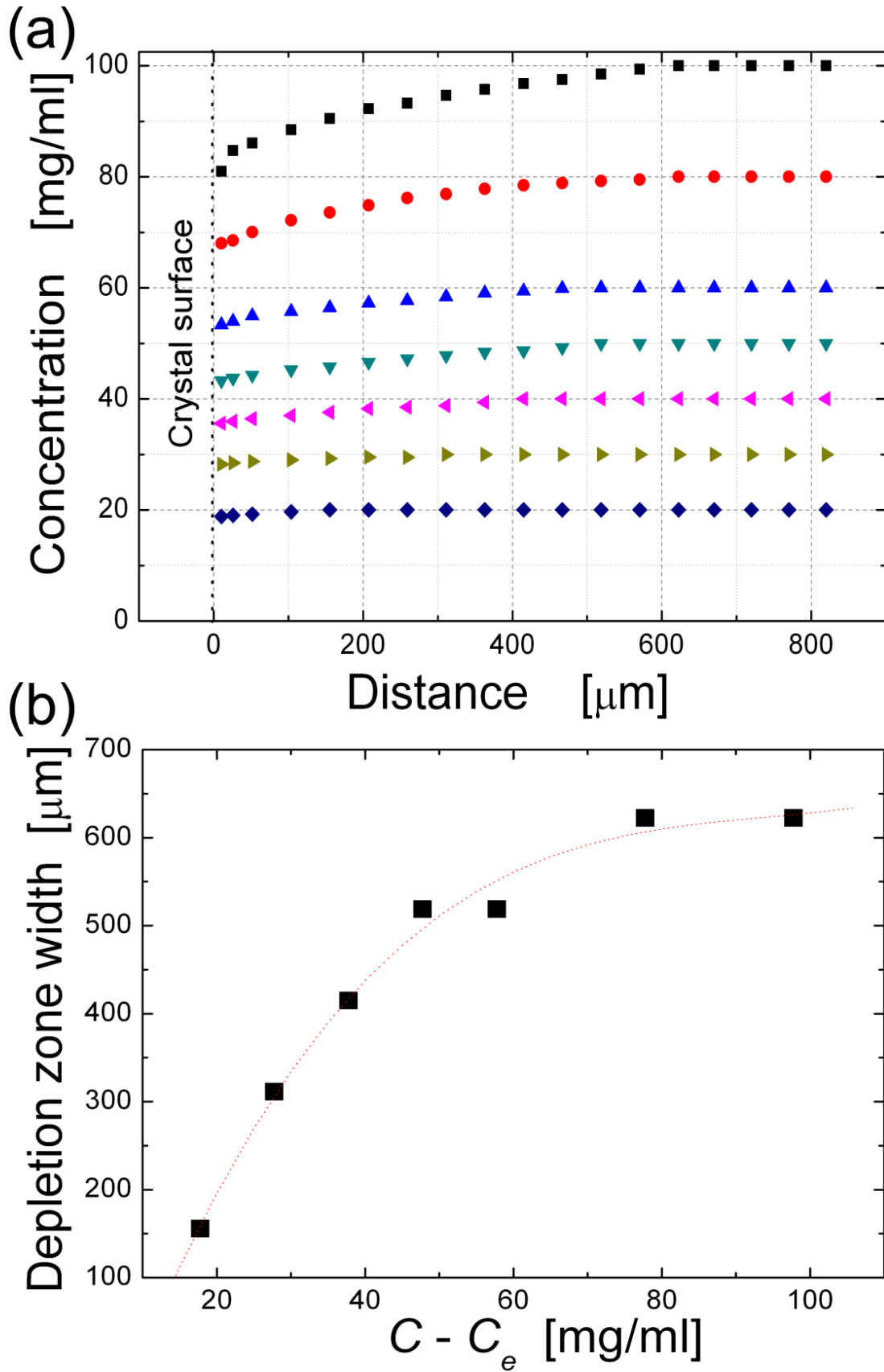


Figure 3.16 (a) Terrestrial concentration profiles around a growing tetragonal lysozyme crystal at different supersaturations. (b) Evolution of depletion zone width in function of supersaturation. (Kurihara, 1998)

The kinetic coefficient β is an aggregate measure of the kinetics of diffusion, adsorption, and incorporation of protein molecules with the rate-limiting step dominant. From all the previously shown observations it can be concluded, indirectly, that for lysozyme crystallization the process of incorporation of molecules into the growing crystal contributes most to the value of β in the studied supersaturation range of $C-C_e < 0.45$ mg/ml. But it was also shown that when determining the growth regime, i.e. rate determining step of a crystal it is important to account for the geometry of the observation cell, supersaturation range and crystal size. Thus when comparing experimental results these factors have to be considered. Actually, the best way to quantify the relative importance of bulk transport and interface kinetics in the growth process is by determining a dimensionless parameter k (often referred to as “kinetic Peclet number” in the literature). This number represents the ratio of the rate constants for incorporation kinetics and bulk transport in the form of

$$k = \beta_{st} h \delta / D \lambda \quad (3.6)$$

where β_{st} is the step kinetic coefficient, D is the solute diffusivity, and δ is a characteristic diffusion length, i.e. width of the boundary layer around the crystal which commensurate with crystal size (Chernov, 1984). Values of $k \ll 0.1$ or $\gg 1$ indicate purely kinetic or transport-controlled growth respectively. Intermediate values characterize mixed growth control.

To obtain a value of k for terrestrial growth a typical diffusion length of $\delta = 200 \mu\text{m}$ was chosen (Miyashita et al., 1994; Lin et al., 1995; Kurihara, 1998). The fact that the diffusion length changes with supersaturation will not be considered here. The Diffusion coefficient of lysozyme monomer is $D = 1.1 \times 10^{-6} \text{ cm}^2/\text{s}$. (Muschol and Rosenberger, 1995) and β_{st} values were obtained from fitting step velocities. The last variable is the interstep distance, which is a function of supersaturation in case of tetragonal lysozyme. Figure 3.17 shows the variation of the interstep distance on the $\{110\}$ face of 2D islands and spiral hillocks with increasing supersaturation.

In the case of spiral hillocks above the supersaturation of $C-C_e > 20$ mg/ml interstep distances could not be measured because they were beyond the lateral resolution of the LCM-DIM. Evolution of k as a function of supersaturation is shown in Figure 3.15b. k changes because interstep distance depends strongly on supersaturation, especially in the low to middle supersaturation range (0-45mg/ml). Probably at higher supersaturations the interstep distance reaches a constant value.

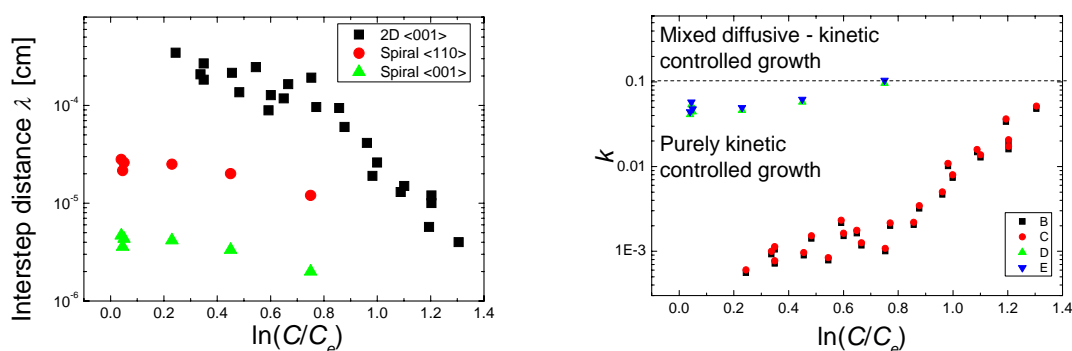


Figure 3.17 (a) Evolution of interstep distance in function of supersaturation for 2D nucleation growth and spiral growth. (b) Peclet number dependency on supersaturation for spiral growth and 2D nucleation growth.

For lysozyme, k values reflect kinetics-dominated growth for low to middle supersaturation levels, but at higher supersaturation levels lysozyme growth enters a mixed diffusive-kinetic regime. From earlier works it was already suggested that lysozyme growth is mainly kinetically controlled (Miyashita *et al.*, 1993; Miyashita *et al.*, 1994; Lin *et al.*, 1995; Vekilov *et al.*, 1995; Vekilov *et al.*, 1996; Vekilov and Alexander, 2000) but no relation was made with supersaturation yet. Thus, in terrestrial conditions the growth regime of lysozyme is determined by the supersaturation level; up to a certain supersaturation natural convection is able to maintain surface concentration constant at the crystal interface. At higher supersaturation levels, difference in surface concentration and bulk concentration becomes more significant, i.e. a larger depletion zone is formed) and consequently diffusion will contribute to the rate-limiting step.

It can be supposed that in conditions of microgravity, i.e. purely diffusive media, the rate limiting step will be dominated by diffusion then in the terrestrial case. It was experimentally shown that a stable, and large, depletion zone is formed around growing crystals in microgravity (Otalora *et al.*, 2001). When dealing with a stagnant solution a quasi-steady-state formulation is applied (Chernov, 1984). This model also contains a dimensionless parameter

$$k = \frac{\beta R}{D} \quad (3.7)$$

where R is the radius of the crystal (assumed to be spherical), D is the diffusion coefficient of the growth units in solution and β is the kinetic coefficient of growth from solution. β and β_{st} are related by $\beta = p\beta_{st}$ where p is the slope from the direction of the singular face. Also here the parameter k is a function of the ratio of surface incorporation rate to the bulk transport rate, the slower one being the rate controlling process and hence $\beta R/D \ll 1$ reflects a kinetic growth regime and $\beta R/D \gg 1$ a diffusion controlled regime, both separated by a mixed regime. In microgravity the relative importance of surface kinetics and bulk diffusion were studied for tetragonal lysozyme growth (Otalora *et al.*, 2002) and a value of $k=0.9$ was found corresponding to a mixed growth regime.

From these results it can be argued that for an increase of bulk-transport contributions to growth rate control under reduced gravity no improvement in the structural perfections should be expected for tetragonal lysozyme crystals. This corresponds to the results for space-grown lysozyme crystals from high purity lysozyme solution (<0.3% impurities) compared to ground-grown crystals (Broutin *et al.*, 1997). Exceptions observed in earlier tests with lysozyme (Snell *et al.*, 1995) may be due to reduced impurity supply in the absence of convection in space (Carter *et al.*, 1998) and/or the lack of sedimentation (DeLucas *et al.*, 1986).

3.3.3. Step fluctuations

In the case of lysozyme, a multitude of papers have reported under constant growth conditions, step velocity fluctuations up to a 100% (Rosenberger *et al.*, 1996; 1999; Vekilov and Alexander, 2000; Vekilov and Rosenberger, 1998a;1998b;1998c; Vekilov *et al.*, 1995b; 1996; 1997; 1998, 1999). These fluctuations are reported for low supersaturation (e.g. $\sigma = \ln(C/C_{eq}) = 0.41$) and high supersaturation conditions (e.g. $\sigma = 2.84$) (Vekilov *et al.*, 1996), for spiral growth (Vekilov and Rosenberger, 1998a; Vekilov *et al.*, 1998; 1999) and 2D-island growth of the birth-and-spread type (Vekilov *et al.*, 1996). The authors argued that the fluctuations are a consequence of the coupling of bulk transport with nonlinear interface kinetics and that the fluctuations are intrinsic (Vekilov *et al.*, 1996; Vekilov *et al.*, 1999). Therefore, step velocities directly measured *in situ* with LCM-DIM were analyzed for this type of fluctuations. From *in situ* observations of step advancement time-space plot are obtained for the tangential growth of specific 2D islands or growth hillocks. Such plots represent step advancements as a function of time and the movement of the step front is clearly imaged (Figure 3.18). These time-space plot are obtained by extracting the pixels of a specific line (white line in Figure 3.18a) along which the step advancement is followed. Intensity values of pixels from this line in the first image are transferred into the first row of a new image; the pixels from the second image are put into the second row and so on, until a complete time-space plot is created. Besides these time-space plots, step velocities were also measured independently at certain time intervals (Figure 3.18c).

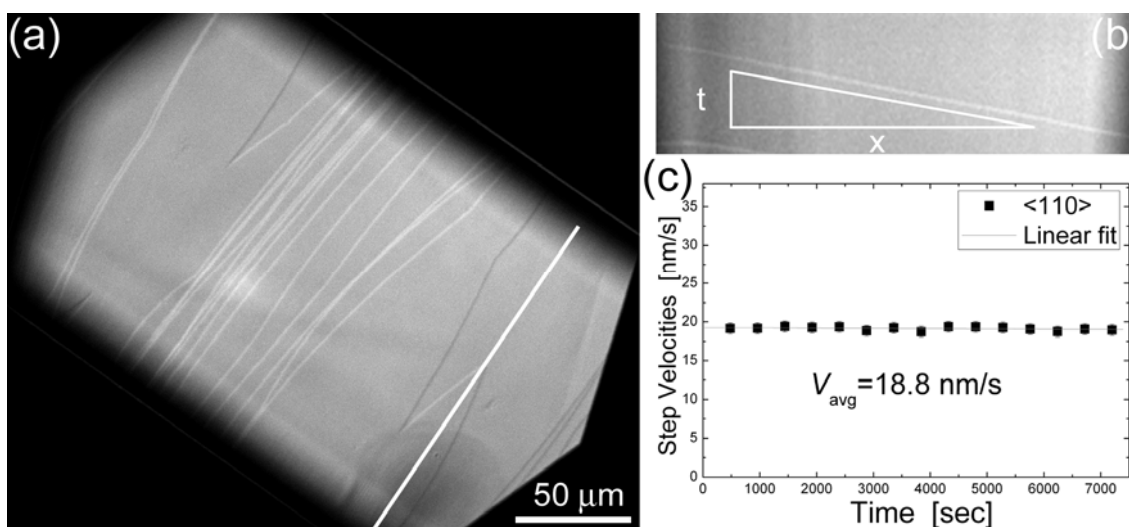


Figure 3.18: Analysis of step velocity. (a) Photomicrograph of a $\{110\}$ face covered with 2D-island steps. (b) A time-space plot composed of extracted pixels along the white line of the image at $t=0$. (c) Step velocity measured at constant time intervals.

In Figure 3.18 the growth of a monolayer 2D island is shown. Along the white line shown in Figure 3.18a along the $\langle \bar{1}10 \rangle$ direction, a time-space plot was constructed (Figure 3.18b) and no fluctuations of the step front are observed. During the experiment temperature was maintained constant ($T=23.9^\circ\text{C}$), and supersaturation was $C-C_e=17.9 \text{ mg/ml}$. The averaged calculated step velocity was 18.8 nm/s and no significant deviations are detected, i.e. all measurements are within the experimental errors and nicely fitted by a straight line (Figure 3.18c). In Figure 3.19 the time-space plot of the birth and spread of a new island is shown. The island spreads with equal velocity, $v = 8.7 \text{ nm/s}$, into the positive and negative $\langle -110 \rangle$ direction, and no change of step velocity is found over the entire range. Also here the line representing the step front does not show any kind of detectable fluctuations. The same observations were made for the $\langle 001 \rangle$ direction ($v = 1.4 \text{ nm/s}$, Figure 3.19). Analyses of step velocities, at constant supersaturations, on $\{101\}$ faces did also not show any significant fluctuations.

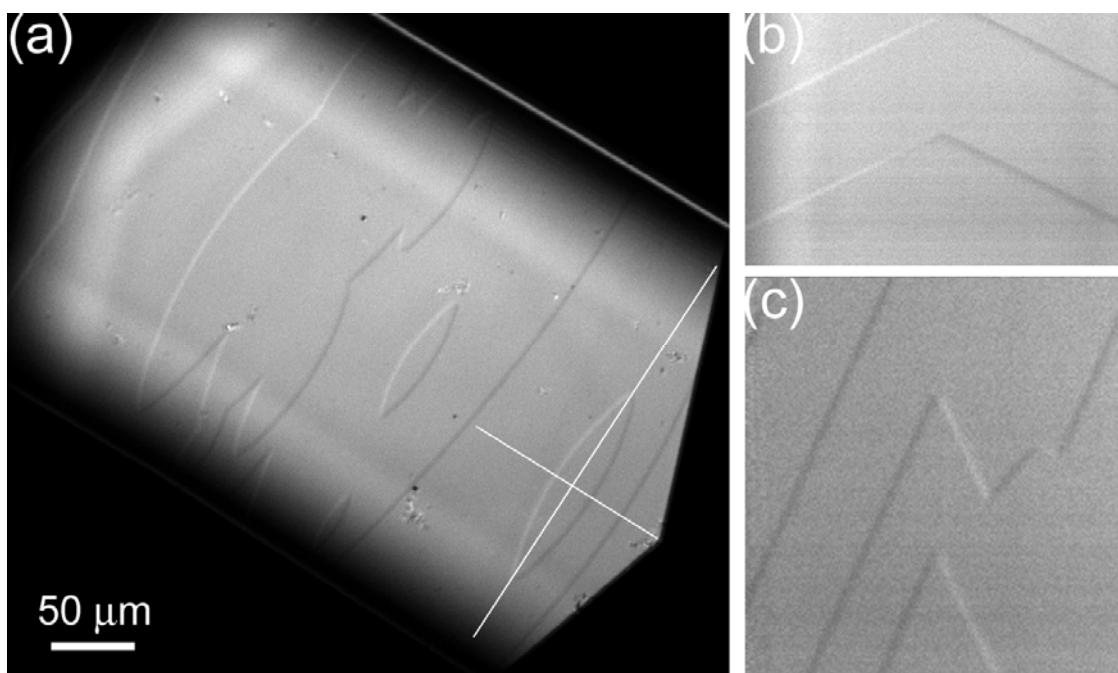


Figure 3.19 Constant step velocities of 2D-islands. (a) $\{110\}$ surface with islands of molecular height, (b) time-space plot into the fast growing $\langle -110 \rangle$ direction and (c) time-space plot into the slow growing $\langle 001 \rangle$ direction. ($T^a=18.4^\circ\text{C}$, $C-C_e= 9.9 \text{ mg/ml}$)

The time evolution of step advancement for spiral hillocks at constant supersaturation was also analyzed. In Figure 3.20 a spiral hillock is shown which has been growing several intervals at different temperatures, i.e. different supersaturations, this produced along the slopes of the hillock areas with different interstep distances (arrows in Figure 3.20a). Even so, once the hillock is growing at constant supersaturation all steps are advancing at a constant velocity (traces of individual and bunched steps – the dark lines in the time-space plot – are straight without any visible irregularities). Following one step over a time period of 4000 s (Fig 2c), no deviation from the average step velocity ($v_{\langle -110 \rangle} = 24.1 \text{ nm/s}$, $v_{\langle 001 \rangle} = 4.0 \text{ nm/s}$) is detected, except for a bright area visible in the time-space plot (white arrows Figure 3.20b,c). This bright area corresponds with the failure of the air-conditioning in the laboratory which resulted in a slight temperature increase and thus slightly lower supersaturation. As a consequence step velocity decreased*. This indicates that steps react fast to changes of supersaturation, and therefore, temperature fluctuations, in the case of lysozyme, can induce step velocity fluctuations. It is obvious that a good

temperature control, at least 0.1°C, is absolutely necessary when studying growth kinetics of tetragonal lysozyme crystals.

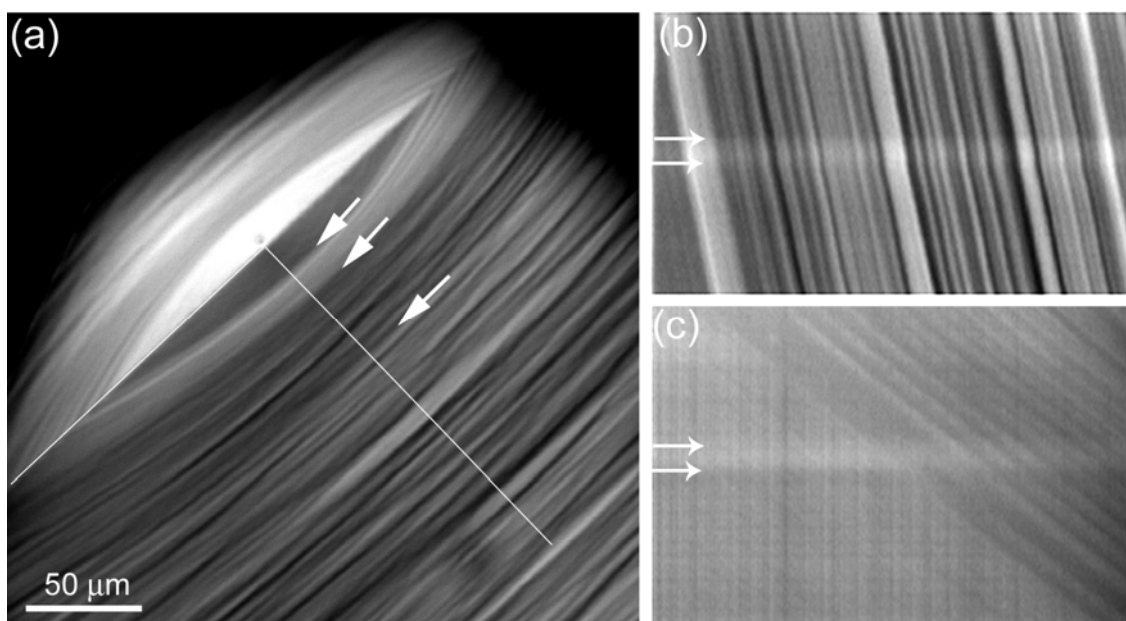


Figure 3.20 Spiral growth at low supersaturation, {110} face. (a) LCIM image of a section of the crystal surface. (b) Time-space plot along the <-110> direction. (c) Time-space plot along the <001> direction. (T = 24.0°C, C - C_e = 20.2mg/ml).

From the analysis of these experimental observations it can be concluded that step advancement of 2D islands and spiral hillocks on both faces is constant. These results are in clear contradiction to those published by Vekilov and coworkers for tetragonal lysozyme crystals (Rosenberger *et al.*, 1996; 1999; Vekilov and Alexander, 2000; Vekilov and Rosenberger, 1998a; 1998b; 1998c; Vekilov *et al.*, 1995b; 1996; 1997; 1998; 1999). These above cited reports about step fluctuations are all based on interferometry measurements (even the ones for the analysis of 2D-island growth by the birth-and-spread mode) and individual steps were not resolved.

Step velocities from interferometry measurements can be obtained by applying (Chernov, 1984)

$$v_{\text{step}} = R/p \quad (3.8)$$

*Because of the temperature shift in the laboratory, the focus depth of the lens is also slightly shifted resulting in a brighter imaged. This demonstrated that the confocal system is relatively sensitive for temperature changes which is a good qualitative indicator of temperature stability during the experiments.

where p is the slope of the hillock and R the normal growth rate. But, the use of the surface slope for the analysis of step velocities is restricted to spiral growth and cannot be applied to 2D-island growth by the birth-and-spread mode (see Chernov, 1984). Analysis of step velocities according to this relation is only valid, if the local slope is constant. Variations of the local slope can originate from step bunching or any kind of variations of supersaturation or temperature. If the local slope is not constant, slope values will be correlated to inaccurate normal growth rates and artificial fluctuations of the step velocity result. A more detailed discussion on the use of the slopes for calculating step velocities from interferometry data is given by Dold and coworkers (2007). Variations of the local slope induce artificial fluctuations of the calculated step velocity, which might exceed the average value by 100% and more. Thus for an accurate measurement of step velocities, either the slope of a hillock has to be constant or single steps have to be observed directly.

The observations made for this work put in serious doubt the theory of intrinsic instabilities of layer growth dynamics of tetragonal lysozyme crystal growth proposed by Vekilov and coworkers for crystals growth under steady solution conditions.

3.4. Impurity effect on growth step kinetics

3.4.1. Introduction

In order to grow protein crystals of high quality, it is indispensable to clarify the effects of impurities, since impurities can significantly affect the growth kinetics (Vekilov and Rosenberger, 1996; Hirschler and Fontecilla-Camps, 1997; Judge *et al.*, 1998; Thomas *et al.*, 1998a; 1998b; Matsui *et al.*, 2006; Sasaki *et al.*, 1994; Burke *et al.*, 2001; Nakada *et al.*, 1999; Van Driessche *et al.*, 2007), morphology (Abergel *et al.*, 1991; Hirschler and Fontecilla-Camps, 1996; Ewing *et al.*, 1996; Bhamidi *et al.*, 1999) and hence quality of protein crystals (Dobrianov *et al.*, 1999; Caylor *et al.*, 1999; Carter *et al.*, 1999; Snell *et al.*, 2001; Robert *et al.*, 2001; Yoshizaki *et al.*, 2004; Moreno *et al.*, 2005; Yoshizaki *et al.*, 2005). Generally, impurities are considered to exhibit their effects on the growth of a crystal after they adsorb on the crystal surface. Thus, to fully understand the mechanisms of impurity effects it is necessary to observe *in situ* both 1) dynamics of elementary steps and 2) adsorption of impure molecules on a crystal surface, at a molecular level. Only one such observation was so far carried out by atomic force microscopy (AFM). Nakada and coworkers (1999) observed elementary growth steps and individual molecules of covalently-bonded dimer of lysozyme (hereafter dimer) at the same time, on a {101} face of a tetragonal lysozyme crystal. They revealed that dimer molecules adsorb randomly on terraces and suppress the advancement of elementary growth steps. The relation between adsorption of impurities and their effects on step dynamics has to be studied thoroughly to obtain better general understanding on impurity effects.

At present, the most popular technique for molecular level *in situ* observation of surface morphology and growth kinetics of protein crystals is

AFM (Malkin *et al.*, 1999; McPherson *et al.*, 2001; McPherson *et al.*, 2003). However, since the scan of a cantilever stirs the concentration-depleted zone in the vicinity of a growing crystal surface, AFM tends to overestimate step velocities. Thus non-invasive observation techniques are much more appropriated for growth kinetics measurements as was already discussed in section IV.1. Optical microscopy is an excellent alternative and both LCM-DIM and phase shift interferometry have been applied to observe advancement of elementary growth steps on growing protein crystals and observe the effect of impurities on surface processes.

To observe individual impure molecules on a crystal surface, a single-molecule visualization (SMV) technique (Funatsu *et al.*, 1995; Wazawa *et al.*, 2005) was adopted, by which one can track the movement of individual molecules of fluorescent-labeled proteins. So far a SMV of a thin-solution-layer type was devised for the observation at the crystal-solution interface. It was reported that the diffusion of fluorescent-labeled lysozyme (F-lysozyme) molecules diffuse at the interface four orders of magnitude slower than in a bulk solution due to the strong interactions (Sazaki *et al.*, 2007). In addition, the transient processes during the adsorption of F-lysozyme molecules on {110} face of tetragonal lysozyme crystals were measured (Dai *et al.*, 2007).

In this study, LCM-DIM and SMV of the thin-solution-layer type was used to observe elementary growth steps on {110} faces of tetragonal crystals and fluorescent-labeled protein molecules adsorbed on the {110} faces simultaneously. As impure proteins, F-lysozyme, dimer and 18kDa protein (the last two are major impurities of Seikagaku lysozyme (Thomas *et al.*, 1996)), were used for the observation of impurity effects on dynamics of elementary growth steps. F-lysozyme and fluorescent labeled dimer (F-dimer) were used for the observation of adsorption sites on crystal surfaces. From these observations, it was tried to clarify the relation between effects of the impure proteins on the advancement of elementary steps and

adsorption sites of impurities on the crystal surfaces. Using phase shifting Michelson interferometry dynamics of single and bunched step were observed and the influence of impurities on the process of step bunching studied. Finally the influence of impure proteins present in commercial lysozyme on step morphology and growth kinetics was also investigated.

3.4.2. Step morphology

The impurity effects of F-lysozyme, dimer, 18kDa and impurities included in Seikagaku lysozyme (98.5% purity) on the morphology of elementary 2D islands on {110} faces of tetragonal lysozyme crystals were observed *in situ* by LCM-DIM. As shown in Figure 3.21, 2D islands formed in a 99.99% pure solution (Figure 3.21a) are lens-shaped with sharp tips. This shape results from an intrinsic anisotropy in the step velocity, being $\langle 001 \rangle$ the slow direction and $\langle \bar{1}10 \rangle$ the fast direction. The ratio of fast to slow directions is ~ 6 . In contrast, when pure lysozyme solution was intentionally contaminated with F-lysozyme, dimer or 18kDa 2D islands exhibit rounded tips (Figures 3.21b-d, f). The same behavior was observed for Seikagaku lysozyme solution (Figure 3.21e). Their ratios of fast to slow directions become significantly smaller, 3-5, than that in the 99.99% purity solution. These results clearly indicate that the growth in the fast direction is more affected by impurities than that in the slow direction. This was also observed by Dold and coworkers (2006) for tetragonal lysozyme crystals growing from Seikagaku solution. Thus, the impurity effects on step velocities were studied in the fast growing $\langle \bar{1}10 \rangle$ direction.

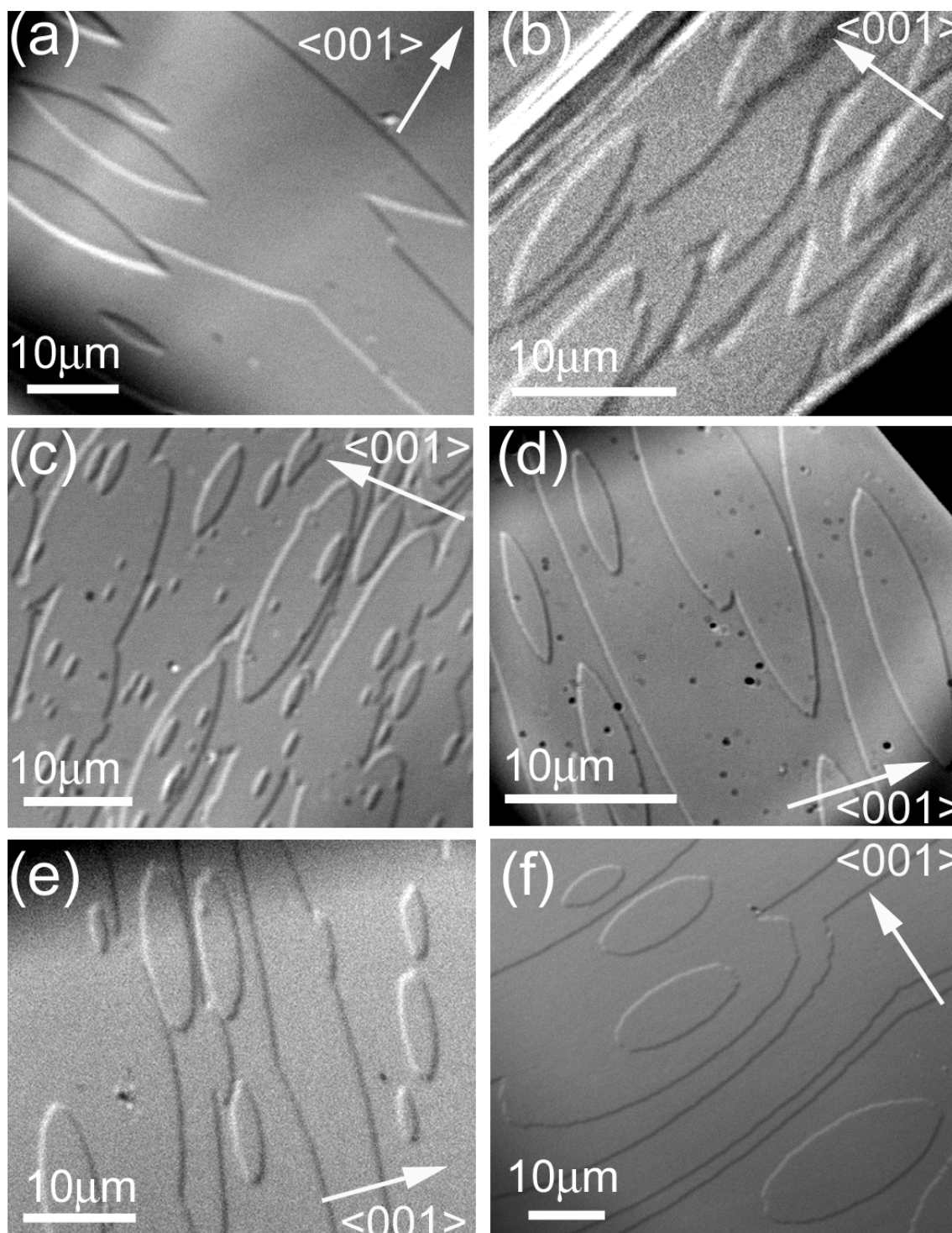


Figure 3.21 Photomicrographs of 2D islands on $\{110\}$ faces of tetragonal lysozyme crystals taken by LCM-DIM. Impure proteins added intentionally: (a) none, (b) 0.1 wt% F-lysozyme, (c) 0.5 wt% dimer, (d) 1.0 wt% 18kDa, and (e) 0.5 wt% dimer and 1.0 wt% 18kDa. In (f), a crystal was grown from Seikagaku lysozyme (98.5% purity) is shown.

In Figure 3.21, 0.1 wt% F-lysozyme (b) shows weaker effects on the step morphology (less rounded 2D islands) than 0.5 wt% dimer (c) and 1.0

wt% 18kDa (d), probably because of the lower concentration (0.1 wt% was the maximum concentration of F-lysozyme available for the experiments). In addition, the solution containing both 0.5 wt% dimer + 1.0 wt% 18kDa (e) presents stronger effects on the step morphology than those of 0.5 wt% dimer (c) or 1.0 wt% 18kDa (d), because of the larger amount of impure proteins. However, note that Seikagaku lysozyme (f), which contains mainly 0.5 wt% dimer and 1.0 wt% 18kDa as impurities (Thomas *et al.*, 1996), shows significantly stronger effects (more rounded 2D islands) than the 99.99% pure lysozyme with intentionally added 0.5 wt% dimer and 1.0 wt% 18kDa (e). These results indicate that trace amounts of other impurities included in Seikagaku lysozyme (Thomas *et al.*, 1996; 1998b) may play an important role.

3.4.3. Impurity effect on step velocities

Since the growth of elementary 2D islands in the fast direction ($\langle\bar{1}10\rangle$) was more affected by impurities than in the slow direction ($\langle 001\rangle$), step velocities in the fast direction were measured by LCM-DIM. Experiments were done with and without impure proteins under various supersaturations. Figure 3.22 presents changes in step velocity as a function of supersaturation. As shown in Figure 3.22, even in the case of the 99.99% purity solution without any impurities added intentionally (solid squares), the step velocity vs. supersaturation plot shows a slightly concave shape, in particular under a low supersaturation range. This result indicates that the impurity concentration smaller than 0.01 wt% maybe affecting the step velocity of lysozyme crystals. It was reported previously that impurities of very low concentration also significantly affects 2D nucleation rates under a low supersaturation range (Van Driessche *et al.*, 2007). Figure 3.22 also demonstrates that all three impure proteins decreased the step velocity, as well as the case of Seikagaku lysozyme. In particular, the suppression of the step velocity by 18kDa and impurities included in Seikagaku lysozyme (mainly 0.5% dimer and 1% 18kDa) are significant. With increasing

impurity concentration, the suppression of the step velocity increased, and the shape of the plots became more concave. Although the effects of dimer on the growth kinetics of $\{110\}$ and $\{101\}$ faces of tetragonal lysozyme crystals have already been reported (Nakada *et al.*, 1999; Yoshizaki *et al.*, 2004; 2005), this is the first time the impurity effects of 18kD on the growth kinetics of tetragonal lysozyme crystals is studied.

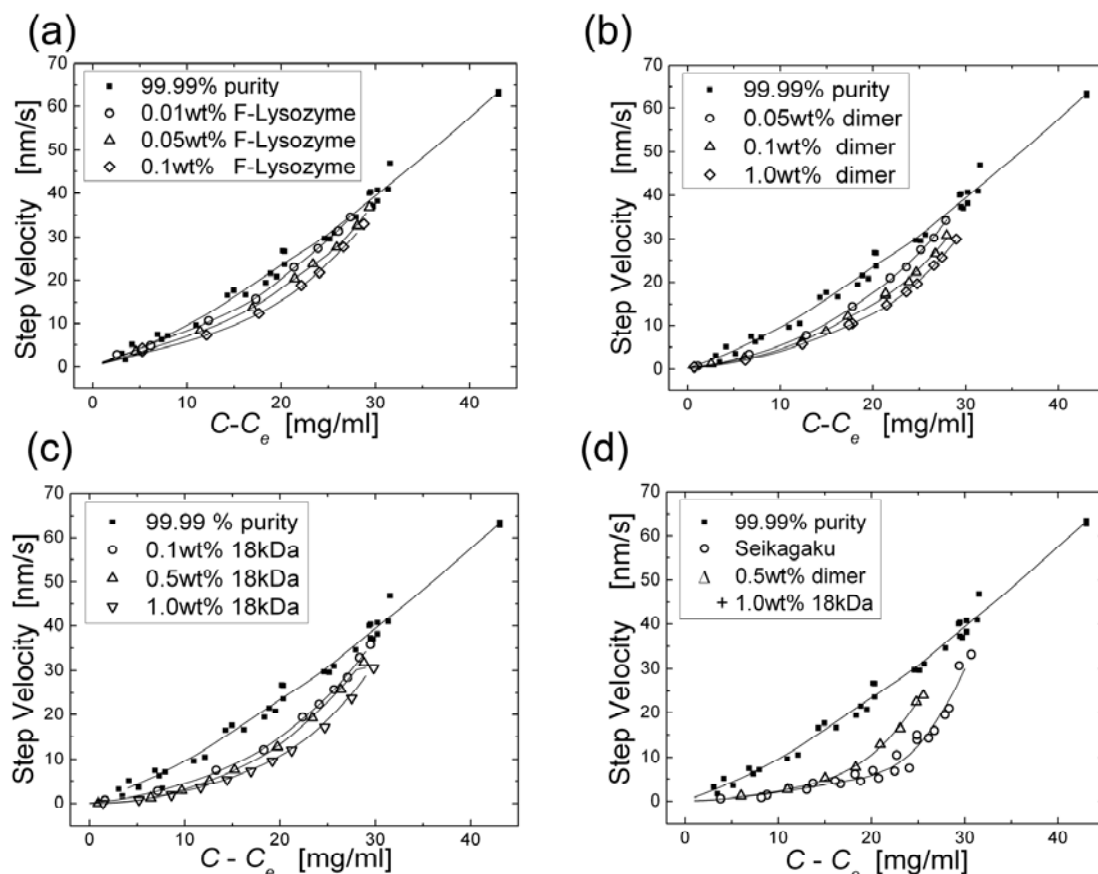


Figure 3.22 Step velocities in $\langle 110 \rangle$ directions measured on $\{110\}$ faces of tetragonal lysozyme crystals under various supersaturations and impurity concentrations by LCM-DIM. All crystals were grown under 99.99% pure lysozyme of 40 mg/ml. Impure proteins added intentionally: (a) 0.01-0.5 wt% F-lysozyme, (b) 0.01-1.0 wt% dimer, (c) 0.1-1.0 wt% 18kDa, and (d) 0.5 wt% dimer and 1.0 wt% 18kDa. In (d), the result of Seikagaku lysozyme (98.5% purity) is also plotted. The data points were fitted using a local polynomial regression (dotted curves).

As shown in Figure 3.22d, Seikagaku lysozyme (open circles) exhibits the strongest suppressions of the step velocity and hence the strongest impurity effects, under the experimental conditions adopted in this study.

To simulate Seikagaku lysozyme 0.5 wt% dimer and 1.0 wt% 18kDa together with 99.99% pure lysozyme were used however the suppression of this solution (open triangles) was not as strong as that observed with Seikagaku lysozyme. This result implies that trace amount of other impurities present in Seikagaku lysozyme contribute to the larger suppression of the step velocity.

To evaluate the effects of these impure proteins quantitatively, the ratio, R , of the step velocity in the 99.99% pure lysozyme solution, V_{pure} , to the step velocity in the solutions containing impurities, $V_{\text{F-lysozyme}}$, V_{dimer} , $V_{18\text{kDa}}$ and $V_{98.5\% \text{ purity}}$, at the same supersaturation was calculated. The ratio R corresponds to the amount of the suppression of the step velocity by impurities. When the value of the ratio R becomes unity, there is no suppression of the step velocity by impurities. To calculate the ratio R at the same supersaturation, all the experimental data shown in Figure 3.22 were fitted with local polynomial regression (LOESS: Cleveland, 1979; Cleveland and Devlin, 1988). The solid curves in Figure 3.22 show that the fitting curves represent well the supersaturation dependencies of the step velocity. Using the values obtained from the curve fitting, the ratio R at the same supersaturation was calculated (Figure 3.23). Since in Figure 3.22 the typical error in the step velocity measurement at one supersaturation was about 1% for 99.99% pure lysozyme and 3% for Seikagaku lysozyme, the step velocity measurement was accurate enough. Hence, the error of the ratio R mainly came from the local polynomial regression. The errors shown in Figure 3.23 were calculated from the standard error (90% statistical significance) and the propagation of errors.

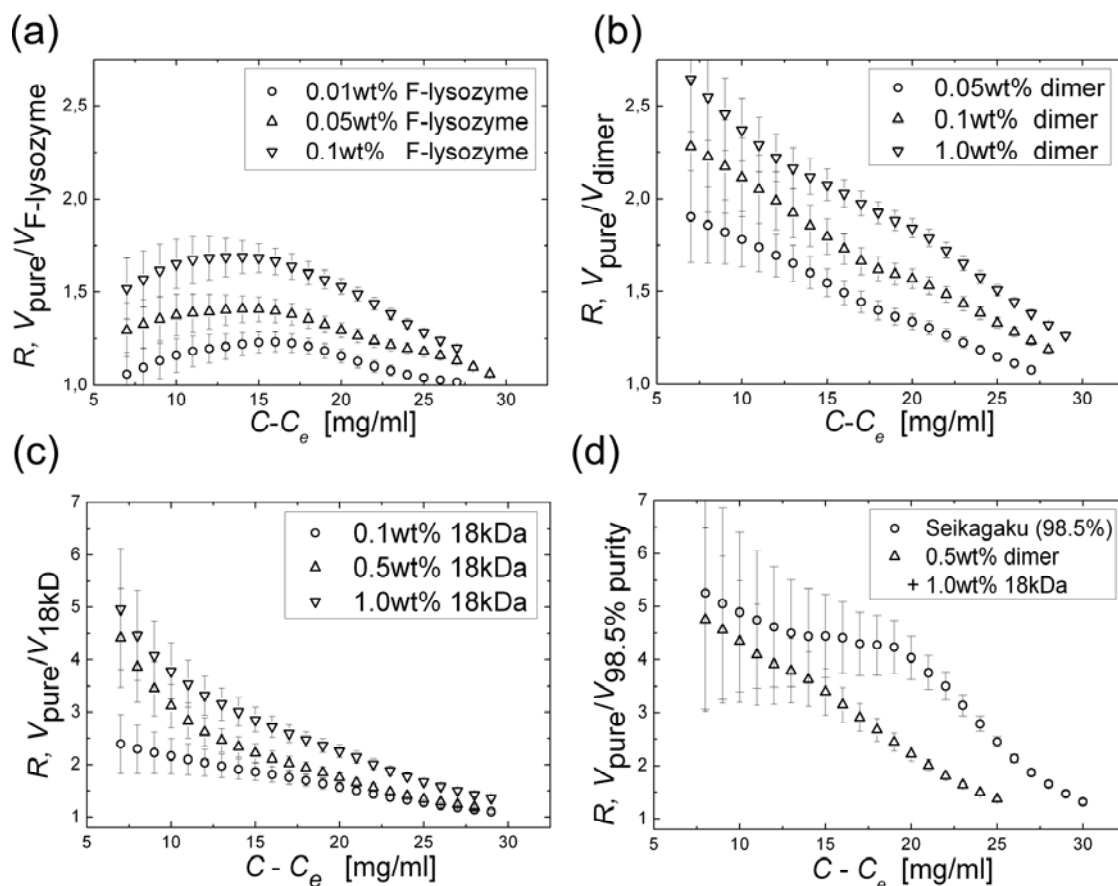


Figure 3.23 Changes in the ratio R of the step velocity in a 99.99% purity solution, $V_{purified}$, to that in the solution containing impurity, $V_{F-lysozyme}$, V_{dimer} , V_{18kD} and $V_{98.5\%}$ purity as a function of supersaturation. All crystals were grown under 99.99% pure lysozyme of 40 mg/ml. Impure proteins added intentionally: (a) 0.01-0.5 wt% F-lysozyme, (b) 0.01-1.0 wt% dimer, (c) 0.1-1.0 wt% 18kDa, and (d) 0.5 wt% dimer and 1.0 wt% 18kDa. In (d), the result of Seikagaku lysozyme (98.5% purity) of 40 mg/ml was also plotted. C is a solute concentration and C_e the solubility. Other growth conditions: 25 mg/ml NaCl, in 50mM sodium acetate buffer (pH 4.5), at 18.0-26.0°C.

As shown in Figure 3.23, the value of ratio R increases with increasing impurity concentration for all three impure proteins. However, note that different impure proteins have different R values and show different shapes of the R vs. supersaturation plots. Taking into account the large error of the ratio R in a low supersaturation range (in particular, $C - C_e < 10$ mg/ml), the differences in the values and shapes of the R vs. supersaturation plots are still significant. In the case of F-lysozyme (Figure 3.23a), the R vs. supersaturation plots show a convex shape, and have maximum values in the supersaturation range of 12-17 mg/ml. In contrast, the R vs. supersaturation plots of dimer and 18kDa (Figure 3.23b and c)

exhibit a concave shape, and decrease monotonically with increasing supersaturation. In addition, the R values of 18kDa are remarkably larger than those of F-lysozyme and dimer all through the supersaturation range, suggesting the necessity to pay more attention on 18kDa, because the effect of 18kDa has not been considered to be important. In the case of Seikagaku lysozyme (Figure 3.23d), the R vs. supersaturation plot shows a more complex shape: a significant shoulder is observed around a supersaturation of 18 mg/ml. Furthermore, the solution containing 0.5% dimer and 1.0% 18kDa with 99.99% pure lysozyme could not reproduce the plot of Seikagaku lysozyme, as explained in Figure 4. For a same impurity the shape of R vs supersaturation plots does not change with increasing impurity concentration this indicates that the impurity incorporation mechanism stays the same for different impurity concentrations. It is emphasized that different impure proteins show different shapes and values of the R vs. supersaturation plots.

3.4.4. Adsorption sites of impure proteins

To clarify the cause of the different dependencies of the ratio R on supersaturation shown in Figure 3.23, the adsorption sites of the impure proteins on the crystal surface were observed by SMV of the thin-solution-layer type (Sazaki *et al.*, 2007; Dai *et al.*, 2007). Observations of adsorption sites of F-lysozyme and F-dimer molecules on {110} faces of tetragonal lysozyme crystals were carried out as follows. The observation cell used for SMV observation (Fig. 1c) was prepared according to the recipe reported in previous work (Sazaki *et al.*, 2007; Dai *et al.*, 2007). Lysozyme concentration used for the observation was 27 mg/ml, at which the growth of elementary steps was negligibly small at 24.5°C. Individual molecules of F-lysozyme and F-dimer (both used in a concentration of 0.01 nM) were observed *in situ* on {110} faces of the crystals by SMV. Before and after the SMV observation, the same field of view was observed by LCM-DIM to check if steps had moved during SMV observation (the step movement was negligible). From

the comparison between the images taken by LCM-DIM and SMV, adsorption sites of F-lysozyme and F-dimer could be determined.

With respect to the adsorption of F-lysozyme on the {110} faces of tetragonal lysozyme crystals, Dai and coworkers (2007) recently reported that F-lysozyme molecules adsorb preferentially on steps rather than terraces. Figure 3.24a shows a typical single-molecule image: one bright dot corresponds to one F-lysozyme molecule adsorbed on the crystal surface. Figure 3.24b represents the same field of view observed by LCM-DIM, showing bunched steps (arrow) on the crystal surface. As Dai and collaborators (2007) reported, the comparison between these images clearly demonstrates the preferential adsorption of F-lysozyme on steps. Since the molecular weight of the fluorescent label is smaller than 3% of that of F-lysozyme (Matsui *et al.*, 2006), almost all the molecular surfaces of F-lysozyme is the same as that of native lysozyme. Hence, F-lysozyme molecules preferentially adsorb on steps on the crystal surface as solute (native lysozyme) molecules, and thus, are incorporated into a crystal at steps (more precisely, kinks on steps).

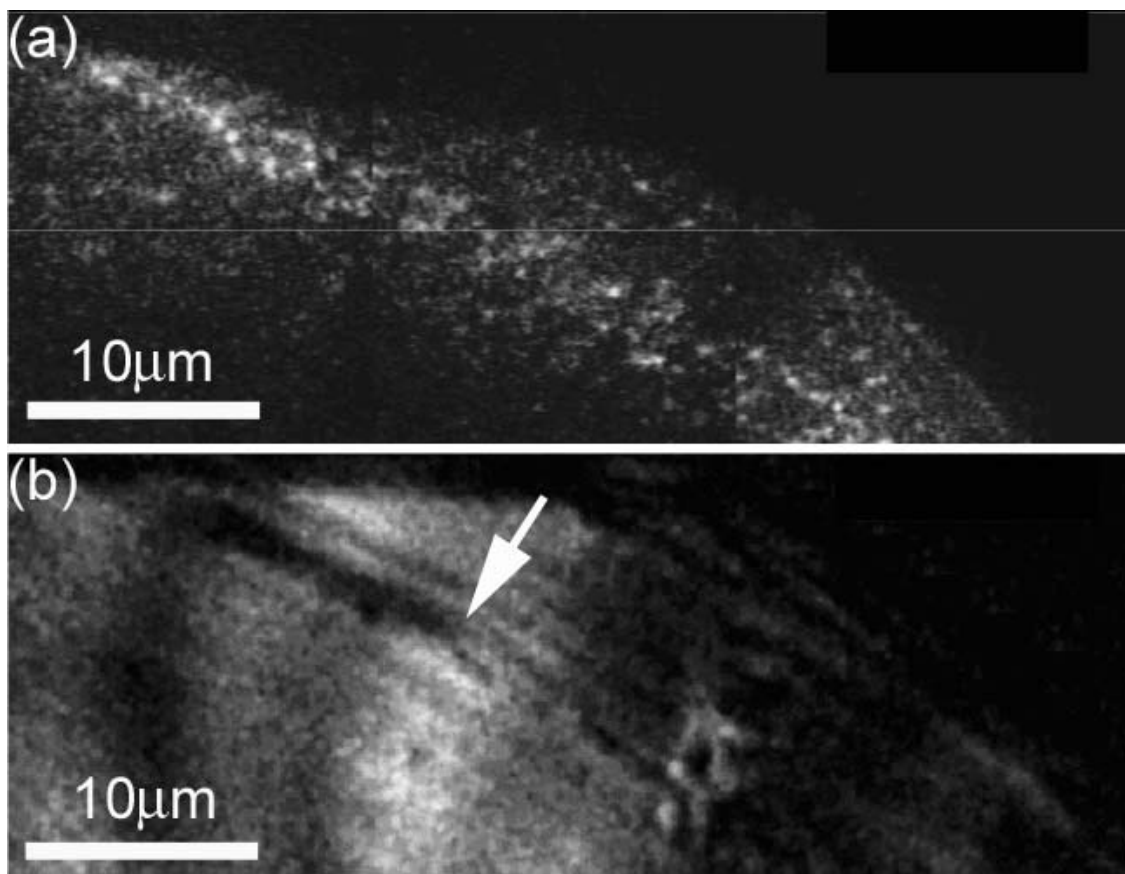


Figure 3.24 Comparison of two images taken by SMV of a thin-solution-layer type (a) and by LCM-DIM (b). The same field of view on a {110} surface of a tetragonal lysozyme crystal was observed by both methods. (a) One bright dot corresponds to one F-lysozyme molecule adsorbed on the crystal surface. (b) The white arrow shows the position of bunched steps on the crystal surface.

In the case of dimer, Nakada and coworkers (1999) revealed by *in situ* AFM observation, that dimer molecules adsorb randomly on terraces of {101} faces of tetragonal lysozyme crystals; however, for {110} faces, no one has ever succeeded in clarifying the adsorption sites. To determine the adsorption sites of dimer on the {110} face, we adopted F-dimer, since almost all the molecular surface of F-dimer is expected to be the same as that of native dimer. Iimura and coworkers (2003) reported that incorporation rates of dimer and F-dimer into a tetragonal lysozyme crystal do not differ, hence, the labeling of the dimer molecule has no influence on the incorporation process. Therefore, the adsorption process of F-dimer on the crystal surface was also observed *in situ* by SMV of the thin-solution-layer type. Figure 3.25a shows a typical single-molecule image: here also one bright dot

corresponds to one F-dimer molecule adsorbed on the crystal surface. Figure 3.25b indicates the same field of view observed by LCM-DIM. In Figure 3.25b, bunched steps and elementary steps are marked by white arrows and white arrowhead. The comparison between Figures 3.23a and b clearly indicates that F-dimer molecules adsorb randomly on terraces of the {110} face, in contrast to the case of F-lysozyme.

Since dimer is composed of two covalently bonded lysozyme molecules (Thomas *et al.*, 1996), the bonding between two monomeric lysozyme molecules inside a dimer molecule differs from those of two neighboring lysozyme molecules in a single crystal (mainly via hydrogen bonding, (Matsuura and Chernov, 2003)). Hence, the bonding between a dimer molecule and a crystal surface would also significantly differ from those between a solute lysozyme molecule and a crystal surface. Thus dimer could not be preferentially incorporated into a step (a kink in a step) as a solute molecule but adsorbed randomly on a terrace as a foreign impure molecule. The results shown in Figures 3.22 and 3.23 experimentally demonstrate, for the first time, that a foreign impure molecule whose intermolecular bonding is close to that of a solute molecule adsorbs preferentially on a step, and that a foreign impure molecule whose intermolecular bonding differs from that of a solute molecule can be adsorbed on different sites on a crystal surface.

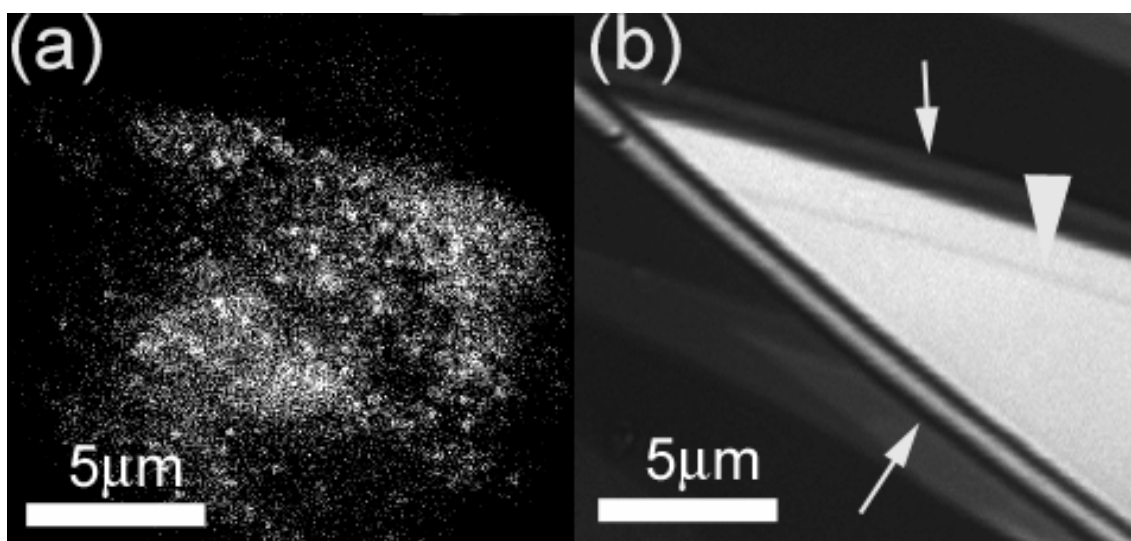


Figure 3.25 Comparison of two images taken by, SMV of a thin-solution-

layer type [ref] (a) and by LCM-DIM (b). The same field of view on a {110} surface of a tetragonal lysozyme crystal was observed by both methods. (a) One bright dot corresponds to one F-dimer molecule adsorbed on the crystal surface. (b) White arrows show the position of bunched steps on the crystal surface and the red arrow indicates a monolayers step.

3.4.5. Adsorption sites and supersaturation dependencies of step velocities

From the difference in the adsorption sites of F-lysozyme and dimer on the {110} faces of the tetragonal lysozyme crystals, it was attempted to explain the different dependencies of the ratio R on supersaturation shown in Figure 3.23. It seems that the balance between the density of adsorption sites and the exposure time of adsorption sites to impurity is probably the key to understand the different impurity effects on step velocities.

For F-lysozyme, steps (probably kinks on steps) are the major adsorption sites on the {110} faces, as shown in Figure 3.24. In a low supersaturation range, 2D nucleation rates are low, and thus very few new 2D islands are formed. In addition, Dai and coworkers (2007) revealed that the adsorption of F-lysozyme on the steps proceeds relatively slowly (it takes more than several ten minutes). Hence, after F-lysozyme molecules already adsorbed on steps are fully incorporated into newly grown layers following step advancement, bare steps unoccupied with F-lysozyme would appear. Consequently, in a low supersaturation range, the increase in step velocity with increasing supersaturation would increase the amount of steps unoccupied with F-lysozyme, i.e. the density of the adsorption sites (Figure 3.26a). In addition, in a middle supersaturation range, supersaturation higher than a certain critical value ($\sigma=0.7-0.8$) significantly increases 2D nucleation rates and hence the density of bare steps (adsorption sites). Therefore, in low to middle supersaturation ranges, with increasing supersaturation, the density of adsorption sites of F-lysozyme increases and this tends to increase the impurity effects.

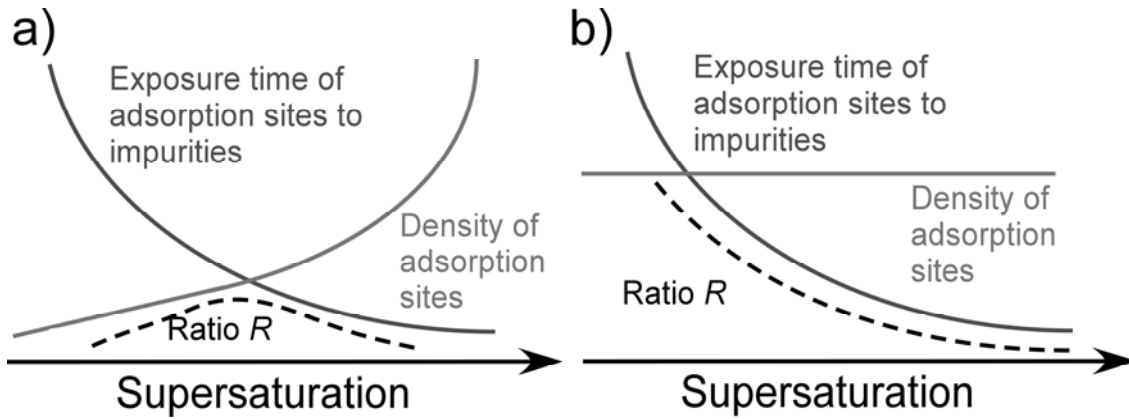


Figure 3.26 Schematic illustrations of the effects of F-lysozyme (a) and dimer (b) on the R vs. supersaturation plots. Balance between density of adsorption sites and exposure time of adsorption sites to impurities determines the supersaturation dependence of the ratio R .

In contrast, the increase in step velocity has a second contribution. The increase in step velocity with increasing supersaturation decreases the exposure time of adsorption sites to impurities in a solution (van der Eerden, 1993), and this tends to decrease the impurity effects. In low to middle supersaturation ranges, the decrease in the exposure time with increasing supersaturation is not large enough because of low step velocity; hence, the increase in the density of adsorption sites with increasing supersaturation would predominantly increase the amount of impurity adsorbed and consequently increase the impurity effect (the ratio R), as shown schematically in Figure 3.26a. On the other hand, in a high supersaturation range, with increasing supersaturation, the decrease in the exposure time of the adsorption sites to impurity would dominate the impurity effect, resulting in the decrease of the impurity effect. Hence, the ratio R would have a maximum value at certain supersaturation, and then decrease monotonically with increasing supersaturation.

In the case of dimer, terraces are the major adsorption sites on the $\{110\}$ faces, as shown in Figure 3.25. Hence, irrespective of supersaturation, the density of adsorption sites remains constant (Figure 3.26b). In contrast, the exposure time of terraces to dimer in a solution decreases with increasing supersaturation, because of larger step velocity and faster 2D

nucleation rates in a higher supersaturation range. Therefore, as supersaturation increases, the amount of the impurity effect (the ratio R) will decrease monotonically.

In the case of 18kDa, we observed a very similar dependency of R on supersaturation to that observed for dimer (Figures. 3.21b, c), hence, 18kDa probably adsorbs randomly on terraces. In contrast, the impurity effects observed for Seikagaku lysozyme were more complex (Figure 3.23d), and could not be reproduced by the solution containing 0.5 wt% dimer and 1.0 wt% 18kDa, although these two are the main impurities included in Seikagaku lysozyme (Thomas *et al.*, 1996). This result indicates that trace amount of other impure molecules present in Seikagaku lysozyme play an important role: one possibility is two very large oligomers (1700 kDa and 320 kDa (Thomas *et al.*, 1998b)) and the other possibility is a 39kDa polypeptide (Thomas *et al.*, 1996).

3.4.6. Spiral growth versus 2D growth

The results of step advancements measured for 2D islands and spiral hillocks growing from Seikagaku lysozyme (98.5%) are presented in Figure 3.27a. A clear difference in supersaturation dependencies between step velocities of spiral hillocks and 2D islands is found in the $\langle 110 \rangle$ and $\langle 001 \rangle$ directions (data of $\langle 001 \rangle$ are not shown). Also a difference in step morphology is observed, in case of 2D islands a ratio of $a/b \approx 3$ is found, while for spiral hillocks a ratio of $a/b \approx 5$ is found at similar supersaturations. It was shown before that for purified solution steps from spiral hillocks and 2D islands travel at the same speed and step advancements are independent of their source. Hence, the presence of impurities in the solutions affects differently the step advancement of 2D islands and spiral hillock. From the observed surface morphologies it is clear that steps on spiral hillocks are less affected by impurities. This is most likely due to the smaller interstep distances of spiral hillocks ($<1 \mu\text{m}$)

compared to interstep distances of 2D islands at identical supersaturation (Figure 3.27). It was experimentally shown before that exposure time of terraces to impurities is the key to understand the poisoning effect of molecules that randomly adsorb on terraces. The smaller interstep distance of spiral hillocks reduces the exposure to impurities and thus reduces the amount of impurities that randomly adsorb on terraces. As a consequence impurity poisoning is reduced. This explains the increased step velocity and changed step morphology for spiral hillocks. These results correspond well with etching experiments done on terraces of spiral hillocks and 2D islands. It was found that many shallow etch pits were found on terraces of 2D islands but almost non on terraces of spiral hillocks (Ono *et al.*, 2006). It is generally accepted that point defects (shallow etch pits) are the result of incorporated impurities in the crystal lattice.

Additionally spiral hillocks with large interstep distance, i.e. large terraces, were sometimes observed and the morphology of these hillocks showed the same ratio $a/b \approx 3$ as 2D islands growing from Seikagaku lysozyme. This observation also strongly suggests that exposure time of terraces is the key to impurity poisoning of particles that randomly adsorb on terraces.

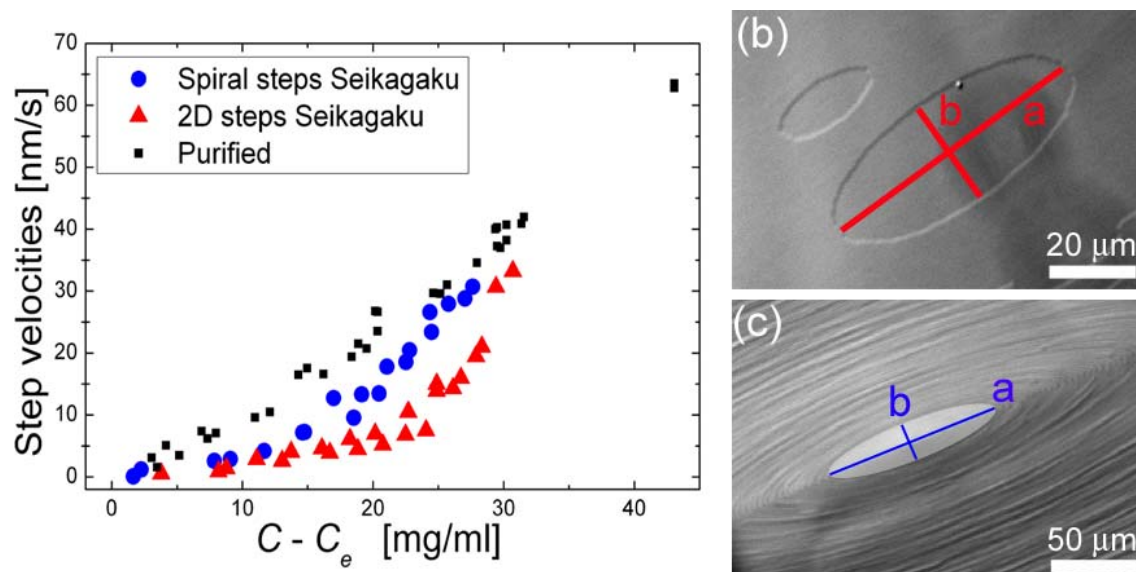


Figure 3.27 (a) Step velocities of 2D islands and spiral hillocks growing from seikagaku lysozyme at different supersaturation. Morphology of 2D islands

(b) and spiral hillocks (c) growing from Seikagaku lysozyme.

3.4.7. Commercial lysozyme solutions

To test for the influence of impure proteins present in commercial lysozyme solutions, morphologies of 2D islands were observed and step velocities were measured on {110} faces of tetragonal lysozyme with LCM-DIM. Three commercially available lysozyme solutions were used for this study: Fluka, Seikagaku (98.5% pure) and Sigma (94.3%) (for detailed information see section III.1.4.).

In Figure 3.28 typical step morphologies of 2D islands growing from different lysozyme solutions are shown. Surprisingly, 2D islands grown from Fluka lysozyme, generally considered as less pure, are showing the fewest impurity poisoning, i.e. 2D islands shapes are close to those found in 99.99% pure solution. Step morphologies for crystal growing from Seikagaku solution have been discussed earlier. The strongest impurity effect was observed for 2D islands growing from Sigma lysozyme. The islands are completely rounded and strong step pinning is clearly visible (Figure 3.28c). If a same surface is observed at relatively high supersaturation, the shape of the 2D islands changes drastically and lens shaped islands are found comparable to those found for Seikagaku.

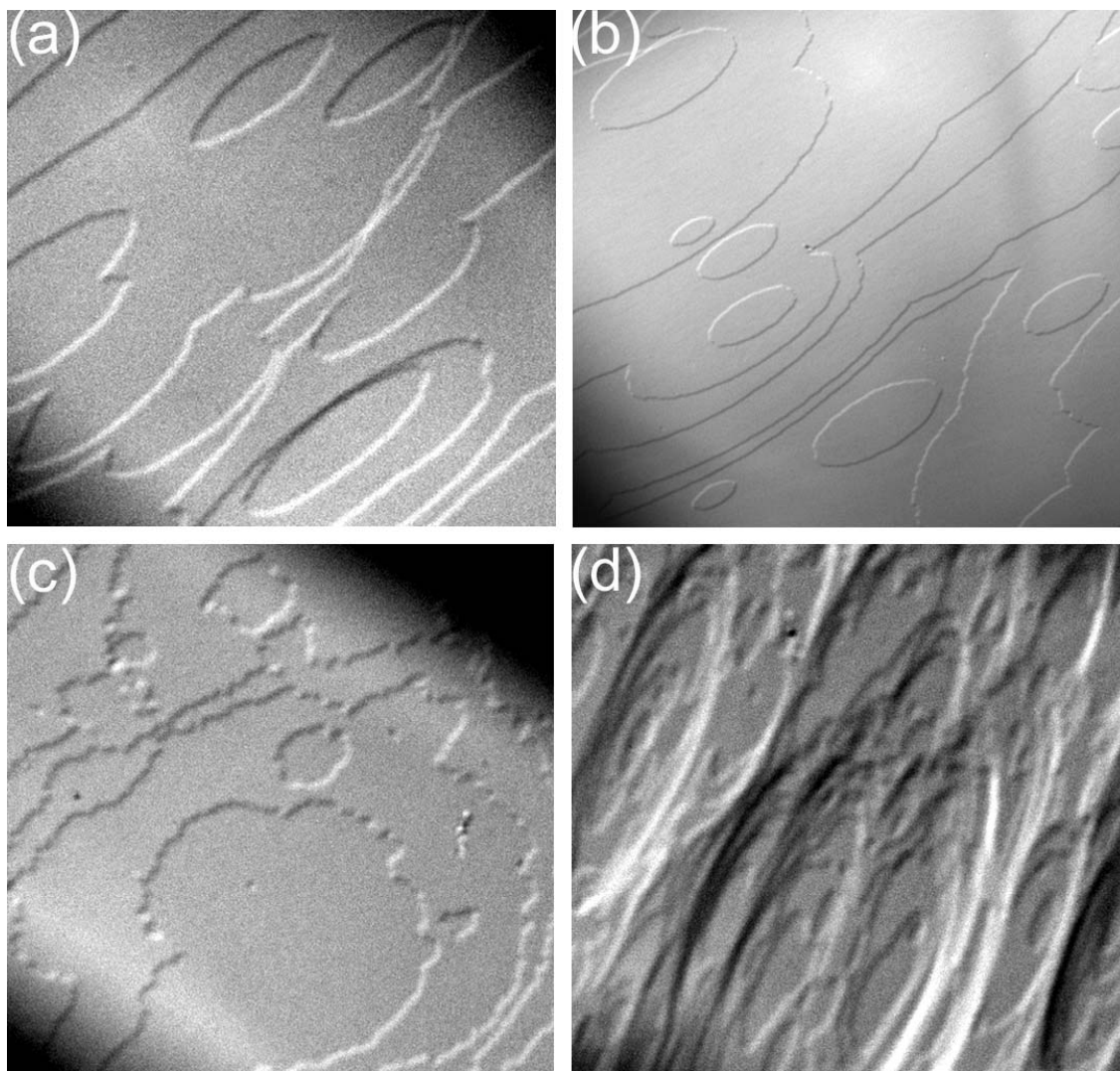
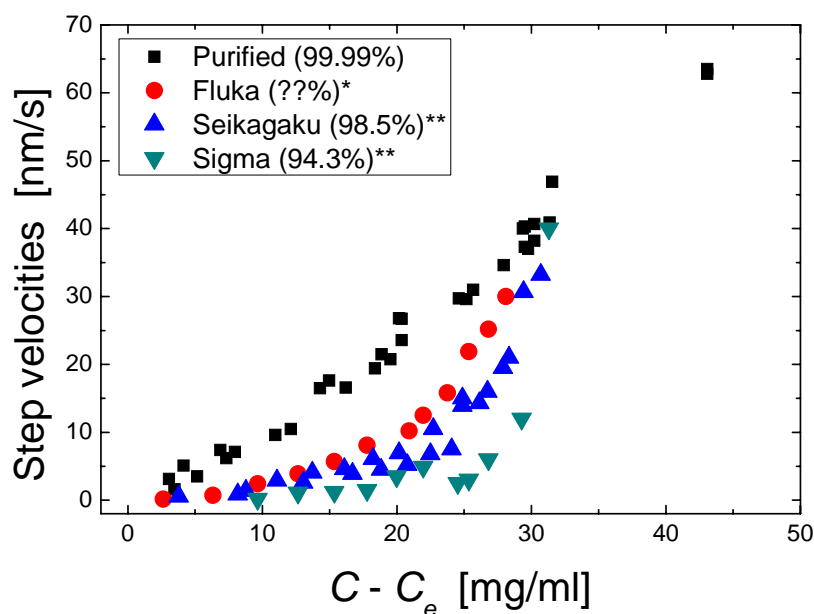


Figure 3.28 Step morphologies of 2D islands grown in different commercial lysozyme solutions. (a) Fluka lysozyme, (b) Seikagaku lysozyme, Sigma lysozyme low supersaturation (c), high supersaturation (d).

Step velocities of 2D islands growing from different commercially available lysozyme solutions were measured in the $\langle 110 \rangle$ and $\langle 001 \rangle$ direction on $\{110\}$ faces of tetragonal lysozyme crystals were measured in a broad supersaturation range $C - C_e = 0 - 32$ mg/ml. Results are shown in Figure 3.29. All three lysozyme solutions decrease significantly the step velocity. In particular, the suppression of step velocity by Sigma is significant, almost no step advancement in both $\langle 110 \rangle$ and $\langle 001 \rangle$ direction is observed for the supersaturation range $C - C_e = 0 - 25$ mg/ml. Thus no macroscopic growth is observed and a death zone is present.

Sigma lysozyme contains both ovotransferrin (78 kDa) and Ovalbumin (43 kDa) (Thomas *et al.*, 1996). These impure proteins are not found in Seikagaku while the amounts of lysozyme dimer and 18kDa found in Seikagaku and Sigma lysozyme are comparable (see section III.1.4). It was shown before that ovotransferrin is preferentially incorporated into growing crystals while ovalbumin is predominantly rejected by the crystals (Vekilov *et al.*, 1995a). Additionally no effect of ovalbumin was found on the normal growth rates of tetragonal lysozyme crystals (Judge *et al.*, 1998) Thus most likely ovotransferrin is responsible for the strong impurity effect observed in the low to middle supersaturation range for 2D islands growing from Sigma solution. It is reasonable to assume that this large impurity (78 kDa) is randomly adsorbed on the crystal surface, and not incorporated into kink sites because of the large difference in intermolecular bonding compared to those of monomeric lysozyme molecules.



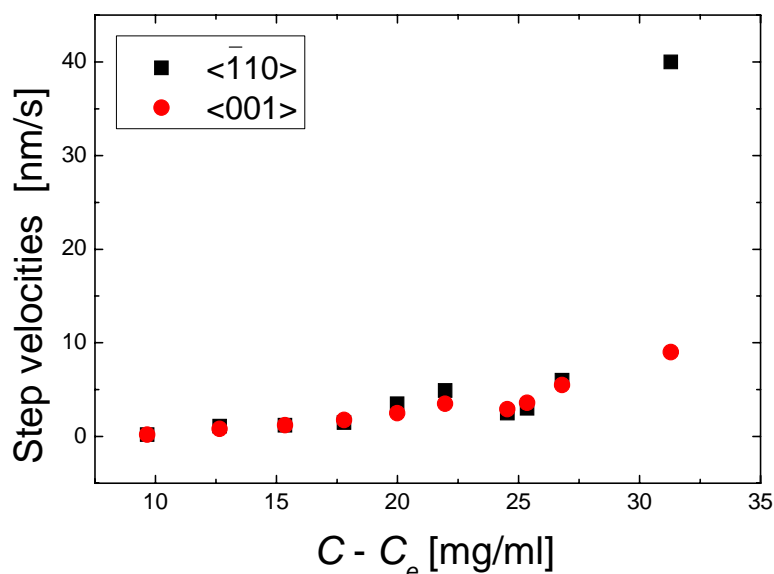


Figure 3.29 (a) Step velocities in the $\langle 110 \rangle$ direction measured on $\{110\}$ faces of tetragonal lysozyme crystals under various supersaturations and impurity contents by LCM-DIM. (b) Step velocities in $\langle 110 \rangle$ and $\langle 001 \rangle$ directions measured on $\{110\}$ face of tetragonal lysozyme growing in a commercial Sigma solution.

In Figure 3.29b step velocities of 2D islands growing from sigma solution measured in the $\langle 110 \rangle$ and $\langle 001 \rangle$ direction are shown. In both directions step advancement is approximately the same until a certain supersaturation, $C - C_e = 27$ mg/ml is reached. Above this supersaturation a very rapid increase in step velocity is found. The exact mechanism is still unclear but, it was shown before that some of the impure proteins most likely are adsorbed on terraces and thus, unmistakably, the impurity poisoning will be related with the exposure time of terraces to impurities. Probably at high enough supersaturation levels the adsorption time needed for a blocking impurity is longer than the exposure time of the terrace. Thus, once a step manages to break through the impurity fence a rapid increase in step velocities should be found because impurities don't have enough time anymore to get adsorb on the terraces. Even so, step velocities are still lower than those found for purified lysozyme, this indicates that other impure proteins, which most likely are directly incorporated into step

(i.e. kink sites), keep reducing step advancement at higher supersaturation levels.

3.4.9. Step bunching

Introduction

In some cases a uniform step train travelling across the crystal surface becomes kinetically unstable and steps tend to aggregate together to form step bunches, sometimes of macroscopic size, separated by wide terraces. Step bunches trap point defects, e.g. impurities, in amounts different from that incorporated by single steps. This difference contributes to striations sectoriality and vicinal sectoriality within the grown crystals (Vekilov *et al.*, 1996; 1998; Chernov, 2003). Crystal imperfections on the scale of micrometers (e.g., striations) affect the diffraction resolution that can be obtained from a given crystal (Vekilov and Alexander, 2000). For this reason the study of step bunching in protein crystallization is highly relevant and a better understanding of the general mechanism of step bunching can help choose experimental conditions which reduce this step phenomenon.

The physical origin of the step bunching phenomena is not clear and several mechanisms have been proposed to explain it:

- A widely cited mechanism, proposed by Schwoebel and Shipsey (1966), relates the instability of the uniform step train during growth to an asymmetry in the attachment-detachment rates of atoms at step edges.
- Dynamic step bunching has also been associated with surface diffusion (van Leeuwen *et al.*, 1974; Uwaha *et al.*, 1995; Sato and Uwaha, 1995).
- Impurities also are known to cause step bunching (van Enckevort, 1984; van der Eerden and Muller-Krumbhaar, 1986a; 1986b; Kandel and Weeks, 1994).

For the specific case of lysozyme growth a different mechanism for the formation of step bunches on tetragonal crystals was proposed by Vekilov and coworkers (Vekilov *et al.*, 1996; Vekilov and Rosenberger, 1998a; Vekilov *et al.*, 1999). They argue that step bunching originate from the coupling of bulk transport with nonlinear interface kinetics. According to this model of growth rate fluctuations caused by intrinsic kinetic instabilities, step bunching should be independent of impurities and independent of the distance to the spiral outcrop (Vekilov *et al.*, 1996). Thus, step bunching should be found with similar intensity for growth from high purity solution and for crystallization from solution containing higher levels of impurities. Furthermore, due to the concept of acceleration and deceleration of step velocities (bunching and debunching) it should be found with the same intensity all over the crystal face, independently of the local position and the distance with respect to the center of the spiral hillock.

Step bunching observed by PSMI and LCM-DIM

During this work, bunched steps were observed mainly when spiral growth dominated the crystal surface. When 2D nucleation was the dominant growth mechanism only the nucleation of multilayered islands was observed generating stacks of layers but no real step bunching. The origin of a multilayered island is not related to the mechanism of step bunching and the subject of multilayered islands is treated in section 4.5.2 of this work.

In Figure 3.30 some typical LCM-DIM images of bunched steps on the {110} face are shown. The crystals in images (a) and (b) are grown from Seikagaku lysozyme and crystals in images (c)-(g) from highly purified lysozyme solution. Experimental conditions, i.e. supersaturation, were kept constant for several days. The first important observation that can be made is that step bunching is never observed close to the spiral dislocation

outcrop, but starts at a certain distance (see white and black lines in Figure 3.30). This would explain why step bunching is hardly observed on {101} faces, except for very large tetragonal lysozyme crystals, when {101} faces also reached a considerable size. Secondly, when comparing spiral hillocks grown from highly purified lysozyme and Seikagaku lysozyme it becomes clear that step bunching is much more pronounced for crystal growth from solutions containing impurities.

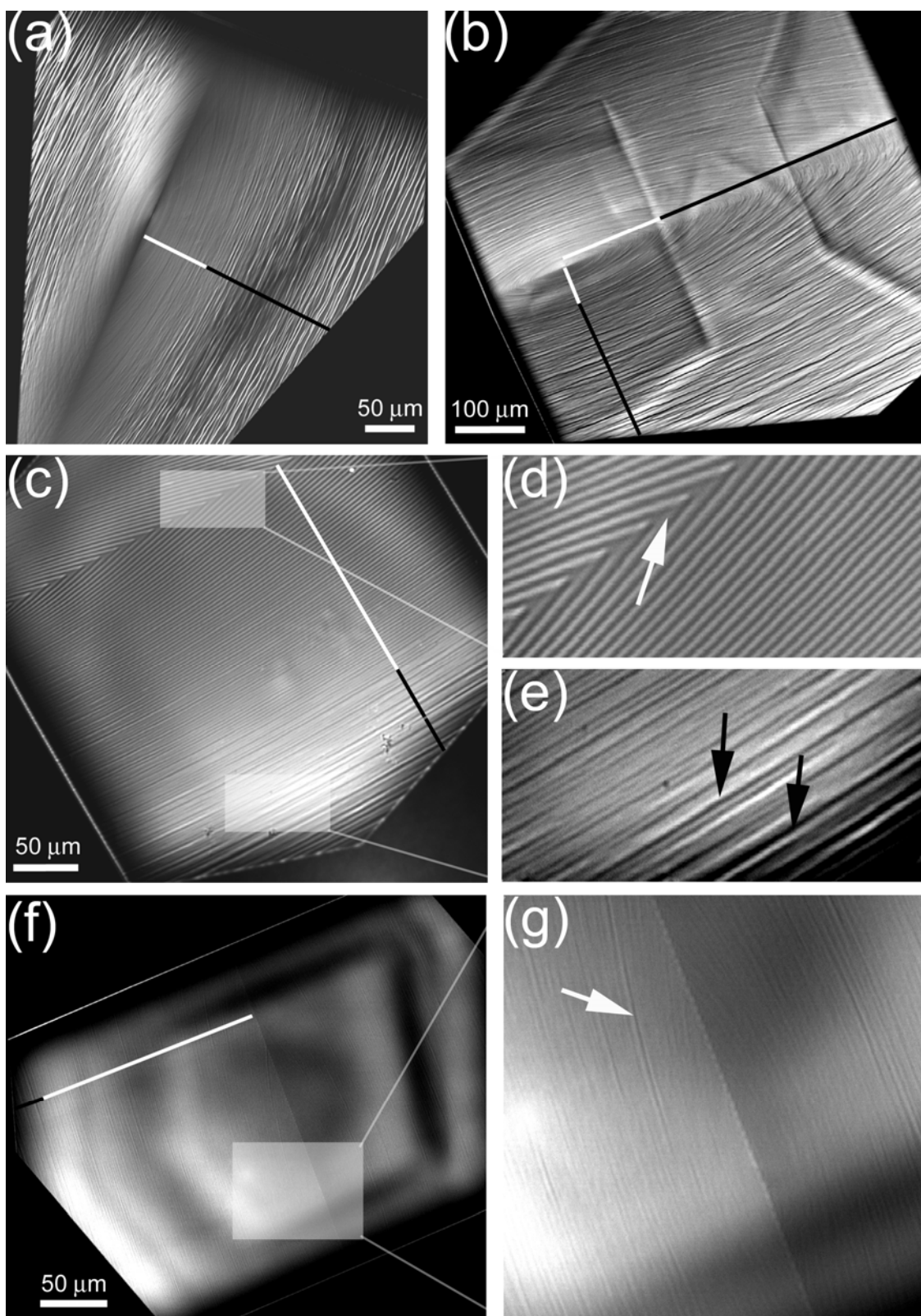


Figure 3.30 Step bunching observed by LCM-DIM on spiral hillocks. (a)(b) Spiral hillocks formed in commercial lysozyme. (c) Spiral hillock formed in purified lysozyme, close up of the central area of the spiral (d) and edge of the crystal(e). Spiral hillock formed in purified lysozyme with close up of the center of the dislocation (f). White arrows and lines indicate monolayer steps. Black arrows and lines indicate bunched steps.

Analysis of spiral growth of tetragonal lysozyme by PSI is presented in Figure 3.31. The crystal is growing from Seikagaku lysozyme ($C-C_e = 22$ mg/ml) and the surface is covered by one large spiral hillock. In the upper right-hand corner (Figure 3.31b) an overview of the crystal micromorphology is shown (LCM-DIM image). The outcrop of the spiral is marked with a white cross. Since the crystal is growing from a commercial grade solution containing 1.5% of protein impurities, the morphology of the growth steps changes and the sharp tip of growth islands, observed under growth from pure solution, disappear as discussed before. Due to the interaction with impurities, the ratio of the step velocity between the fast growing and slow growing direction is reduced from 6 to $\approx 4-5$.

Figure 3.31c and 3.32d shows the height evolution over time for two fixed points indicated by red arrows in the PSI interferogram (Figure 3.31a). Near the spiral center (Figure 3.31a), at position “1”, the height increase over time is a rather smooth line indicating that steps are moving at constant velocity as a equidistant step train (Figure 3.31c). At position “2” ($\approx 100 \mu\text{m}$ from the spiral center), the formation of terraces and macrosteps is already evident. Macrosteps of some 30 to 60 nm in height (i.e. ≈ 6 to 12 layers) have been formed into the $\langle 110 \rangle$ as well as the $\langle 001 \rangle$ direction (Figure 3.31d). At both positions, the average slope is similar, which indicates that large macrosteps move with approximately the same step velocity than the single steps near the spiral center. This confirms the results of directly measured step velocities by LCM-DIM for single and multilayer steps (see Figure 3.13), and thus at a constant supersaturation, steps move with approximately the same velocity independent on the degree of step bunching. This shows again that no overlap of the diffusion fields of steps exist because all steps move at the same velocity. It is generally accepted that steps moving within a group of steps (bunched steps) compete for nutrient supply and move slower (Chernov, 2003), but this is not observed here.

Further away from the spiral dislocation outcrop the formation of bunched steps and terraces increases and near the crystal edge, big macrosteps have been formed separated by relatively wide terraces (white arrows, Figure 3.32b). Unfortunately no PSI interferograms are available of the surface close to the crystal edges.

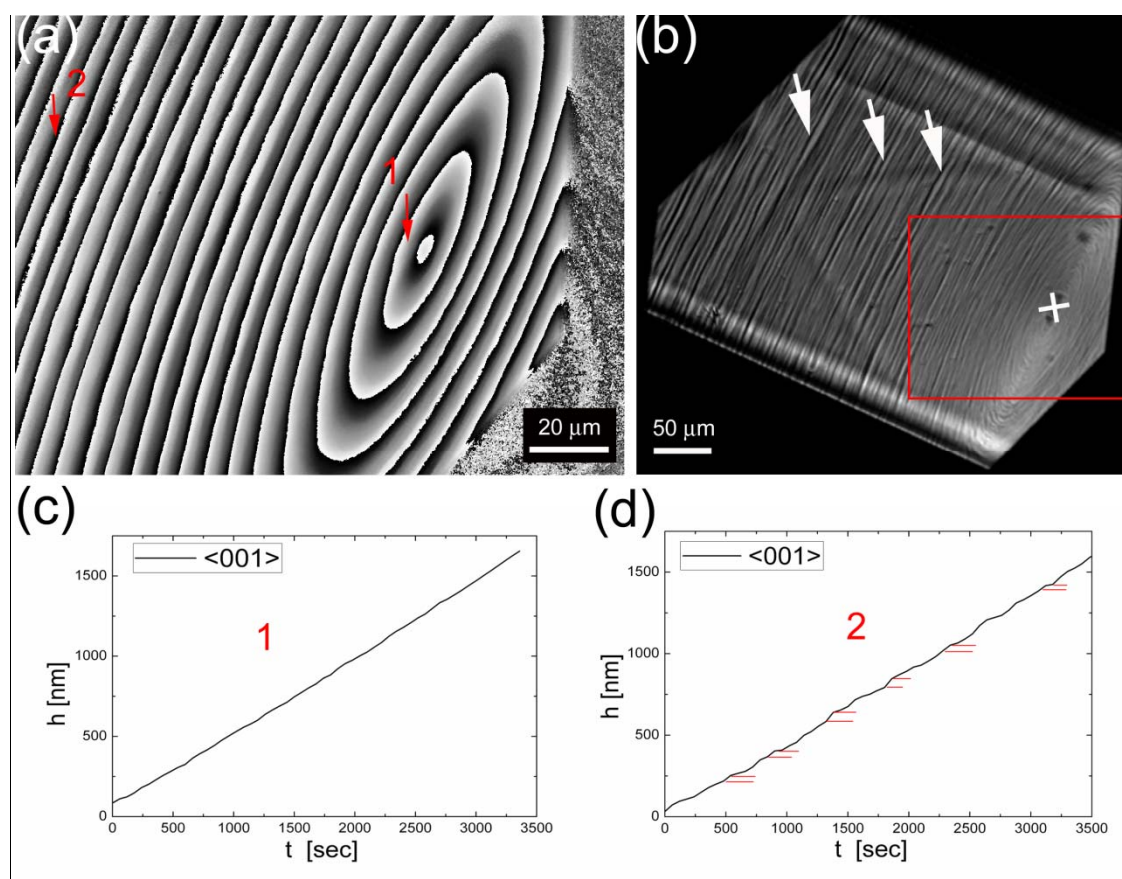


Figure 3.31 Spiral growth from commercial solution at high supersaturation ($C-C_e=39.3$ mg/ml). Michelson phase shift interferogram of a growth hillock. (b) LCM-DIM images of spiral hillock on $\{110\}$ face, red square indicates observed area with MI and white arrows indicate heavy step bunching. Height profile evolution over time at point 1 (c) and point 2 (d). Red lines indicate bunched steps in height profil taken in point 2.

The evolution of spiral growth and step bunching during growth from commercial grade solution shows the progressive development of macrostep formation with the distance steps have traveled relative to their origin, e.g. spiral dislocation outcrop. Since impurity incorporation is related to exposure time to the solution, especially in the case of impurities adsorbing on the terraces (Van Driessche *et al.*, 2007), it can be concluded that

macrostep formation is correlated to the interaction with impurities (see for example van Enkevort, 1984; van der Eerden and Muller-Krumbhaar, 1986a; 1986b; Kandel and Weeks, 1994) and not to intrinsic kinetic instabilities, as previously assumed (Vekilov *et al.*, 1996; Vekilov and Rosenberger, 1998a; Vekilov *et al.*, 1999).

The observation of step bunching during growth from highly purified solution (99.99%), can be understood if this high purity material is compared with conditions used for the growth of inorganic materials, especially semiconductor crystals. In this case, “high purity” means 3 to 4 orders of magnitude less impurities, compared to the material used for this work. A purity of 99.99% is excellent for protein growth, but still could not be high enough to avoid interaction of impurities with the step front.

The relation between supersaturation and step bunching is not completely clear but from the experimental data obtained in this work it seems that with increasing supersaturation step bunching is reduced. This seems reasonable when considering impurities as the main cause of step bunching. At higher supersaturations the influence of impurities on the step advancement is reduced considerably (see section 3.4.5), mainly because the exposure of time of the terraces to the impurities is reduced, and thus less step bunching is to be expected. This corresponds well with the observations made during this work; even so, more experimental data are necessary to confirm this.

Formation of a macrostep pattern

In Figure 3.32 a new mechanism for macrosteps, i.e. bunched steps, formation is presented. In this peculiar case, on a crystal growing from purified solution, macrosteps are formed at a dislocation outcrop which is related with a microcrystal (red circle in Figure 3.32a,b) attached to the crystal surface. Figure 3.32a shows the initial stage of this process were

only half of the surface is covered with macrosteps. In less than one day the entire $\{110\}$ face shows macrosteps. Two days later a new, dominant, dislocation hillock has emerged and is covering the entire surface. At this point almost no bunched steps can be observed because the crystal is growing in purified lysozyme solution. Only at the crystal edge, i.e. far away from the dislocation outcrop, some relatively small bunched steps are observed (white arrows in Figure 3.32c). Also in Figure 3.32a a second, smaller microcrystal is attached to the surface (blue circle), in the consecutive images this microcrystal is completely buried inside of the larger crystal. Most likely this incorporated microcrystal gave birth to the spiral hillock observed in Figure 3.32c. A large microcrystal ($\approx 30 \mu\text{m}$) is also slowly being buried but at the same time is still growing. The bright space adjacent to the microcrystal represents the crystal area already incorporated into the larger crystal. Apparently, a tetragonal lysozyme crystal has no problem with incorporating large microcrystals (i.e. small crystals). This type of behavior has been observed for several other proteins (McPherson *et al.*, 2003 and references there in) and seems to be a common feature of protein crystal growth.

In Figure 3.32d a Michelson phase shift interferogram is shown. From this image it was possible to measure the height of the macrosteps (Figure 3.32e). It is found that all macrosteps had an approximate height of 80 nm, or 15-16 monolayer steps. In between these bigger macrosteps, some smaller macrosteps are present as well (± 20 nm). The interstep distance of these macrosteps is roughly constant (white line, Figure 3.32b). This indicates that the formation mechanism of these bunched steps is closely related to the “rotation” of the steps at the spiral dislocations outcrop, but the exact mechanism remains unclear. It was observed before by AFM that the formation of multilayer steps is promoted by the edges of adsorbed microcrystals on the crystal surface (Keel, 2004). Thus high resolution images obtained by AFM could be very useful to get a better understanding of this phenomenon. This macrostep pattern was observed on several

crystals and all were related to microcrystals attached to the surface (see for example Figure 3.4). This novel mechanism for step bunching has no apparent relation with impurity induced step bunching mentioned before. No references of this mechanism were found in the literature.

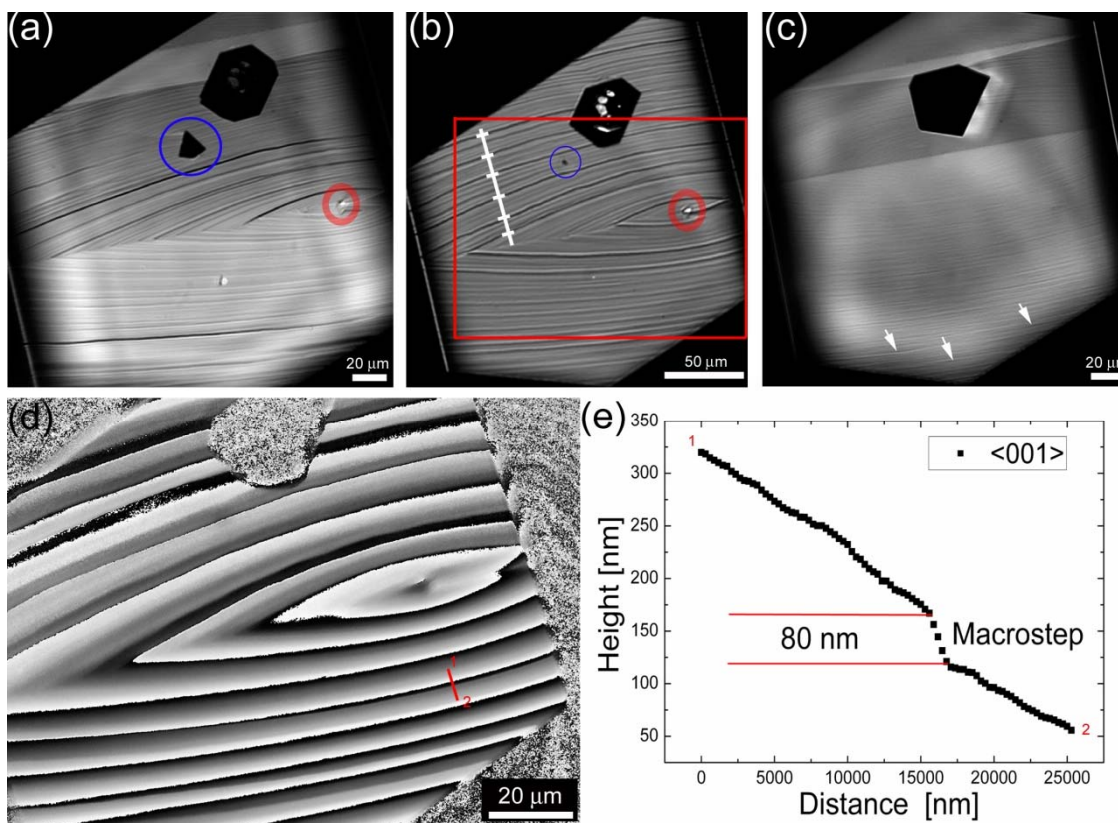


Figure 3.32 Formation of a macrostep pattern on a spiral hillock related to a microcrystal attached to the surface. (a)(b)(c) LCM-DIM images of {110} face of tetragonal lysozyme, showing the appearance (a,b) and disappearance of a macrostep pattern generated by a spiral dislocation at a microcrystal attached to the growing surface. (c) Michelson phase shift interferogram of the same {110} surface. (d) Height profile of red line in (c).

3.5. Two dimensional nucleation kinetics

3.5.1. Introduction

Two-dimensional (2D) nucleation is an important crystal growth mechanism under middle and high supersaturation ranges. In particular, in the case of protein crystallization, due to relatively high supersaturation necessary for initial three-dimensional (3D) nucleation and subsequent growth, 2D nucleation is a main growth mechanism. Hence many qualitative observations on 2D nucleation have been reported so far, but few quantitative studies have been tried until now.

Direct observation of 2D nucleation processes on inorganic and protein crystals have been carried out mainly by atomic force microscopy (AFM), by which individual 2D islands appearing on a crystal surface could be observed directly. 2D nucleation rates were reported for thaumatin (Malkin *et al.*, 1996a; 1999b) and catalase crystals (Malkin *et al.*, 1999b), however the scan of a cantilever potentially disturbs solute concentration distribution in the vicinity of a crystal surface as was shown in section 1 of this chapter. In addition, only a small part of a crystal surface can be observed by AFM. Therefore, 2D nucleation rates should be measured with a non-invasive technique which can visualize an entire face.

Optical microscopy is a promising alternative to observe *in situ* a whole crystal surface non-invasively. There are many reports that studied 2D nucleation growth by measuring normal growth rates of crystal faces. By analyzing supersaturation dependency of normal growth rates using a 2D nucleation growth model of the birth-and-spread type, one can indirectly determine ledge free energies for 2D nucleation of protein crystals (Kurihara *et al.*, 1996; Kashimoto *et al.*, 1998; Suzuki *et al.*, 2000; 2005; Nagatoshi *et al.*, 2003; Asai *et al.*, 2004). However, since ledge free energies

were determined indirectly from averaged normal growth rates, only averaged information on 2D nucleation was obtained.

In order to achieve non-invasive and direct observation of individual 2D islands, various kinds of optical microscopy are available. *In-situ* observations of monomolecular steps were made on protein crystals by transmission type phase-contrast microscopy (Tsukamoto *et al.*, 2003; Yai, 2003; Dold *et al.*, 2006). LCM-DIM also gives good contrast of elementary growth steps of protein crystals (Sazaki *et al.*, 2004; 2005; Suzuki *et al.*, 2005). In this study, utilizing LCM-DIM, 2D nucleation was observed on {110} and {101} faces without any spiral growth hillock. Observations were carried out in the supersaturation range $\sigma = 0 - 1.4$. Supersaturation σ at a given temperature was defined as:

$$\sigma = \ln (C/C_e), \quad (3.9)$$

where C is a bulk concentration of lysozyme and C_e the solubility. Above this supersaturation range, 2D nucleation was too fast to measure. To analyze 2D nucleation rates, the number of newly appeared islands between adjacent time-lapse images was counted and divided by the surface area of the observed crystal surface and elapsed time.

From the obtained data using 99.99% pure lysozyme the intrinsic ledge free energy of lysozyme crystals, was determined. Furthermore, the effect of impure molecules on 2D nucleation, using 98.5% pure lysozyme (Seikagaku Co.) and intentionally added impure proteins: fluorescent-labeled lysozyme (Matsui *et al.*, 2006) covalently-bonded dimer of lysozyme and impure protein of 18 kDa molecular weight (Thomas *et al.*, 1996) was studied. Homogeneous and heterogeneous nucleation is discussed, which will be a step toward a better understanding of nucleation and growth phenomena in protein and inorganic crystallization.

3.5.2. Two dimensional nucleation behavior

2D nucleation behaviour on the $\{110\}$ and $\{101\}$ faces of the growing tetragonal lysozyme crystals was observed *in situ* by LCM-DIM. As shown in a sequence of photomicrographs (Figure 3.33), 2D islands of elementary step height by LCM-DIM could be clearly visualized and the time course of the 2D nucleation growth of the birth-and-spread type could be followed. Here only significant parts of the images are shown, although we observed elementary steps on entire crystal surfaces. Arrows in the micrographs indicate the appearance of new 2D islands during the time intervals of the sequence of images.

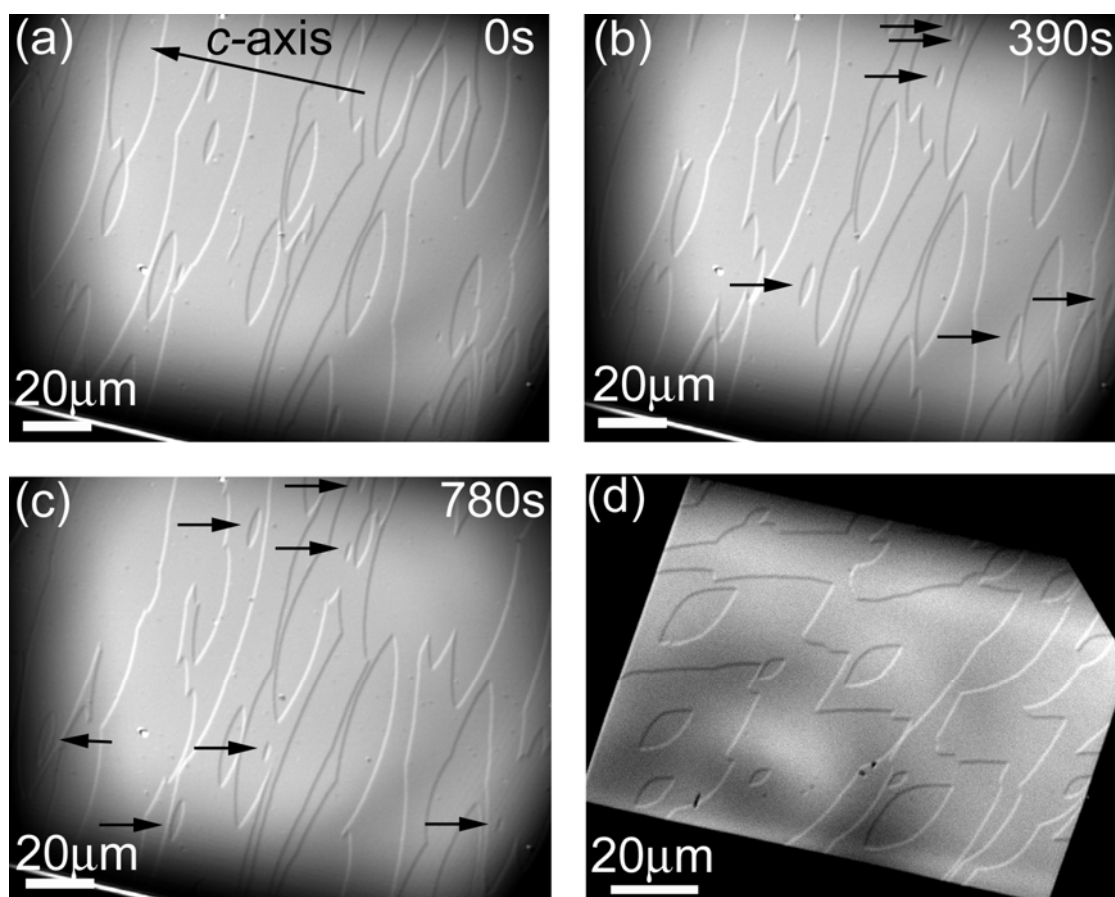


Figure 3.33 Photomicrographs of 2D nucleation behaviour on $\{110\}$ (a-c) and $\{101\}$ (d) faces of growing tetragonal lysozyme crystals, observed by LCM-DIM. The sequence of micrographs shows the time course of 2D nucleation growth of the birth-and-spread type: 0 s (a), 390 s (b) and 780 s (c). Arrows indicate the appearance of new 2D islands during the time intervals of the sequence of images. Growth conditions: 99.99% pure lysozyme 56 mg/ml (a-

c) and 40 mg/ml (d), NaCl 25mg/ml, in 50 mM sodium acetate buffer (pH 4.5), at 22.0°C (a-c) and at 26.0°C (d).

Within the range of supersaturations ($\sigma=0-1.4$) and for all solutions used in our observations, it was found that 2D nucleation occurred randomly on the entire crystal surfaces. At higher supersaturations, $\sigma>1.4$, crystal edges became preferential nucleation regions because of the Berg effect (Berg, 1938), and a complex response of the facet morphology arose from nonuniformities in nutrient and impurity supply. Such facet response has been observed experimentally (Vekilov *et al.*, 1995) and explained quantitatively by numerical simulations (Lin *et al.*, 1996) for tetragonal lysozyme crystals by Rosenberger's group. In this study, all the experiments were carried out within the lower supersaturation range ($\sigma=0-1.4$), where the Berg effect was not significant. From the sequences of photomicrographs taken by LCM-DIM, 2D nucleation rates were determined systematically at different supersaturations (discussed later). To analyze 2D nucleation rates, the number of newly appeared islands between adjacent time-lapse images was counted and divided by the surface area of the observed crystal surface and elapsed time.

In addition to the random 2D nucleation shown in Figure 3.33, also some peculiar 2D nucleation events were observed at rare intervals. Arrows in a sequence of photomicrographs shown in Figure 3.34 indicate the regions in which 2D islands having their centers at the same position were generated repeatedly. Note that the interstep distances of the concentric 2D islands generated repeatedly are irregular (bars in Figure 3.34). Although two screw dislocations with opposite signs can generate a similar surface structure composed of concentric islands, the irregular interstep distances clearly indicate that the 2D islands nucleated repeatedly at irregular time intervals at the same site. The repeated 2D nucleation normally continued for 3 to 4 layers and could be observed irrespective of the supersaturation. The repeated nucleation was mainly observed when impure proteins were present in the lysozyme solutions. In the case of the 99.99% purity lysozyme

solution, the ratio of the occasions on which we could find the repeated nucleation was about 20%, but 60% for the solutions that contained the impurities. This is a strong indication that the impure proteins are responsible for the repeated 2D nucleation, although other materials related with impure sample, e.g. fibrous materials (Hondoh and Nakada, 2005) could be also responsible. Liu *et al.* (1996) gave a theoretical explanation and experimental examples for the heterogeneous 2D nucleation on inorganic crystals. They explained that any kind of foreign particle, such as dust, gas or liquid bubbles, macro or polymer molecules, secondary nuclei formed during the growth of host crystals and even impurity molecules, can potentially serve as nucleation centers for 2D nucleation, and they will promote nucleation by lowering 2D nucleation barriers. In addition, after the impure molecules were incorporated into the crystal surface, the strain fields generated around the impurities would also play an important role to lower step-ledge free energies (Chernov, 1997) and thus promoted the 2D nucleation repeatedly, until the effects of the strain field did not reach the crystal surface (3 to 4 layers in this study).

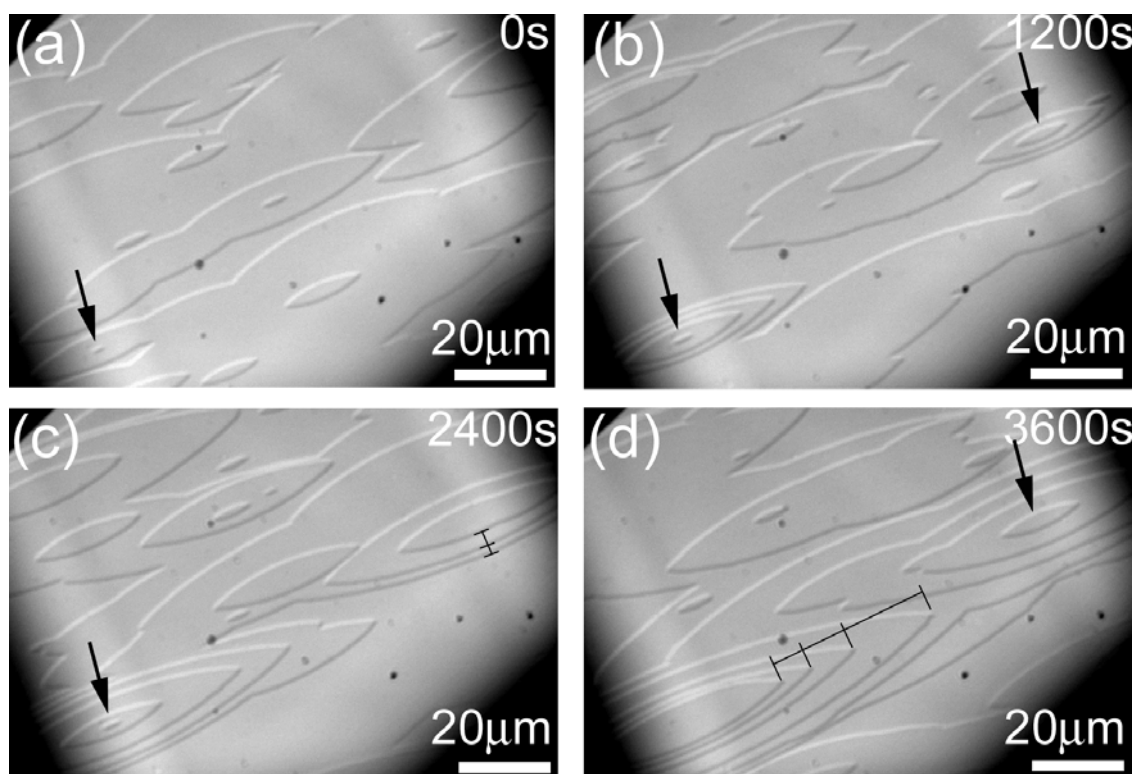


Figure 3.34. Photomicrographs of repeated 2D nucleation on a {110} face of

a growing tetragonal lysozyme crystal taken by LCM-DIM. The sequence of micrographs shows the time course of the repeated 2D nucleation: 0 s (a), 1200 s (b), 2400 s (c), 3600 s (d). Black arrows show the regions in which 2D islands having their centers at the same position were generated repeatedly. The repeated 2D nucleation normally continued for 3 to 4 layers. Bars indicate that interstep distances of the concentric 2D islands generated repeatedly are irregular. The crystal was growing from a solution containing 0.05 wt% F-lysozyme.

A sequence of photomicrographs in Figure 3.35 shows 2D nucleation and subsequent lateral growth of a multilayer island that exhibits much higher contrast than the elementary islands. In Figure 3.35, a white arrow indicates the existence of a foreign particle on the crystal surface, since the particle did not grow at the same rate as other islands grew. After 80 s (Figure 3.35), a 2D island appeared at this foreign particle (white arrow) and a second 2D island appeared next to the first one (black arrow). After 230 s (Figure 3.35), the first island nucleated at the foreign particle is overgrowing the second island (black arrowhead). This observation demonstrates that the first island had multiple layer height. Sometimes foreign particles adsorbed on a crystal surface were observed at the center of the multilayer islands. In addition, multilayer islands frequently appeared on the crystal surfaces after the replacement of the solution inside the cell and also after the crystals were transferred from stock tubes of seed crystals to the observation cell. Furthermore, no strong correlation was found between the presence of the impure proteins and the appearance of multilayer islands. Taking into account these results, we concluded that relatively large foreign particles, probably microcrystals generated by flow and/or clash of seed crystals, and then adsorbed on a crystal surface, are responsible for the formation of the multilayer islands. The relatively large height of the foreign particles would result in the lateral growth of the multilayer islands. It is also noteworthy that only a small percentage of the foreign particles promoted the nucleation of the multilayer islands (Figure 3.35). Only microcrystals that had specific relations with the crystal surface, e.g. small angle grain boundaries, might work as heterogeneous centers of the multilayer islands.

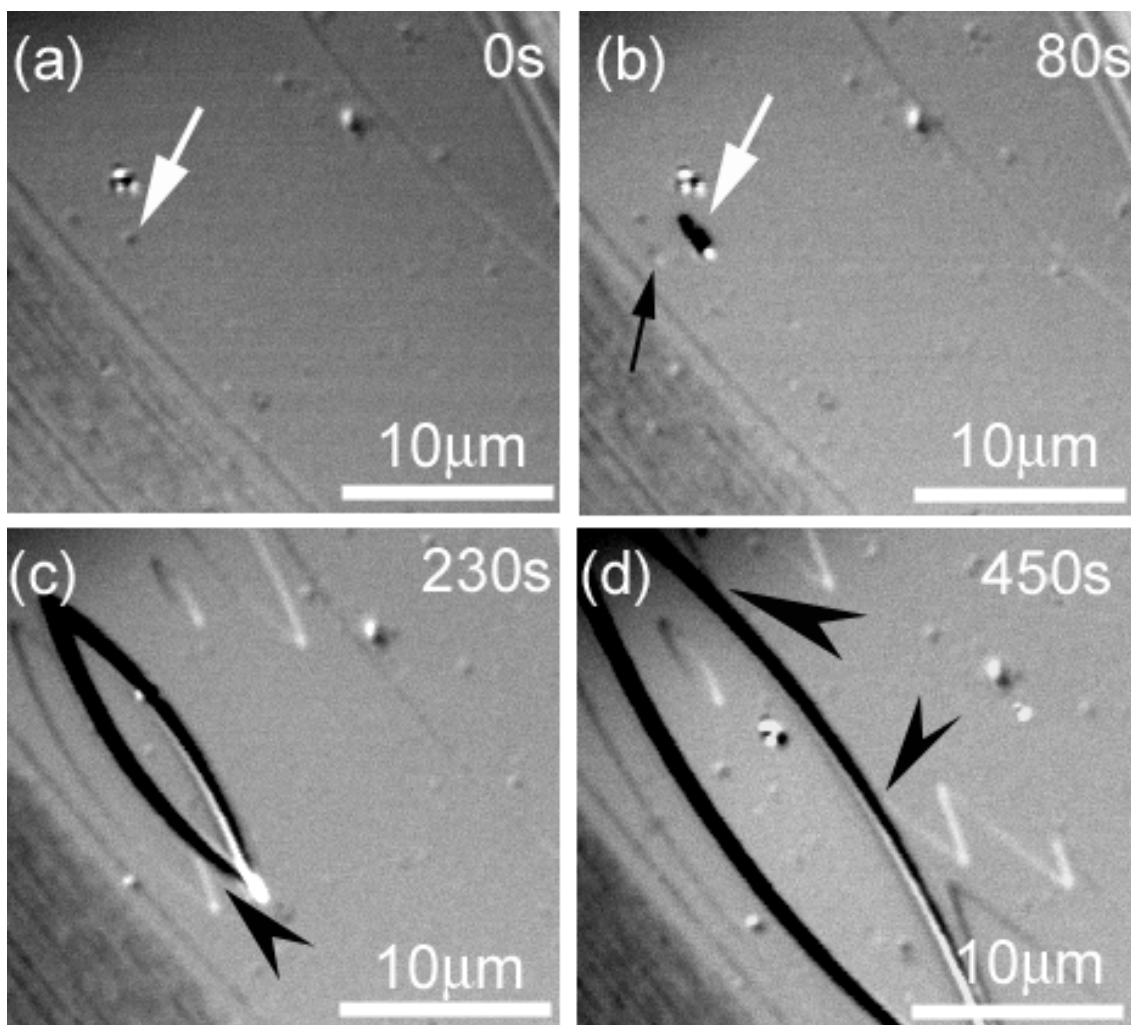


Figure 3.35 Photomicrographs of 2D nucleation and subsequent lateral growth of a multilayer island on a $\{110\}$ face of a growing tetragonal lysozyme crystal, taken by LCM-DIM. The sequence of micrographs shows the time course of the multilayer island: 0 s (a), 80 s (b), 230 s (c), and 450 s (d). White arrows indicate the presence of foreign particles on the surface. A black arrow shows the nucleation of a 2D island with elementary step height. Black arrowheads indicate the positions at which the multilayer island overgrows the single layered islands.

In some very rare cases, many consecutive layers were formed leading to the formation of “2D hillocks” that dominated the whole surface, as shown in Figure 3.36. The interstep distances between the consecutive layers are irregular (bars in Figure 3.36). This result indicates that these islands were not formed by screw dislocations but by nucleation, as the case shown in Figure 3.34. The surface of the 2D hillocks was slightly dissolved by increasing temperature, and it was found that no point-bottomed etch pit,

corresponding to the outcrop of a dislocation, appeared at the center of the consecutive 2D hillock. Many flat- and point-bottomed etch pits appeared randomly on the 2D hillock. Nevertheless, after the decrease in temperature, the consecutive 2D islands appeared again. These observations suggest that some fibrous materials (Hondoh and Nakada, 2005), although no point-bottomed etch pit could be found at the center, might be responsible for the formation of the consecutive 2D nucleation hillock. Further studies are necessary for clarifying the formation mechanisms. To the authors knowledge this is the first report of this growth mechanism for protein crystals.

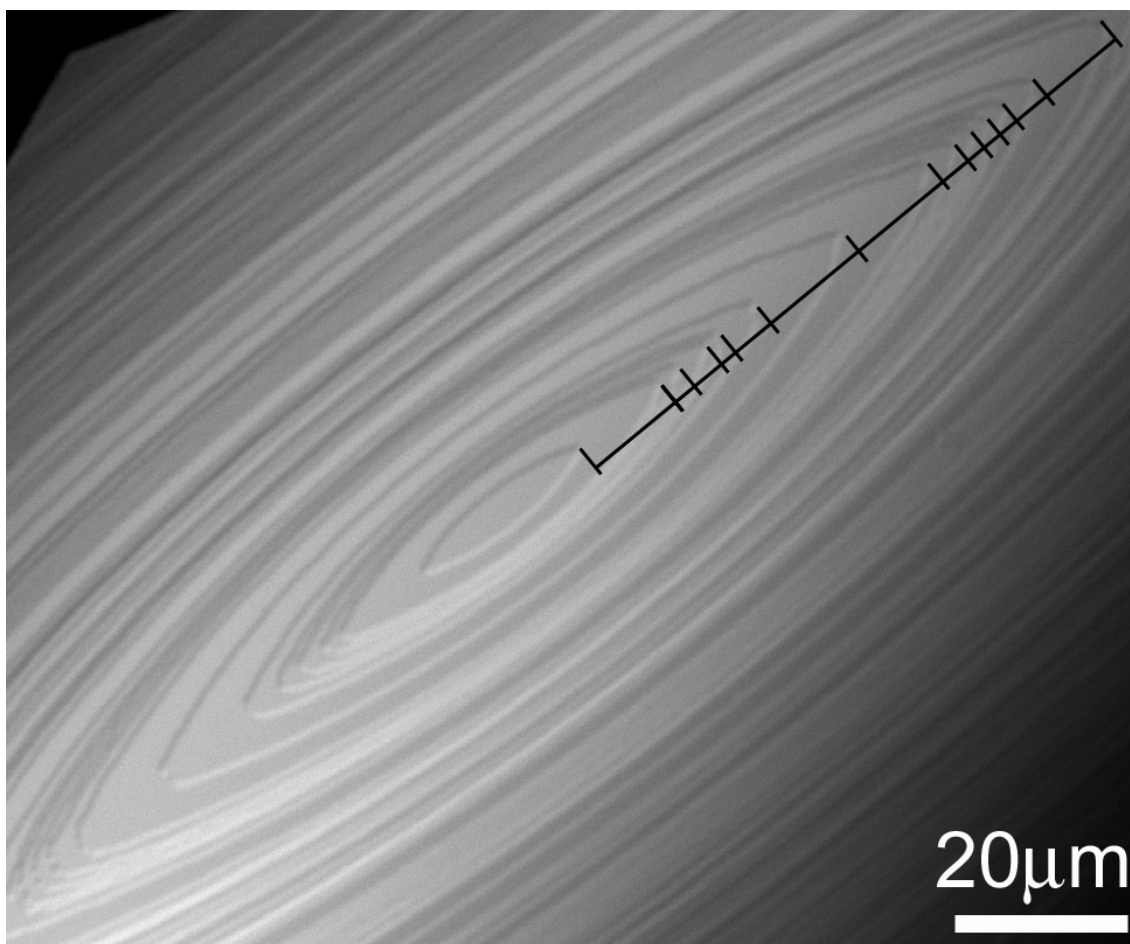


FIGURE 3.36 Photomicrograph of consecutive layers of 2D islands that dominate a whole $\{110\}$ face of a growing tetragonal lysozyme crystal, taken by LCM-DIM. Bars indicate the irregular interstep distance between consecutive 2D islands.

3.5.3. Two dimensional nucleation rates

– Surface free energy –

2D nucleation rates on the {110} faces of the tetragonal lysozyme crystals by LCM-DIM at different supersaturations and in the presence of various impure proteins were measured *in situ*. All results are summarized in Figure 3.37, which includes the data of the random nucleation and the repeated nucleation for 3 to 4 layers. Since elementary steps on the {110} faces involve two molecules per step (Durbin and Feher, 1990; Durbin and Carlson, 1992; Konnert *et al.*, 1994), 2D nuclei composed of a double layer were considered. By modifying the classical expression for homogenous 2D nucleation (Markov, 2003) considering double-layered circular islands, the Gibbs free energy of a 2D cluster can be written as:

$$\Delta G = -\frac{2\pi r^2}{s} \Delta\mu + 2\pi r \kappa, \quad (3.10)$$

where r is a radius of a 2D cluster, $\Delta\mu$ is a chemical potential difference between molecules in a crystal and a solution, $s=1.06 \times 10^{-17} \text{ m}^2$ is the area one molecule occupies inside a nucleus (Nadajarah *et al.*, 1997) and κ is a ledge free energy of a 2D cluster. Following the classical nucleation theory, the steady state 2D nucleation rate, J , can be expressed as follows (Markov, 2003):

$$\ln J = \ln(\varpi \Gamma Z) - \frac{\pi s \kappa^2}{2k^2 T^2 \ln(C/C_e)}, \quad (3.11)$$

where ϖ is an attachment frequency of a solute molecule to a critical nucleus, Γ the Zeldovich factor, Z a 2D concentration of solute molecules on a crystal surface, k the Boltzman constant, C a solute concentration and C_e the solubility.

Figure 3.37 shows changes in $\ln J$ as a function of $1/[T^2 \ln(C/C_e)]$. On the {110} faces, excellent linear relationship was found for all the data points under a higher supersaturation range $\sigma > 0.80$ (orange solid line). This result demonstrates clearly that these data can be satisfactorily expressed

by Eq. (3) and the impurities did not affect the 2D nucleation rates in this higher supersaturation range: that is homogeneous 2D nucleation. However, the plots of lysozyme with impurities exhibit a kink at supersaturation $\sigma \approx 0.80$ (orange arrow), leading to the line with much smaller slope under a lower supersaturation range $\sigma < 0.80$ (orange dash-dotted line). This smaller slope indicates the occurrence of heterogeneous 2D nucleation in this lower supersaturation range.

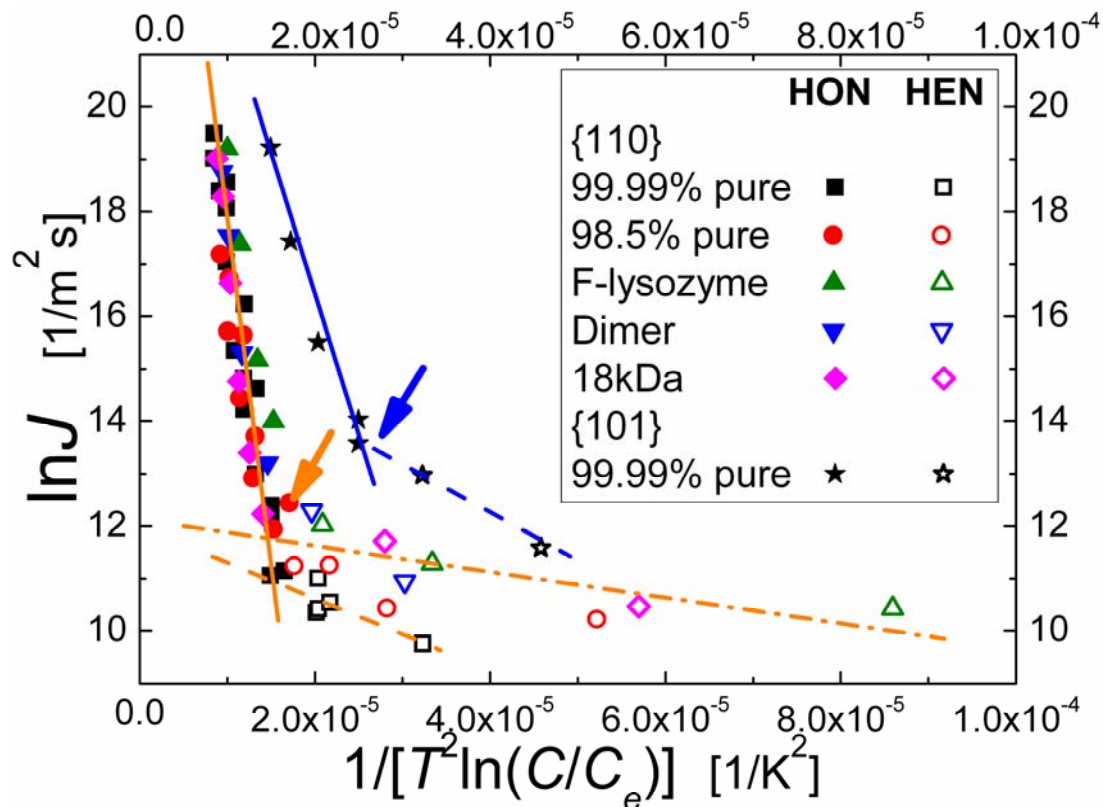


Figure 3.37 Changes in $\ln J$ as a function of $1/[T^2 \ln(C/C_e)]$, measured on $\{110\}$ and $\{101\}$ faces of tetragonal lysozyme crystals. Here, J is a 2D nucleation rate, T absolute temperature, C solute concentration and C_e the solubility. HON and HEN denote homogeneous and heterogeneous nucleation, respectively. Orange and blue solid lines represent homogeneous 2D nucleation under a higher supersaturation range, orange and blue broken lines for heterogeneous 2D nucleation in the purified lysozyme solution under a lower supersaturation range, and an orange dash-dotted line for heterogeneous 2D nucleation in the solution containing impure proteins under a lower supersaturation range. Arrows show kinks, at which solid and broken lines intersect each other.

On the {110} faces, even 99.99% pure lysozyme shows data points (orange broken line in Figure 3.37), at low supersaturation $\sigma < 0.80$, that deviate from the linear relationship found under the higher supersaturation range. Taking into account that 99.99% pure lysozyme solution contains less than 0.01% of impure molecules, it can be pointed out that the presence of very small amounts of impurities can influence the growth kinetics of protein crystals, as in the case of inorganic crystals (Botaris *et al.*, 1966). Although data are not shown, a certain induction time was observed for impurity effects on 2D nucleation. In the case of dimer, 1 day after the replacement of the solution in the cell with that containing dimer, the heterogeneous 2D nucleation became more pronounced. In contrast, in the case of F-lysozyme, a couple of hours after the replacement were enough to observe the significant heterogeneous 2D nucleation. The difference in the adsorption kinetics of these impure proteins would be responsible. Further studies are necessary to clarify the details of the adsorption kinetics. Also in case of F-lysozyme, at concentrations as low as 0.01%, heterogeneous nucleation could be observed (data not shown), this is an important indication that the heterogeneous nucleation observed for the purified solution (99.99%) was also caused by impure molecules.

Regarding the heterogeneous 2D nucleation under the lower supersaturation range ($\sigma < 0.80$), the possible contribution of strain induced on the crystal surfaces should be discussed. After seed crystals were grown in 98.5% pure lysozyme solutions, the crystals were placed in lysozyme solutions of different purity. Hence, it can be supposed that strain was induced in the crystals (origin of striations). However, in the case of 98.5% pure solutions (Seikagaku Co.), seeds crystal did not experience the replacement of solutions with different purity, hence such seed crystals did not include the strain induced by different purity. As shown in Figure 3.37, all the plots (including 98.5% pure lysozyme solutions) under the lower supersaturation range looked to follow the same line (orange dash-dotted line). Therefore, it is expected that the possible contribution of the strain

was not so significant under the experimental conditions used in this study, although the effects of strain cannot be excluded because of the small number of the data points measured in this supersaturation range. In contrast, under the higher supersaturation range ($\sigma > 0.80$), such strain did not give any significant effects since the large number of the data points clearly followed the same single line (orange solid line). Further systematic studies are necessary to clarify influence of strain on heterogeneous 2D nucleation in the near future.

The 2D nucleation rates measured on the {101} faces for the 99.99% pure lysozyme are also summarized in Figure 3.37. In the case of {101} faces, since elementary steps on the {101} faces involve one molecule per step (Durbin and Feher, 1990; Durbin and Carlson, 1992; Konnert *et al.*, 1994), the steady state 2D nucleation rate J can be written as follow, according to the classical nucleation theory (Markov, 2003):

$$\ln J = \ln(\omega \Gamma Z) - \frac{\pi s \kappa^2}{k^2 T^2 \ln(C/C_e)}, \quad (3.12)$$

where $s = 7.84 \times 10^{-18} \text{ m}^2$ (Nadarajah *et al.*, 1997). As shown in Figure 3.37, very similar results were obtained on the {101} faces. The $\ln J$ vs. $1/[T^2 \ln(C/C_e)]$ plots exhibit a kink at ≈ 0.45 (blue arrow), providing two straight lines corresponding to the homogeneous and heterogeneous 2D nucleation under high and low supersaturation ranges, respectively. Note that the homogeneous nucleation of the {101} faces (blue solid line) shows a smaller slope (smaller ledge free energy) than in the case of the {110} faces. This would correspond to the smaller step height (3.4 nm) of the {101} faces than that of the {110} faces (5.6 nm). It is also note worthy that much more significant heterogeneous 2D nucleation (blue broken line) was promoted on the {101} faces than on the {110} faces (orange broken line) by small amount of impurities (<0.01%) present in the 99.99% pure lysozyme solution. This result indicates that the different crystal structure of the {101} face from that of the {110} face would result in the larger amount of impurity effects. This corresponds well with observation done F-lysozyme (Matsui *et al.*,

2006) and dimer (Nakada *et al.*, 1999; Yoshizaki *et al.*, 2004) were a much stronger impurity was found on the {101} face.

Heterogeneous 2D nucleation under a low supersaturation range was for the first time reported in protein crystallization by Malkin and collaborators (1996a, 1999b) using AFM. They observed directly the appearance of individual 2D islands under a low supersaturation range for thaumatin and catalase. They suggested that nucleation in the low supersaturation range occurred at hyperactive sites e.g. on impurity particles and defects. In addition, molecular-level lateral resolution of AFM provides the possibility to observe near-critical-size clusters and their structure, as demonstrated by Yau and Vekilov (2002). However, Land and coworkers (1996) reported that the growth rates of canavalin crystals were enhanced by the scan of a cantilever of AFM, and Gliko *et al.* (2005) also argued that the variations in the step velocities of lumazine synthase crystals measured by AFM would result from the effects of a cantilever. The observation made for this work show that step velocities and 2D nucleation rates measured by AFM are considerably higher than those measured by LCM-DIM. The scan of a cantilever potentially affects the kinetics of 2D nucleation and also the small scanning size most likely biases the experimental data, although further detailed studies are necessary. In the case of indirect measurements of normal growth rates by traditional optical microscopy and interferometry ((Kurihara *et al.*, 1996; Kashimoto *et al.*, 1998; Suzuki *et al.*, 2000; 2005; Nagatoshi *et al.*, 2003; Asai *et al.*, 2004; Kurihara, 1997), no one has yet succeeded in observing the heterogeneous 2D nucleation of protein crystals, since normal growth rates of protein crystals are too slow at low supersaturation to obtain reliable data. Therefore, non-invasive and direct observation by advanced optical microscopy would have the highest potential to clarify 2D nucleation kinetics in protein crystallization.

From Equation 3.11 and the slopes in Figure 3.37, the ledges free energies on the {110} faces were determined. The values for the homogeneous and heterogeneous nucleation were summarized in Table 3.1. From the linear fitting of all data points under the higher supersaturation range $\sigma > 0.8$, the ledge free energies for the homogenous 2D nucleation (HON in Table 1) was obtained, and the ledge free energy for the heterogeneous 2D nucleation (HEN in Table 1) from the linear fits for the data points of the 99.99% pure solution and the solutions containing impurities under the lower supersaturation range, $\sigma < 0.8$. Kurihara *et al.* (1996) measured, by traditional optical microscopy, normal growth rates of {110} and {101} faces of tetragonal lysozyme crystals, under the same crystallization conditions adopted in this study (using 98.5% pure lysozyme, Seikagaku). They found no heterogeneous 2D nucleation under a lower supersaturation range, because of the measurements of averaged normal growth rates. By analyzing normal growth rates under a higher supersaturation range with the bird-and-spread model and considering double layered 2D islands, Kurihara (1997) obtained a value of $\alpha = 0.62$ mJ/m². This value agrees very well with our value for the homogeneous 2D nucleation. It is also note worthy that the ledge free energy of the heterogeneous nucleation for the 99.99% pure solution is larger than that for the solutions intentionally containing impure proteins. This would result from the difference in the impurity concentrations. But the difference between both curves is not significant enough and all data were fitted together.

The ledge free energies on the {101} faces determined from Equation 3.12 and the slopes in Figure 3.37 were also summarized in Table 3.1. For the homogeneous 2D nucleation, smaller ledge free energy were obtained on the {101} faces than on the {110} faces, as discussed above. However note that the surface free energies of the step ledges of the {101} and {110} faces are almost the same. This result clearly demonstrates that the difference in the ledge free energies of the {101} and {110} faces resulted from the

difference in the step heights. Our value of homogeneous nucleation for the {101} faces also agrees very well with that reported by Kurihara (1997).

Table 3.1 Ledge free energies κ [J/m] and surface free energies α [mJ/m²] obtained by the linear curve fittings of the experimental data shown in Figure 3.37 using Equations 3.11 and 3.12; α was calculated as $\alpha=\kappa/h$, here h is a step height (5.6 nm for {110} faces and 3.4 nm for {101} faces); HON and HEN denote homogeneous and heterogeneous 2D nucleation, respectively.

	Slope	κ (J/m)	α (mJ/m ²)	α (mJ/m ²) of other study
{110} faces				
HON	$(1.05\pm 0.10)\times 10^6$	$(3.5\pm 0.2)\times 10^{-12}$	0.62 ± 0.03	$0.62\pm 0.08^*$
HEN 99.99% pure				
	$(7.03\pm 2.8)\times 10^4$	$(0.89\pm 0.2)\times 10^{-12}$	0.16 ± 0.03	
HEN impurities				
	$(2.10\pm 0.89)\times 10^4$	$(0.5\pm 0.1)\times 10^{-12}$	0.09 ± 0.02	
{101} faces				
HON	$(5.42\pm 0.51)\times 10^6$	$(2.0\pm 0.1)\times 10^{-12}$	0.60 ± 0.02	$0.64\pm 0.13^*$
HEN 99.99% pure				
	$(1.04\pm 0.06)\times 10^4$	$(0.9\pm 0.04)\times 10^{-12}$	0.26 ± 0.01	

* These values were obtained by analyzing normal growth rates in 98.5% pure lysozyme (from Seikagaku Co.) solutions using the birth-and-spread model (5,41

Galkin and collaborators (2000), measured three-dimensional (3D) nucleation rates of tetragonal lysozyme crystals under the same conditions using 98.5% pure lysozyme (Seikagaku), and obtained a value of 0.64 mJ/m². This value also agrees well with our data obtained for the {110} and {101} faces. From this result, it can be conclude that there is no intrinsic difference between the surface free energies obtained from 2D and 3D nucleation rates, when intermolecular bonding inside a crystal are relatively symmetrical.

In the case of the 99.99% pure solution, the critical supersaturation σ^* for the {110} faces, below which 2D nucleation could not be observed, was $\sigma^*\approx 0.4$, and $\sigma^*\approx 0.2$ in the case of the solutions containing impurities. Below the critical supersaturation, no new 2D island appeared and growth only

occurred at the steps of 2D islands that already exist on the crystal surface. Once these steps completely spread over the entire surface, crystal growth stopped. In the field of structure analyses, it is generally believed that the advancement of steps is blocked by impurities under a low supersaturation range: this supersaturation range is called dead zone. However, by direct observation, it could be observed that in the case of tetragonal lysozyme crystals, there was no such dead zone caused by impurities. Although Vekilov *et al.* (1996) indirectly suggested the absence of such dead zone by interferometry, this study provided the direct evidence for the absence of the impurity-induced dead zone in protein crystallization.

In this study, it was demonstrated that impurities promote heterogeneous 2D nucleation under a low supersaturation range, even at very low impurity concentrations (0.01%), hence impurities of low concentration can be potentially used under a low supersaturation range to promote growth of protein crystals large enough to give high-resolution diffraction spots, since very small amounts of impurities do not give measurable effects on crystal quality (Yoshizaki *et al.*, 2004), although a very long time period will be necessary for obtaining such crystals.

3.6. Normal growth rate

Over the last 30 years, growth rates of tetragonal lysozyme crystals have been extensively studied by several groups. Normal growth rates were measured in function of supersaturation (Kam *et al.*, 1978; Pusey and Naumann, 1986; Monaco and Rosenberger, 1993; Kurihara *et al.*, 1996; Forsythe *et al.*, 1994), temperature (Forsythe and Pusey, 1994; Nadajarah *et al.*, 1995), precipitant concentration (Forsythe and Pusey, 1994) and impurity content (Vekilov and Rosenberger, 1996). The effect of pressure (Suzuki *et al.*, 2000) and forced flow (Vekilov and Rosenberger, 1998) on normal growth rates was also investigated. Recently, the kinetic roughening transition of tetragonal crystals was studied (Gorthi *et al.*, 2004; Gorthi *et al.*, 2005). For all these studies, both, regular optical microscopy and interferometry were applied.

In this work phase shifting interferometry, PSMI and CPSI, was used for measuring normal growth rates of spiral hillocks on {110} faces of tetragonal lysozyme crystals growing from purified solution (99.99%) in a supersaturation range of $C-C_e = 0 - 40$ mg/ml. Also a few measurements of 2D nucleation mediated growth were done. Results are shown in Figure 3.36a. In sections IV.1 and III.3 a detailed explanation of phase shift interferogram analysis can be found.

Data for normal growth obtained directly by PSI are shown in Figure 3.38a. In the low and intermediate supersaturation range normal growth rates of spiral hillocks are one or two orders of magnitude higher than 2D nucleation mediated growth. At higher supersaturations, $1.2 < \ln(C/C_e) < 1.6$, a small range of supersaturations exists where both a spiral growth mechanism and two dimensional nucleation becomes dominant. Once higher levels of supersaturation are reached, $\ln(C/C_e) > 1.6$, 2D nucleation mediated growth is dominant and a steep increase of growth rate is found.

Vekilov and coworkers also observed that in the supersaturation range of $1.4 < \ln(C/C_e) < 1.6$ 2D nucleation became the dominant growth mechanism.

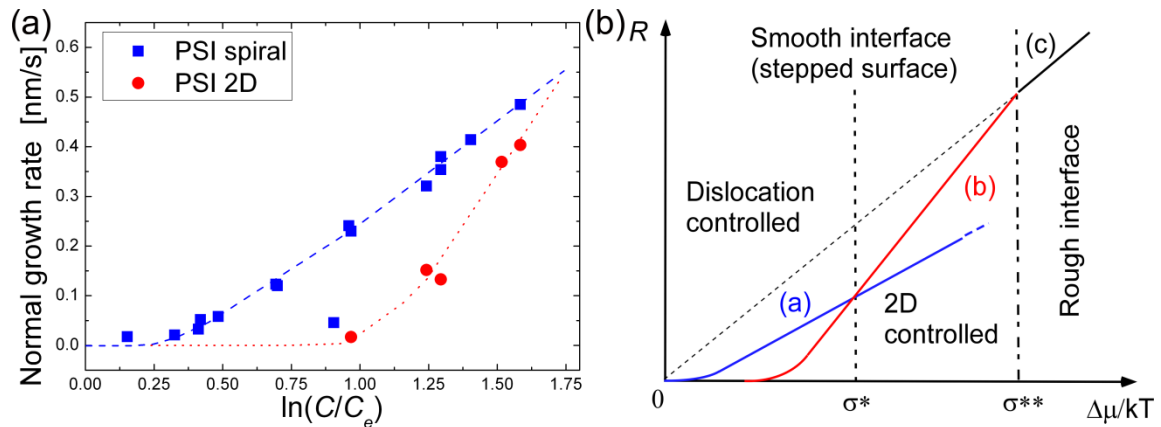


Figure 3.38 Normal growth rates measured by PSI for $\{110\}$ of tetragonal lysozyme growing from purified solution (a) R versus absolute supersaturation. (b) Schematic diagram showing the relation between growth rate R and chemical potential difference $\Delta\mu/kT$ for spiral growth, Birth and spread, continuous growth and the regions for smooth and rough interfaces.

The trend of the normal growth rate in function of chemical potential difference is described by the so called Sunagawa diagram shown in Figure 3.38d (Sunagawa, 1987). In the low supersaturation range the growth rate is dominated by dislocations and above a transitional supersaturation σ^* , the 2D nucleation mechanism is dominant. In the transitional region both spiral dislocations and 2D nucleation may operate and nucleation on the surface of spiral is also possible (van der Eerden, 1979). In this diagram a third regime is normally present, above a second transitional supersaturation σ^{**} , i.e. very high supersaturations, and corresponds to adhesive type growth. In this study not high enough levels of supersaturation were reached to observe adhesive growth. At these high supersaturations kinetic roughening occurs since critical nuclei will get the size of one atom. The need to grow with a layer mechanism is absent and the surface will roughen up and lose its crystallographic orientation. This type of growth has been reported for the growth of tetragonal lysozyme crystals by Pusey and coworkers (2004, 2005), who studied the kinetic roughening limit of lysozyme by ordinary optical microscopy. Kurihara and

cowokers (1996) also found that an adhesive growth mode may occur at very high supersaturation but they argued that examination of the growth mode at such high levels of supersaturation is difficult because spontaneous nucleation takes place. Thus in real crystallization experiments little growth will occur in the adhesive growth mode, because spontaneous nucleation will significantly lower supersaturation.

Growth rates fluctuations

Sometimes significant differences in normal growth rates for different crystals growing at the same supersaturation were found (blue circles in Figure 3.38a). This is most likely the result of changes in activity between different dislocation sources. In case of canavalin crystal growth (Kuznetsov *et al.*, 1995; 1995) it was even found that a same spiral dislocation during growth changed activity. In the observations made for this work spiral dislocations were growing at a constant rate in case of stable experimental conditions. In Figure 3.39 growth of a {110} face was observed for 19 hours and phase shifting images were taken every 67 s. The crystal was growing at a supersaturation of $C-C_e = 42.1$ mg/ml or $\ln(C/C_e) = 1.3$ ($T = 21.0^\circ\text{C}$). At the start of the experiment one spiral dislocation in the middle of the crystal surface dominates the entire face. As is clearly observed, growth is constant for the first 5 hours ($R = 0.34$ nm/s), after that the dislocation source suddenly disappears and 2D nucleation occurs ($R = 0.133$ nm/s) on the large terrace of the spiral hillock. Meanwhile in one of the corners a new spiral dislocations has emerged and, since the generation rate of growth layers is much higher for a dislocation at this supersaturation the spiral hillock is covering the area growing by 2D nucleation. This new spiral is growing at approximately the same rate, $R = 0.38$ nm/s, as the former one. After 12h the focus position of the interferometer has shifted slightly and good contrast interference fringes are lost.

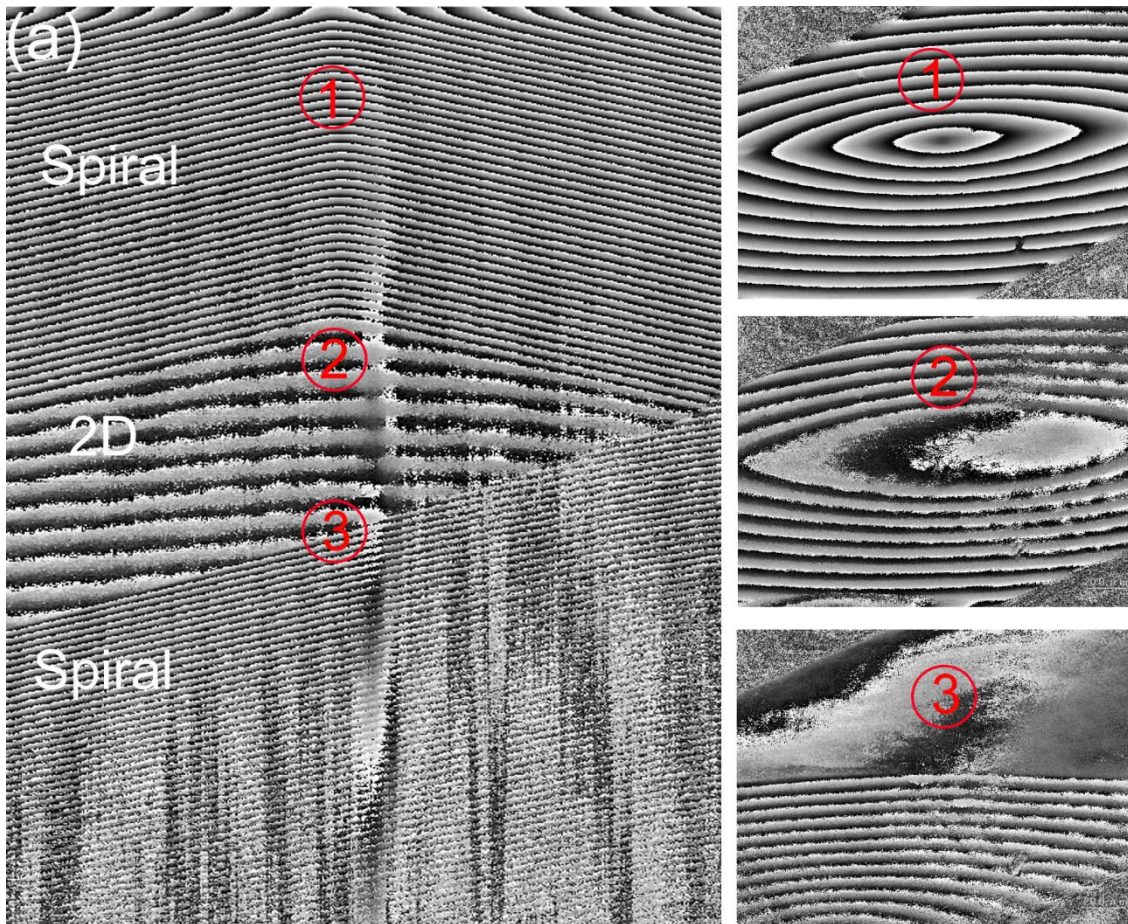


Figure 3.39 Time-space plot of phase shifting interferometry observation of spiral and 2D growth on a {110} face of tetragonal lysozyme.

From this experiment several preliminary conclusions can be drawn. First of all normal growth rate is constant provided a same source of step is present. Secondly, on the surface rapid changes between growth mechanisms can occur for no apparent reason.

Modeling normal growth rates

Besides direct observation by PSI, normal growth rates were also obtained from 2D nucleation rates and step velocities measured with LCM-DIM. When the dominant growth mechanism is 2D nucleation, growth rates can be calculated with the help of 2D nucleation models (Malkin *et al.*, 1989). Different models are available in the literature (Ohara and Reid, 1973; Chernov, *et al.* 1984, Malkin *et al.*, 1989):

1. Mononuclear two-dimensional model:

$$R = hSJ \quad \text{if} \quad S^{1/2} < (v/J)^{1/3} \quad (3.13)$$

2. Polynuclear two-dimensional model:

$$R = h\pi^2 J \quad \text{if} \quad v=0 \quad (3.14)$$

3. Birth and spread model:

$$R = h(v^2 J)^{1/3} \quad \text{if} \quad S^{1/2} > (v/J)^{1/3} \quad (3.15)$$

Here R is the normal growth rate, S crystal surface, v step velocity and J nucleation rate.

For tetragonal lysozyme only model (1) and (3) can be considered, since steps move at a certain velocity v and thus model (2) is not representative. In case of model (1), inequality of model 1 is not valid for any supersaturation level. Thus, over the entire supersaturation range, even at very low supersaturations inequality of model (3) is valid, or, in other words, growth proceeds by the Birth and Spread model. These observation complement with the results of Kurihara and collaborators (1996) how found for tetragonal lysozyme crystals that experimentally obtained normal growth rates in the supersaturation $1.9 < \ln(C/C_e) < 3.0$ were best fitted by the birth and spread model. Thus, surprisingly, tetragonal lysozyme crystals growth, even at low supersaturation, is of the Birth and Spread type. This is probably the result of low step velocity and relatively low nucleation barrier and the presence of heterogeneous nucleation.

The results of normal growth rates obtained from 2D nucleation rates and step velocities of {110} faces in the supersaturation range $\ln(C/C_e) = 0 - 1.6$ using mononuclear and Birth and Spread model are shown in Figure 3.38c. Clearly the mononuclear model strongly overestimates the normal growth rates. On the other hand the Birth and Spread model also drastically fails to reproduce the values of directly measured normal growth rates by interferometry. Most likely this due to strong anisotropy present in 2D islands shapes. The Birth and spread model is based on circular islands.

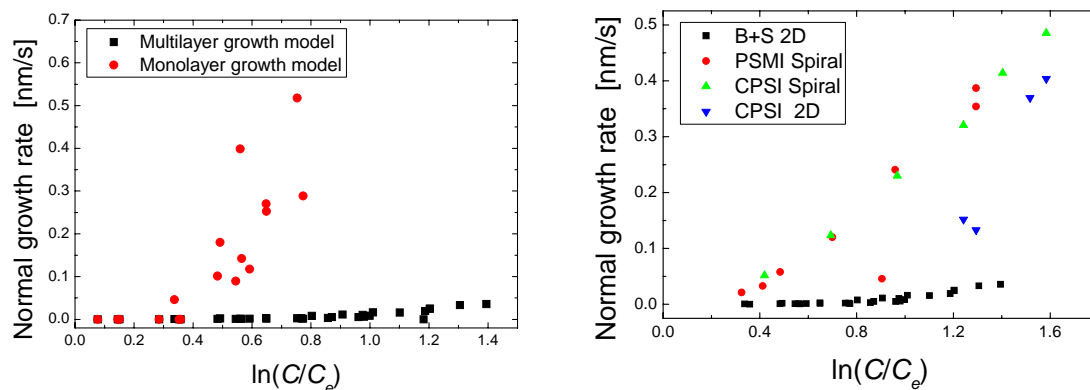


Figure 3.40 (a) Normal growth rates obtained from 2D nucleation growth models. (b) Normal growth rates measured by PSI for {110} of tetragonal lysozyme growing from purified solution.

3.7. Summary and conclusions

Step sources, surface morphologies and growth kinetics of tetragonal lysozyme crystals in unstirred solution with characterized protein composition have been studied. An overview of the most relevant observations is given here.

Growth mechanisms

2D nucleation of the birth and spread type was found to be the dominant growth mechanism for tetragonal lysozyme crystals under the conditions used in this study. For this reason most of the growth studies were done on faces showing 2D nucleation growth.

Spiral growth was occasionally observed only when microcrystals were adsorbed on the crystal surface and incorporated, or the crystals suffered mechanical stress. Spiral dislocations usually appeared in bundles but only one or two growth hillocks dominated an entire face and small secondary spiral hillocks were also found, which didn't significantly contribute to the normal growth rate. No relation was found between solution purity and density of growth hillocks. Spiral dislocations sometimes suddenly died leaving behind a large multilayer island spreading across the surface.

Step kinetics

2D islands formed in a 99.99% pure solution (Figure 3.19a) are lens-shaped with sharp tips. This shape results from an intrinsic anisotropy in the step velocity, being $\langle 001 \rangle$ the slow direction and $\langle \bar{1}10 \rangle$ the fast direction. The ratio of fast to slow directions is ~ 6 .

Intrinsic step kinetics were studied for crystal growth from purified solution (99.99%). Spiral hillocks and two dimensional islands formed in a 99.99% purity solution on {110} faces are lens-shaped with sharp tips and leaf-shaped (lozenge shape) with sharp tips on the {101} face. These shapes results from an intrinsic anisotropy in the step velocity. The anisotropy is much more pronounced on {110} face. The intrinsic anisotropy of step velocity is constant for the studied supersaturation range on both faces. The kinetic coefficients β were determined for the first time for different crystallographic directions, and it was found that β values for both faces are independent of temperature in the studied range 16.0 – 27.0°C, which indicates that the activation energy barrier for incorporation of solute molecules into the crystal is relatively high.

Experimental results showed clearly that incorporation of solute molecules is the rate determining step for lysozyme crystallization from unstirred solution. It was also found that surface diffusion was insignificant. Thus growth is mainly kinetically controlled for a low to middle supersaturation range $C-C_e = 0 - 45$ mg/ml, at higher supersaturation levels diffusion of solute molecules becomes more important.

From the analysis of step velocities it can be concluded that step advancement of 2D islands and spiral hillocks on both faces of tetragonal lysozyme crystals is constant over time provided steady experimental conditions. These results are in clear contradiction to those published by Vekilov and coworkers for tetragonal lysozyme crystals (Rosenberger *et al.*, 1996; 1999; Vekilov and Alexander, 2000; Vekilov and Rosenberger, 1998a; 1998b; 1998c; Vekilov *et al.*, 1995b; 1996; 1997; 1998; 1999). Thus observations made during this work put in serious doubt the theory of intrinsic instabilities of layer dynamics of tetragonal lysozyme crystal growth under steady solution conditions proposed by Vekilov and coworkers.

Impurity effect on step kinetics

To study the impurity effect on surface morphology and step kinetics of {110} faces purified solution with intentionally added impurities (F-lysozyme, Dimer and 18 kDa) and commercial available lysozyme solution containing a variety of impurities were used.

2D islands formed in a 99.99% pure solution (Figure 3.19a) are lens-shaped with sharp tips. In contrast, when pure lysozyme solution was intentionally contaminated with F-lysozyme, dimer or 18kDa 2D islands exhibit rounded tips. The same behavior was observed for Seikagaku lysozyme solution. Growth in the fast direction is more affected by impurities than that in the slow direction because of the higher kink density.

It was found that different impure proteins exhibited different dependencies of the suppression of the step velocity on supersaturation. The R vs. supersaturation plots of F-lysozyme showed a convex shape, whereas the plots of dimer and 18kDa presented a concave shape. The R vs. supersaturation plots of Seikagaku lysozyme exhibited a complex shape, which could not be reproduced by 99.99% pure lysozyme with intentionally added dimer and 18kDa.

To understand better the incorporation mechanisms of impurities the adsorption sites of individual molecules of F-lysozyme and F-dimer were observed *in situ* on {110} faces by Single Molecule Visualization. SMV and LCM-DIM observations of the same field of view revealed that F-lysozyme adsorbed preferentially on steps, whereas F-dimer adsorbed randomly on terraces. Indicating that impure molecules whose intermolecular bonding is close to that of the solute molecule adsorbs preferentially on a step, and that impure molecules whose intermolecular bonding differs from that of the solute molecule adsorbs on different sites of a crystal surface.

The R vs. supersaturation plots of F-lysozyme and dimer, taking into account the different adsorption sites of these impure proteins on the crystal surface could be successfully explained. The balance between the density of the adsorption sites and the exposure time of the adsorption sites to impurity played a key role.

The fact that R vs. supersaturation plot of 18kDa is similar to those of dimer suggested that 18kD also was adsorbed randomly on terraces. The complex R vs. supersaturation plots of Seikagaku lysozyme could not be reproduced, using two major impurities (dimer and 18kDa) and purified lysozyme, suggesting that trace amounts of other impurities (<0.01%) in Seikagaku lysozyme played a crucial role.

The effect of impurities presents in Seikagaku lysozyme on spiral hillocks was also studied. Steps on spiral hillocks were less affected by impurities. This is most likely due to the smaller interstep distances of spiral hillocks (<1 μm) compared to interstep distances of 2D islands at identical supersaturation. The smaller interstep distance of spiral hillocks reduced the exposure to impurities and thus reduced the amount of impurities that randomly adsorb on terraces.

The influences of other commercially available lysozyme solutions were studied. Surprisingly Fluka showed the fewest impurity effects. On the contrary Sigma lysozyme showed very severe step pinning, most likely produced by ovotransferrin a protein also present in hen egg white. The pinning effect was strongly reduced at high supersaturation because impurity molecules were not able to adsorb on the terraces anymore. This demonstrated again that exposure time of incorporation sites is crucial in case of impurity effects.

The evolution of spiral growth and step bunching during growth from Seikagaku (98.5%) solution showed the progressive development of macrostep formation with the distance steps had traveled relative to their origin. Growth from purified solution showed much less step bunching. This showed that macrostep formation is related with the interaction of steps and impurities (see for example van Enkevort, 1984; van der Eerden and Muller-Krumbhaar, 1986a; 1986b; Kandel and Weeks, 1994) and not only to intrinsic kinetic instabilities, as previously assumed (Vekilov *et al.*, 1996; Vekilov and Rosenberger, 1998a; Vekilov *et al.*, 1999). A new mechanism for step bunching was observed. Microcrystals adsorbed on the crystal surface induced the formation of periodic bunched step trains.

2D nucleation kinetics

Since 2D nucleation was the dominant growth mechanism and therefore was studied in detail. 2D nucleation rates were measured directly and non-invasively on the {110} and {101} face of the tetragonal lysozyme crystals by LCM-DIM for purified solutions and contaminated solutions.

2D nucleation occurred randomly on the entire crystal surface within the studied supersaturation range ($\sigma = 0 - 1.4$). Repeated 2D nucleation, continued for 3 to 4 layers, was observed mainly when impure proteins were present in the solution. The interstep distances of the concentric 2D islands generated repeatedly were irregular. The multilayer 2D islands were formed when relatively large foreign particles were adsorbed on the crystal surface. In some very rare case, many consecutive layers were formed leading to the formation of 2D hillocks that dominated the whole surface. This growth mechanism was never observed before in protein crystal growth.

On {110} faces, the homogeneous 2D nucleation occurred under higher supersaturation range $\sigma > 0.8$, irrespective of the presence of impure proteins. In contrast, the significant heterogeneous 2D nucleation was

observed under the lower supersaturation range $\sigma < 0.8$, mainly when the impure proteins were present in the solution. The {101} faces exhibited similar homogeneous and heterogeneous 2D nucleation, however {101} faces showed more significant heterogeneous nucleation than {110} faces in case of 99.99% pure lysozyme solutions.

Ledge free energies of homogeneous and heterogeneous 2D nucleation were determined. The latter did not show significant dependence on the kinds of impure proteins within the experimental conditions adopted in this study. The difference in ledge free energies of homogeneous nucleation on {110} and {101} faces could be satisfactorily explained by the difference in the step heights.

For the entire supersaturation tetragonal lysozyme crystal grow by the Birth and Spread model, even at low supersaturation no mononuclear growth is observed. Modeling normal growth rates from 2D nucleation rates and step velocities fails to reproduce experimentally obtained normal growth rate data probably because the model assumes circular 2D islands and in case of the {110} a strong anisotropy of the 2D islands shape was present. If spiral dislocations are present on a crystal surface the normal growth rates will be 1 to 2 orders higher compared to 2D nucleation mediated growth. Once middle supersaturation levels are reached the dominant step generating mechanism is 2D nucleation.

4. Growth kinetics of tetragonal lysozyme crystals in gelled solution

4.1. Introduction

Efforts to produce higher quality crystals have led to the search for conditions which may benefit crystal growth. One of the methods used to obtain higher quality protein crystals is growth in gelled media (Robert and Lefauchaux, 1988; Provost and Robert, 1991; Miller, He and Carter, 1992; Narayana *et al.*, 1991; Robert *et al.*, 1992). The use of gels may benefit crystal growth in several ways. By reducing or eliminating density driven and Marangoni convective flow patterns, a more controlled environment may be generated around crystal growth surfaces. The sedimentation of nucleated crystals is minimized with the gel matrix. Protein crystals grown in gels have exhibited lower percentages of growth defects, e.g. better quality, by X-ray topography analysis (Robert and Lefauchaux, 1988; Provost and Robert, 1991, Lorber *et al.*, 1999a, Vidal *et al.*, 1999; Lorber *et al.*, 1999b, Moreno *et al.*, 2005). Gel media also extended the domain for which usable monocrystals are obtained by minimizing the impact of contaminant (Provost *et al.*, 1995; Hirschler *et al.*, 1996), and reduces the influence of nucleation factors (Hirschler *et al.*, 1995). It was also found that lysozyme concentrations and interactions in agarose gel and gel-free media are essentially the same (Finet *et al.*, 1998; Vidal *et al.*, 1998). In this respect, gel is neutral and supersaturation is not changed. On the other hand it was shown that agarose gel acts as a nucleation promoter (Hirschler *et al.*, 1995; Vidal *et al.*, 1998). Agarose gel has also been extensively characterized as a crystallization media (García-Ruiz *et al.*, 2001, Gavira and García-Ruiz, 2002) and a wide variety of macromolecules have been successfully crystallized in gelled media. (Biertumpfel *et al.*, 2002).

A striking peculiarity of crystals grown in gel is that they “trap” the gel within the crystal volume, incorporating the apparently undistorted three dimensional frameworks of cross-linked agarose fibers (Gavira and García-Ruiz, 2002). Although incorporation of gel fibers does not seem to have any major impact on the X-ray diffraction quality of the crystals (Lorber *et al.*, 1999), chemical interaction must exist between the gel fibers and the protein molecules, thus agarose gel can be qualified as a potential impurity for the crystal growth process. The study of the impact of gel fibers on crystal growth kinetics has been restricted to three dimensional nucleation, showing (Hirschler *et al.*, 1995; Vidal *et al.*, 1998). But crystal quality is much more related to growth kinetics than to nucleation and, up today, it is not know if agarose gels operate as an impurity, as an impurity filter or both.

In this chapter the dual character of agarose gels in crystal growth experiments is investigated from the viewpoint of growth kinetics. LCM-DIM was used to observe 2D nucleation and advancement of elementary growth steps on {110} faces of tetragonal crystals growing in a gelled solution. First, highly purified lysozyme (99.99%) was used to study the possible influence of gel on the growth kinetics of protein crystals and secondly, commercially available lysozyme (98.5%) was used to study the effect(s) of impure proteins on growth kinetics in gelled solution. Gelled solutions at different concentrations (Ca), 0.025%, 0.075%, 0.125% and 0.175% (w/v) were prepared following the protocol given by Gavira (2000).

4.2. Effect of agarose gel on growth kinetics

To test for the effects of agarose gel on lysozyme crystallization, a series of experiments were performed using exclusively purified lysozyme

solutions (99.99% pure). All results in this subsection come from these “almost” impurity-free experiments.

4.2.1. Step Morphology

Lens-shaped 2D islands, pointed in the $\langle\bar{1}10\rangle$ direction and having an elementary step height of 5.6 nm (Durbin and Carlson, 1992; Konnert *et al.*, 1994; Li *et al.*, 1999), develop on the {110} face of tetragonal lysozyme crystals growing from ungelled purified solutions (Figure 4.1a). When the same experiment is repeated using gelled solutions (Figure 4.1b-e), images look noisier owing to the presence of gel fibers in the confocal plane and show the steps roughed to some degree, most likely due to local inhomogeneities of the step velocity induced by the trapping of fibers (Gavira and García-Ruiz, 2002), but the overall island shape is very similar to the one observed for free solution growth (Figure 4.1a). Consequently the presence of gel fibers has not a major impact on the overall island morphology.

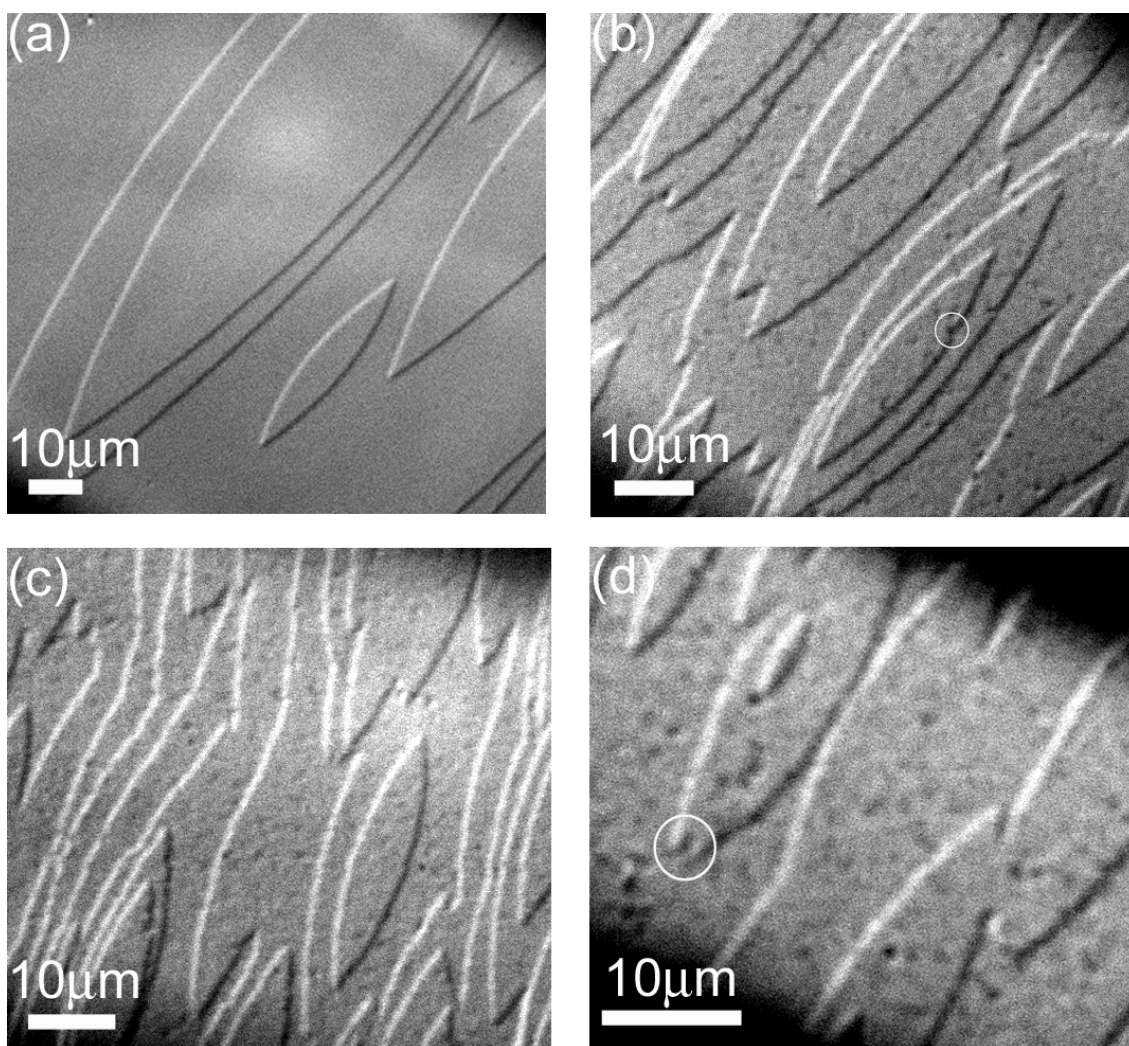


Figure 4.1 LCM-DIM photomicrographs of the morphology of 2D islands on $\{110\}$ faces of growing tetragonal lysozyme crystals. (a) 0% gel, (b) 0.075% (w/v) gel, (c) 0.125% (w/v) and (d) 0.175% (w/v). White circle indicate trapping of gel fibers by advancing step fronts.

4.2.2. 2D nucleation rates

Within the range of supersaturation $\ln(C/C_e) = 0.3 - 1.3$ and agarose concentration $C_a = 0 - 0.175\%$ used in our experiments, 2D nucleation was observed to occur randomly over the entire crystal surface, as was the case in free solutions (Van Driessche *et al.*, 2007), neither repeated nucleation nor growth of multilayer islands was observed in purified gelled solutions (99.99%). Most likely a gelled solution prevents foreign particles or microcrystals from reaching the crystal surface. 2D nucleation rates

measured for different supersaturations and gel concentrations are shown in Figure 4.2.

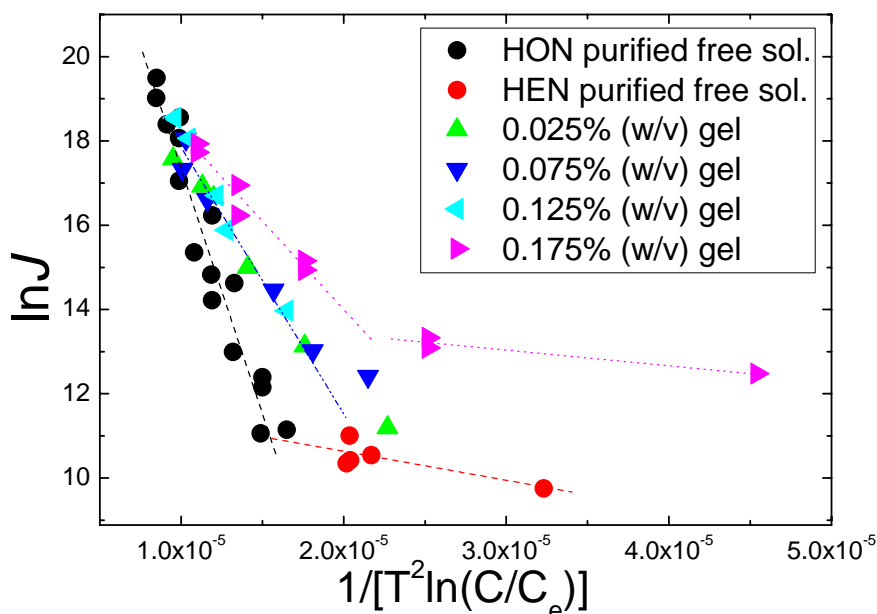


Figure 4.2 Changes in $\ln J$ as a function of $1/[T^2 \ln(C/C_e)]$, measured on $\{110\}$ faces of tetragonal lysozyme crystals.

Two clearly different regimes are observed for the 2D nucleation rate from ungelled solutions (filled disks in Figure 4.2) as indicated by the two dashed regression lines. The crossover between these regimes is around $\ln(C/C_e) = 0.8$. This behavior in the case of tetragonal lysozyme has been explained as due to the transition from heterogeneous to homogeneous nucleation as supersaturation increased (Van Driessche *et al.*, 2007). This crossover was also observed in the gelled solution experiments (triangles in Figure 4.2) as indicated by the two dotted regression lines fitted to the data of agarose concentration $C_a=0.175\%$, but more data, at different gel concentrations, are necessary to confirm this observation. If this crossover is observed for both gelled and ungelled solution this transition is not due to heterogeneous nucleation on gel fibers but would probably be related to impurities adsorbed on the crystals as was discussed previously for heterogeneous 2D nucleation on crystal growing from free solution (Van Driessche *et al.*, 2007).

The 2D nucleation rates in purified solutions of gelled and ungelled experiments were fitted to linear relations accounting for the expected supersaturation dependency of the homogeneous nucleation rate given by Equation 3.3 (section IV.3.5). Analysis of variance³³ of the data factorized by agarose concentration was used to test for statistically significance differences in slopes. Only the homogeneous nucleation part of the data under a higher supersaturation range was used for the regression. Three distinct groups of data showing statistically significant differences of slopes within the 5% confidence level were identified by this analysis. They correspond to: a) the free solution data (black dashed line in Figure 4.2), b) the highest agarose concentration ($C_a=0.175\%$, bark yellow dotted line) and c) the low and middle agarose concentration experiments together (blue dash-dotted line). Consequently there is a clear effect of gel in the exponential term of the nucleation rate equation; this effect has the same magnitude for agarose concentrations up to 0.125% and is larger for $C_a=0.175\%$. Probably in the range 0.025% - 0.125% (w/v) of gel concentrations a gradual increase of nucleation rate should be found as well but due to experimental error this tendency was not observed clearly in the data.

4.2.3. Step velocities

Figure 4.3 shows average step velocities v measured for different supersaturations and agarose concentrations for crystals growing from purified lysozyme solutions. Step velocity is intrinsically anisotropic, typically 6 times larger in the $\langle\bar{1}10\rangle$ (fast) direction than in the $\langle 001\rangle$ (slow) direction. Only the data in the $\langle\bar{1}10\rangle$ direction are plotted for clarity, but the same conclusions are derived from the data in the $\langle 001\rangle$ direction. In the Kossel model, the step velocity is expected to be a linear function of supersaturation. The data points for ungelled solutions (filled disks in Figure 4.3) shows this linear dependency for $C-C_e > 10$ mg/ml, below this

limit, the slope continuously decreases for decreasing supersaturation probably due to the presence of impurities, even in the highly purified samples as was discussed before. Step velocity values for all the experiments in gelled solutions (open symbols) are also linearly dependent on the supersaturation with the same trend but with slightly smaller velocity, at least at low supersaturation. These data were fit and tested for significant differences as well, but no significant slope differences were found within the 5% or even 10% confidence limit. This means that the effect of gel, if any, only account for a small decrease in the step velocity that is not statistically significant.

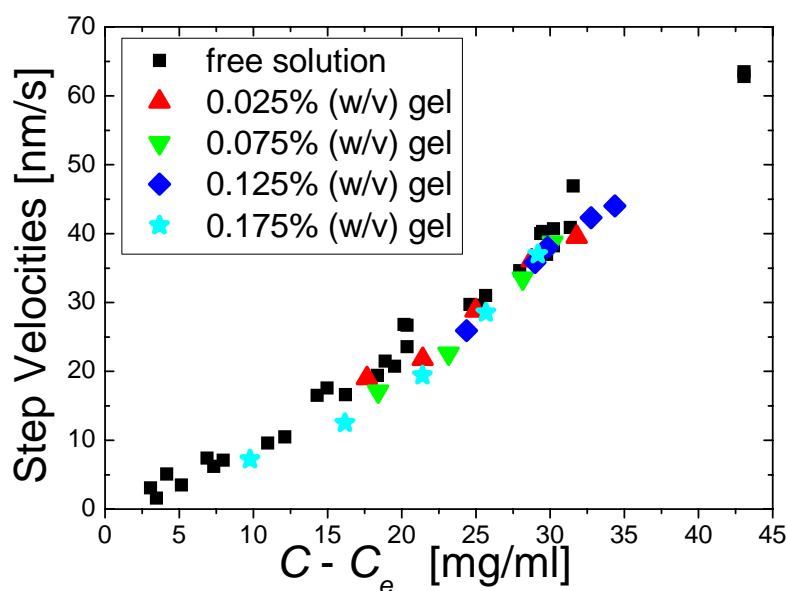


Figure 4.3. Step velocities v in $\langle\bar{1}10\rangle$ directions measured on $\{110\}$ faces of tetragonal lysozyme crystals under various supersaturations and agarose gel concentrations by LCM-DIM.

4.3. Effect of impurities on growth kinetics in gelled solution

A second series of experiments were performed using the same setup and procedures but this time protein solutions were prepared from

commercial grade lysozyme (98.5% pure) to test for the effect of protein impurities. All the results reported in this subsection refer to these “commercial grade lysozyme” experiments.

4.3.1. Step morphology

Figure 4.4a shows the typical elliptical shape of 2D islands growing from an ungelled commercial grade lysozyme solution. This shape is clearly different from the pointed lens shape shown in Figure 4.1 due to the anisotropic effect of impurity incorporation that results in a larger retardation of the steps in the fast (pointed) direction. Surprisingly, the morphology of 2D islands growing from gelled commercial grade lysozyme solution (Figure 4.4b-e) is closer to that of purified solutions (Figure 4.1a-e). This lens-like morphology is systematically observed in gelled solutions at $C-C_e > 25$ mg/ml despite the presence or absence of impurities.

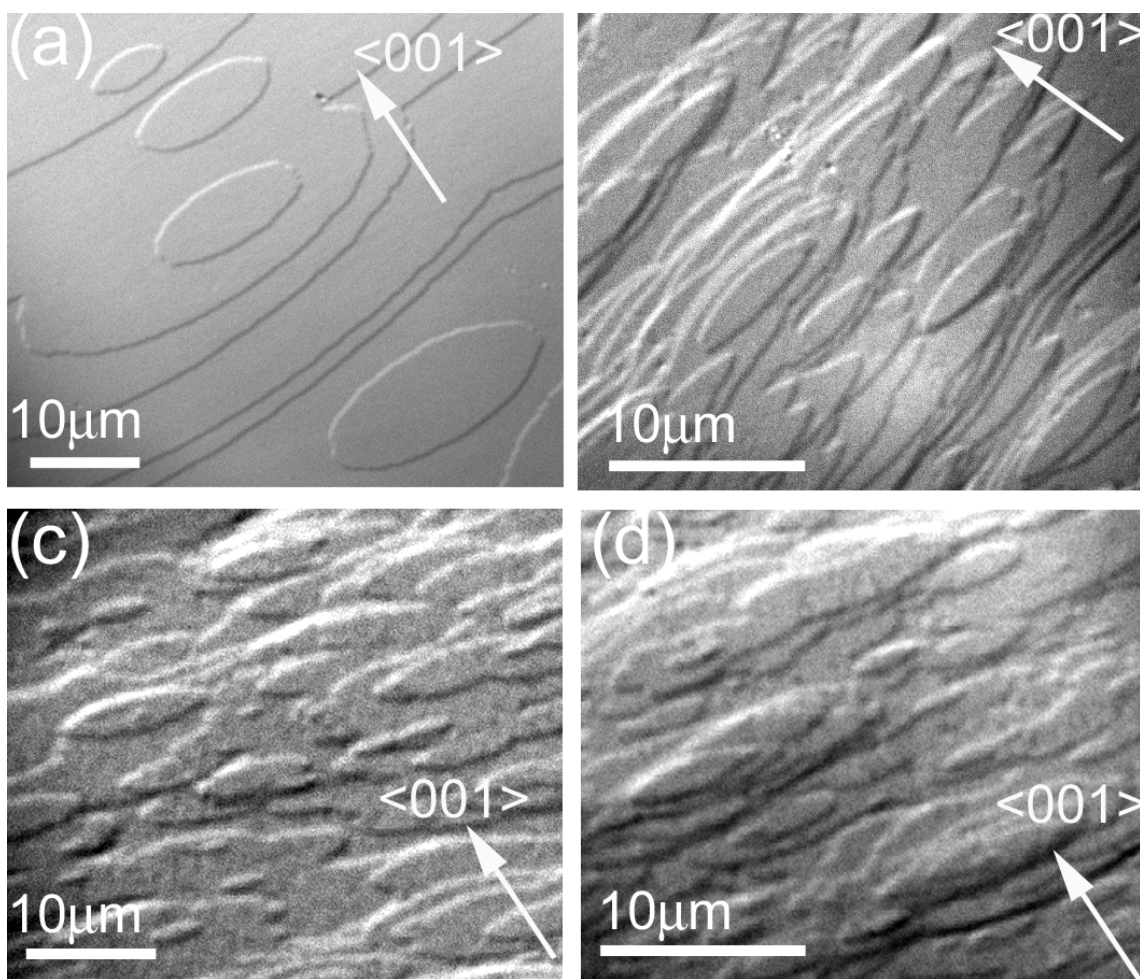


Figure 4.4 LCM-DIM photomicrographs of the morphology of 2D islands on $\{110\}$ faces of tetragonal lysozyme crystals. (a) 0% gel, (b) 0.075% (w/v) gel, (c) 0.125% (w/v) and (d) 0.175% (w/v).

4.3.2. 2D nucleation rates

As in the experiments using purified lysozyme, 2D nucleation was observed to occur randomly over the entire crystal surface without repeated nucleation or formation of multilayer islands. As shown in Figure 4.5, the 2D nucleation rates are also increased in these experiments by the presence of agarose gel, but this effect is almost independent of the gel concentration and, in overall, significantly smaller than in the case of purified lysozyme. 2D nucleation rate slightly increases from agarose concentration $C_a = 0.025\%$ to 0.075% and then stays constant for 0.125% and 0.175% but the difference in slopes and hence step ledge energies κ between these two

groups are not statistically significant so they are fitted together by the dotted regression line in Figure 4.5.

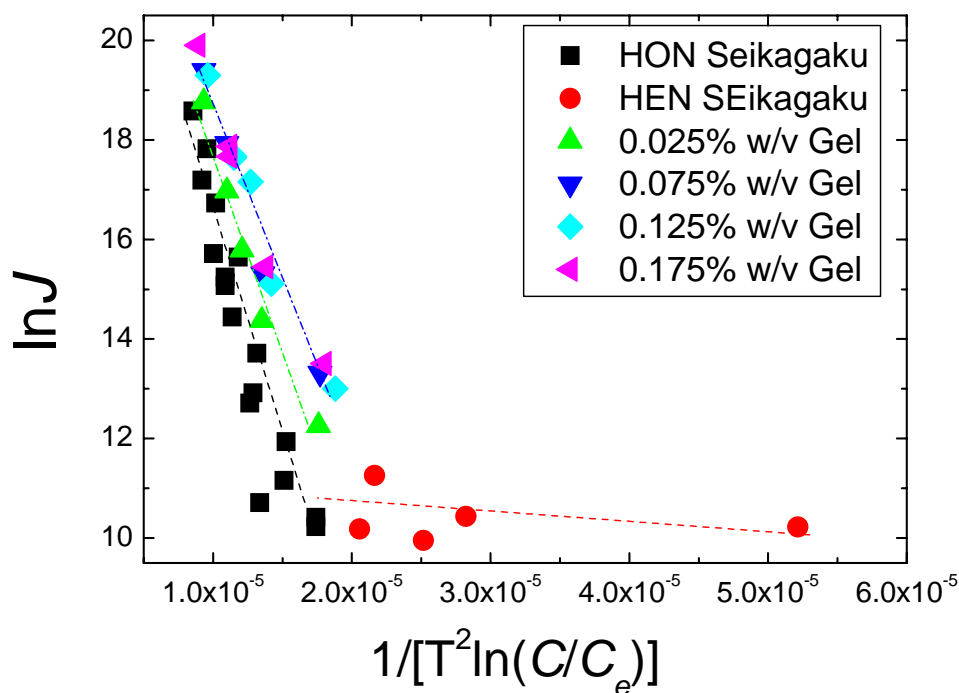


Figure 4.5 Changes in $\ln J$ as a function of $1/[T^2 \ln(C/C_e)]$, measured on $\{110\}$ faces of tetragonal lysozyme crystals.

4.3.3. Step velocities

As reported before, crystals grown from a free solution of commercial grade lysozyme (solid disks and dashed regression lines in Figure 4.6) experienced a significant reduction of the step velocities with respect to purified solutions (red dots in Figure 4.6) especially in the lower supersaturation range indicating a strong impurity effect. Above a critical supersaturation at $C-C_e = 20$ mg/ml, a rapid increase in step velocity occurred and step velocities become similar to the purified solution experiments around $C-C_e \approx 35$ mg/ml. Figure 4.6 also shows the step velocities found for commercial grade lysozyme in gelled solution (open symbols and dotted regression line). There is a clear influence of the gelled solution on the step velocity for commercial grade lysozyme solutions. The velocity of the step is still reduced but lies between the values for purified

free solutions and commercial grade free solutions. The slope of gelled impure solutions is practically the same as that of ungelled impure solutions. No significant effect of the gel concentration in the step velocity was observed.

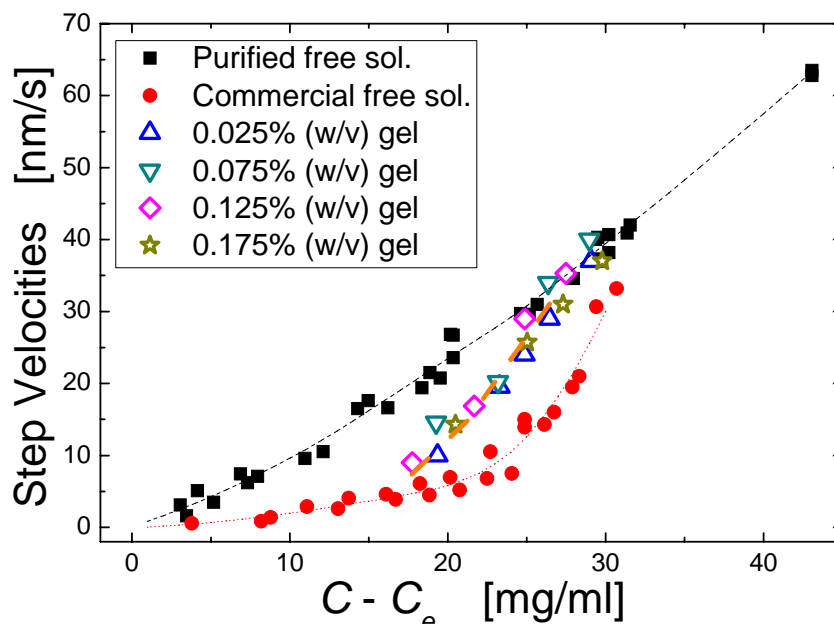


Figure 4.6 Step velocities v in $\langle 110 \rangle$ directions measured on $\{110\}$ faces of tetragonal lysozyme crystals under various supersaturations and agarose gel concentrations.

4.4. Discussion

2D nucleation

The birth and spread mechanism for crystal growth, of widespread application to most growth situations at intermediate supersaturation levels, explains the growth of the crystal interface as a consequence of successive events of 2D nucleation and lateral spread of such nuclei to cover the crystal surface. Both the nucleation of 2D islands and the growth of these islands are modified by the presence of impurities.

In the classical theory nucleation rate for 2D islands with bimolecular height is expressed as (Markov, 2003; Van Driessche *et al.*, 2007)

$$J = A \exp\left(-\frac{\pi s \kappa^2}{2k^2 T^2 \ln(C/C_e)}\right), \quad (4.1)$$

In our previous work we showed that above a certain supersaturation $\ln(C/C_e) > 0.8$ data obey this relationship for crystals grown from a free solution. From our measured 2D nucleation rates in gelled solution it is observed that presence of gel fibers increases nucleation rates. It was shown before that lysozyme concentrations and interactions in agarose gel and gel-free media are essentially the same (Vidal *et al.*, 1998; Finet *et al.*, 1998). In this respect, gel is neutral and supersaturation is not changed. If an increase of supersaturation would be the cause of increased nucleation rates then no change in the slope would be observed but a parallel displacement of the nucleation curve should be found, which is not the case. Figure 4.2 shows clearly a change in slope for 2D nucleation rates in gelled solution. Thus gel fibers act as heterogeneous nucleation sites by lowering the nucleation barrier.

Heterogeneous 2D nucleation has been addressed seldom in the literature, despite the wide field of application in real crystal growth experiments. The basic idea is that an impurity present at the crystal surface can promote or reduce 2D nucleation depending on the energies of heterogeneous nucleation. Impurities that reduce the surface energy contribution for the 2D nuclei will increase the 2D nucleation frequency while impurities increasing this surface energy will reduce 2D nucleation poisoning the surface growth. The analysis of this problem by Liu and collaborators (1997) predicts an effect of impurities leading to a nucleation frequency

$$J = A \delta \exp\left(-\frac{\pi s \kappa^2}{2k^2 T^2 \ln(C/C_e)} f\right), \quad (4.2)$$

where f and δ range from zero to one and account for all the effects of nucleating particles involved in heterogeneous nucleation. This also means that setting $f = \delta = 1$, Equation 4.2 reduces to the common equation for homogeneous nucleation (Equation 4.1). Therefore in case of heterogeneous nucleation, a plot $\ln J$ versus $1/[(kT)^2 \log(C/C_e)]$ will produce a line with a slope f times larger than the one of the experiment lacking nucleating particles and an intercept shifted by $\ln \delta$. Since $f \leq 1$ and $\ln \delta \leq 0$, f and δ accounts, respectively, for an exponential increase and a linear decrease of the nucleation rate. Usually, the exponential increase due to f is dominant as was the case in the experiments reported in this paper. A complete discussion of this heterogeneous 2D model is given by Liu and co-workers (1997) but to consider our results only f will be considered because changes in δ are negligible. It is know that f is a function of the wetting angle θ and the ratio x between the impurity radius R^s and the radius of the critical nucleus r_c .

$$f(m, x) = \frac{1}{\pi} \left\{ \begin{array}{l} \arccos[(xm - 1)/w] + (x^2 - 2xm) \\ \times \arccos[(x - m)/w] - (1 - xm) \\ \times [w^2 - (1 - xm)^2]^{1/2} / w^2 - x^2(x - m) \\ \times [w^2 - (x - m)^2]^{1/2} / w^2 \end{array} \right\} \quad (4.3)$$

where $w(m, x) = (1 + x^2 - 2xm)^{1/2}$. The wetting angle θ at the crystal-solution-fiber interface is defined by the Young equation:

$$m(\theta) = \cos \theta = (\gamma_{sf} - \gamma_{sc}) / \gamma_{cf} \quad (4.4)$$

where γ_{sc} , γ_{sf} and γ_{cf} are specific surface energy of the interfaces of nucleating particle-embryo, nucleating particle-mother phase and embryo-mother phase. A schematic representation is show in Figure 4.7. The ratio x is obtained from:

$$x(R^s, r_c) = R^s / r_c \quad (4.5)$$

where R^s is the radius of a nucleating particles, r_c is radius of a critical nucleus.

Notice that when $x \rightarrow 0$ solid particles stop acting as nucleating particles, i.e. if embryos are much larger than the nucleating particles no heterogeneous nucleation will occur.

If $m \rightarrow -1$ the nucleating particle cannot be wetted by the embryo and the nucleation particle will be rejected from the crystal. On the other hand when $m \rightarrow 1$ complete wetting exists between the embryo and nucleation particle and the nucleating particle will be preferentially incorporated into the crystal. When $m \approx 0$, nucleation particles will be little wetted by the embryos. In this case characteristics of the nucleating particle, e.g. elasticity of gel fibers, will determine if these particles are incorporated or not.

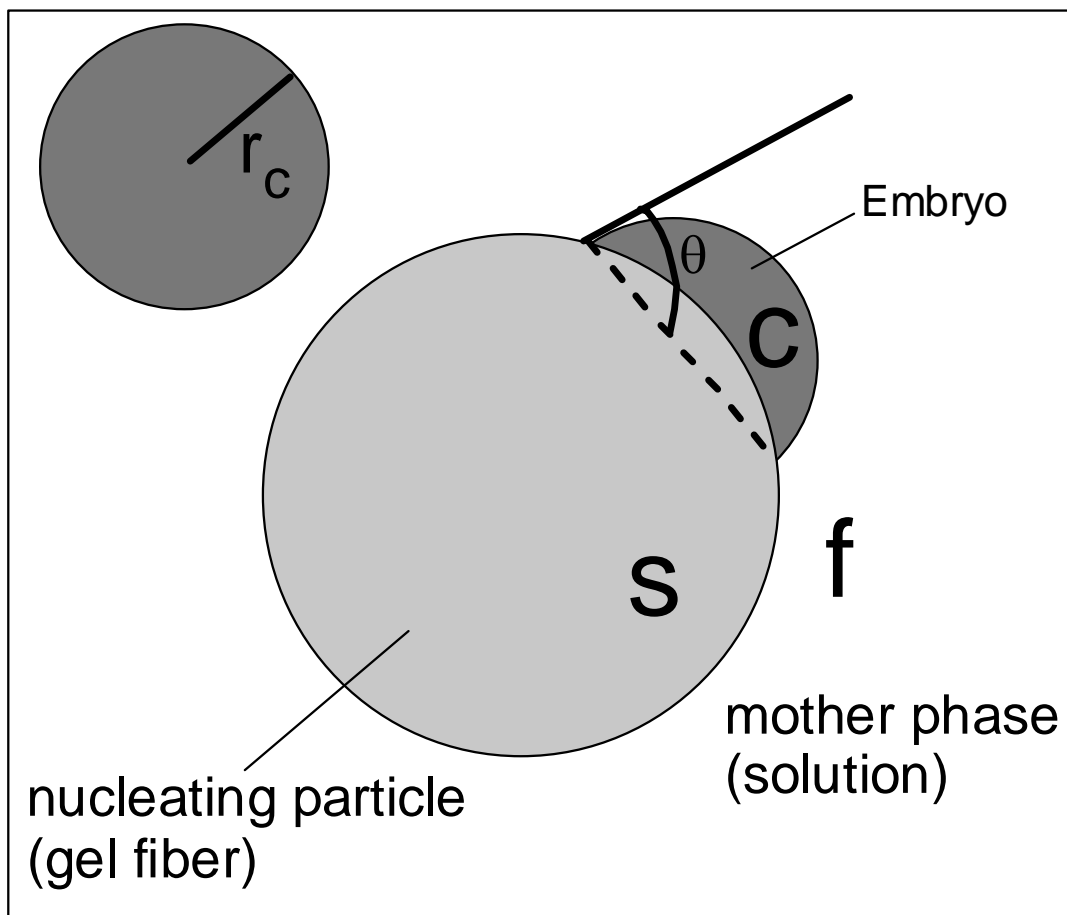


Figure 4.7 Schematic illustration of heterogeneous 2D nucleation. Embryo “c” on nucleating particle “s” in mother phase “f”. (Adapted from Liu *et al.*, 1997)

From the fitted data in Figure 4.2, f factors are obtained for the different agarose concentrations: $f_{0.025}=0.64$, $f_{0.075}=0.58$, $f_{0.125}=0.62$ and $f_{0.175}=0.39$. The critical 2D nuclei radius r_c for free solution, within the $0.8 < \ln(C/C_e) < 1.4$ range for homogeneous nucleation, is obtained from

$$r_c = \frac{\Omega\gamma_{cf}}{2kT \ln(C / C_e)} \quad (4.6)$$

and ranges between 1.7 nm and 3.2 nm. Assuming a mean value of 6 nm for the radius of the agarose fibers (Waki *et al.*, 1982), the values of $x = R^S/r_c$ in our experiments will be in the range 1.87—3.52. Using these values, it is possible to compute the value of m (Figure 4.8) applying Equation 4.5. Within this range of x values, the m values experimentally obtained correspond to $-0.132 < m_{0.025} < -0.056$, $-0.033 < m_{0.075} < 0.046$, $-0.099 < m_{0.125} < -0.021$ and $0.266 < m_{0.175} < 0.348$. This means that the value of m is close to zero but negative except in the cases of higher agarose concentration. Probably at high agarose concentration the radius of the agarose fiber increases (Waki *et al.*, 1982) but at present no precise data on gel fiber diameters are available. The fact that for $C_a = 0.075\%$, $m_{0.075}$ becomes positive at low supersaturation is most likely due to experimental error.

After Equation 4.6, Figure 4.8 indicates that interactions of agarose fibers within the crystal lattice are weak. At higher gel concentration ($C_a = 0.175\%$) the incorporation of gel fibers is energetically favorable because the specific surface energy of the fiber/solution interface is higher than the specific surface energy of the fiber/crystal interface. This result is in good agreement with the previously reported observations of agarose fibers incorporated into the lysozyme crystal volume (Gavira and García-Ruiz, 2002). For the lower gel concentrations the excess energy is probably smaller than the elasticity of gel fibers and thus fibers will be preferentially incorporated. The fact that $m \approx 0$ is also consistent with the almost negligible effect of agarose fibers on the step velocity. Gel fibers will interact weakly with the advancing steps and no strong step pinning will occur.

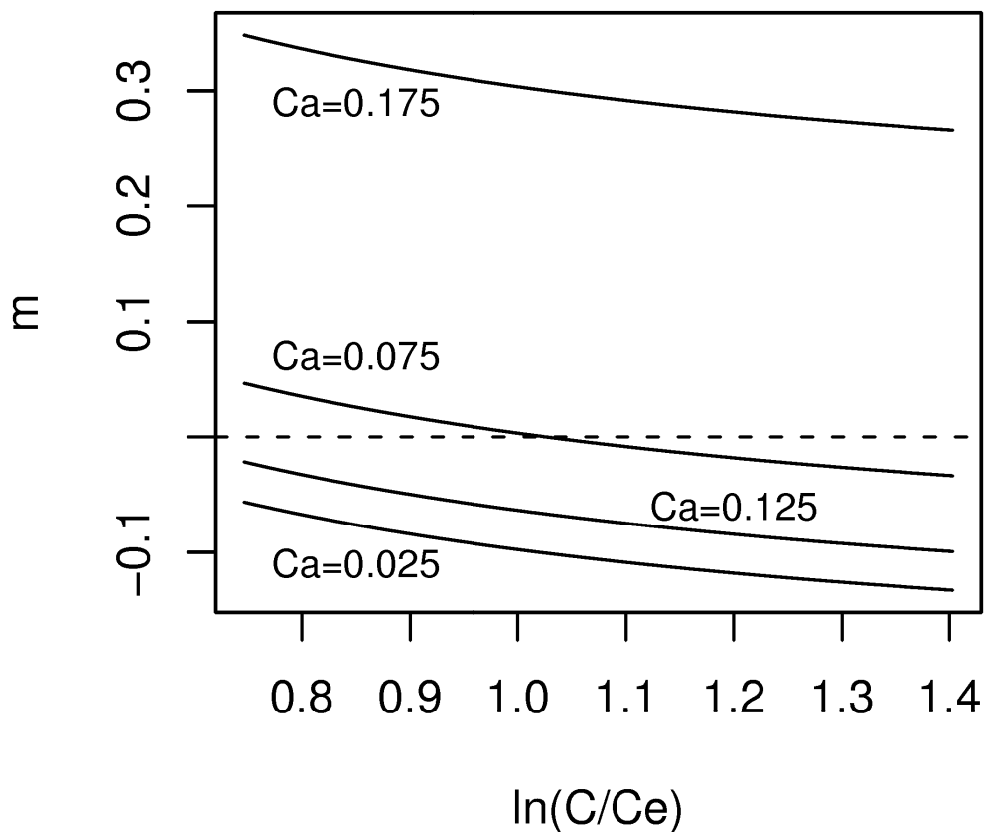


Figure 4.8 Computed values for the cosine of the wetting angle, m , (Equation 4.4) as a function of supersaturation for different values of agarose concentration Ca .

The observed reduction of the nucleation rate in gelled impure solutions with respect to gelled pure solutions is more difficult to explain with the data available from these experiments. One plausible hypothesis could be that the impurities have more affinity for the gel fibers than the lysozyme molecules and attaches preferentially to the gel fibers. This could decrease m either via γ_{sc} or γ_{sf} leading to an increase of f and consequently a reduction of J , but no data are currently available to check this effect.

From Equation 4.1 and the slopes in Figures 4.2 and 4.5 the ledges free energies on the $\{110\}$ faces were determined for crystals growing from

free solution. For gelled solution effective ledge free energies κ^{eff} were determined. Obtained values are shown in Table 4.1.

Table 4.1 Ledge free energies κ [J/m] and surface free energies α [mJ/m²] obtained by the linear curve fittings of the experimental data shown in Figure 2 using Eqs. (3); α was calculated as $\alpha=\kappa/h$, here h is a step height (5.6 nm for {110} faces and 3.4 nm for {101} faces); Apparent Ledge free energies κ^{eff} [J/m] and surface free energies α^{eff} [mJ/m²] obtained by the linear curve fittings of the experimental data shown in Figure 4.2 and 4.5 using Equation 4.1; α^{eff} was calculated as $\alpha^{eff}=\kappa^{eff}/h$.

	Slope	κ and κ^{eff} (J/m)	α and α^{eff} (mJ/m ²)
Purified			
Free solution	(1.09±0.09)x10 ⁶	(3.5±0.1)x10 ⁻¹²	0.63±0.03
Gelled solution			
0.025%-0.125%	(6.07±0.31)x10 ⁵	(2.6±0.1)x10 ⁻¹²	0.47±0.01
0.175%	(4.17±0.44)x10 ⁵	(2.2±0.1)x10 ⁻¹²	0.39±0.02
Seikagaku			
Free solution	(9.3±1.30)x10 ⁵	(3.3±0.2)x10 ⁻¹²	0.58±0.03
Gelled solution			
0.025 % (w/v)	(7.75±0.89)x10 ⁵	(3.0±0.1)x10 ⁻¹²	0.53±0.03
0.125% - 0.175%	(6.62±0.49)x10 ⁵	(2.8±0.1)x10 ⁻¹²	0.50±0.01

The observed reduction of the nucleation rate in gelled impure solutions with respect to gelled pure solutions is more difficult to explain with the data available from these experiments. One plausible hypothesis could be that the impurities have more affinity for the gel fibers than the lysozyme molecules and attaches preferentially to the gel fibers.

Step velocities

For purified lysozyme the step advancement is not strongly affected by the presence of gel fibers as was explained before. No decrease in step velocities at higher supersaturation levels was observed, this indicates that the solute depletion zone is not significantly increased with respect to the one formed in free solution. The diffusion coefficient of lysozyme in light gel (i.e. 0.2% (w/v) agarose) is not significantly changed with respect to diffusion

in a gel-free medium (Robert, 1992). This would explain why the measured step velocities are similar in free and gelled solution.

On the other hand higher step velocities for commercial grade lysozyme in a gelled solution than in free solution were observed. Also, islands grown in gelled commercial grade solution show a similar morphology to those grown in free or gelled purified solution. It was shown before (section IV.3.4) that impurities significantly change the step morphology. There are basically two (possibly coexistent) mechanisms for impurities to affect the step growth rate: the local modification of the chemical potential close to charged impurities and the pinning of steps (van der Eerden, 1993). The strength of both processes is proportional to the impurity concentration, but the first process only operates at high impurity concentration while the second (pinning) can be very important at low concentration of impurities. Despite some quantitative differences, all models for the effect of impurities on step velocity predict a reduction of the step velocity by a factor proportional to the density of impurities on the surface and the step stiffness (van der Eerden, 1993),

$$v_{st}(\Gamma_i) = v_{st}(\Gamma_i = 0) \left(1 - \frac{4\Gamma_i}{(K^*)^2} \right) \quad (4.8)$$

where Γ_i is the surface concentration of impurities (number of impurity molecules per unit area), and $K^* = \sigma/d_0$ is the critical curvature for which steps stop advancing due to stress accumulation. Here σ is the relative supersaturation and d_0 is the edge capillary length.

As shown in figure 4.6, the agarose gel plausibly has an effect in reducing the pinning effect of impurities. To verify this observation a reduction of Γ_i must be found in gelled systems. Equation 4.8 can be rearranged as follows:

$$\frac{v_{st}(\Gamma_i = 0)}{v_{st}(\Gamma_i = 0) - v_{st}(\Gamma_i)} = \frac{1}{4d_0^2\Gamma_i} \sigma^2 \quad (4.9)$$

by plotting data in this way the relation between Γ_i for ungelled and gelled experiments can be found. As shown in Figure 4.9, data is reasonably fitted by straight lines and there is a clear difference in Γ_i . The slope of the plots is 0.041 ± 0.005 (p-value= 4.145×10^{-08}) for the ungelled experiments and 0.284 ± 0.076 (p-value=0.002) for the gelled experiments. Based on t-test statistics p-values are determined and represent the likelihood of the null hypothesis. Because d_0 depends mainly on the step stiffness (van de Eerden, 1993) which is independent on the presence of gel, we can conclude that the presence of agarose gels has a “filtering effect” reducing the impurity concentration at the crystal surface by a factor of approximately 7.

Previous studies of crystal growth in gels (Chernov *et al.*, 2001) and microgravity (Carter *et al.*, 1999) already indicated the possible existences of an impurity depletion zone but this is the first time the impurity filtering has been quantified, indicating that low concentration agarose gels are an effective method for reducing the impurity concentration at the crystal-solution interface.

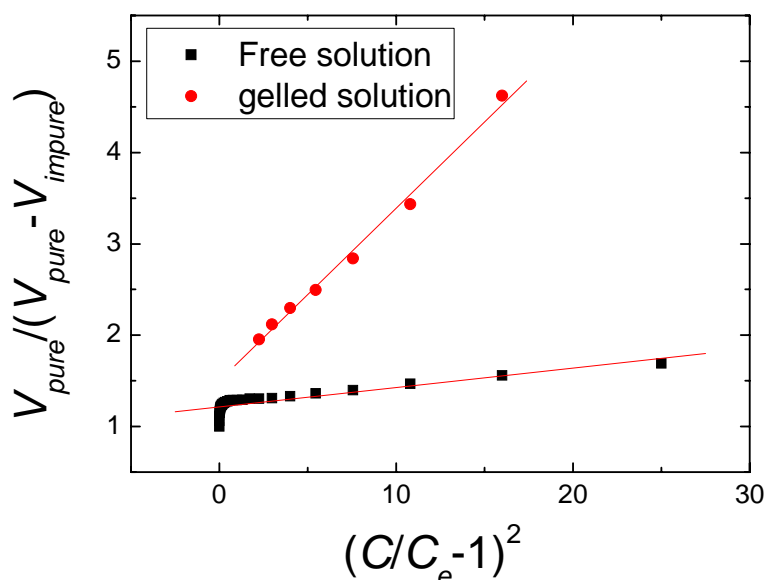


Figure 4.9 Plot of the inverse step deceleration as a function of supersaturation (Equation 9). The slope of the plot is inversely proportional to the concentration of surface adsorbed impurities.

4.5. Conclusions

The duality of agarose gels as either impurity or impurity filter in protein crystal growth experiments has been discussed frequently. The results on crystal growth kinetics in terms of two dimensional nucleation rate and step velocity reported in this work show that agarose plays both roles simultaneously, promoting 2D nucleation as an impurity but reducing the concentration of other impurities on the crystal surface by a factor around 1/7 at the same time. The overall effect on growth kinetics is a net increase of the growth rate due to the increased 2D nucleation and a reduced pinning effect. The benefits of the impurity filtering effect are not counterbalanced by the agarose/crystal interactions due to a close value of the specific surface energy of the solution/agarose and agarose/crystal interfaces, which also explains the incorporation of gel fibers within the crystal lattice.

V. GENERAL CONCLUSIONS

General Conclusions

Advanced optical techniques as a tool for *in situ* observation of protein crystal growth

Different observation techniques, AFM, Interferometry and LCM-DIM, were compared in their ability to measure growth kinetics of protein crystals. Each of these three techniques has an optimum supersaturation range of operation and it was shown that AFM is not the most appropriated choice for precise quantitative determination of mesoscopic and macroscopic growth parameters. For the first time, direct observation of 2D islands steps of molecular height during protein crystal growth was achieved by phase shifting interferometry. Also steps heights of spiral hillocks were observed and measured. The recently developed LCM-DIM technique is an ideal instrument to study mesoscopic growth kinetics *in situ* and noninvasively. For example step velocities and 2D nucleation rates could be measured precisely and from the obtained data kinetic parameters such as ledge free energy and kinetic coefficient were quantitatively estimated. Impurity effects on growth kinetics can be studied and with the aid of single molecule visualization adsorption mechanisms on crystal surfaces of fluorescence labeled impurity molecules can be observed *in situ*. Also with this technique direct observation of step dynamics on crystals growing from gelled solution was achieved for the first time.

Hence, it was demonstrated in this work that LCM-DIM is a valuable new tool for *in situ* observations of crystal growth in a variety of conditions. Until now there has been a lack of mesoscopic data, connecting atomic and macroscopic observation. With this technique quantitative mesoscopic data of crystal growth process can be easily obtained.

Protein as models systems for crystal growth studies

Macromolecular crystals are excellent systems for studying the general phenomenon of crystal growth. The particle size is relatively large, 3-to 10-nm diameter for most proteins, many times that for viruses. This is an order of magnitude or larger than conventional molecules that crystallize. Thus aggregates can be seen on the surfaces of crystals (Kuznetsov, *et al.*, 1999a; Land *et al.*, 1997; Malkin *et al.*, 1999a), and even the mobility of individual molecules on the crystal surface can be recorded (Sazaki *et al.*, 2007). The kinetics of growth of macromolecular crystals are several orders of magnitude slower than for conventional crystals, thus the course of events during growth is compatible with the temporal resolution of the instrument. Unit cells are one to two orders of magnitude larger than for conventional crystals, and this dramatically enhances the definition of growth steps, dislocations, incorporation of impurities and defect structure. (McPherson *et al.*, 2003).

Protein crystals are also excellent model systems for studying impurity effects on the growth process. In this work it was shown that impure molecules could be directly visualized on the surface and the influence of these impurity could be precisely measured from these observation it was experimentally demonstrate, for the first time, that a foreign impure molecule whose intermolecular bonding is close to that of a solute molecule adsorbs preferentially on a step, and that a foreign impure molecule whose intermolecular bonding differs from that of a solute molecule adsorbs on different sites on a crystal surface.

Future perspectives

In this work quantitative data of a model protein system crystal growth process were obtained from which kinetic parameters could be estimated precisely. This fulfils the first need for a more comprehensive understanding of protein crystals growth. Now these data can be applied for testing existing and developing crystal growth models that will be useful for the broad part of the crystal growth community.

en de boer hij ploegde voort...

VI. REFERENCES

References

A

- Abergel, C., Nesa, M.P., Fontecilla-Camps, J.C. *J. Cryst. Growth* **110**, 11-19, 1991.
- Alderton, G., Fevold, H. L. *J. Biol. Chem.* **164**, 1-5, 1946.
- Aquilano, D., Veessler, S., Astier, J. P., Pastero, L. *J. Cryst. Growth* **247**, 541-550, 2003.
- Asai, T., Suzuki, Y., Sasaki, G., Tamura, K., Sawada, T. *Cell. Mol. Biol.* **50**, 329-334, 2004.
- Astier, J. P., Bokern, D., Lapena, L., Veessler, S. *J. Cryst. Growth* **226**, 294-302, 2001.

B

- Baird, J.K., Meehan, E.J., Xidis, A.L., Howard, S.B. *J. Cryst. Growth* **76**, 694-700, 1986.
- Berg, W.F. *Proc. Roy. Soc.* **A164**, 79-95, 1938.
- Berman, H. M., Westbrook, J., Feng, Z., Gilliland, G., Bhat, T. N., Weissig, H., Shindyalov, I. N. and Bourne, P. E. *Nucl. Acid. Res.* **28**, 235-242, 2000.
- Bhamidi, V., Hanson, B.L., Edmundson, A., Skrzypczak-Jankun, E., Schall, C. *J. Cryst. Growth* **204**, 542-552, 1999.
- Biertumpfel, C., Basquin, J., Suck, D., Sauter, C. *Acta Cryst.* **D58**, 1657-1659, 2002.
- Binnig, G., Quate, C. F. and Gerber, C. *Phys. Rev. Lett.* **56**, 930-933, 1986.
- Binnig, G., Rohrer, H., Gerber, C. and Weibel, E. *Appl. Phys. Lett.* **40**, 178-180, 1982.
- Binnig, G. and Rohrer, H. *Helv. Phys. Acta.* **55**, 726-735, 1982.
- Blake, C. C., Johnson, L. N., Mair, G. A., North, A. C. T., Phillips, D. C. and Sarma, V.R. *Proc. Roy. Soc. B* **167**, 378-388, 1967.
- Blake, C. C., Koenig, D. F., Mair, G. A., North, A. C., Phillips, D. C., Sarma, V. R. *Nature* **206**, 757-761, 1965.
- Bliznakov, G. in Adsorption et Croissance Cristalline, Centre National de la Recherche Scientifique, Paris, 291-330, 1965.

- Boistelle, R., Astier, J.P. *J. Cryst. Growth* **90**, 14-30, 1988.
- Bonnete, F., Finet, S., Tardieu, A. J. *J. Cryst. Growth* **196**, 403-413, 1999.
- Botaris, G.D., Mason, E.A., Reid, R.C. *J. Chem. Phys.* **45**, 1893, 1996.
- Braun, N., Tack, J., Fischer, M., Bacher, A., Bachmann, L. and Weinkauff, S. *J. Cryst. Growth* **212**, 270-282, 2000.
- Broutin, I., Ries-Kautt, M., Ducruix, A. *J. Cryst. Growth* **181**, 97-108, 1997.
- Burke., M.W., Leardi, R., Judge, R.A., Pusey, M.L. *Cryst. Growth & Design* **1**, 333-337, 2001.

C

- Cabrera, N and Vermileya, D.A. in: *Growth and Perfection of Crystals*, eds. Doremus R., Roberts B., Turnbull D., Wiley, New York, pg. 393, 1958.
- Carter, D.C., Lim, K., Ho, J.X., Wright, B.S., Twigg, P.D., Miller, T.Y., Chapman, J., Keeling, K., Ruble, J., Vekilov, P.G., Thomas, B.R., Rosenberger, F., Chernov, A.A. *J. Cryst. Growth* **196**, 623-637, 1999.
- Caylor, C., Dobrianov, I., Lemay, S. G., Kimmer, C., Kriminski, S., Finkelstein, K. D., Zipfel, W., Webb, W. W., Thomas, B. R., Chernov, A. A. and Thorne, R. E. *Proteins: Struct., Func., Genet.* **36**, 270-281, 1999.
- Chen, K., Vekilov, P.G.. *Physical Review E* **66**, 021606, 2002.
- Chernov, A. A. *Modern Crystallography, vol. III: Growth of Crystals*, Springer-Verlag: Berlin, 1984.
- Chernov, A.A. *Contemp. Phys.* **30**, 251, 1989.
- Chernov, A.A. *J. Cryst. Growth* **174**, 354-361, 1997.
- Chernov, A.A. *Acta Cryst.* **A54**, 859-872, 1998.
- Chernov, A.A. *J. Struct. Bio.* **142**, 3-21, 2003.
- Chernov, A.A. *J. Optoelectronics and Adv. Materials* **5**, 575-587, 2003.
- Chernov, A.A., García-Ruiz, J.M., Thomas, B.R. *J. Cryst. Growth* **232**, 184-187, 2001.
- Chernov, A.A., Komatsu, H. In: *Science and technology of Crystal Growth* van Eerden, J.P., Bruinsma, O.S.L., Eds., Kluwer Academic Publishers, Dordrecht, 1995.
- Chernov, A. A., Rashkovich, L. N., Yaminsky, I. V. and Gvozdev, N. V. *J. Phys.: Condens. Matter* **11**, 9969-9984, 1999.

Cleveland, W.S. *J. Am. Stat. Assoc.* **1979**, *74*, 829-836.

Cleveland, W.S., Devlin, S.J. *J. Am. Stat. Assoc.* **1988**, *83*, 596-610.

Conroy, M., Armstrong, J. *J. Phys.: Conference series* **13**, 458-465, 2005.

D

Dai, G., Sazaki, G., Matsui, T., Tsukamoto, T., Nakajima, K., Kang, Q., Hu, W. *Nature Materials*, to be submitted.

Davey, R. J., Garside, J. *From molecules to crystallizers - An introduction to crystallization*, Oxford University Press, Oxford, UK, 2000.

DeLucas, L. J., Sudath, F. L., Snyder, R., Naumann, R., Broom, M. B., Pusey, M., Yost, V., Herren, B., Carter, D., Nelson, B., Meehan, E. J., McPherson, A., Bugg, C. E. *J. Cryst. Growth* **76**, 681-693, 1986.

Dobrianov, I., Caylor, C., Lemay, S.G., Finkelstein, K.D., Thorne R.E. *J. Cryst Growth* **196**, 511-523, 1999.

Dold, P. Private Communication, 2005.

Dold, P., Ono, E., Tsukamoto, K., Sazaki, G. *J. Cryst. Growth* **293**, 102-109, 2006.

Duan, L., Kang, Q., Hu, W.R., Li, G.P., Wang, D.C., *Biophysical chemistry* **97**, 189-201, 2002.

Ducruix, A., Guilloteau, J., Ries-Kautt, M., Tardieu, A. *J. Cryst. Growth*, **168**, 28-39, 1996.

Durbin, S. D. and Carlson, W. E. *J. Cryst. Growth* **122**, 71-79, 1992.

Durbin, S. D., Carlson, W. E. and Saros, M. T. *J. Phys. D Appl. Phys.* **26**, 128-132, 1993.

Durbin, S. D. and Feher, G. *J. Cryst. Growth* **76**, 583-592, 1986.

Durbin, S. D. and Feher, G. *J. Mol. Biol.* **212**, 763-774. 1990.

E

Eberstein, W., Georgalis, Y., Saenger, W. *J. Cryst. Growth* **143**, 71-78, 1994.

Ewing, F.L., Forsythe, E.L., van der Woerd, M., Pusey, M.L. *J. Cryst. Growth* **160**, 389-397, 1996.

F

- Forsythe, E., Ewing, F., Pusey, M.L. *Acta Cryst.* **D50**, 614-619, 1994.
- Forsythe, E., Pusey, M.L. *J. Cryst. Growth* **139**, 89-94, 1994.
- Funatsu, T., Harada, Y., Tokunaga, M., Saito, K., Yanagida, T. *Nature* **374**, 555-559, 1995.

G

- Galkin, O., Vekilov, P. G. *J. Am. Chem. Soc.* **122**, 156-163, 2000.
- Garcia-Ruiz, J. M. *J. Struct. Biol.* **142**, 22-31, 2003.
- Garcia-Ruiz, J.M., Moreno, A., Viedma C., Coil, M. *Mater. Res. Bull.* **28**, 541-546, 1993.
- Garcia-Ruiz, J.M., Moreno, A. *Acta Cryst.* **D50**, 484-, 1994.
- Garcia-Ruiz, J.M., Moreno, A., Parraga, A., Coil, M. *Acta Cryst.* **D51**, 278-, 1995.
- García-Ruiz, J.M., Novella, M.L., Moreno, R., Gavira, J.A. *J. Cryst. Growth* **232**, 165-172, 2001.
- Gavira, J.A. Tesis doctoral, U. de Granada, Granada, 2000.
- Gavira, J.A., García-Ruiz, J.M. *Acta Cryst.* **D58**, 1653-1656, 2002.
- Georgalis, Y., Umbach, P., Raptis, J., Saenger, W. *Acta Cryst.* **D53**, 703-712, 1997.
- Georgalis, Y., Umbach, P., Saenger, W. *J. Am. Chem. Soc.* **121**, 1627-1635, 1999.
- Georgalis, Y., Zouni, A., Eberstein, W., Saenger, W. *J. Cryst. Growth* **126**, 245-260, 1993.
- Georgiou, D.K., Vekilov, P.G. *PNAS* **103**, 1681-1686, 2006.
- Gliko, O., Booth, N.A., Rosenbach, E., Vekilov, P.G. *Cryst. Growth & Design* **2**, 381-385, 2002a.
- Gliko, O., Booth, N.A., Vekilov, P.G. *Acta Cryst.* **D58**, 1622-1627, 2002b.
- Gliko, O., Neumaier, N., Pan, W., Haase, I., Fischer M., Bacher, A., Weinkauff, S., Vekilov, P. *J. Am. Chem. Soc.* **127**, 3433-3438, 2005a.

Gliko, O., Neumaier, N., Fischer M., Haase, I., Bacher, A., Weinkauff, S., Vekilov, P.. *J. Cryst. Growth* **275**, e1409-e1416, 2005b.

Glocker, D.A., Soest, J.F. *J. Chem. Phys.* **51**, 3143, 1969.

Gorti, S., Forsythe, E.L., Pusey, M.L. *Cryst. Growth & Design* **4**, 691-699, 2004.

Gorti, S., Forsythe, E.L., Pusey, M.L. *Cryst. Growth & Design* **5**, 473-482, 2005a.

Gorti, S., Konnert, J., Forsythe, E.L., Pusey, M.L. *Cryst. Growth & Design* **5**, 535-545, 2005b.

Grant, M.L., Saville, D.A. *J. Cryst. Growth* **108**, 8-18, 1991.

Gray, R.J., Hou, W.B., Kudryavtsev, A.B., DeLucas, L.J. *J. Cryst. Growth* **232**, 10-16, 2001.

H

Haas, C., Drenth, J., Wilson, W. *J. Phys. Chem. B* **103**, 2808-2811, 1999.

Hansma, P. K., Cleveland, J. P., Radmacher, M., Walters, D. A., Hillner, P. E., Bezanilla, M., Fritz, M., Vie, D., Hansma, H. G., Prater, C. B., Massie, J., Fukunage, L., Gurley, J. and Elings, V. *Appl. Phys. Lett.* **64**, 1738-1740, 1994.

Hirschler, J., Charon, M.H., Fontecilla-Camps, J.C. *Protein Sci.* **4**, 2573-2577, 1995.

Hirschler, J., Fontecilla-Camps, J.C. *Acta Cryst. D***52**, 806-812, 1996.

Hirschler, J., Fontecilla-Camps, J.C. *J. Cryst. Growth* **171**, 559-565, 1997.

Hondoh, H., Nakada, T. *J. Cryst. Growth* **275**, e1423-e1429, 2005.

I

Iimura, Y., Yoshizaki, I., Nakamura, H., Yoda, S., Komatsu, H. *Jpn J. Appl. Phys.* **2003**, *42*, 5831-5836.

J

Judge, R.A., Forsythe, E.L., Pusey, M.L. *Biotechnol. Bioeng.* **59**, 776-785, 1998.

K

- Kandel, D., Weeks, D. *Phys. Rev.* **B49**, 5554-5564, 1994.
- Kam, Z., Shore, H.B., Feher, G. *J. Mol. Biol.* **123**, 539, 1978.
- Kashimoto, E., Sazaki, G., Hasegawa, K., Nakada, T., Miyashita, S., Komatsu, H., Sato, K., Matsuura, Y., Tanaka, H. *J. Cryst. Growth* **186**, 461-470, 1998.
- Kitamura, N., Lagally, M.G., Webb, M. B. *Phys. Rev. Lett.* **71**, 2082, 1993.
- Komatsu, H., Miyashita, S. *Jpn. J. Appl. Phys.* **32**, 1478-1479, 1993.
- Komatsu, H., Miyashita, S., Suzuki, Y. *Jpn. J. Appl. Phys.* **32**, 1855-1857, 1993.
- Konnert, J. H., D'Antonio, P. and Ward, K. B. *Acta Cryst.* **D50**, 603-613, 1994.
- Koyunca, I., Brant, J., Lüttge, A., Wiesner, M.R. *J. Membrane Sci.* **278**, 410-417, 2006.
- Kurihara, K. Ph.D. thesis, Graduate School of Science, Tohoku University, 1998.
- Kurihara, K., Miyashita, S., Sazaki, G., Nakada, T., Suzuki, Y., Komatsu, H. *J. Cryst. Growth* **166**, 904-908, 1996.
- Kuznetsov, Y. G., Konnert, J., Malkin, A. J. and McPherson, A. *Surf. Sci.* **440**, 69-80, 1999a.
- Kuznetsov, Yu.G., Malkin, A.J., Greenwood, A., McPherson, *J. Struct. Biol.* **114**, 184-196, 1995.
- Kuznetsov, Y. G., Malkin, A. J., Glantz, W. and McPherson, A. *J. Cryst. Growth* **168**, 63-73, 1996a.
- Kuznetsov, Y. G., Malkin, A. J., Greenwood, A. and McPherson, A. *J. Cryst. Growth* **166**, 913-918, 1996b.
- Kuznetsov, Y. G., Malkin, A. J., Land, T. A., DeYoreo, J. J., Barba, A. P., Konnert, J. and McPherson, A. *Biophys. J.* **72**, 2357-2364, 1997.
- Kuznetsov, Y.G., Malkin, A.J., Lucas, R.W., McPherson, A. *Colloids and Surfaces B: Biointerfaces* **19**, 333-346, 2000.
- Kuznetsov, Y. G., Malkin, A. J. and McPherson, A. *Phys. Rev. B* **58**, 6097-6103, 1998.
- Kuznetsov, Y. G., Malkin, A. J. and McPherson, A. *J. Cryst. Growth* **196**, 489-502, 1999b.

Kuznetsov, Y. G., Malkin, A. J. and McPherson, A. *J. Cryst. Growth* **232**, 114-118, 2001.

L

Lacapere, J. J., Stokes, D. L. and Chatenay, D. *Biophys. J.* **63**, 303-308, 1992.

Land, T. A. and DeYoreo, J. J. *J. Cryst. Growth* **208**, 623-637, 2000.

Land, T. A., DeYoreo, J. J. and Lee, J. D. *Surf. Sci.* **384**, 136-155, 1997.

Land, T. A., Malkin, A. J., Kuznetsov, Y. G. A. McPherson, DeYoreo, J. J. *J. Cryst. Growth* **166**, 893-899, 1996.

Land, T. A., Malkin, A. J., Kuznetsov, Y. G., McPherson, A., DeYoreo, J. J. *Phys. Rev. Lett.* **75**, 2774-2777, 1995.

Li, J., Li, D., Zhang, X., Li, X., Zhao, A. *Proc. SPIE* **3557**, 336-344, 1998.

Li, M., Nadarajah, A., Pusey, M.L. *Acta Cryst. D***55**, 1012-1022, 1999a.

Li, M., Perozzo, M. A., Konnert, J. H., Nadarajah, A. and Pusey, M. L. *Acta Cryst. D***55**, 1023-1035, 1999b.

Li, M., Nadarajah, A., Pusey, M. L. *Acta Cryst. D***55**, 1036-1045, 1999c.

Lin, H., Rosenberger, F., Alexander, J. I. D., Nadarajah, A. *J. Cryst. Growth* **151**, 153-162, 1995.

Lin, H., Vekilov, P.G., Rosenberger, F. *J. Cryst. Growth* **158**, 552-559, 1996.

Lin, H., Yau, S.-T., Vekilov, P.G. *Phys. Rev.* **E67**, 031606, 2003.

Lindseth, I., Bardal, A. *Surface and Coatings Tech.* **111**, 276-286, 1999.

Littke, W., John, C. Protein crystal growth under microgravity. *Science* **225**, 203-205, 1984.

Liu, X. Y., Maiwa, K., Tsukamoto, K. *J. Chem. Phys.* **106**, 1870-1879, 1996.

Lorber, B., Sauter, C., Robert, M.C., Capelle, B., Giegé, R. *Acta Cryst.*, **55**, 1491-1494, 1999.

M

Maiwa, K., Tsukamoto, K., Sunagawa, I. *J. Cryst. Growth* **102**, 43, 1990.

- Malfois, M., Bonnete, F., Belloni, L., Tardieu, A. *J. Phys. Chem.* **105**, 3290-3300, 1996.
- Malkin, A.J., Chernov, A.A., Alexeev, I.V. *J. Cryst. Growth* **97**, 765, 1989.
- Malkin, A. J., Kuznetsov, Y. G. and McPherson, A. *J. Struct. Biol.* **117**, 124-137, 1996b.
- Malkin, A. J., Kuznetsov, Y. G. and McPherson, A. *Proteins: Struct. Func. Gen.* **24**, 247-252, 1996c.
- Malkin, A. J., Kuznetsov, Y. G. and McPherson, A. *Surf. Sci.* **393**, 95-107, 1997.
- Malkin, A. J., Kuznetsov, Y. G. and McPherson, A. *J. Cryst. Growth* **196**, 471-488, 1999b.
- Malkin, A. J., Kuznetsov, Y. G., Glantz, W. and McPherson, A. *J. Phys. Chem.* **100**, 11736-11743, 1996a.
- Malkin, A. J., Kuznetsov, Y. G., Land, T. A., DeYoreo, J. J. and McPherson, A. *Nat. Struct. Biol.* **2**, 956-959, 1995a.
- Malkin, A. J., Kuznetsov, Y. G., Lucas, R. W. and McPherson, A. *J. Struct. Biol.* **127**, 35-43, 1999a.
- Malkin, A. J., Land, T. A., Kuznetsov, Y. G., McPherson, A. and DeYoreo, J. *J. Phys. Rev. Lett.* **75**, 2778-2781, 1995b.
- Malkin, A.J., McPherson, A. *J. Crystal Growth* **126**, 544-554, 1993.
- Malkin, A.J., McPherson, A. *Acta Cryst.* **D50**, 385-395, 1994.
- Malkin, A.J., McPherson, A. *J. Phys. Chem.* **B106**, 6718-6722, 2002.
- Malkin, A.J., Thorne, R.E. *Methods* **34**, 273-299, 2004.
- Markov, I. V. *Crystal Growth for Beginners*, 2nd Edition, World Scientific Publishing Co. Pte. Ltd., 2003.
- Matsui T., Sazaki G., Hondoh H., Matsuura Y., Nakada T., Nakajima K. *J. Cryst. Growth* **293**, 415-422, 2006.
- Matsuura, Y., Chernov, A.A. *Acta Crystallogr., Sect. D: Biol. Crystallogr.* **2003**, *59*, 1347 -1356.
- Matsuzuki, Y., Kubota, T., Liu, X. Y., Ataka, M. and Takano, K. J. *J. Cryst. Growth* **242**, 199-208, 2002.
- McPherson, A. *Preparation and analysis of protein crystals*, Wiley-Interscience, New York, 1982.
- McPherson, A. *Methods in Enzym.* **114**, 112-120, 1985a.

- McPherson, A. *Methods in Enzym.* **114**, 120-125, 1985b.
- McPherson, A. *Crystallization of biological macromolecules*, Cold Spring Harbor Laboratory Press, New York, 1999.
- McPherson, A., Malkin, A.J., Kuznetsov, Y.G. *Structure* **3**, 759-768, 1995.
- McPherson, A., Malkin, A. J. and Kuznetsov, Y. G. *Annu. Rev. Biophys. Biomol. Struct.* **29**, 361-410, 2000.
- McPherson, A., Malkin, A.J., Kuznetsov, Yu.G., Koszelak, S. *J. Cryst. Growth* **168**, 74-92, 1996.
- McPherson, A., Malkin, A.J., Kuznetsov, Y.G., Koszelak, S., Wells, M., Jenkins, G., Howard, J., Lawson, G. *J. Cryst. Growth* **196**, 572-586, 1999.
- McPherson, A., Malkin, A. J., Kuznetsov, Y. G. and Koszelak, S. *J. Cryst. Growth* **168**, 74-92, 1996.
- McPherson, A., Malkin, A. J., Kuznetsov, Y. G. and Plomp, M. *Acta Cryst.* **D57**, 1053-1060, 2001.
- McPherson, A., Kuznetsov, Y. G., Malkin, A. J. and Plomp, M. *J. Struct. Biol.* **142**, 32-46, 2003.
- Michinomae, M., Mochizuki, M. and Ataka, M. *J. Cryst. Growth* **197**, 257-262, 1999.
- Minsky M.: Microscopy Apparatus, U.S. Patent 3013467 (19 Dec. 1961, filed 7 November 1957).
- Minsky M. *Scanning* **10**, 128-138, 1988.
- Miyashita, S., Komatsu, H., Suzuki, Y. *Jpn. J. Appl. Phys.* **32**, L1855-L1857, 1993.
- Miyashita, S, Komatsu, H., Suzuki, Y., Nakada, T. *J. Cryst. Growth* **141**, 419-424, 1994.
- Mohan, K. S., Das, S., Chockalingam, C., Shanthi, V. and Sekar, K. LySDB - Lysozyme Structural DataBase. *Acta cryst.* **D60**, 597-600, 2004.
- Monaco, L. A., Rosenberger, F. *J. Cryst. Growth* **129**, 465-484, 1993.
- Moreno, A., Theobald-Dietrich, A., Lorber, B., Sauter, C., Giege, R. *Acta Cryst.* **D61**, 789 -792, 2005.
- Muschol, M., Rosenberger, F. *J. Chem. Phys.* **103**, 10424-10432, 1995.

N

- Nadarajah, A., Forsythe, E.L., Pusey, M.L. *J. Cryst. Growth* **151**, 163-172, 1995.
- Nadarajah, A., Li, M., Pusey, M.L. *Acta Cryst. D***53**, 524-534, 1997.
- Nadarajah, A., Pusey, M.L. *Acta Cryst.* **D52**, 983 -996, 1996.
- Nagatoshi, Y., Sazaki, G., Suzuki, Y., Miyashita, S., Matsui, T., Ujihara, T., Fujiwara, K., Usami, N., Nakajima, K. *J. Cryst. Growth* **254**, 188-195, 2003.
- Nakada, T. private communication, 2005.
- Nakada, T., Sazaki, G., Miyashita, S., Durbin, S. D. and Komatsu, H. *J. Cryst. Growth* **196**, 503-510, 1999.
- Neal, B., Asthagiri, D., Lenhoff, A., *Biophys. J.* **75**, 2469-2477, 1998.
- Neal, B., Asthagiri, D., Velov, O., Lenhoff, A., Kaler, E. *J. Cryst. Growth* **196**, 377-387, 1999.
- Ng, J. D., Kuznetsov, Y. G., Malkin, A. J., Keith, G., Giege, R. and McPherson, A. *Nucl. Acid. Res.* **25**, 2582-2588, 1997.
- Niimura, N., Minezaki, Y., Ataka, M., Katsura, T. *J. Cryst. Growth* **154**, 136-144, 1995.

O

- Ono, E., Dold, P., Koizumi, M., Tsukamoto, K., Sazaki, G. *Poster presentation*, ISBC, Granada, may 22-26, 2006.
- Onuma, K., Kameyama, T., Tsukamoto, K. *J. Cryst. Growth* **137**, 610-622, 1994.
- Otálora, F., Novella, M.L., Gavira, J. A., Thomas, B., Garcia-Ruiz., J.M. *Acta Cryst. D***57**, 412-417, 2001.

P

- Plomp, M., McPherson, A., Larson, S. B. and Malkin, A. J. *J. Phys. Chem.* **B105**, 542-551, 2001.
- Plomp, M., McPherson, A. and Malkin, A. J. *J. Cryst. Growth* **237-239**, 306-311, 2002.
- Plomp, M., McPherson, A. and Malkin, A. J. (2003). *Proteins: Struct. Func. Gen.* **50**, 486-495, 2003.

- Provost, K., Robert, M.C. *J. Cryst. Growth* **110**, 258-264, 1991.
- Provost, K., Robert, M.C. *J. Cryst. Growth* **156**, 112-120, 1995.
- Pusey, M. L. *Rev. Sci. Instrum.* **54**, 3121-3125, 1993.
- Pusey, M. L., Naumann, R. *J. Cryst. Growth* **76**, 593-599, 1986a.
- Pusey, M.L., Snyder, S.R., Naumann, R. *J. Biol. Chem.* **261**, 6524-6529, 1986b.
- Pusey, M.L., Witherow, W.K., Naumann, R. *J. Cryst. Growth* **90**, 105-111, 1988.

Q

R

- Rashkovich, L. N., Chernevich, T. G., Gvozdev, N. V., Shustin, O. A. and Yaminsky, I. V. *Surf. Sci.* **492**, L717-L722, 2001.
- Rashkovich, L. N., Gvozdev, N. V., Sil'nikova, M. I. and Chernov, A. A. *Cryst. Rep.* **47**, 859-866, 2002.
- Rashkovich, L. N., Gvozdev, N. V. and Yaminsky, I. V. *Cryst. Rep.* **43**, 696-700, 1998.
- Riès-Kautt, M., Ducruix, A. *Methods in Enzym.* **276**, 23-59, 1997.
- Robert, M.C., Capelle, B., Lorber, B, Giege, R. *J. Cryst. Growth* **232**, 489-497, 2001.
- Robert, M.C., Provost, K., Lefauchaux, F. in: *Crystallization of Nucleic Acids and Proteins: A Practical Approach*, Eds. A. Ducruix and R. Giegé, Oxford University Press, Oxford, 1992.
- Robert, M.C., Lefauchaux, F. *J. Cryst. Growth* **1988**, *90*, 358-367.
- Rodriguez, L. *Crystallization of lumazine synthase from Bacillus subtilis: electron microscopic observations*, Thesis, Technische Universität München, 2003.
- Rong, L., Yamane, T. and Niimura, N. *J. Cryst. Growth* **217**, 161-169, 2000.
- Rosenbaum, D. Zukoski, C., *J. Cryst. Growth* **169**, 752-758, 1996.
- Rosenberger, F., Vekilov, P. G., Muschol, M., Thomas, B. R. *J. Cryst. Growth* **168**, 1-27, 1996.
- Rosenberger, F., Lin, H., Vekilov, P.G. *Phys. Rev.* **E59**, 3155, 1999.

Ruppert, S., Sandler, S., Lenhoff, A. *Biotechnol. Prog.* **17**, 182-187, 2001.

S

Sato, M., Uwaha, M., *Phys. Rev.* **B51**, 11172, 1995.

Sauter, C., Otalora, F., Gavira, J. A., Vidal, O., Giege, R. and Garcia-Ruiz, J. M. *Acta cryst.* **57**, 1119-1126, 2001.

Sazaki, G., Aoki, S., Ooshima, H., Kato, J. *J. Cryst. Growth* **139**, 95-1003, 1994.

Sazaki, G., Kurihara, K., Nakada, T., Miyashita, S., Komatsu, H. J. *J. Cryst. Growth* **169**, 355-360, 1996.

Sazaki, G., Matsui, T., Tsukamoto, K., Usami, N., Ujihara, T., Fujiwara, K., Nakajima, K. *J. Cryst. Growth* **262**, 536-542, 2004.

Sazaki, G., Okada, M., Matsui, T., Watanabe, T., Higuchi, H., Tsukamoto K., Nakajima K. *J. Phys. Chem. B*, submitted.

Sazaki, G., Tsukamoto, K., Yai, S., Okada, M., Nakajima, K. *Cryst. Growth Des.* **5**, 1729-1735, 2005.

Schaper, A., Georgalis, Y., Umbach, P., Raptis, J. and Saenger, W. *J. Phys. Chem.* **106**, 8587-8594, 1997.

Seifter and England *Methods Enzymol.* **182**, 626-646, 1990.

Snell, E.H., Judge, R.A., Crawford, L., Forsythe, E.L., Pusey, M.L., Sportiello, M., Todd, P., Bellamy, H., Lovelace, J., Cassanto, J.M., Borgstahl, G.E.O. *Cryst. Growth Des.* **1**, 151-158, 2001.

Snell, E. H., Weisgerber, S., Helliwell, J. R., Weckert, F., Holzer, K., Schroer, K. *Acta Crystallogr., Sect. D* **51**, 1099-1102, 1995.

Stranski, I.N. *Z. Phys. Chem.* **136**, 259, 1928. (W. K. Burton, N. Cabrera, F. C. Frank, *Philos. Trans. R.Soc. London* **243**, 299 (1951).

Sunagawa, I. *Morphology of Minerals. In Morphology of Crystals, part B*, Ed. Sunagawa, I., Terra Scientific Publishing Company (TERRAPUB), Tokyo, 511-587, **1987**.

Suzuki, Y., Miyashita, S., Sazaki, G., Nakada, T., Sawada, T., Komatsu, H. *J. Cryst. Growth* **208**, 638-644, 2000.

Suzuki, Y., Sazaki, G., Matsui, T., Nakajima, K., Tamura, K. *J. Phys. Chem.* **B109**, 3222-3226, 2005.

Schwoebel, R.L., Shipsey, E.J. *J. Appl. Phys.* **37**, 3682-3686, 1966.

T

- Tersoff, J. *Physical Review* **75**, 2730-2733, 1995.
- Thomas, B.R., Carter, D., Rosenberger, F. *J. Cryst. Growth* **187**, 499-510, 1998a.
- Thomas, B.R., Chernov, A.A., Vekilov, P.G., Carter, D.C. *J. Cryst. Growth* **211**, 149-156, 2000.
- Thomas, B.R., Chernov, A.A. *J. Cryst. Growth* **232**, 237-243, 2001.
- Thomas, B. R., Vekilov, P.G., Rosenberger, F. *Acta Cryst.* **D54**, 226 -236, 1998b.
- Tsukamoto, K. *J. Cryst. Growth* **61**, 199-209, 1983.
- Tsukamoto, K., Nishimura, Y., Dold, P. *in preparation*, 2007.
- Tsukamoto, K., Yai, S., Sazaki, G. *J. Jpn. Assoc. Cryst. Growth* **30**, 81-86, 2003.

U

- Uwaha, M. Saito, Y. Sato, M. *J. Cryst. Growth* **146**, 164-170, 1995.

V

- van der Eerden in *Handbook of Crystal Growth 1: Fundamentals*, Edited by Hurle, D.T.J., North-Holland: Amsterdam, 1993, 307-479.
- van der Eerden, J. P., Muller-Krumbhaar, H. *Phys. Rev. Lett.* **57**, 2431 **1986a**.
- van der Eerden, J. P., Muller-Krumbhaar, H. *Electrochim. Acta* **31**, 1007-1012, **1986b**
- Van Driessche, A.E.S., Sazaki, G., Otálora, F., Gonzalez-Rico, F.M., Dold, P., Tsukamoto, K., Nakajima, K. *Cryst. Growth & Design* **7**, 1980-1987, 2007.
- van Enckevort, W. J. P. *Prog. Cryst. Growth Charact.* **9**,1-50, 1984.
- van Leeuwen, C., van Rosmalen, R., P. Bennema *Surf. Sci.* **44**, 213-236, 1974.

- Vekilov, P. G. In *Studies and Concepts in Crystal Growth*, Komatsu, H., Ed., Pergamon Press, Oxford, 1993.
- Vekilov, P. G., Alexander, I. D. *Chem. Rev.* **100**, 2061-2089, 2000.
- Vekilov, P. G., Alexander, J. I. D., Rosenberger, F. *Phys. Rev.* **E54**, 6650-6660, 1996.
- Vekilov, P. G., Ataka, M., Katsura, T. *J. Cryst. Growth* **130**, 317-320, 1993.
- Vekilov, P. G., Ataka, M., Katsura, T. *Acta Cryst.* **D51**, 207-219, 1995.
- Vekilov, P.G., Kuznetsov, Yu.G., Chernov, A.A. *J. Cryst. Growth* **121**, 643, 1992.
- Vekilov, P. G., Lin, H., Rosenberger, F. *Phys. Rev.* **E55**, 3202-3214, 1997.
- Vekilov, P.G., Monaco, L.A., Thomas, B.R., Stojanoff, V., Rosenberger, F. *Acta Cryst.* **D52**, 785-798, 1996.
- Vekilov, P.G., Monaco, L.A., Rosenberger, F. *J. Cryst. Growth* **156**, 267-278, 1995a.
- Vekilov, P.G., Monaco, L.A., Rosenberger, F. *J. Cryst. Growth* **148**, 289-296, 1995b.
- Vekilov, P. G., Rosenberger, F. *J. Cryst. Growth* **158**, 540-551, 1996.
- Vekilov, P. G., Rosenberger, F. *Phys. Rev.* **E57**, 6979-6981, 1998a.
- Vekilov, P. G., Rosenberger, F. *J. Cryst. Growth* **186**, 251-261, 1998b.
- Vekilov, P. G., Rosenberger, F. *Phys. Rev. Lett.* **80**, 2654-2656, 1998c.
- Vekilov, P. G., Rosenberger, F., Lin, H., Thomas, B.R. *J. Cryst. Growth* **196**, 261-275, 1999.
- Vekilov, P. G., Thomas, B. R., Rosenberger, F. *J. Phys. Chem.* **B102**, 5208-5216, 1998.
- Vidal, O., Robert, M.C., Boué, F. *J. Cryst. Growth* **192**, 257-270, 1998.
- Vidal, O., Robert, M.C., Arnoux, B., Capelle, B. *J. Cryst. Growth* **196**, 559-571, 1999.
- Voronkov and Rashkovich *Sov. Phys. Crystallogr.* **37**, 289-295, 1992.

W

- Waizumi, K., Plomp, M., van Enkevort, W. *Colloids and Surfaces B: Biointerfaces* **30**, 73-86, 2003.

- Waki, S., Harvey, J.D., Bellamy, A.R. *Biopolymers* **21**, 1909-1926, 1982.
- Wazawa, T., Ueda, M. *Adv. Biochem. Eng. Biotechnol.* **95**, 77-106, 2005.
- Wiechmann, M., Enders, O., Zeilinger, C. and Kolb, H.-A. *Ultramic.* **86**, 159-166, 2001.
- Wieneck, J.M. *Annu. Rev. Biomed. Eng.* **1**, 505-534, 1999.
- Wilcox, W.R. *J. Crystal Growth* **65**, 133-142, 1983.
- Wilkinson, G. N. and Rogers, C. E. *Appl. Statistics* **22**, 392-399, 1973.
- Wilson, W.W. *Methods* **1**, 110-117, 1990.
- Wittmann, H.G. *Biochem. Int.* **5**, 629-636, 1981.
- Wold, F., Moldave, K. *Methods Enzymol.* 106 and 107, Academic Press, San Diego, California, 1984.

X

Y

- Yaminsky, I. V., Gvozdez, N. V., Sil'nikova, M. I. and Rashovich, L. N. *Cryst. Rep.* **47**, S149-S158, 2002.
- Yai, S. Graduation thesis, Tohoku University, 2003.
- Yau, S.-T., Petsev, D.N., Thomas, B. R. and Vekilov, P. G. *J. Mol. Biol.* **303**, 667-678, 2000.
- Yau, S.-T., Thomas, B. R., Galkin, O., Gliko, O., Vekilov, P. G. *Proteins Struct. Funct. Genet.* **43**, 343-352, 2001.
- Yau, S.-T., Thomas, B. R., Vekilov, P. G. *Phys. Rev. Lett* **85**, 353-356, 2000a.
- Yau, S.-T. and Vekilov, P. G. *Nature* **406**, 494-497, 2000.
- Yau, S.-T. and Vekilov, P. G. *J. Am. Chem. Soc.* **123**, 1080-1089, 2001.
- Yip, C. M. and Ward, M. D. *Biophys. J.* **71**, 1071-1078, 1996.
- Yip, C. M., Brader, M. L., DePhilippis, M. R. and Ward, M. D. *Biophys. J.* **74**, 2199-2209, 1998a.
- Yip, C. M., DePhilippis, M. R., Frank, B. H., Brader, M. L. and Ward, M. D. *Biophys. J.* **75**, 1172-1179, 1998b.

Yonath, A., Khavitch, G., Tesche, B., Muessig, J., Lorenz, S., Erdmann, V.A., Wittmann, H.G. *Biochem. Int.* **5**, 629-636, 1982.

Yoshizaki, I., Fukuyama, S., Koizumi, H., Tachibana, M., Kojima, K., Matsuura, Y., Tanaka, M., Igarashi, N., Kadowaki, A., Rong, L., Adachi, S., Yoda, S., Komatsu, H. *J. Cryst. Growth* **290**, 185-191, 2006.

Yoshizaki, I., Kadowaki, A., Imura, Y., Igarashi, N., Yoda, S., Komatsu, H. *J. Synchrotron Rad.* **11**, 30-33, 2004.

Yoshizaki, I., Sakai, M., Matsuura, Y. *Acta. Cryst.* **D61**, 755-758, 2005.

Z

VII. APPENDIX

Laser confocal phase-shift interferometry

The recently developed laser confocal phase-shift interferometer (CPSI, Tsukamoto *et al.*, 2007, Nishimura *et al.*, 2007) is shown in Figure 1. It consists of a small Michelson interferometer (Linnik configuration) attached to a commercially available laser confocal microscope. A polarization phase-shift system is incorporated to measure precisely the phase value precisely the polarization type phase-shift interferometry (Onuma *et al.*, 1993). Therefore an analyzer is automatically rotated (0° , 45° , 90°), and three interferograms are captured. The phase-shift interferogram is then calculated form

$$\phi_{x,y} = \arctan \frac{I(1)_{x,y} - I(2)_{x,y}}{I(2)_{x,y} - I(3)_{x,y}} \quad (1)$$

where $\phi_{x,y}$ and $I(m)_{x,y}$ are the phase value and the intensity at position (x,y) of a interferogram. The intensity of the phase-shift image is proportional to the phase value, from which the height can be calculated using following equation

$$h_{x,y} = \frac{\lambda_{532}}{2 \cdot n} \cdot \frac{I_{x,y}}{256} \quad (2)$$

where $h_{x,y}$ is the height of the surface in a position (x,y) , n corresponds with the refractive index o the crystal and λ is the wavelength of the light source. The vertical resolution of this system is approximately 1 nm and lateral resolution is close to 0.25 μm . The acquisition time needed to capture three interferograms is 3 sec. Time resolutions is improved compared to LCM-DIM. In the buildup of a confocal image the limiting step is the scanning speed of the galvano mirrors. In this confocal setup one of the galvano mirrors is replaced by an Acoustic Optical Deflector in order to speed up the scanning. This uses a high-frequency sound wave in a special crystal to create a diffraction grating, which deflects the laser light (actually, the first diffraction peak is used, with the zero-order peak being thrown away). By

varying the frequency of the sound wave, the AOD changes the angle of the diffracted light, helping scan the sample quickly, (scanspeed = 1/15 sec).

Compared to white light PSI, adjustment for *in situ* observation of the surface is much easier and both lateral and vertical resolving power is nearly equal.

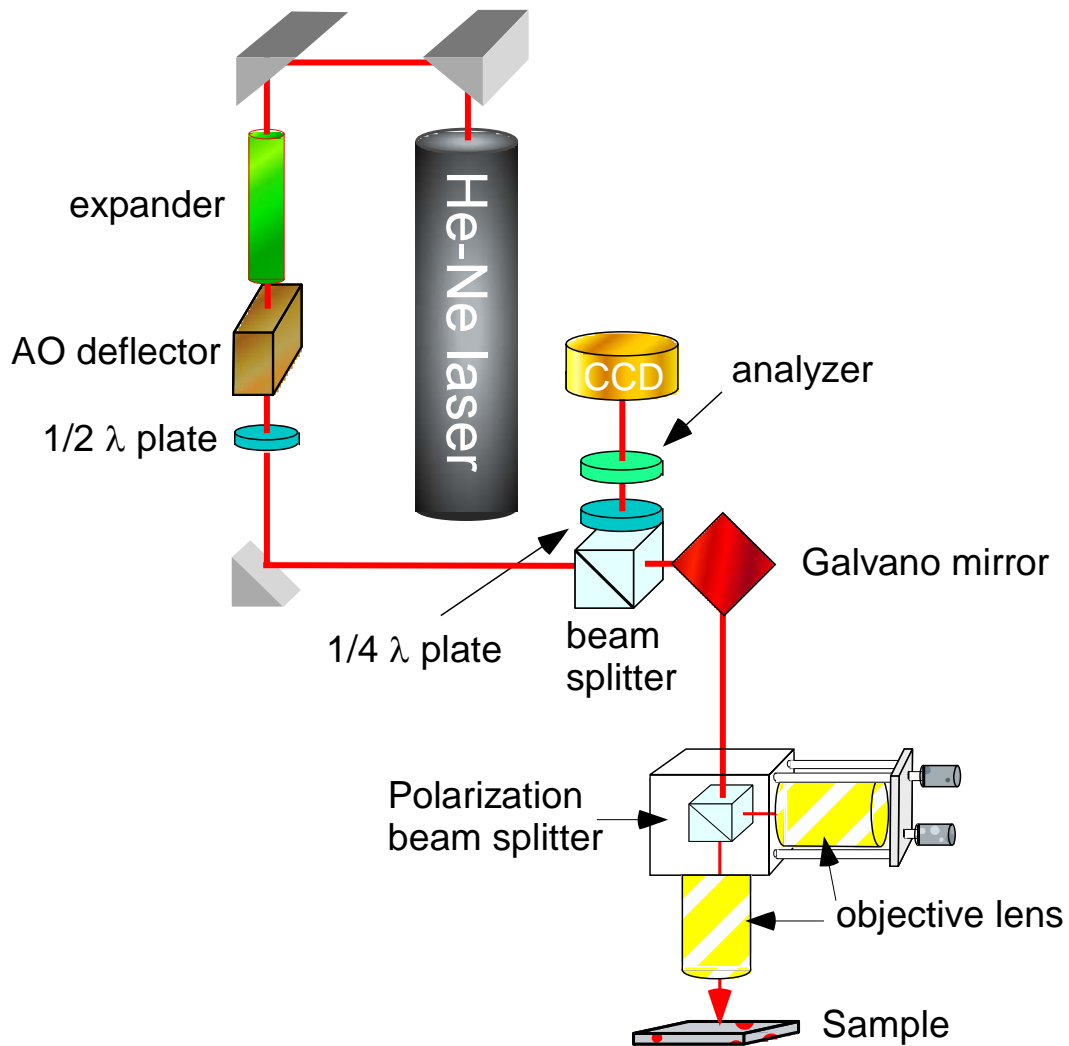


Figure 1: Schematic representation of the confocal phase shifting interferometer

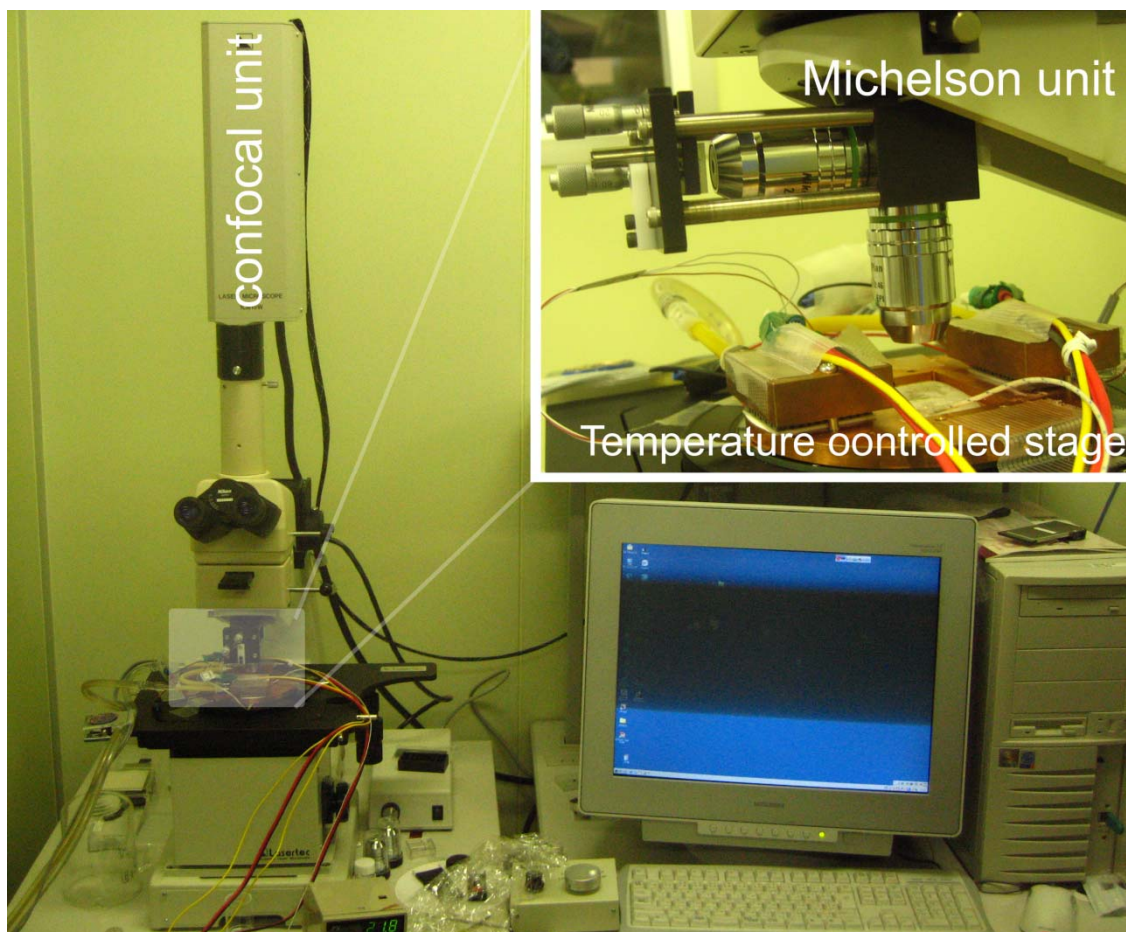


Figure 3. Photograph of the confocal phase shifting interferometry microscope.

Measurements of step velocities and two dimensional nucleation rates in agarose gel.

Tetragonal seed crystals of model protein hen egg-white lysozyme were grown at $20.0 \pm 0.1^\circ\text{C}$ from a solution containing 70 mg/ml commercial grade lysozyme (98.5% purity: 6x recrystallized, Seikagaku Co.), 25 mg/ml NaCl and 50 mM sodium acetate (pH 4.5) buffer. After seed crystals were transferred to an observation cell ($1 \times 10 \times 20 \text{ mm}^3$), the solution inside the cell was replaced with a supersaturated solution of purified lysozyme (99.99%: Maruwa food industries, Inc.) or commercial grade lysozyme (98.5%: Seikagaku, Co.) and given concentration of agarose gel (D-5, Hispanagar) and was incubated for 24 hours at 23.0°C until the surfaces of the seed crystals were completely covered with purified lysozyme or

commercial lysozyme and the crystals had grown into the gelled solution. There after step velocities and 2D nucleation rates of elementary 2D islands were measured on {110} faces of tetragonal lysozyme crystals by LCM-DIM.

To change the solubility of the protein solution, the observation cell was set on a temperature controlled stage with Peltier elements and the temperature was changed at given time intervals. The solubility was calculated from the data reported by Sasaki and coworkers (1996) Step velocities were represented following the equation (Chernov, 1984):

$$v = \Omega \beta (C - C_e), \quad (3)$$

where Ω is the volume of one lysozyme molecule inside a tetragonal crystals ($= 3 \times 10^{-20} \text{ cm}^3$), β is the kinetic coefficient, C is a bulk concentration of lysozyme and C_e the solubility at a given temperature. Observations were carried out in the supersaturation range $C - C_e = 18\text{-}34 \text{ mg/ml}$.

Direct and Noninvasive Observation of Two-Dimensional Nucleation Behavior of Protein Crystals by Advanced Optical Microscopy

Alexander E. S. Van Driessche,^{†,‡} Gen Sasaki,^{*,‡,§} Fermín Otálora,[†]
Francisco M. González-Rico,[†] Peter Dold,^{||} Katsuo Tsukamoto,^{||} and Kazuo Nakajima[§]

Laboratorio de Estudios Cristalográficos, IACT, CSIC, P.T. Ciencias de la Salud, Avenida del conocimiento s/n, 18100 Armilla (Granada), Spain, Center for Interdisciplinary Research, Tohoku University, Aramaki, Aoba-ku, Sendai 980-8578, Japan, Institute for Materials Research, Tohoku University, 2-1-1 Katahira, Aoba-ku, Sendai 980-8577, Japan, and Department of The Earth and Planetary Science, Graduate School of Science, Tohoku University, Aramaki, Aoba-ku, Sendai 980-8578, Japan

Received December 23, 2006; Revised Manuscript Received May 9, 2007

ABSTRACT: We observed two-dimensional (2D) nucleation behavior on {110} and {101} faces of tetragonal crystals of model protein lysozyme by laser confocal microscopy combined with differential interference contrast microscopy (LCM-DIM). We measured, for the first time directly and noninvasively, the 2D nucleation rates using 99.99% pure lysozyme, 98.5% pure lysozyme (Seikagaku Co.), and 99.99% pure lysozyme with intentionally added impure proteins (fluorescent-labeled lysozyme, covalently bonded dimer of lysozyme, and 18 kDa polypeptide). We found that 2D nucleation was the dominant growth mechanism under conditions adopted in this study, and the 2D nucleation occurred randomly on the entire crystal surface irrespective of supersaturation within the range of $\sigma = \ln(C/C_e) = 0-1.4$, where C is a bulk lysozyme concentration and C_e the solubility (crystal size: 0.2–0.3 mm). Repeated 2D nucleation, which continued for 3–4 layers, was also observed mainly when the impure proteins were present. In addition, multilayered 2D islands were formed after the adsorption of relatively large foreign particles on the crystal surface. From the comparison between the 2D nucleation rates determined on the {110} faces with and without the impure proteins, we concluded that homogeneous 2D nucleation occurred under a higher supersaturation range ($\sigma > 0.8$), irrespective of the presence of the impurities. In contrast, under a lower supersaturation range ($\sigma < 0.8$), we found that significant heterogeneous 2D nucleation dominated the growth mainly when the impure proteins were present. The {101} faces exhibited more significant heterogeneous 2D nucleation induced by smaller amounts of impurities than in the case of the {110} faces. We also determined the ledge free energies of the homogeneous and heterogeneous nucleation. Within the experimental conditions used in this study, we could not find significant dependence of the ledge free energies of the heterogeneous nucleation on the kinds of impure proteins.

1. Introduction

Two-dimensional (2D) nucleation is an important crystal growth mechanism under middle and high supersaturation ranges. In particular, in the case of protein crystallization, due to relatively high supersaturation necessary for initial three-dimensional (3D) nucleation and subsequent growth, 2D nucleation is a main growth mechanism. Hence, many qualitative observations on 2D nucleation have been reported so far but few quantitative studies have been tried until now.

Direct observation of 2D nucleation processes on inorganic and protein crystals have been carried out mainly by atomic force microscopy (AFM), by which individual 2D islands appearing on a crystal surface could be observed directly. In some studies, 2D nucleation rates were reported for protein crystals (thaumatin^{1,2} and catalase²); however, the scan of a cantilever potentially disturbs solute concentration distribution in the vicinity of a crystal surface,^{3,4} although the effects of a cantilever on growth kinetics have not yet been revealed in detail. In addition, only a small part of a crystal surface can be observed by AFM. Therefore, noninvasive techniques, which enable us to observe a whole crystal surface at a time, are necessary for measuring 2D nucleation rates precisely.

Optical microscopy is a promising alternative to observe in situ a whole crystal surface noninvasively. There are many

reports that studied 2D nucleation growth by measuring normal growth rates of crystal faces. By analyzing supersaturation dependency of normal growth rates using a 2D nucleation growth model of the birth-and-spread type, one can indirectly determine ledge free energies for 2D nucleation of protein crystals^{5–10} and inorganic crystals.^{11,12} However, since ledge free energies were determined indirectly from averaged normal growth rates, only averaged information on 2D nucleation was obtained.

To achieve noninvasive and direct observation of individual 2D islands, various kinds of optical microscopy are available. In situ observations of monomolecular steps were made on inorganic crystals¹³ and protein crystals^{14–17} by transmission type phase-contrast microscopy. Laser confocal microscopy combined with differential interference contrast microscopy (LCM-DIM) also gives good contrast of elementary growth steps of protein crystals.^{10,18,19} In addition, phase shift interferometry is applicable to measure the height of elementary growth steps of inorganic crystals²⁰ and protein crystals.²¹ Hence, advanced optical microscopy techniques are suitable for 2D nucleation rates measurements.

In this study, utilizing LCM-DIM, we have documented in situ measurements of 2D nucleation rates of tetragonal lysozyme crystals, which is one of the most commonly used model protein crystals for crystal growth studies. We measured the 2D nucleation rates of lysozyme crystals under a wide supersaturation range $\sigma = 0-1.4$ and tried to determine intrinsic ledge free energy of lysozyme crystals, using 99.99% pure lysozyme. Furthermore, we also studied effects of impure molecules on 2D nucleation, using 98.5% pure lysozyme (Seikagaku Co.) and intentionally added impure proteins: fluorescent-labeled lysozyme,²²

* To whom correspondence should be addressed. E-mail address: saasaki@cir.tohoku.ac.jp.

[†] LEC, IACT, CSIC, P.T. Ciencias de la Salud.

[‡] Center for Interdisciplinary Research, Tohoku University.

[§] Institute for Materials Research, Tohoku University.

^{||} Graduate School of Science, Tohoku University.

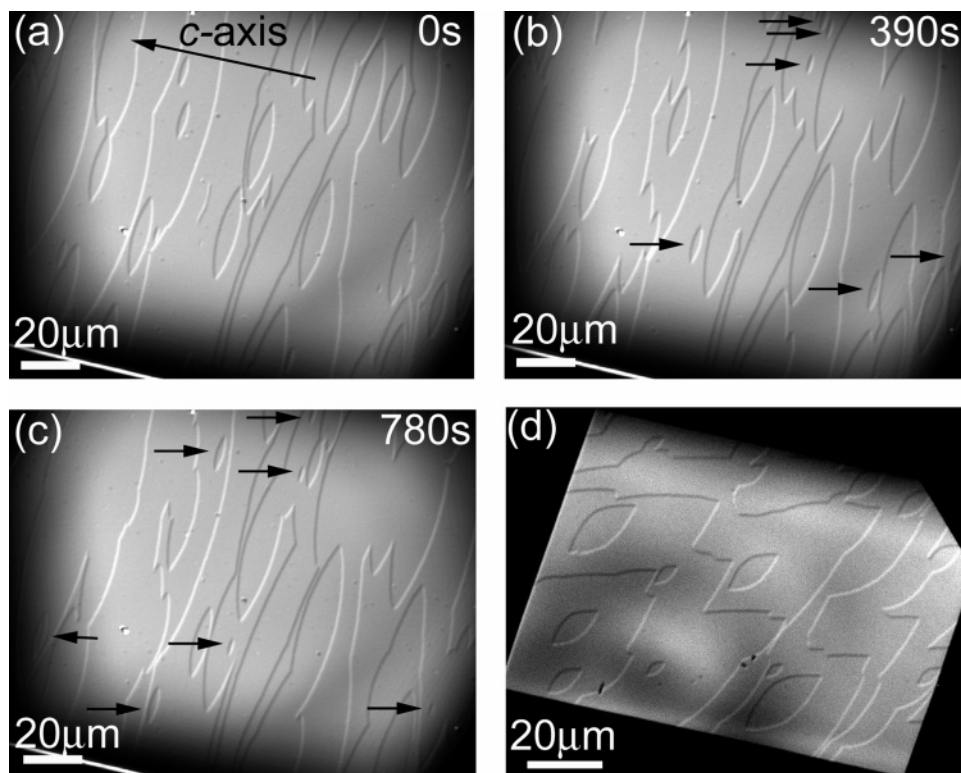


Figure 1. Photomicrographs of 2D nucleation behavior on {110} (a–c) and {101} (d) faces of growing tetragonal lysozyme crystals, observed by LCM-DIM. The sequence of micrographs shows the time course of 2D nucleation growth of the birth-and-spread type: 0 s (a); 390 s (b); 780 s (c). Arrows indicate the appearance of new 2D islands during the time intervals of the sequence of images. Growth conditions: 99.99% pure lysozyme 56 mg/mL (a–c) and 40 mg/mL (d), NaCl 25 mg/mL, in 50 mM sodium acetate buffer (pH 4.5), at 22.0 °C (a–c) and at 26.0 °C (d).

covalently bonded dimer of lysozyme, and impure protein of 18 kDa molecular weight (the last two are main impurities present in hen egg-white lysozyme).²³ We discussed homogeneous and heterogeneous nucleation, which will be a step toward a better understanding of nucleation and growth phenomena in protein and inorganic crystallization.

2. Experimental Methods

2.1. In Situ Observation by LCM-DIM. Growing {110} and {101} faces of tetragonal lysozyme crystals were observed in situ by LCM-DIM. An observation cell was made of two glass plates (0.15 mm thickness) and plastic spacers of 1.0 mm thickness (thickness of a protein solution): all of these parts were glued by silicone adhesive. After the solidification of the adhesive, the cell was carefully washed by ultrasonic cleaning with pure (Milli-Q) water. Then the lysozyme crystals of 0.2–0.3 mm in height were placed in the observation cell, and the faces parallel to the bottom glass plate were observed. First we carefully examined whether the silicone adhesive gave any contamination on the growth of lysozyme crystals by comparing crystals growing in our observation cell with those grown in a quartz cell without any adhesive; then we concluded that the silicone adhesive did not give any significant contamination in our experimental conditions. All in situ observations were carried out at the free solution–crystal interface. Because of the morphology of the tetragonal lysozyme crystals,²⁴ the {110} faces were mainly observed. In our previous studies,^{18,19} we reported that the elementary growth steps (5.6 nm in height) on the {110} face of the tetragonal lysozyme crystal could be observed in situ with sufficient contrast using a LCM-DIM system. To eliminate interference fringes, the LCM-DIM system was equipped with a super luminescent diode (Amonics Ltd., model ASLD68-050-B-FA: 680 nm), whose coherence length is about 10 μm. Photomicrographs of 1024 × 1024 pixels were acquired over a 9 s scan time, and the images were recorded at 10–300 s intervals, depending on supersaturation and nucleation rates. Other details of the experimental setup were already described in our previous works.^{18,19}

2.2. Measurements and Analyses of 2D Nucleation Rates. Seed crystals were grown at 20.0 ± 0.1 °C from a solution containing 70

mg/mL hen egg-white lysozyme (98.5% purity: Seikagaku Co.), 25 mg/mL NaCl, and 50 mM sodium acetate (pH 4.5). Hereafter, lysozyme supplied by Seikagaku Co. is just called 98.5% pure lysozyme. After the seed crystals had reached desirable size (0.2–0.3 mm), they were transferred to the observation cell. The solution inside the cell was then replaced with a solution of 99.99% pure lysozyme (Maruwa Food Industries, Inc.: in March 2007, this sample was discontinued), and the seed crystals were incubated for 5–6 h until the surfaces of the seed crystals were completely covered with newly formed layers of 99.99% pure lysozyme. Just before each measurement of 2D nucleation rates, the solution inside the cell was replaced again with a newly prepared lysozyme solution. On the {110} and {101} faces without any spiral growth hillock, 2D nucleation was observed by LCM-DIM under three kinds of lysozyme solutions: 99.99% pure lysozyme solutions; 98.5% pure lysozyme solutions; 99.99% pure lysozyme solutions containing given concentrations of impure proteins. We changed supersaturation by changing the temperature of the lysozyme solution in the range 15–30 °C using Peltier elements. Supersaturation σ at a given temperature was defined as

$$\sigma = \ln(C/C_e) \quad (1)$$

where C is a bulk concentration of lysozyme and C_e the solubility. The solubility was calculated from the data reported by Sazaki et al.²⁵ Observations were carried out in the supersaturation range $\sigma = 0$ –1.4. Above this supersaturation range, 2D nucleation was too fast to measure. To analyze 2D nucleation rates, the number of newly appeared islands between adjacent time-lapse images was counted and divided by the surface area of the observed crystal surface and elapsed time.

To measure the ratio of tetragonal lysozyme crystals grown by 2D nucleation, we carried out a different series of experiments. The 98.5% pure lysozyme solutions of an initial concentration of 70 mg/mL were transferred into the observation cells, and the crystals were nucleated in the cell. The growth of the {110} and {101} faces was observed from the moment the crystals reached the minimum size needed for observation (≈ 10 μm) until step advancement became almost zero.

2.3. Impurities. The effects of three different kinds of impurities on 2D nucleation were studied: fluorescent-labeled lysozyme (F-

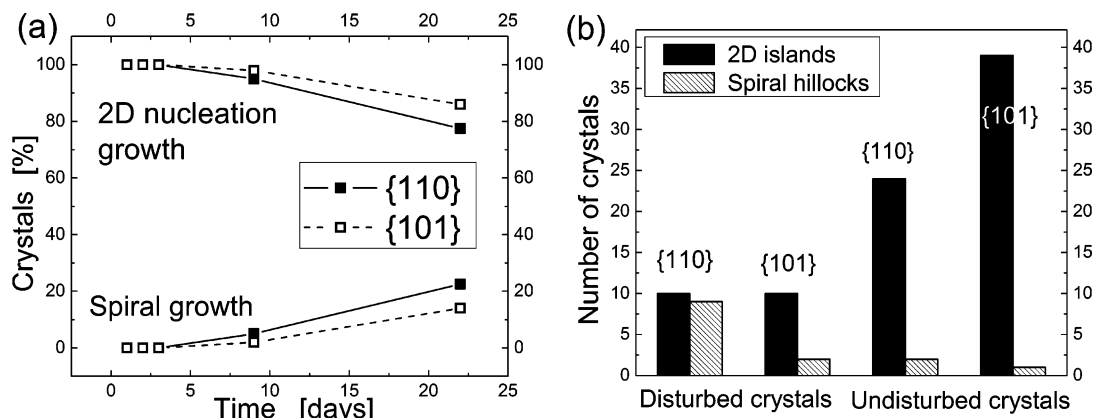


Figure 2. Importance of 2D nucleation growth on {110} and {101} faces of tetragonal lysozyme crystals: (a) changes in the ratio of the crystals on which the growth of {110} or {101} face was dominated by 2D nucleation growth or spiral growth, as a function of time; (b) number of the crystals whose {110} or {101} face was grown by 2D nucleation growth or spiral growth, after 22 days. The notation “disturbed crystals” refers to the cases in which microcrystals were adsorbed on the crystal surfaces or the crystals suffered mechanical stress, and the notation “undisturbed crystals” refers to the crystals that were free from such incidents. Growth conditions: 98.5% pure lysozyme 70 mg/mL (initial concentration), NaCl 25 mg/mL, in 50 mM sodium acetate buffer (pH 4.5), at 20.0 °C.

lysozyme); covalently bonded dimer of lysozyme (dimer); 18 kDa polypeptide (18kDa). The last two are main impurities present in hen egg-white lysozyme.²³ F-lysozyme was prepared according to the recipe of Matsui et al.²² Dimer and 18kDa were purchased from Maruwa Food Industries Inc. (these samples were also discontinued). We intentionally added these impure proteins to 99.99% pure lysozyme solutions and measured 2D nucleation rates. We also measured 2D nucleation rates using a 98.5% pure lysozyme solution, which contains 1.0% 18kDa and 0.5% lysozyme dimer as major impurities.²³ Only in the case of the 98.5% pure lysozyme, the surfaces of seed crystals were not covered with the layers of 99.99% pure lysozyme before the measurements of 2D nucleation rates.

3. Results and Discussions

3.1. Two-Dimensional Nucleation Behavior. We observed in situ the 2D nucleation behavior on the {110} and {101} faces of the growing tetragonal lysozyme crystals by LCM-DIM. As shown in a sequence of photomicrographs (Figure 1), we could clearly visualize 2D islands of elementary step height (5.6 nm for the {110} face and 3.4 nm for the {101} face)^{26–29} by LCM-DIM and could follow the time course of the 2D nucleation growth of the birth-and-spread type. Here we only showed significant parts of the images, although we observed elementary steps on whole crystal surfaces. Arrows in the micrographs indicate the appearance of new 2D islands during the time intervals of the sequence of images. These images clearly demonstrate that individual 2D islands nucleated on the {110} and {101} faces can be observed by LCM-DIM.

Within the range of supersaturations ($\sigma = 0–1.4$) and for all solutions used in our observations, we found that 2D nucleation occurred randomly on the entire crystal surfaces. At higher supersaturations, $\sigma > 1.4$, crystal edges became preferential nucleation regions because of the Berg effect,³⁰ and a complex response of the facet morphology arose from nonuniformities in nutrient and impurity supply. Such facet response has been observed experimentally³¹ and explained quantitatively by numerical simulations³² for tetragonal lysozyme crystals by Rosenberger’s group. In this study, we carried out all the experiments within the lower supersaturation range ($\sigma = 0–1.4$), where the Berg effect was not significant. From the sequences of photomicrographs taken by LCM-DIM, we determined 2D nucleation rates systematically at different supersaturations (discussed later).

To demonstrate that 2D nucleation growth plays an important role in the growth of tetragonal lysozyme crystals, we crystal-

lized tetragonal lysozyme crystals under widely adopted conditions (98.5% pure lysozyme from Seikagaku Co., batch crystallization in containers with mm height) and monitored the growth of the crystals for 22 days. The results of the {110} and {101} faces are summarized in Figure 2. At the beginnings of the observations, all crystals were growing by 2D nucleation on both faces, and after 22 days still 80% of the crystals were growing by 2D nucleation (Figure 2a). Figure 2b shows the breakdown of the crystals after 22 days. Note that the spiral growth hillocks appeared occasionally, mainly when microcrystals were adsorbed on a crystal surface or when crystals suffered mechanical stress (i.e., two or more crystals bumped into each other during their growth; disturbed crystals in Figure 2b). From these results, we can conclude that 2D nucleation is the dominant growth mechanisms of tetragonal lysozyme crystals under the crystallization conditions used in this experiment. Since these conditions fall in the range of widely adopted ones, Figure 2 shows typical results, although growth mechanisms strongly depend on growth conditions. In addition, as reported in our previous study,¹⁹ Figure 2b clearly indicates that solid inclusions play an important role in the generation of dislocations and hence spiral growth hillocks.

In addition to the random 2D nucleation shown in Figure 1, we also observed peculiar 2D nucleation events at rare intervals. Arrows in a sequence of photomicrographs shown in Figure 3 indicate the regions in which 2D islands having their centers at the same position were generated repeatedly. Note that the interstep distances of the concentric 2D islands generated repeatedly are irregular (bars in Figure 3). Although two screw dislocations with opposite signs can generate a similar surface structure composed of concentric islands, the irregular interstep distances clearly indicate that the 2D islands nucleated repeatedly at irregular time intervals at the same site. The repeated 2D nucleation normally continued for 3–4 layers and could be observed irrespective of the supersaturation. The repeated nucleation was mainly observed when impure proteins were present in the lysozyme solutions. In the case of the 99.99% purity lysozyme solution, the ratio of the occasions on which we could find the repeated nucleation was about 20% but 60% for the solutions that contained the impurities. This is a strong indication that the impure proteins are responsible for the repeated 2D nucleation, although other materials related with impure sample (e.g., fibrous materials)³³ would be also responsible. Liu et al.³⁴ gave a theoretical explanation and experimental

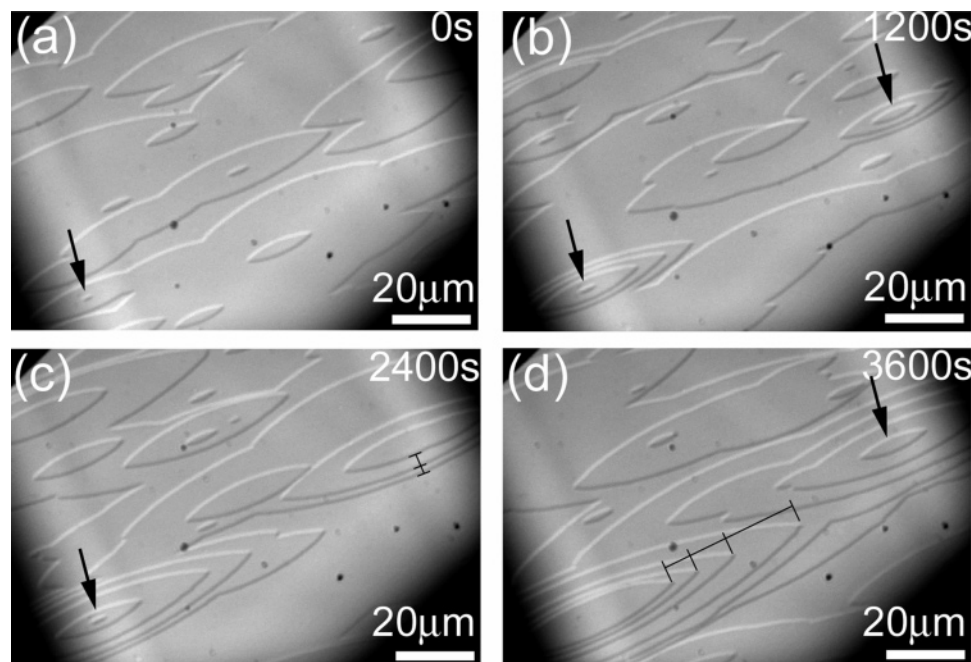


Figure 3. Photomicrographs of repeated 2D nucleation on a $\{110\}$ face of a growing tetragonal lysozyme crystal taken by LCM-DIM. The sequence of micrographs shows the time course of the repeated 2D nucleation: 0 s (a); 1200 s (b); 2400 s (c); 3600 s (d). Black arrows show the regions in which 2D islands having their centers at the same position were generated repeatedly. The repeated 2D nucleation normally continued for 3–4 layers. Bars indicate that interstep distances of the concentric 2D islands generated repeatedly are irregular. Growth conditions: 99.99% pure lysozyme 38 mg/mL, 0.05% F-lysozyme, NaCl 25 mg/mL, in 50 mM sodium acetate buffer (pH 4.5), at 24.0 °C.

examples for the heterogeneous 2D nucleation on inorganic crystals. They explained that any kinds of foreign particles, such as dusts, gas or liquid bubbles, macromolecules or polymer molecules, secondary nuclei formed during the growth of host crystals, and even impurity molecules, can potentially serve as nucleation centers for 2D nucleation, and they will promote nucleation by lowering 2D nucleation barriers. In addition, after the impure molecules were incorporated into the crystal surface, the strain fields generated around the impurities would also play an important role to lower step-ledge free energies³⁵ and thus promoted the 2D nucleation repeatedly, until the effects of the strain field did not reach the crystal surface (3–4 layers in this study).

A sequence of photomicrographs in Figure 4 shows 2D nucleation and subsequent lateral growth of a multilayer island that exhibits much higher contrast than the elementary islands. In Figure 4a, a white arrow indicates the existence of a foreign particle on the crystal surface, since the particle did not grow at the same rate as other islands grew. After 80 s (Figure 4b), a 2D island appeared at this foreign particle (white arrow) and a second 2D island appeared next to the first one (black arrow). After 230 s (Figure 4c), the first island nucleated at the foreign particle was overgrowing the second island (black arrowhead). This observation demonstrates that the first island had multiple layer height. Sometimes foreign particles adsorbed on a crystal surface were observed at the center of the multilayer islands. In addition, multilayer islands frequently appeared on the crystal surfaces after the replacement of the solution inside the cell and also after the crystals were transferred from stock tubes of seed crystals to the observation cell. Furthermore, no strong correlation was found between the presence of the impure proteins and the appearance of multilayer islands. Taking into account these results, we concluded that relatively large foreign particles, probably microcrystals generated by flow and/or clash of seed crystals and then adsorbed on a crystal surface, are

responsible for the formation of the multilayer islands. The relatively large height of the foreign particles would result in the lateral growth of the multilayer islands. It is also noteworthy that only a small percentage of the foreign particles promoted the nucleation of the multilayer islands: other foreign particles were observed on the crystal surface (Figure 4). Only microcrystals that had specific relations with the crystal surface, e.g., small angle grain boundaries, might work as heterogeneous centers of the multilayer islands.

Next, we demonstrate very peculiar 2D nucleation. In some very rare cases, many consecutive layers were formed leading to the formation of the 2D hillocks that dominated the whole surface, as shown in Figure 5. The interstep distances between the consecutive layers are irregular (bars in Figure 5). This result indicates that these islands were not formed by screw dislocations but by nucleation, as the case shown in Figure 3. We slightly dissolved the surface of the 2D hillocks by increasing temperature and found that no point-bottomed etch pit, corresponding to the outcrop of a dislocation, appeared at the center of the consecutive 2D hillock (data are not shown). Many flat- and point-bottomed etch pits appeared randomly on the 2D hillock. Nevertheless, after the decrease in temperature, the consecutive 2D islands appeared again. These observations suggest that some fibrous materials³³ (although we could not find any point-bottomed etch pit at the center) might be responsible for the formation of the consecutive 2D nucleation hillock. Further studies are necessary for clarifying the formation mechanisms.

3.2. Two-Dimensional Nucleation Rates. We have measured in situ 2D nucleation rates on the $\{110\}$ faces of the tetragonal lysozyme crystals by LCM-DIM at different supersaturations and in the presence of various impure proteins. All results are summarized in Figure 6, which includes the data of the random nucleation and the repeated nucleation for 3–4 layers. Since elementary steps on the $\{110\}$ faces involve two molecules/

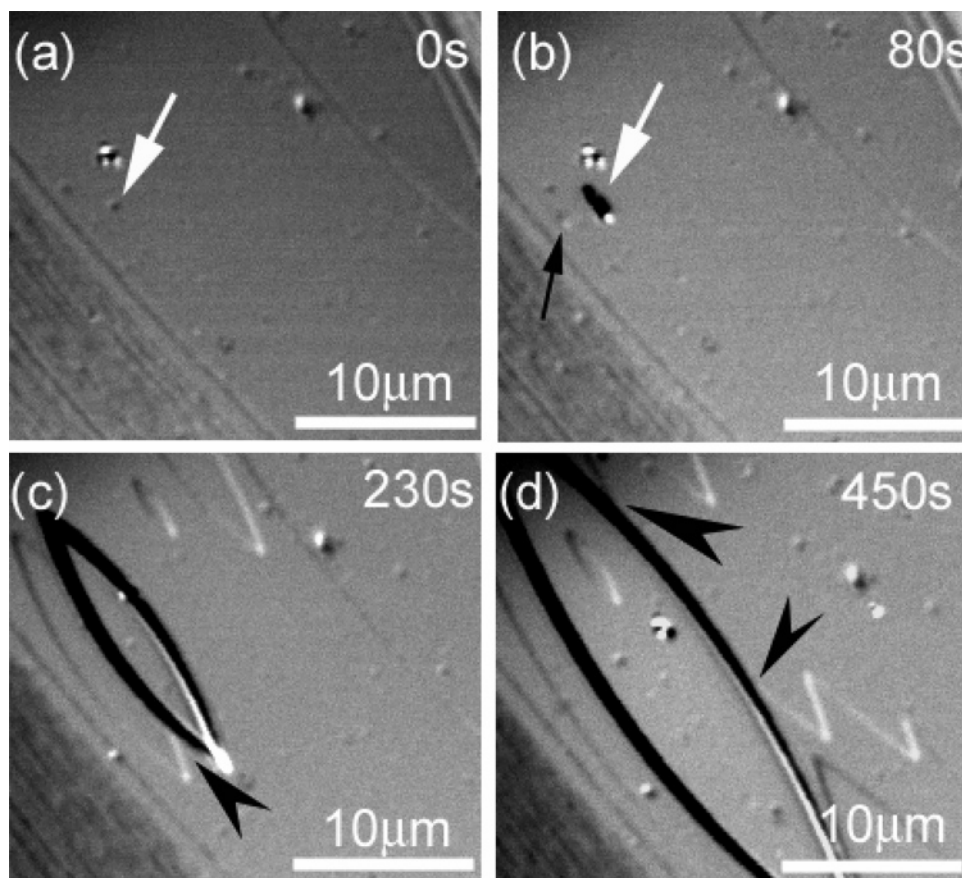


Figure 4. Photomicrographs of 2D nucleation and subsequent lateral growth of a multilayer island on a {110} face of a growing tetragonal lysozyme crystal, taken by LCM-DIM. The sequence of micrographs shows the time course of the multilayer island: 0 s (a); 80 s (b); 230 s (c); 450 s (d). White arrows indicate the presence of foreign particles on the surface. A black arrow shows the nucleation of a 2D island with elementary step height. Black arrowheads indicate the positions at which the multilayer island overgrows the single layered islands. Growth conditions: 99.99% pure lysozyme 38 mg/mL, NaCl 25 mg/mL, in 50 mM sodium acetate buffer (pH 4.5), at 23.0 °C.

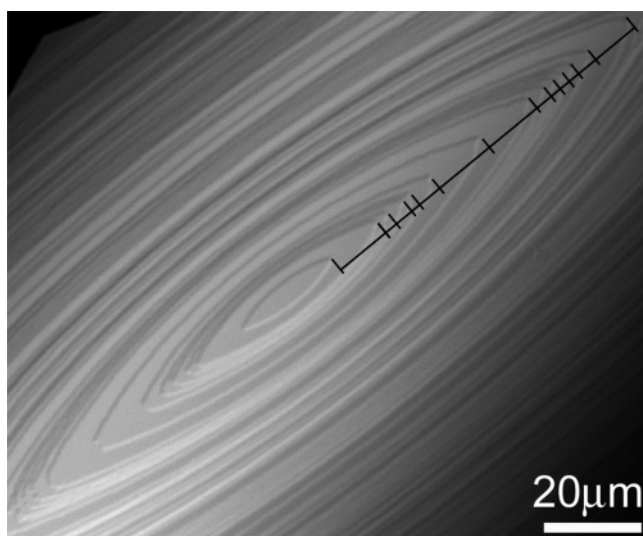


Figure 5. Photomicrograph of consecutive layers of 2D islands that dominate a whole {110} face of a growing tetragonal lysozyme crystal, taken by LCM-DIM. Bars indicate the irregular interstep distance between consecutive 2D islands. Growth conditions: 98.5% pure lysozyme 45 mg/mL, NaCl 25 mg/mL, in 50 mM sodium acetate buffer (pH 4.5), at 22.0 °C.

step,^{26–29} we considered 2D nuclei composed of a double layer. By modification of the classical expression for homogeneous 2D nucleation³⁶ considering double-layered circular islands, the

Gibbs free energy of a 2D cluster can be written as

$$\Delta G = -\frac{2\pi r^2}{s} \Delta\mu + 2\pi r \kappa \quad (2)$$

where r is a radius of a 2D cluster, $\Delta\mu$ is a chemical potential difference between molecules in a crystal and a solution, s is the area one molecule occupies inside a nucleus ($s = 1.06 \times 10^{-17} \text{ m}^2$),³⁷ and κ is a ledge free energy of a 2D cluster. From eqs 1 and 2 and following the classical nucleation theory, the steady-state 2D nucleation rate, J , can be expressed as follows:³⁶

$$\ln J = \ln(\varpi\Gamma Z) - \frac{\pi s \kappa^2}{2k^2 T^2 \ln(C/C_e)} \quad (3)$$

Here ϖ is an attachment frequency of a solute molecule to a critical nucleus, Γ the Zeldovich factor, Z a 2D concentration of solute molecules on a crystal surface, k the Boltzman constant, C a solute concentration, and C_e the solubility.

Figure 6 shows changes in $\ln J$ as a function of $1/[T^2 \ln(C/C_e)]$. On the {110} faces, excellent linear relationship was found for all the data points under a higher supersaturation range $\sigma > 0.80$ (orange solid line). This result demonstrates clearly that these data can be satisfactorily expressed by eq 3 and the impurities did not affect the 2D nucleation rates in this higher supersaturation range, that is, homogeneous 2D nucleation.

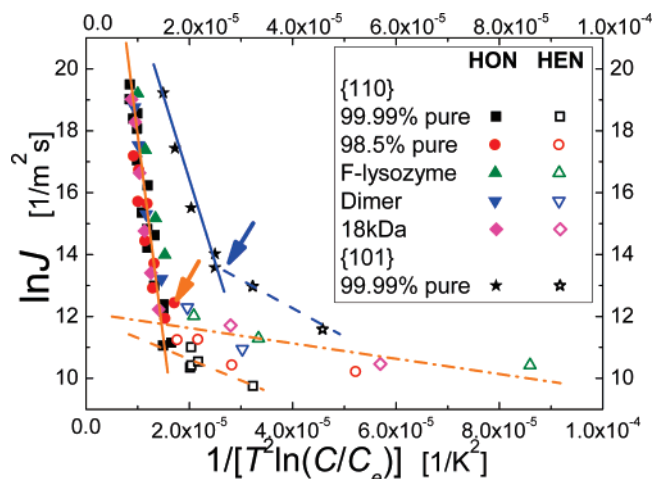


Figure 6. Changes in $\ln J$ as a function of $1/[T^2 \ln(C/C_e)]$, measured on $\{110\}$ and $\{101\}$ faces of tetragonal lysozyme crystals. Here, J is a 2D nucleation rate, T absolute temperature, C solute concentration, and C_e the solubility. HON and HEN denote homogeneous and heterogeneous nucleation, respectively. Orange and blue solid lines represent homogeneous 2D nucleation under a higher supersaturation range, orange and blue broken lines are for heterogeneous 2D nucleation in the purified lysozyme solution under a lower supersaturation range, and an orange dash-dotted line is for heterogeneous 2D nucleation in the solution containing impure proteins under a lower supersaturation range. Arrows show kinks, at which solid and broken lines intersect each other. Impurity concentrations of F-lysozyme, dimer, and 18kDa were 0.1%. The 98.5% pure lysozyme contained 0.5% dimer and 1.0% 18kDa. Growth conditions: supersaturation $\sigma = 0$ –1.4, NaCl 25 mg/mL, in 50 mM sodium acetate buffer (pH 4.5), at 18.0–26.0 °C.

However, the plots of the lysozyme with impurities exhibit a kink at the middle supersaturation $\sigma \approx 0.80$ (orange arrow), leading to the line with much smaller slope under a lower supersaturation range $\sigma < 0.80$ (orange dash-dotted line). This smaller slope indicates the occurrence of heterogeneous 2D nucleation in this lower supersaturation range.

On the $\{110\}$ faces, even 99.99% pure lysozyme shows four data points (orange broken line in Figure 6), at lower supersaturation $\sigma < 0.80$, that deviate from the linear relationship found under the higher supersaturation range. Taking into account the fact that the 99.99% pure lysozyme solution contained impure molecules less than 0.01%, we can point out that the presence of a very small amount of impurities can influence the growth kinetics of protein crystals, as in the case of inorganic crystals. Although data are not shown, a certain induction time was observed for impurity effects on 2D nucleation. In the case of dimer, 1 day after the replacement of the solution in the cell with that containing dimer, the heterogeneous 2D nucleation became more pronounced. In contrast, in the case of F-lysozyme, a couple of hours after the replacement were enough to observe the significant heterogeneous 2D nucleation. The difference in the adsorption kinetics of these impure proteins would be responsible. Further studies are necessary to clarify the details of the adsorption kinetics. Also in the case of F-lysozyme, at concentrations as low as 0.01%, heterogeneous nucleation could be observed (data not shown); this is an important indication that the heterogeneous nucleation observed for the purified solution (99.99%) was also caused by impure molecules.

Regarding the heterogeneous 2D nucleation under the lower supersaturation range ($\sigma < 0.80$), we also point out the possible contribution of strain induced on the crystal surfaces. After we grew the seed crystals in 98.5% pure lysozyme solutions, the crystals were grown in lysozyme solutions of different purity.

Hence, we can suppose that strain was induced in the crystals (origin of striations). However, in the case of 98.5% pure solutions (Seikagaku Co.), seed crystals did not experience the replacement of solutions with different purity; hence, such seed crystals did not include the strain induced by different purity. As shown in Figure 6, all the plots (including 98.5% pure lysozyme solutions) under the lower supersaturation range looked to follow the same line (orange dash-dotted line). Therefore, we expect that the possible contribution of the strain was not so significant under the experimental conditions used in this study, although we cannot exclude the effects of strain because of the small number of the data points measured in this supersaturation range. In contrast, under the higher supersaturation range ($\sigma > 0.80$), such strain did not give any significant effects since the large number of the data points clearly followed the same single line (orange solid line). Further systematic studies are necessary to clarify influence of strain on heterogeneous 2D nucleation in the near future.

The 2D nucleation rates measured on the $\{101\}$ faces for the 99.99% pure lysozyme are also summarized in Figure 6. In the case of $\{101\}$ faces, since elementary steps on the $\{101\}$ faces involve one molecule/step,^{26–29} the steady-state 2D nucleation rate J can be written as follows, according to the classical nucleation theory:³⁶

$$\ln J = \ln(\omega \Gamma Z) - \frac{\pi s \kappa^2}{k^2 T^2 \ln(C/C_e)} \quad (4)$$

Here $s = 7.84 \times 10^{-18} \text{ m}^2$.³⁷ As shown in Figure 6, very similar results were obtained on the $\{101\}$ faces. The $\ln J$ vs $1/[T^2 \ln(C/C_e)]$ plots exhibit a kink at $\sigma \approx 0.45$ (blue arrow), providing two straight lines corresponding to the homogeneous and heterogeneous 2D nucleation under high and low supersaturation ranges, respectively. Note that the homogeneous nucleation of the $\{101\}$ faces (blue solid line) shows a smaller slope (smaller ledge free energy) than in the case of the $\{110\}$ faces. This would correspond to the smaller step height (3.4 nm) of the $\{101\}$ faces than that of the $\{110\}$ faces (5.6 nm). It is also note worthy that much more significant heterogeneous 2D nucleation (blue broken line) was promoted on the $\{101\}$ faces than on the $\{110\}$ faces (orange broken line) by small amount of impurities ($< 0.01\%$) present in the 99.99% pure lysozyme solution. This result indicates that different crystal structure of the $\{101\}$ face from that of the $\{110\}$ face would result in the larger amount of impurity effects, as reported in the case of F-lysozyme²² and dimer.^{38,39}

Heterogeneous 2D nucleation under a low supersaturation range was for the first time reported in protein crystallization by Malkin et al.^{1,2} using AFM. They observed directly the appearance of individual 2D islands under a low supersaturation range for thaumatin^{1,2} and catalase.² They suggested that nucleation in the low supersaturation range occurred at hyperactive sites, e.g., on impurity particles and defects. In addition, molecular-level lateral resolution of AFM provides the possibility to observe near-critical-size clusters and their structure, as demonstrated by Yau and Vekilov.⁴⁰ However, Land et al.³ reported that the growth rates of canavalin crystals were enhanced by the scan of a cantilever of AFM, and Gliko et al.⁴ also argued that the variations in the step velocities of lumazine synthase crystals measured by AFM would result from the effects of a cantilever. Hence, the scan of a cantilever potentially affects the kinetics of 2D nucleation, although further detailed studies are necessary. In the case of the indirect measurements of normal growth rates by traditional optical microscopy and

Table 1. Ledge Free Energies κ (J/m) and Surface Free Energies α (mJ/m²) Obtained by the Linear Curve Fittings of the Experimental Data Shown in Figure 6 Using Eqs 3 and 4^a

species	slope	κ (J/m)	α (mJ/m ²)	α of other study (mJ/m ²)
{110} Faces				
HON	$(1.05 \pm 0.10) \times 10^6$	$(3.5 \pm 0.2) \times 10^{-12}$	0.62 ± 0.03	$0.62 \pm 0.08^*$
HEN 99.99% pure	$(7.03 \pm 2.8) \times 10^4$	$(0.89 \pm 0.2) \times 10^{-12}$	0.16 ± 0.03	
HEN impurities	$(2.10 \pm 0.89) \times 10^4$	$(0.5 \pm 0.1) \times 10^{-12}$	0.09 ± 0.02	
{101} Faces				
HON	$(5.42 \pm 0.51) \times 10^6$	$(2.0 \pm 0.1) \times 10^{-12}$	0.60 ± 0.02	$0.64 \pm 0.13^*$
HEN 99.99% pure	$(1.04 \pm 0.06) \times 10^4$	$(0.90 \pm 0.04) \times 10^{-12}$	0.26 ± 0.01	

^a α was calculated as $\alpha = \kappa/h$, where h is a step height (5.6 nm for {110} faces and 3.4 nm for {101} faces); HON and HEN denote homogeneous and heterogeneous 2D nucleation, respectively. Asterisks indicate values obtained by analyzing normal growth rates in 98.5% pure lysozyme (from Seikagaku Co.) solutions using the birth-and-spread model.^{5,41}

interferometry,^{5–10,41} no one has yet succeeded in observing the heterogeneous 2D nucleation of protein crystals, since normal growth rates of protein crystals are too slow at low supersaturation to obtain reliable data. Therefore, noninvasive and direct observation by advanced optical microscopy would have the highest potential to clarify 2D nucleation kinetics in protein crystallization.

From eq 3 and the slopes in Figure 6, we determined the ledges free energies on the {110} faces. The values for the homogeneous and heterogeneous nucleation were summarized in Table 1. From the linear fitting of all data points under the higher supersaturation range $\sigma > 0.8$, the ledge free energy for the homogeneous 2D nucleation (HON in Table 1) was obtained and also obtained was the ledge free energy for the heterogeneous 2D nucleation (HEN in Table 1) from the linear fits for the data points of the 99.99% pure solution and the solutions containing impurities under the lower supersaturation range, $\sigma < 0.8$. Kurihara et al.⁵ measured, by traditional optical microscopy, normal growth rates of {110} and {101} faces of tetragonal lysozyme crystals, under the same crystallization conditions adopted in this study (using 98.5% pure lysozyme, Seikagaku Co.). They found no heterogeneous 2D nucleation under a lower supersaturation range, because of the measurements of averaged normal growth rates. By analyzing normal growth rates under a higher supersaturation range with the birth-and-spread model and considering double layered 2D islands, Kurihara et al.⁴¹ obtained a value of $\alpha = 0.62$ mJ/m². This value agrees very well with our value for the homogeneous 2D nucleation. It is also note worthy that the ledge free energy of the heterogeneous nucleation for the 99.99% pure solution is larger than that for the solutions intentionally containing impure proteins. This would result from the difference in the impurity concentrations.

The ledge free energies on the {101} faces determined from eq 4 and the slopes in Figure 6 were also summarized in Table 1. For the homogeneous 2D nucleation, we obtained smaller ledge free energy on the {101} faces than on the {110} faces, as discussed above. However, note that the surface free energies of the step ledges of the {101} and {110} faces are almost the same. This result clearly demonstrates that the difference in the ledge free energies of the {101} and {110} faces resulted from the difference in the step heights, as already pointed out by Kurihara.⁴¹ Our value of the homogeneous nucleation for the {101} faces also agrees very well with that reported by Kurihara.⁴¹

Galkin et al.⁴² measured three-dimensional (3D) nucleation rates of tetragonal lysozyme crystals under the same conditions using 98.5% pure lysozyme (Seikagaku) and obtained a value of 0.64 mJ/m². This value also agrees well with our data obtained for the {110} and {101} faces. From this result, we can conclude that there is no intrinsic difference between the

surface free energies obtained from 2D and 3D nucleation rates, when intermolecular bonding inside a crystal is relatively symmetrical.

In the case of the 99.99% pure solution, the critical supersaturation σ^* for the {110} faces, below which 2D nucleation could not be observed, was $\sigma^* \approx 0.4$, and it was $\sigma^* \approx 0.2$ in the case of the solutions containing impurities. Below the critical supersaturation, no new 2D island appeared and growth only occurred at the steps of the 2D islands that had already existed on the crystal surface. Once these steps completely spread over the entire surface, crystal growth stopped. In the field of structure analyses, it is generally believed that the advancement of steps is blocked by impurities under a low supersaturation range: this supersaturation range is called the dead zone. However, by direct observation, we could observe that, in the case of the tetragonal lysozyme crystals, there was no such dead zone caused by impurities. Although Vekilov et al.⁴³ indirectly suggested the absence of such dead zone by interferometry, this study provided the direct evidence for the absence of the impurity-induced dead zone in protein crystallization.

In this study, we have demonstrated that impurities promote heterogeneous 2D nucleation under a low supersaturation range, even at very low impurity concentrations (0.01%); hence, impurities of low concentration can be potentially used under a low supersaturation range to promote growth of protein crystals large enough to give high-resolution diffraction spots, since very small amounts of impurities do not give measurable effects on crystal quality,³⁹ although a very long time period will be necessary for obtaining such crystals. The addition of small amounts of impurities would also be useful for promoting 3D nucleation, as in the case of the dimers that are produced photochemically by UV light irradiation significantly promote heterogeneous 3D nucleation of lysozyme crystals under a metastable supersaturation range, in which homogeneous 3D nucleation hardly occurs.^{44–46}

4. Conclusions

We have measured, directly and noninvasively, the 2D nucleation rates on the {110} and {101} face of the tetragonal lysozyme crystals by LCM-DIM. Key results found in this paper are as follows:

(1) The 2D nucleation occurred randomly on the entire crystal surface, whose crystal size ranged from 0.2 to 0.3 mm, within the range of supersaturation $\sigma = 0–1.4$. The 2D nucleation was the dominant growth mechanism for the tetragonal lysozyme crystals under the conditions used in this study. The spiral growth was occasionally observed only when microcrystals were adsorbed on the crystal surface or the crystals suffered mechanical stress.

(2) The repeated 2D nucleation, continued for 3–4 layers, was observed mainly when the impure proteins were present in

the solution. The interstep distances of the concentric 2D islands generated repeatedly were irregular. The multilayer 2D islands were formed when relatively large foreign particles were adsorbed on the crystal surface. In some very rare case, many consecutive layers were formed leading to the formation of the 2D hillocks that dominated the whole surface.

(3) On the {110} faces, the homogeneous 2D nucleation occurred under the higher supersaturation range $\sigma > 0.8$, irrespective of the presence of the impure proteins. In contrast, the significant heterogeneous 2D nucleation was observed under the lower supersaturation range $\sigma < 0.8$, mainly when the impure proteins were present in the solution. The {101} faces exhibited the similar homogeneous and heterogeneous 2D nucleation; however, the {101} faces showed more significant heterogeneous nucleation than the {110} faces in the case of the 99.99% pure lysozyme solutions.

(4) The ledge free energies of the homogeneous and heterogeneous 2D nucleation were determined. The latter did not show significant dependence on the kinds of impure proteins within the experimental conditions adopted in this study. The difference in the ledge free energies of the homogeneous nucleation on the {110} and {101} faces could be satisfactorily explained by the difference in the step heights.

Acknowledgment. We thank Drs. K. Kurihara and T. Nakada for their valuable discussions. We are grateful for the support by Grant No. 2002-03397 from the Ministry of Education and Science of Spain (F.O.) and the partial support by Grants-in-Aid Nos. 17034007 and 18360003 from the Scientific Research of the Ministry of Education, Science, and Culture of Japan (G.S.). This work was partially supported by Project Research B in the Center for Interdisciplinary Research, Tohoku University. This work has been carried out as a part of "Ground-based Research Announcement for Space Utilization" promoted by the Japan Space Forum.

References

- Malkin, A. J.; Kuznetsov, Yu. G.; Glantz, W.; McPherson, A. *J. Phys. Chem.* **1996**, *100*, 11736–11743.
- Malkin, A. J.; Kuznetsov, Yu. G.; McPherson, A. *J. Cryst. Growth* **1999**, *196*, 471–488.
- Land, A.; T.; Malkin, A. J.; Kuznetsov, Yu. G.; McPherson, A.; De Yoreo, J. J. *J. Cryst. Growth* **1996**, *166*, 893–899.
- Gliko, O.; Neumaier, N.; Pan, W.; Haase, I.; Fischer, M.; Bacher, A.; Weinkauff, S.; Vekilov, P. G. *J. Am. Chem. Soc.* **2005**, *127*, 3433–3438.
- Kurihara, K.; Miyashita, S.; Sazaki, G.; Nakada, T.; Suzuki, Y.; Komatsu, H. *J. Cryst. Growth* **1996**, *166*, 904–908.
- Kashimoto, E.; Sazaki, G.; Hasegawa, K.; Nakada, T.; Miyashita, S.; Komatsu, H.; Sato, K.; Matsuura, Y.; Tanaka, H. *J. Cryst. Growth* **1998**, *186*, 461–470.
- Suzuki, Y.; Miyashita, S.; Sazaki, G.; Nakada, T.; Sawada, T.; Komatsu, H. *J. Cryst. Growth* **2000**, *208*, 638–644.
- Nagatoshi, Y.; Sazaki, G.; Suzuki, Y.; Miyashita, S.; Matsui, T.; Ujihara, T.; Fujiwara, K.; Usami, N.; Nakajima, K. *J. Cryst. Growth* **2003**, *254*, 188–195.
- Asai, T.; Suzuki, Y.; Sazaki, G.; Tamura, K.; Sawada, T. *Cell. Mol. Biol.* **2004**, *50*, 329–334.
- Suzuki, Y.; Sazaki, G.; Matsui, T.; Nakajima, K.; Tamura, K. *J. Phys. Chem. B* **2005**, *109*, 3222–3226.
- Malkin, A. J.; Chernov, A. A.; Alexeev, I. V. *J. Cryst. Growth* **1989**, *97*, 765–769.
- Kanzaki, N.; Onuma, K.; Treboux, G.; Tsutsumi, S.; Ito, A. *J. Phys. Chem. B* **2001**, *105*, 1991–1994.
- Tsukamoto, K. *J. Cryst. Growth* **1983**, *61*, 199–209.
- Tsukamoto, K.; Yai, S.; Sazaki, G. *J. Jpn. Assoc. Cryst. Growth* **2003**, *30*, 81 (in Japanese).
- Yai, S. Graduation Thesis, Tohoku University, 2003.
- Dold, P.; Ono, E.; Tsukamoto, K.; Sazaki, G. *J. Cryst. Growth* **2006**, *293*, 102–109.
- Dold, P.; Nishimura, Y.; Tsukamoto, K.; Yokoyama, E.; Sazaki, G. *J. Cryst. Growth*, submitted for publication.
- Sazaki, G.; Matsui, T.; Tsukamoto, K.; Usami, N.; Ujihara, T.; Fujiwara, K.; Nakajima, K. *J. Cryst. Growth* **2004**, *262*, 536–542.
- Sazaki, G.; Tsukamoto, K.; Yai, S.; Okada, M.; Nakajima, K. *Cryst. Growth Des.* **2005**, *5*, 1729–1735.
- Onuma, K.; Kameyama, T.; Tsukamoto, K. *J. Cryst. Growth* **1994**, *137*, 610–622.
- Dold, P.; Nishimura, Y.; Van Driessche, A.E.S.; Tsukamoto, K.; Sazaki, G. To be submitted for publication.
- Matsui, T.; Sazaki, G.; Hondoh, H.; Matsuura, Y.; Nakada, T.; Nakajima, K. *J. Cryst. Growth* **2006**, *293*, 415–422.
- Thomas, B. R.; Vekilov, P. G.; Rosenberger, F. *Acta Crystallogr., Sect. D: Biol. Crystallogr.* **1996**, *52*, 776–784.
- Durbin, S. D.; Feher, G. *J. Cryst. Growth* **1986**, *76*, 583–592.
- Sazaki, G.; Kurihara, K.; Nakada, T.; Miyashita, S.; Komatsu, H. *J. Cryst. Growth* **1996**, *169*, 355–360.
- Durbin, S. D.; Feher, G. *J. Mol. Biol.* **1990**, *212*, 763–774.
- Durbin, S. D.; Carlson, W. E. *J. Cryst. Growth* **1992**, *122*, 71–79.
- Konnert, J. H.; D'Antonio, P.; Ward, K. B. *Acta Crystallogr., Sect. D: Biol. Crystallogr.* **1994**, *50*, 603–613.
- Li, H.; Nadarajah, A.; Pusey, M. L. *Acta Crystallogr., Sect. D: Biol. Crystallogr.* **1999**, *55*, 1036–1045.
- Berg, W. F. *Proc. R. Soc.* **1938**, *A164*, 79–95.
- Vekilov, P. G.; Monaco, L. A.; Rosenberger, F. *J. Cryst. Growth* **1995**, *156*, 267–278.
- Lin, H.; Vekilov, P. G.; Rosenberger, F. *J. Cryst. Growth* **1996**, *158*, 552–559.
- Hondoh, H.; Nakada, T. *J. Cryst. Growth* **2005**, *275*, e1423–e1429.
- Liu, X. Y.; Maiwa, K.; Tsukamoto, K. *J. Chem. Phys.* **1997**, *106*, 1870–1879.
- Chernov, A. A. *J. Cryst. Growth* **1997**, *174*, 354–361.
- Markov, I. V. *Crystal Growth for Beginners*, 2nd ed.; World Scientific Publishing Co. Pte. Ltd.: Singapore, 2003; Chapter 2, pp 86–108.
- Nadarajah, A.; Li, M.; Pusey, M. L. *Acta Crystallogr., Sect. D: Biol. Crystallogr.* **1997**, *53*, 524–534.
- Nakada, T.; Sazaki, G.; Miyashita, S.; Durbin, S. D.; Komatsu, H. *J. Cryst. Growth* **1999**, *196*, 503–510.
- Yoshizaki, I.; Kadowaki, A.; Iimura, Y.; Igarashi, N.; Yoda, S.; Komatsu, H. *J. Synchrotron Radiat.* **2004**, *11*, 30–33.
- Yau, S.-T.; Vekilov, P. G. *Nature* **2002**, *406*, 494–497.
- Kurihara, K. Ph.D. Thesis, Graduate School of Science, Tohoku University, 1997. The normal growth rates reported previously⁵ were recalculated using the solubility determined posteriorly.²⁵
- Galkin, O.; Vekilov, P. G. *J. Am. Chem. Soc.* **2000**, *122*, 156–163.
- Vekilov, P. G.; Rosenberger, F. *J. Cryst. Growth* **1996**, *166*, 540–551.
- Okutsu, T.; Furuta, K.; Terao, M.; Hiratsuka, H.; Yamano, A.; Ferte, N.; Veessler, S. *Cryst. Growth Des.* **2005**, *5*, 1393–1398.
- Veessler, S.; Furuta, K.; Horiuchi, H.; Hiratsuka, H.; Ferte, N.; Okutsu, T. *Cryst. Growth Des.* **2006**, *6*, 1631–1635.
- Okutsu, T.; Sugiyama, K.; Furuta, K.; Watanabe, I.; Mori, H.; Obi, K.; Horota, K.; Horiuchi, H.; Sazaki, G.; Hiratsuka, H. *J. Cryst. Growth*, in press.